Fluorescent Molecular Hydrogen in the Reflection Nebula NGC 2023

Michael Stephan Karl McCartney

Presented for the Degree of Doctor of Philosophy
The University of Edinburgh
1997

Contents

List of Tables

Acknowledgements

I wish to firstly thank my family: my Mother and Father for their constant encouragement and support during my time at university and my brother Andy and his wife Jenny for their interest and worldly advice. I would also like to thank my supervisor Peter Brand for our many discussions (including the ones we had over raw fish and beer!) and without whom none of this would have been possible and I might have ended up working in Barclays Bank like the rest of my family - thanks for the narrow escape! I would like to thank Mike Burton and Antonio Chrysostomou for their many useful discussions, Suzie Ramsay and Adrian Webster for helping answer my questions and their many useful comments on this thesis.

I have been very lucky being given office mates who became such good friends: Richard for our regular games of 'White-board Connect 4', Bill for making me laugh by a) looking like Garth for three years b) making fun of me going to a boarding school c) being a regular source of rude jokes while I was here, Henry for being 'fluffy, bunny, squirrelkins' and soon to be weather-man and all three for taking the time to bounce ideas around with generally inspiring conversations. I would like to mention a few people who left the Observatory a while ago but I haven't forgotten: Ale for giving me the nickname 'Bianca' (from Eastenders), Harry for being the Jimmy Tarbuck of the Observatory and for being a great source of encouragement when morale was low and 'Scary Rach' for the group hugs! Many other people have helped me in numerous ways including my old flatmate Jo for giving the lower terminal room a sense of 'Winnie the Pooh-ness' and for taking a genuine interest in how things were going and enthusiastically checking up on the fact that I was writing up.

Other acknowledgements I would like to include, for less animated objects, go to: the Royal Observatory for providing an ivory tower so conducive to working in, Blackford Hill for keeping me fit cycling up it, my bike brakes for keeping me alive cycling down it and the area (including duck pond) for being the perfect place to go for walks and get my head together. I would also like to acknowledge the many trees that went into making this thesis.

I would like to acknowledge the author of LaTeX, Leslie Lamport, for producing such a powerful and user-friendly publishing package which made writing up a joy rather than an arduous task. During my PhD I made much use of the SIMBAD database of the Astronomical Data Centre in Strasbourg, France and was greatly assisted by resources found on the World Wide Web especially the NASA Abstracts and Article Data Service housed at Harvard. Finally, I acknowledge the financial support of the funding bodies PPARC and the DSS.

This thesis is dedicated to my Mother and Father

This thesis is my own composition except where specifically indicated in the text.

January 25, 1998

Abstract

Photodissociation regions (PDRs) are described in the context of the interstellar medium and star-forming regions. Observations of PDRs and molecular hydrogen are reviewed and the reflection nebula NGC 2023 is discussed in detail. NGC 2023 is a bright and well-studied reflection nebula at a distance of 450 parsecs in the Orion region. Illuminated primarily by a B-type star, it offers an ideal opportunity to study UV-excited molecular hydrogen.

The theory of the hydrogen molecule is described: the energy states and their relationship with the quantum numbers which represent the vibrational and rotational states of the molecule, the radiative processes which determine the optical and infrared emission spectrum of H_2, the effect collisions have on the excited states of the molecule and the processes which govern the formation and destruction of H_2. Particular attention is given to the process of formation on the surface of dust grains and the resulting energy states of the ejected H_2 molecule.

Infrared and optical far-red observations of fluorescent H_2 line emission from NGC 2023 are presented. The resulting datasets contain flux measurements of over ninety lines. These are combined with published data to produce column densities for 81 energy states of the H_2 molecule, the most extensive dataset yet compiled for a PDR. The processes of observing in the infrared and optical wavelength regimes are outlined. The emission lines of H_2 are intrinsically very faint and thus measurements require careful data reduction to minimise sources of noise wherever possible. The data reduction steps which were applied to the observations are described in detail. An optical extinction of $A_v = 5.7 \pm 1.0$ to the H_2 emission region and ortho/para abundance ratio of 2.0 ± 0.2 are derived from flux ratios of emission lines and by minimising the scatter on a diagram which plots the logarithm of the column density against the energy level of each state.

The theory of photodissociation regions is summarised and the effect of the incident ultraviolet radiation field and hydrogen nucleus number density on the H_2 emission spectrum is discussed. Steady-state and time-dependent PDR models are reviewed and their predictions are compared to the observational data. Deviations from the pure fluorescent case are apparent; the $v = 1$ vibrational level displays a column density distribution indicative of collisional processes. There is also strong evidence for a trend within each vibrational level, for $v > 1$, whereby excess populations increase with rotational level, J, with a possible 'turnover' and peak excess at high J. The overall intensity of the H_2 emission lines is an order of magnitude greater than that predicted by face-on, steady-state PDR models. The emission can be explained by intense ultraviolet radiation ($G_0 \simeq 5 \times 10^3$) incident on dense gas ($n \sim 10^5\,\mathrm{cm}^{-3}$) at a high temperature ($T \sim 1000\,\mathrm{K}$). The ortho/para abundance ratio is discussed and it is proposed that the observed PDR in NGC 2023 has not yet reached equilibrium and the photodissociation front, which is advancing into the molecular cloud, is more accurately described by time-dependent PDR models.

Chapter 1

Introduction

1.1 Star Formation

This thesis is devoted to the understanding of the star-forming environment. Direct observations of star formation, deep within molecular clouds, suffer the effects of considerable obscuration. However, studying the byproducts and deriving diagnostic measures lead to an understanding of the processes and conditions which contribute to the cycle of star formation. This thesis does not directly address the subjects of infall or protostars themselves but is concerned with the study of the environment where star formation takes place and the effects it has on that environment, in particular the response of molecular hydrogen. This is by far the most abundant molecule from which all stars form, and this thesis concentrates on the way it interacts with ultraviolet radiation from newly formed stars. A cloud of molecular hydrogen which fluoresces due to exposure to ultraviolet radiation is termed a photodissociation region. To understand its relevance to star formation it is useful to step back and review the whole cyclic process and then focus on the regions where molecular hydrogen is observable. This chapter outlines star formation and the place photodissociation regions occupy within it.

The Milky way contains $\sim 10^{11}$ stars which cover the complete range of spectral type with ages ranging from 14 giga-years in globular clusters (Winget et al. 1987; Wood 1992) to short-lived OB-type stars in associations with dynamical ages of 10^7 years. The presence of protostars has recently been inferred from submillimetre detections of molecular line profiles consistent with infall (Ward-Thompson et al. 1996). Star formation is therefore an ongoing process and has been established to occur within the dense cores of interstellar molecular clouds (Zuckerman & Palmer 1974; Burton 1976; Lada 1992). There are probably several kinds of events which can trigger star formation. The fact that young stars are often found at the edge of molecular clouds (Loren 1976) may suggest that star formation can be set off by an impact from the outside causing a wave of compression to penetrate into the interior of the cloud. Collisions of interstellar clouds and galaxies passing close by each other may also provide a means by which stars form. The rate at which low mass stars evolve is governed by ambipolar diffusion in clouds which are supported magnetically against gravitational collapse. This depends on the ionisation of the cloud due to the interstellar ultraviolet (UV) radiation field (McKee 1989) and cosmic rays. The formation of stars is accompanied by the release of large quantities of kinetic energy, angular momentum and matter, into the parent molecular cloud, in the form of highly energetic outflows and by radiation of Alfvén waves. The rate at which the surrounding envelope disperses depends primarily on the mass and hence temperature of the star. Newly formed B-type stars produce large quantities of UV photons which erode the surrounding cloud and cause it to fluoresce. Unlike massive O-type stars they do not produce sufficient ionising radiation to create significant ionised hydrogen (HII) regions which would disrupt further star formation (Whitworth 1979). B-type stars often create reflection nebulae and are still young enough to be physically associated with the clouds from which they formed. As such they provide conspicuous signposts to star-forming regions and are the obvious places to explore when searching for quiescent molecular hydrogen emission. The specific environment where this occurs are photodissociation regions. The above processes regulate

the structure of molecular clouds and the rate at which stars form. In the absence of high mass star formation, the gas typically takes of the order of 10^8 years to be converted into a star (McKee 1989). The process of star formation is cyclic whereby stars return matter and energy to the interstellar medium (ISM) from which they were formed. The process is important in terms of describing the structure, evolution and radiation field of the galaxy at both large and small scales.

The contents of this thesis are devoted to the study of the interstellar medium where ultraviolet radiation is incident on dense molecular hydrogen (*i.e.* $n > 10^3\,\mathrm{cm}^{-3}$; where n is the hydrogen nucleon number density). The last two decades have seen the arrival of technology which has opened up possibilities for new areas of observational study. Advances in instrumentation such as UV detectors and increased sensitivities of optical and infrared pixel arrays have now enabled the detailed study of molecular hydrogen. This thesis makes use of recent advances in infrared detector technology and optical CCD detectors, presenting observations of the reflection nebula NGC 2023. The results presented herein are typical of the Galactic star-forming environment but may also be applied more generally to the understanding of molecular hydrogen in other regions such as planetary nebulae and starburst galaxies.

1.2 Photodissociation Regions and Molecular Clouds

Interstellar clouds form from massive condensations of interstellar matter and agglomerations of small clouds (Elmegreen 1990). They appear as sources of continuum and line emission or a weakening of background radiation. Local increases of interstellar extinction or weakening of the surface brightness of nebulae, as observed at visible wavelengths, are usually caused by cold interstellar clouds known as dark clouds. Giant molecular clouds are the most massive physical entities in the Galaxy, $\geq 10^5 M_\odot$ (Solomon et al. 1979). They are observed to be inhomogeneous with clumps having a radius of several parsecs (Perault et al. 1985). Most of the molecular mass is confined to clumps that fill only a small fraction of the volume (*e.g.* Lada, Bally & Stark 1991; Bertoldi & McKee 1992; Williams, Blitz & Stark 1995). They are discrete objects with well defined boundaries suggesting that there are phase transitions at the edges of molecular clouds (Blitz & Thaddeus 1980). Lines visible in the infrared and microwave region are caused mostly by vibrational and rotational transitions of molecules. The most intense emission line sources with the greatest variety of molecules are observed in the vicinity of HII regions. Photodissociation regions (PDRs) are found at the edges of HII regions and are often associated with reflection nebulae which occur where one or more sufficiently bright B2 or earlier spectral type stars are next to a cloud rich in interstellar dust. B-type stars have very weak Lyman continuum emission but can form prominent shells of warm, dissociated hydrogen around their small HII regions. The surface luminosity of a reflection nebula depends on the contribution of scattering to the extinction. The resulting spectral profile is continuous in the optical and corresponds to a superposition of the spectra of each of the stars making significant contributions. The nebulae appear bluer than the illuminating stars due to the increase of interstellar scattering towards shorter wavelengths. PDRs emit brightly in infrared, millimeter and submillimetre line emission. They also account for most of the infrared grain emission in our galaxy and presumably in external galaxies.

Photodissociation regions exist wherever ultraviolet radiation with energy ranging 6–13.6 eV is incident on molecular hydrogen. This occurs at the edges of molecular clouds, often at the interfaces of HII regions. It is the region where ultraviolet photons in the wavelength range 912–1110 Å are absorbed by either molecular hydrogen or dust. Examples of PDRs include dense circumstellar envelopes around newly formed massive stars, reflection nebulae, planetary nebulae, interstellar gas near the nuclei of galaxies and the diffuse interstellar medium. PDRs are the typical environment of the interstellar medium where, by definition, nearly all of the atomic gas resides. The term PDR in this thesis refers to the region where most of the UV radiation is absorbed. These are the infrared-bright surface layers of neutral gas which contain the photodissociated hydrogen. This is in contrast to the cold, low ionisation gas which is dominated thermally and chemically, by UV photons, deep into the molecular cloud. This 'UV-photon-dominated region', often referred to by the same acronym, includes most of the molecular mass of the ISM. The ultraviolet interstellar radiation field significantly affects the chemistry to $A_v \simeq 4$ from the surface of molecular clouds,

and the typical half-thickness through a molecular cloud in the Galaxy is $A_v \simeq 4$ (Solomon et al. 1987). This definition therefore includes nearly all the ISM since only a small fraction of molecular gas is sufficiently shielded that cosmic rays are the main source of ionisation.

Another related class of object which has recently come into study is the X-ray dissociation region (XDR). Where X-rays, instead of UV photons, irradiate molecular gas (*e.g.* in active galactic nuclei, fast shocks, compact accreting objects and young stellar objects with X-ray chromospheres) photo-ionised electrons collisionally excite molecular hydrogen. This causes an infrared response, similar to that found in a PDR, which originates primarily from the first and second vibrational states of the H_2 molecule (Maloney et al. 1996; Tiné et al. 1997). This is a very new area investigation and detailed observations of molecular hydrogen emission from these objects have yet to be made.

1.3 Observations of UV-excited Molecular Clouds

1.3.1 Molecular Hydrogen Observations

Eddington (1937) first suggested that molecular hydrogen could be an important component of the interstellar medium. However it was only until ultraviolet detector and rocket technology had been developed that the first detections of H_2 in the interstellar medium were made (*e.g.* Carruthers 1970). The *Copernicus* satellite followed these observations with further absorption line studies of the Lyman and Werner bands along the line of sight to OB stars (Rogerson et al. 1973). These observations demonstrated that the ratio of molecular to atomic hydrogen is determined primarily by the balance of formation on dust grains and destruction by photoabsorption of ultraviolet photons from the interstellar radiation field. Another important discovery from the *Copernicus* satellite observations was that the fraction of hydrogen in molecular form, integrated over the line of sight, increases dramatically at $A_v \geq 0.5$ (Savage et al. 1977). This sharp transition from atomic to molecular form is due to line self-shielding of H_2 from photodissociation.

The infrared response of molecular hydrogen to ultraviolet radiation was first noted by Gould & Harwit (1963). However, it was only in 1985 that infrared detectors had become sufficiently sensitive to permit its detection (Gatley et al. 1987; Gatley & Kaifu 1987; Hasegawa et al. 1987; Sellgren 1986). The first optical detections of H_2 emission were carried out five years later by Burton et al. (1992a) who observed over 30 transitions arising from excitation levels of up to 41,000 K. The first source to be observed in fluorescent infrared H_2 emission was NGC 2023, a bright reflection nebula in the constellation of Orion. Previous observations had detected infrared H_2 emission due to shocked excitation (Gautier et al. 1976; Treffers et al. 1976; Shull & Beckwith 1982; Brand et al. 1988). In the past, observations of H_2 line ratios had been taken to imply that emission was due to shocked excitation (Zuckerman & Gatley 1988). However, in recent years it has been realised that high density PDRs will have characteristic line ratios very similar to low velocity shocks (Sternberg & Dalgarno 1989; Burton, Hollenbach & Tielens 1990). Chrysostomou (private communication) has recently detected over 100 pure fluorescent H_2 transitions in the planetary nebula Hubble 12. Previous near-infrared observations of the same object (Ramsay et al. 1993; Hora & Latter 1996) had measured over 50 lines from vibrational levels of H_2 as high as $v = 9$, consistent with low density ($\sim 10^3\,\mathrm{cm}^{-3}$) emission. Luhman et al. (1994) have observed large scale UV-excited H_2 emission across the surface of the Orion A molecular cloud extending 12 parsecs. Radiatively excited H_2 has also been observed in a number of extragalactic objects (Israel et al. 1989; Puxley, Hawarden & Mountain 1988). The only H_2 lines which lie well beyond the near-infrared are the pure rotational transitions within the vibrational ground state, which trace gas excitation temperatures down to 512 K. The first detection of the 0–0 S(1) line was from the Orion shock and PDR regions (Parmar et al. 1991) and recently the Infrared Space Observatory has been used to observe several more pure rotational H_2 lines in PDRs (*e.g.* in S140 - Timmermann et al. 1996).

1.3.2 Infrared to Radio Wavelength Observations

The first observational evidence for atomic and partially ionised gas in the photodissociation region between HII regions and neutral clouds came from optical and radio observations of CI and OI lines (*e.g.* Hippelein & Münch 1978; Pankonin, Barsuhn & Thomasson 1977). In 1979 the bright CII emission line at 158 μm was detected in M17. This extended to over 12 parsecs from the central cluster of OB-type stars, which is much greater in extent than the HII region or the carbon recombination line zone (Russell et al. 1980, 1981). HI clouds can only account for a small fraction of the CII radiation. Most of the line radiation comes from the dense, warm molecular gas in the photodissociation region (Genzel, Harris & Stutzki 1989). Extensive observations of the CII 158 μm line have been made throughout the inner Galaxy (Shibai et al. 1991; Bennett et al. 1994). These are useful for studying PDR structure since UV-excited H_2 and C^+ correlate spatially (Luhman & Jaffe 1996). Far-infrared CII observations (Stutzki et al. 1988) show that the diffuse ultraviolet background radiation can propagate deep into clumpy molecular clouds, dissociate the tenuous interclump gas and irradiate the surfaces of dense molecular clumps. CI has been used to map the distribution of material deeper into the molecular cloud behind the surface PDR layers, showing highly clumped material at small scales (White & Padman 1991; Rouan et al. 1997). The CI emission is maximum at edges of clumps but avoids the densest regions where CO emission arises (Harris et al. 1987).

Photodissociation regions are also emitters of diffuse emission features at 3.3, 6.2, 7.7, 8.6, 11.3 μm and excess continuum emission from 1–5 μm (Sellgren et al. 1985). These features are now commonly interpreted to come from very small dust grains with radii of $\sim$ 10 Å, briefly heated to temperatures of 1000 K by single stellar photons (Sellgren, Werner & Dinerstein 1983; Sellgren 1984; Draine & Anderson 1985) or vibrational or electronic fluorescence from large molecules, such as polyaromatic hydrocarbons (Leger & Puget 1984). An alternative line of inquiry which has not been ruled out is the interesting possibility that hydrogenated C_{60} molecules maybe the source of these emission bands (see Webster 1993 and refs. therein).

Chapter 2

The Hydrogen Molecule

Molecular hydrogen is the most abundant molecule in the universe, found everywhere from the diffuse interstellar medium, where there are just a few molecules per cubic centimetre, to the interior of Jupiter, where the number density exceeds $10^{25}\,\mathrm{cm}^{-3}$. Hydrogen is the simplest and lightest neutral molecule; however its simplicity is deceptive. The theoretical basis of H_2 was formulated in the 1920s (*e.g.* Heitler & London 1927) but it was only until the mid-1970s that the higher energy states of H_2 were assigned (*e.g.* Dabrowski & Herzberg 1974). The difficulty in interpreting the spectra arose from the fact that the rotational levels are spaced so widely apart that successive rotational lines associated with a single electronic state are often interspersed with numerous other lines from different electronic transitions. Also perturbations can cause the energy levels to shift from the predictions given by simple formulae, making the sequence of rotational and vibrational lines irregular. The theory of diatomic molecules is covered extensively in Herzberg (1950) and more specifically H_2 is reviewed in an astrophysical context by Field, Somerville & Dressler (1966). The main points relating to the data presented in this thesis are summarised below.

2.1 Quantization and Energy States

Molecular hydrogen consists of two protons and two electrons which interact with each other via the Coulomb force. This depends on the separation and charge of the particles. Each particle also has two possible spin projections and therefore the molecule must be given a full quantum mechanical description involving spin and space. As a diatomic molecule, it can rotate around its centre of mass, and the two nuclei can also vibrate about their equilibrium separation. The energies associated with both of these motions are quantized, as is the energy of the electrons in the molecule. This leads to three sets of molecular energy levels: electronic, vibrational and rotational. Of these, the electronic states are the most widely spaced, followed by the vibrational and then the rotational states. In particular the ground electronic state has 348 rotational and vibrational (rovibrational) levels, of which 301 are bound. There are fifteen vibrational levels, $v = 0$–14, each of which is split into a large number of rotational levels, $J = 0$–J_{max}, where J_{max} depends on the vibrational level (*e.g.* J_{max} varies from $38 \rightarrow 4$ for $v = 0 \rightarrow 14$) (see Fig. 2.1).

The Coulomb potential of the ground state resembles a harmonic oscillator close to the equilibrium separation of the nuclei. This causes a regular spacing of vibrational energy levels but with increasing potential it becomes progressively anharmonic reducing the separation of higher vibrational levels. The energy associated with the rotational levels, however, behaves more like a rigid rotator (*i.e.* $E_J \propto J(J+1)/\mathcal{I}$) with the energy levels separating with increasing values of J. The wide spacing of the rotational levels is due to the low moment of inertia of the molecule, $\mathcal{I}$. For high values of J the moment of inertia increases, owing to centrifugal distortion, to the point where the separation of the energy levels begins to decrease (see Fig. 2.1).

The ground electronic state is represented by the expression, $\mathrm{X}^1\Sigma_g^+$, where X simply labels the state and ${}^1\Sigma_g^+$ describes the electronic angular momentum, spin and symmetries of the state.

The orbital electronic angular momentum, $\boldsymbol{L}$, is not conserved. It is strongly coupled to the internuclear axis, k, and only quantized states of this component are allowed. These are specified by Λ which indicates the projection of $\boldsymbol{L}$ along k, (*i.e.* $\Lambda = |k.\boldsymbol{L}|$). The first three values ($\Lambda = 0, 1, 2$) are represented by Σ, Π and Δ respectively. These are analogous to the first three *atomic* orbital angular momentum states S, P and D. The component of $\boldsymbol{L}$ perpendicular to k is not a constant, since the Hamiltonian for the electronic motion does not possess symmetry about any axis perpendicular to k. The superscript preceding Σ refers to the degeneracy of the ground state due to the electronic spin. The total electron spin, $\boldsymbol{S}$, is also quantized and has a degeneracy given by $2S + 1$. The electrons in the ground electronic state are anti-parallel with a combined spin, $\boldsymbol{S}$, of zero and therefore the ground state is a singlet state[1].

Since there exists an electronic angular momentum component along the symmetry axis one might expect the molecule to exhibit quantum-mechanical motion analogous to precession. In fact, for states with $\Lambda \neq 0$, $\boldsymbol{L}$ precesses rapidly about the field direction, k. An internal magnetic field in this direction arises from the orbital motion of the electrons causing a precession of $\boldsymbol{S}$ about k, with a constant component M_S. The total electronic angular momentum along the internuclear axis is given by $\Omega = |k.(\boldsymbol{L}+\boldsymbol{S})|$. Since the component of $\boldsymbol{S}$, measured with respect to the k axis, is also quantized, the degeneracy is also given by $2S + 1$. In Σ states there is no magnetic field in the k direction and if there is no rotation M_S is undefined and consequently no splitting occurs. If the molecule rotates then the perpendicular vector quantities: Ωk and nuclear rotation, $\boldsymbol{R}$, combine to form the rotation vector, $\boldsymbol{J}$ around which the molecular axis, k nutates. The spin of the nuclei, $\boldsymbol{I}$, have an insignificant interaction with the electrons and may be considered separately as a constant of the motion. The second and third stable excited electronic states are the $^1\Sigma_u^+$ and $^1\Pi_u$ states which are labelled by the prefixes B and C.

In the ground state (or any $^1\Sigma$ state) the electronic spin and electronic angular momentum are both zero. Therefore the total angular momentum, $\boldsymbol{J}$, is simply the angular momentum due to the nuclear rotation and so the molecule may be treated as a simple rotator. Since the electronic spin is zero there are no lines due to fine structure ($\boldsymbol{S}$ interacting with Λk) nor electron-nuclear hyperfine structure ($\boldsymbol{S}$ interacting with $\boldsymbol{I}$ or $\boldsymbol{R}$). Other couplings do exist (*e.g.* nuclear spin and nuclear rotation) which are discussed in Herzberg (1950) but do not contribute to the data in this thesis. The total degeneracy, or statistical weight, of each level j, is given by $g_j = (2J+1)(2I+1)$, where the total nuclear spin I is 1 or 0.

2.2 Symmetry Properties

To aid a description of the how the overall wavefunction symmetry determines the allowed states, I will introduce notation whereby ψ_e and ψ_p represent the spatial or orbital angular momentum wavefunctions of the electrons and protons and ϕ_e and ϕ_p represent the spin wavefunctions. These wavefunctions are linearly independent and the overall wavefunction for the molecule is the product[2] $\psi_e\psi_p\phi_e\phi_p$. The protons and electrons which comprise the H_2 molecule are fermions. As such they cannot occupy the same quantum state and therefore the states which they occur in must be distinguished by different quantum numbers. The wavefunction which describes the whole molecule must also be antisymmetric with respect to an interchange of nuclei or electrons (*i.e.* ψ_p and ϕ_p must have opposite symmetries, similarly so must ψ_e and ϕ_e) *e.g.* the state $b^3\Sigma_u^+$ is a triplet state and therefore the electron spins are aligned parallel, ϕ_e is therefore symmetric and so ψ_e must be antisymmetric. The shape of the antisymmetric spatial wavefunction means the electrons are much less likely to be found between the nuclei and hence the state is repulsive (indicated by the lower case b). If the proton spins are anti-parallel, then ϕ_p is antisymmetric, so ψ_p must be symmetric. The overall state is referred to as 'para' hydrogen and is characterised by even values of $\boldsymbol{J}$. In the lowest rotational state this quantum number is zero and the orientation of the molecular axis

[1] Quantum theory states that angular momentum, $\boldsymbol{l}$, can take the values $\sqrt{l(l+1)}\hbar$ for integer l. The projection of the vector quantity along an axis of measurement, $\boldsymbol{z}$, is also quantized taking on discrete values of $m_l\hbar$ where $m_l = l, (l-1), (l-2), ..., -l$. As a consequence only certain angles of $\boldsymbol{l}$ with respect to $\boldsymbol{z}$ are allowed causing a $(2l+1)$-fold degeneracy.

[2] As long as the coupling between the spin and orbital motion is small (*i.e.* for light molecules) the electronic eigenfunction may be written as a product of the spatial and spin wavefunctions, the same is true for the nuclei.

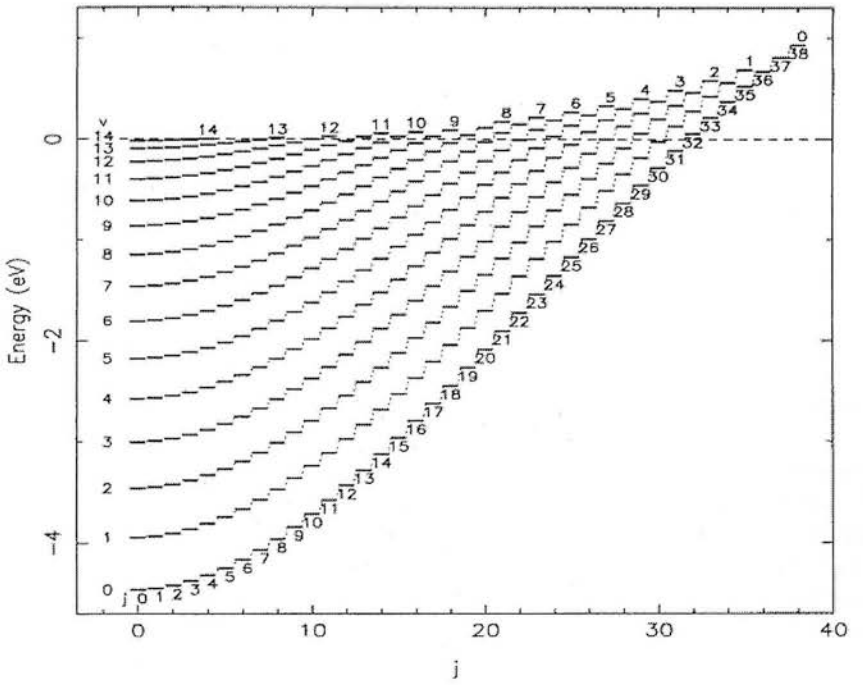

Figure 2.1: Energy levels for each rovibrational state of the H_2 molecule in its ground electronic state taken from Martin, Schwarz & Mandy (1996). The dissociation energy is indicated by the dashed line. The rotational quantum number is denoted by j along the x-axis and the vibrational level by v along the y-axis.

is distributed with uniform probability over the unit sphere. If the proton spins are parallel (*i.e.* symmetric ϕ_p) then ψ_p is antisymmetric with odd values of $\boldsymbol{J}$; this is 'ortho' hydrogen. The term 'ortho/para abundance ratio' is used many times later in this thesis. Unless specified for a particular vibrational level it refers to the total column density ratio of ortho-H_2 to para-H_2 divided by their respective statistical weights due to rotational degeneracy $(2J+1)$.

The superscript and subscript following the Λ term refer to the symmetry properties of the electronic wavefunction, ψ_e, with respect to spatial reflections. For nuclei with the same charge there exists a centre of symmetry between them. As a consequence the electronic wavefunctions remain unchanged 'g' or change sign 'u' when reflected through this point[3]. This spatial symmetry property does not affect whether the electronic wavefunction is symmetric with respect to an interchange of particles. For example, the second electronic excited state is $B^1\Sigma_u^+$ which has an antisymmetric spin wavefunction, ϕ_e, (since it is a singlet state) therefore a symmetric spatial wavefunction, ψ_e, but is uneven. For Σ states one must distinguish between Σ^+ and Σ^- states, whose wavefunctions either keep or reverse sign with reflection of the electrons through a plane containing the k axis. In H_2, all known Σ states have Σ^+ symmetry.

2.3 Excitation and De-excitation

When H_2 is exposed to ultraviolet photons of energy less than 14.7 eV, electronic excitations take place immediately followed by radiative decays into the rovibrational levels of the ground electronic state. This absorption has been observed directly in diffuse clouds along the line of sight toward bright stars (van Dishoeck & Black 1988). These energy states decay by electric quadrupole transitions on time scales of the order of a year. Consequently a 'cascade' takes place where

[3] from the German: *gerade* meaning even and *ungerage* meaning odd.

infrared photons are emitted as the molecules enter lower rovibrational energy states. Another environment where H_2 can also be detected is shocks where collisions excite molecules into these energy states (Brand et al. 1988). Since the first excited state from which rotational emission originates occurs at 512 K, molecular hydrogen cannot be detected in quiescent clouds; it can only be directly observed under extreme conditions where high energy densities are present.

Excitation mechanisms for molecular hydrogen can be conveniently classified into two groups as thermal or non-thermal. Thermal excitation occurs when collisions populate the low energy levels of the molecule, such as occurs in hot gas or shocks. Non-thermal excitation processes include fluorescence, collisions with high energy electrons and H_2 formation on dust grains. These non-thermal mechanisms tend to populate the higher energy levels first.

2.3.1 Dipole Transitions between Electronic States - UV Radiation

In the ground electronic state, the centre of mass coincides with the centre of charge and therefore the ground state of H_2 possesses no permanent dipole moment. This fact alone is sufficient to prevent any dipole transitions occurring within the ground state. Additionally the exclusion principle ensures the total nuclear wavefunction must remain antisymmetric, with respect to an interchange of protons, and since the nuclear spin and nuclear rotation do not interact sufficiently to cause one of the nuclei to flip its spin, this causes a selection rule which prevents the absorption of IR photons with odd quantum numbers of angular momentum.

Quantum mechanical dipole moments do exist for electronic UV transitions between the ground state and electronically excited states. Therefore electric dipole transitions are possible where the molecule absorbs or emits a photon which changes the orbital angular quantum number by one. Since the electrons are then in different orbital angular momentum states from each other, no exclusion principle is violated. The selection rules for electric dipole transitions require that $\Delta\Lambda = \pm 1$ or 0, $\Delta J = \pm 1$ or 0, $\Delta S = 0$ and Δv is unrestricted. The transition must also satisfy the symmetry requirements $g \leftrightarrow u$ and $\Sigma^+ \not\leftrightarrow \Sigma^-$. The Lyman and Werner bands arise from electric dipole transitions between the ground state and the 2nd and 3rd electronic states respectively. The states are represented by $B^1\Sigma_u^+$ and $C^1\Pi_u$. They occur at excitation temperatures of 130,000 K (11.2 eV) and 143,000 K (12.3 eV) and are excited by photons of wavelength less than 112 nm and 102 nm respectively.

Under interstellar conditions H_2 molecules are almost entirely concentrated in the ground electronic state. Molecules in this state can absorb an ultraviolet photon and jump to the rovibrational levels of the B and C electronic states from where they rapidly re-emit an ultraviolet photon and jump back down to any vibrational level of the ground electronic state X. This corresponds to an overall change in the rotational orbital angular momentum (ΔJ) which is even. Therefore the overall ortho/para abundance ratio is unaffected by absorption to these levels.

2.3.2 Quadrupole Transitions within the Electronic Ground State - IR Radiation

Once the molecule has reached a bound level of the electronic state X, it will continue to cascade down in a series of rovibrational transitions via weak quadrupole transitions. The spontaneous emission probabilities for such transitions are very small and vary from level to level in a complicated way. Values for transition rates between individual levels $(v'J') \rightarrow (vJ)$ have been calculated by Turner, Kirby-Docken & Dalgarno (1977) and Abgrall & Roueff (1989). Figure 2.2 shows the total probability (or transition rate per molecule) of radiative de-excitation out of each upper level $(v'J')$. Thus for any excited rovibrational level the sum of the spontaneous emission probabilities to lower levels is $\sim 10^{-6}$ s^{-1} (Black & Dalgarno 1976). This produces optically thin radiation which aides the determination of column densities. The nuclear spins have virtually no interaction with the electrons of the molecule or with any other outside influence. This ensures that the nuclear spin wave function is almost exactly a constant of the motion and in particular will remain unchanged during a radiative transition of the molecule. Therefore, since the spin symmetry re-

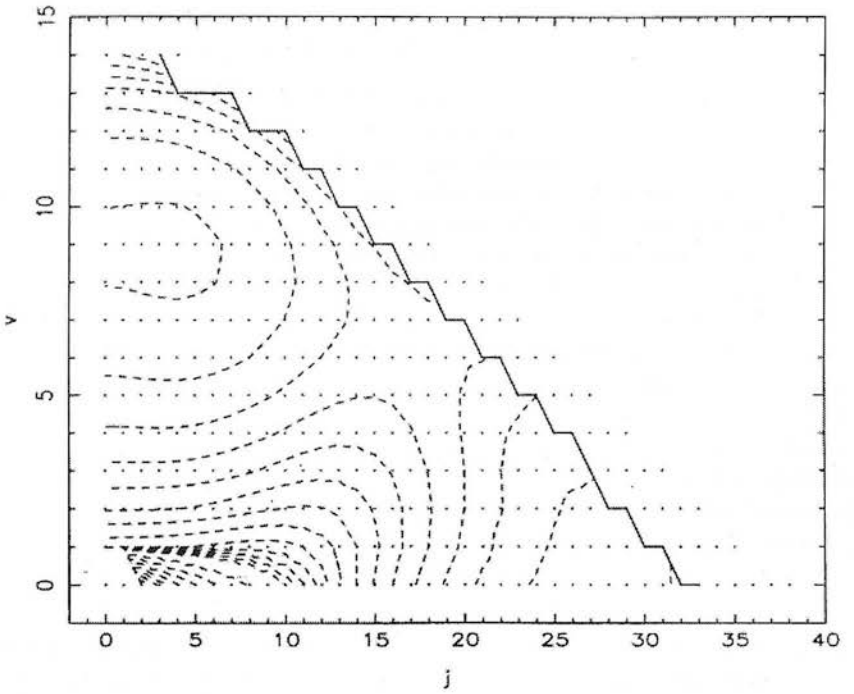

Figure 2.2: Contour plots of the probabilities of energy states depopulating by quadrupole radiative emission taken from Martin, Schwarz & Mandy (1996). The rotational quantum number is denoted by j along the x-axis and the vibrational level by v along the y-axis. The first set of 13 contours are at 0.1 dex intervals ($\times 1/10^{0.1}$), decreasing from a value of 5×10^{-6} s^{-1} for the contour encircling the maximum at (27,0) and the local maximum at (3,9) [the contour passing near (15,5) dividing these two maxima is at a value 2.5×10^{-6} s^{-1}]. Thereafter, in the lower left as the probabilities continue to decrease, at contour level -6.5 dex the contour interval increases to 0.5 dex.

mains unchanged during a transition the space symmetry also remains unchanged and radiative transitions must involve an even change in J. Thus radiative quadrupole transitions preserve the ortho/para abundance ratio of molecular hydrogen. The permitted changes in the rotational quantum number, for quadrupole transitions, are $\Delta J = (J' - J) = +2, 0, -2$ (except $J' = 0 \rightarrow 0$ which is forbidden) and these transitions are labelled $O(J), Q(J)$ and $S(J)$ respectively. There are no selection rules governing the changes in the vibrational quantum numbers.

The rovibrational spectrum has its brightest lines in the near-infrared spectral region many of which fortunately coincide with the K-band atmospheric window (2–2.4 μm). The pure rotational transitions occur further into the mid and far-infrared regions. In the rigid rotator case for pure rotational lines, the energy levels are given by $\hbar^2 J(J+1)/2\mathcal{I}$. Therefore it can easily be shown that quadrupole transitions across pairs of energy levels consist of almost equally spaced lines[4].

2.3.3 Collisions

A full treatment for the statistical energy distribution of molecular clouds must include all other processes which redistribute the populations such as inelastic collisions with atoms, molecules, electrons and protons and proton interchange reactions. The most important collisional partners

[4]The moment of inertia, $\mathcal{I}$, increases with J depressing the higher energy states and decreasing the radiation frequency.

of H_2 in interstellar space are H, He, H^+, e^- and H_2 (Tiné et al. 1997) and for PDRs the dominant contribution comes from H-H_2 and H_2-H_2 collisions (Sternberg & Dalgarno 1989).

Excited electronic states of H_2 decay rapidly ($\sim 10^{-8}$ s - Abgrall & Roueff 1989) compared with to the typical time between collisions in hot, dense gas within molecular clouds (*e.g.* $\sim 10^5$ s for $n \sim 10^5\,\mathrm{cm}^{-3}$ at 1000 K). Therefore collisional processes are only considered for the rovibrational levels of the ground electronic state. At temperatures and densities found in photodissociation regions, excitation through inelastic collisions occurs only in the lower energy levels, mainly in the first vibration level (Sternberg & Dalgarno 1989). Inelastic collisions can excite H_2 into the lower energy levels or de-excite H_2 out of higher energy levels. When the gas density is sufficiently high that collisional de-excitation out of an excited level is as probable as radiative de-excitation, the gas is said to have reached the critical density for that level. This for most levels of H_2, interacting with H atoms in gas at 2000 K, this is $\sim 10^3\,\mathrm{cm}^{-3}$. In the $v = 0$ level the critical density rises rapidly from $6.2 \times 10^{-1}\,\mathrm{cm}^{-3}$ for $J = 2$ to a maximum of $1.2 \times 10^4\,\mathrm{cm}^{-3}$ for $J = 17$ (Martin, Schwarz & Mandy 1996). Collisions with between H_2 molecules are less likely to bring about large changes in vJ. Since this quantity is temperature dependent one would expect the critical density of H_2 within a PDR ($\lesssim$ 1000 K) to be somewhat greater. The relative contributions of these processes along with the ultraviolet radiation field determine the resultant infrared spectrum. Sternberg & Dalgarno (1989) define three different PDR scenarios:

- A *radiative* fluorescent emission spectrum is produced when gas, at densities much smaller than the critical density, is sufficiently cold that the UV-pumping rates of all the H_2 vibrational levels are much larger than the collisional excitation rates of these levels. The relative intensities of the lines in such spectra depend primarily on the spontaneous emission rates which are molecular constants and therefore the shapes of the emission spectra are insensitive to the gas density and the UV field intensity (Black & Dalgarno 1976; Black & van Dishoeck 1987).

- A *collisional* fluorescent emission spectrum is produced when gas, at densities much larger than the critical density, is sufficiently cold that the UV-pumping rates of the vibrational levels are much larger than the collisional excitation rates of these levels.

- A *thermal* emission spectrum is produced in gas which is beyond the critical density and is sufficiently warm such that the excitation of at least some of the vibrational levels are dominated by collisional processes. The relative and absolute intensities of such thermal emission depend on the size and temperature of the warm part of the photodissociation region.

Only limited theoretical and experimental information is available regarding the interaction cross sections of these collisions. Computational speeds have only recently reached the point where the complete set of rate coefficients can be calculated. Mandy & Martin (1995) have calculated rate coefficients for collisional excitation and dissociation of H_2 molecules by H atoms (reliable within the range T = 600–10,000 K). These confirm that the branching ratios of a collisional cascade differ significantly from those of a radiative cascade and therefore radiative fluorescent spectra can be expected to be substantially different from spectra for gas containing significant collisional processes.

In addition to redistributing the populations of the energy levels, another important effect of collisions is the change they bring in the ortho/para abundance ratio. This ratio is first set at the formation of H_2 on dust grains. As mentioned in Section 2.3 the fluorescence process does not change this ratio and collisions of H_2 with H or H_2 result in $\Delta J = \pm 2$ (Black & van Dishoeck 1987). However spin exchange reactions can occur via collisions with H_2, H^+, H and H_3^+ (Dalgarno et al. 1973; Flower & Watt 1984; Takayanagi et al. 1987). In this case a proton is physically exchanged with one of the nuclei and if the initial spins of the two particles being exchanged were different then the spin state of the molecule changes. The variety of factors affecting this ratio and the implications of the observed value are discussed in Chapter 5.

2.4 Formation on Dust Grains

The time required for two hydrogen atoms in their ground state to form a stable molecule by radiative association ($\sim 10^{-8}$ s) far exceeds the duration of a collision ($\sim 10^{-13}$ s). Three-body reactions are also made extremely inefficient due to the low atomic hydrogen densities in photodissociation regions (*i.e.* $R(3\mathrm{H} \rightarrow \mathrm{H_2} + \mathrm{H}) \simeq 5 \times 10^{-32}\,\mathrm{cm^6\,s^{-1}}$). Other pathways to forming H_2 exist involving the creation of H_2^+ and H^- but for the conditions found in PDRs the reaction rates (see Duley & Williams 1984) are much smaller than those inferred from observations of the interstellar medium (Jura 1975). It is generally accepted that in the interstellar medium, H_2 formation requires dust to act as a catalytic third body on which it may form (Gould & Harwit 1963; Hollenbach & Salpeter 1971). These grains also shield the newly formed molecules from dissociation by interstellar UV radiation. The rate of formation is given by

$$0.5\, n_H n_d < \sigma_d v > \tag{2.1}$$

where n_d and σ_d are the number density and interaction cross section of dust grains and n_H and v are the number density and velocity of hydrogen atoms. The factor of 0.5 represents the fact two H atom collisions are required to form a molecule. Since the ratio of dust to protons can be taken as constant ($\simeq 10^{-12}$), the formula can be rewritten

$$n_H n R \tag{2.2}$$

where n is the proton number density ($n_H + 2n_2$ where n_2 is the H_2 density) and R is the coefficient for the rate of formation. Since the formation rate is proportional to the kinetic velocity of the gas it increases with the square root of the gas temperature. However, there is a critical temperature beyond which hydrogen atoms will evaporate before combining to form molecules ($T_{cr} \simeq 75$ K - Tielens & Hollenbach 1985) thus lowering the rate of formation. The value of R has been derived from observations of H_2 along the line of sight to OB-type stars to be $3 \times 10^{-17}\,\mathrm{cm^3\,s^{-1}}$ (Jura 1975). Hollenbach & McKee (1979) have used this result to derive an expression for R which depends on the gas temperature, T, and dust temperature, T_d,

$$R = 3 \times 10^{-17} \frac{\sqrt{T_2} f}{1 + 0.4\sqrt{T_2 + T_{d2}} + 0.2T_2 + 0.08T_2^2}\ \mathrm{cm^3\,s^{-1}} \tag{2.3}$$

where $T_2 = T/100$, $T_{d2} = T_d/100$ and f is the fraction of adsorbed H atoms which combine to form H_2.

Dust is thought to be composed mainly of silicates and amorphous carbon. In regions of high extinction these grains are coated with mantles which are largely H_2O ices. At extinctions of $A_v \geq 5$ the mantles also incorporate CO (see Duley & Williams 1993, and refs therein). The temperatures and incident radiation fields present in PDRs make it unlikely that any dust there will have H_2O mantles. If however the photodissociation front is not stationary and is passing through into the molecular cloud away from the UV source then the H_2 emission may originate from molecules newly formed on the icy mantles of dust grains previously shielded from UV photons. The theoretical details of H_2 formation on dust grains vary greatly depending on the assumed surface chemistry, however different models share the following steps:

1. collision of a hydrogen atom with a grain
2. thermal accommodation and adsorption
3. retention on the grain surface until another hydrogen atom arrives and is adsorbed
4. migration to a reaction site
5. recombination to form H_2
6. evaporation of H_2 molecule, possibly in an excited state

Various conflicting suggestions have been made concerning how the 4.476 eV of binding energy is distributed among the degrees of freedom of the dust grain and resulting molecule. Also considerable uncertainties remain regarding the dependence of this formation mechanism on the gas and dust grain temperatures (T and T_d). If a significant fraction of the binding energy remains within the nascent H_2 molecule then it is formed vibrationally excited and will contribute to rovibrational emission (Black & Dalgarno 1976). If a large fraction of the recombination energy is converted into translational energy of the H_2 molecule then it can be a major source of kinetic heat energy into the gas cloud (Barlow & Silk 1976). In addition to understanding the heating processes within a PDR, H_2 formation is also important since the ortho/para ratio is first established at the formation of H_2. Since radiative transitions cannot cause interchanges between the ortho and para forms only proton exchange reactions alter the ratio in dense clouds (see Section 2.3.3), this allows the ratio to be used as a diagnostic tool to probe the physical conditions of molecular clouds. The predicted conditions under which H_2 forms and the resulting energy distributions depend greatly on the assumed surface composition of the dust grain.

For crystalline surfaces the second step of the above process, thermal accommodation, becomes important allowing the molecule to thermalise to the grain temperature before being ejected with kinetic energy kT_d (Leonas & Pjarnpuu 1981) whereas similar calculations which do not assume this (Hunter & Watson 1978) provide only upper limits on the translational energy (0.2 eV). Defect sites on the surfaces of dust grains, caused by radiation or cosmic rays, provide enhanced binding over that provided by pure graphite and once the hydrogen atom has become thermalised on the grain surface the recombination efficiency is almost 100% (Hollenbach & Salpeter 1971). For temperatures less than 70 K covalent binding allows graphite grains to act as the principal sites for H_2 formation, with a formation rate of $R \sim 4 \times 10^{-17}\,\mathrm{cm^3\,s^{-1}}$ (Barlow & Silk 1976). Predictions concerning the resultant rovibrational state of the molecule also vary greatly depending on surface constituents and structure *i.e.* formation on aromatic carbonaceous material results in $v = 0, 1$ (Duley & Williams 1993), polymeric carbonaceous $v = 13$ (Duley & Williams 1993) while experimental evidence of formation on pure carbon surfaces composed of amorphous and polycrystalline carbon $v \leq 7, J = 0$ (Gough et al. 1996).

Since only a few sites per grain are necessary to establish efficient $2H \rightarrow H_2$ conversion (Hollenbach & Salpeter 1971) the primary mechanisms limiting the formation rate are steps 2 and 3 in the above sequence. An investigation of formation on hydrogenated amorphous carbons showed that incoming H atoms reacted promptly with surface hydrogens without a requirement for adsorption and thermal accommodation (Duley 1996). This mechanism has a reaction rate which increases with temperature thus formation is a significant process even for warm dust at gas temperatures greater than 300 K. On warm dust H atoms will be strongly bonded to the surface and H_2 will be ejected in a relatively low vibrational state while on cold ($T_d \leq 40$ K) dust, hydrogen atoms maybe more weakly bound improving the formation efficiency and forming H_2 in excited vibrational states.

Adsorption of hydrogen atoms on ices is generally weak (Duley & Williams 1993) and the critical temperature above which H_2 formation will not take place, due to thermal desorption of H atoms, is 20 K for ice mantles (Barlow & Silk 1976). Since the bond strength is so weak, little energy is transferred to the grain upon formation and the molecule leaves in a highly excited state ($v = 13$) and thus does not contribute significantly to the heating of dust grains.

Duley & Williams (1986) considered formation on highly defected amorphous silicate grains. These had a high surface coverage of OH^- sites from which H_2 was ejected with a kinetic energy less than 0.2 eV in a vibrationally excited ($v \leq 7$) but rotationally cool ($J \leq 1$) state. This mechanism may be less significant in photodissociation regions compared to shocked regions where the carbonaceous surface has been stripped of to reveal the underlying silicate structure.

In summary, molecular hydrogen forms from the collisions of hydrogen atoms with dust grains. If the surface of the dust grain has an ice mantle or is carbonaceous covered with weakly bound hydrogen atoms then the molecule is predicted to form in a highly excited vibrational state (*i.e.* $v = 13$ - Duley & Williams 1993). It may be harder to distinguish between formation on silicate surfaces and formation on graphite surfaces where hydrogen atoms are strongly bound since in both cases they may be produced in low rotational ($J \leq 1$) but excited vibrational ($v \leq 7$) states (Duley & Williams 1986; Duley & Williams 1993; Gough et al. 1996). If the surface is icy or

hydrogenated then the newly formed H_2 molecule may be released before it has thermalised to the grain temperature. The large exothermicity of the process is then likely to produce a population of ortho and para states with an abundance ratio of 3. If, however, H_2 does not immediately evaporate upon formation it may undergo energy loss reactions with the surface and if it resides long enough it will eventually evaporate into the gas with an equilibrium ortho/para ratio typical of the grain temperature.

Observational evidence of rovibrational states populated in excess of model predictions would provide a powerful diagnostic in determining the nature of the surface of dust grains found in PDRs and the process of molecular hydrogen formation itself. Synthetic spectra of infrared H_2 emission lines have been produced for different formation models in the context of fluorescent PDRs (Black & van Dishoeck 1987; Sternberg 1988; Draine & Bertoldi 1996) and dark clouds (Le Bourlot et al. 1995). Mouri & Taniguchi (1995) have calculated the effect of H_2 formation on ratios of infrared lines and made comparisons with observations of the merging galaxy NGC 6240. Their results tentatively suggest there may be a partial contribution to certain line ratios (for $v = 1 \rightarrow 0$ transitions) due to formation pumping, in highly excited rotational states, downstream of dissociative molecular shocks.

2.5 Destruction

The various processes by which molecular hydrogen can be destroyed include ionisation by cosmic rays or UV photons, direct photodissociation and chemical reactions. Although the hydrogen molecule is bound by only 4.48 eV (52,000 K), direct photodissociation by IR-photons into the vibrational continuum of the ground state can be neglected since the interaction cross section for infrared quadrupole radiation is extremely small and infrared dipole transitions are highly forbidden. The thresholds for photoionisation (15.4 eV) and direct photodissociation through an excited electronic state (14.7 eV) exceed the ionisation potential of atomic hydrogen (13.6 eV). Thus while molecular hydrogen is ionised or dissociated rapidly in HII regions, the direct process can be neglected in photodissociation regions. Another way of destroying H_2 is through collisions with fast electrons. These can excite H_2 from the $X^1\Sigma_g^+$ state to the repulsive $b^3\Sigma_u^+$ stage (Hollenbach & McKee 1980); the equivalent radiative transition is strongly forbidden. This process is important in regions with significant numbers of high energy electrons (*e.g.* low-density shocks, molecular clouds irradiated by intense X-rays) but can be neglected in the case of most Galactic PDRs. Collisions with atomic hydrogen may also induce dissociation. The H_2 reformation rate coefficient $R \simeq 3 \times 10^{-17}\,\mathrm{cm^3\,s^{-1}}$ (Jura 1975) and Fig. 2.3 shows that under equilibrium conditions at temperatures of a few thousand degrees collisionally induced dissociation can begin to contribute to the dissociation rate. Therefore this process is mainly significant in high-speed shocks (Blais & Truhlar 1982) and will not affect PDR emission appreciably. Collisions between H_2 molecules are less effective at increasing the excitation state than a collision between H and H_2 therefore this mechanism can also be discounted.

The most important destruction mechanism in HI regions is the two stage process discussed by Stecher & Williams (1967). A UV photon with energy 11.2–13.6 eV ($\lambda = 91.2$–110.8 nm) which penetrates the molecular cloud may excite a hydrogen molecule to the $B^1\Sigma_u^+$ or $C^1\Pi_u$ state from where it decays spontaneously to the ground state. If it decays to the vibrational continuum ($v > 14$) the molecule dissociates. The destruction rate of molecular hydrogen, by an ultraviolet flux F_ν, at wavelength ν, is given by

$$\eta n_2 \sigma_2 F_\nu e^{-(\tau_d + \tau_2)} \tag{2.4}$$

where σ_2 is the interaction cross section of molecular hydrogen and τ_d and τ_2 are the optical depths due to dust and molecules of hydrogen, respectively. The factor of η represents the electronic transitions which result in photodissociation (Dalgarno & Stephens 1970, estimated this to be 0.10; Abgrall et al. 1992, used 0.13; and more recent calculations by Draine & Bertoldi 1996, estimate 0.16).

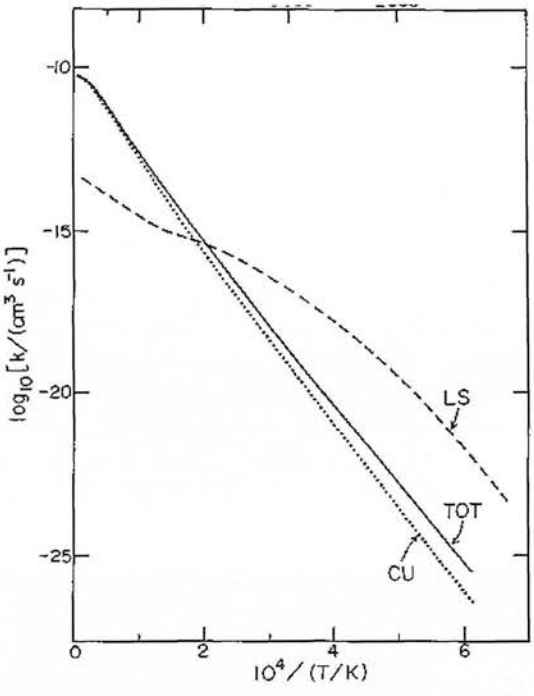

Figure 2.3: Temperature dependence of dissociation rate coefficients for H_2-H collisions at low densities taken from Dove & Mandy (1986). CU refers to transitions into the classically unbound states and TOT for transitions into the quasi-bound and classically unbound states, calculated by Dove & Mandy (1986). LS is the dissociation rate coefficient calculated by Lepp and Shull (1983).

Chapter 3

The Reflection Nebula - NGC 2023

3.1 Observations

NGC 2023 is a well-studied, bright reflection nebula at a distance of 450–500 pc (Racine 1968; Lee 1968; de Boer 1983) in the Orion region (see Goudis 1982, for an overview) situated 14 arcminutes northeast of the Horsehead Nebula (see Fig 3.1). It is embedded on the near-side edge of the dark cloud Lynds 1630 which is a site of recent star formation that became active between 1 and 3×10^5 years ago (Strom et al. 1975) and shows many features including molecular outflows, bright reflection nebulae and Herbig-Haro objects. NGC 2023 is illuminated by HD 37903, a B1.5 V spectral type star (Sharpless 1952) and a highly reddened pre-main-sequence star, S108 (Scarrott et al. 1989; Sellgren et al. 1992). It contains a cluster of young stars and a $10\,\mathrm{km\,s^{-1}}$ outflow has been detected $\sim 0\farcm5$ southwest of HD 37903 (Bally & Lada 1983). The proximity of this nebula and the a priori knowledge of the region make it an ideal object to study the interaction of UV radiation with molecular gas.

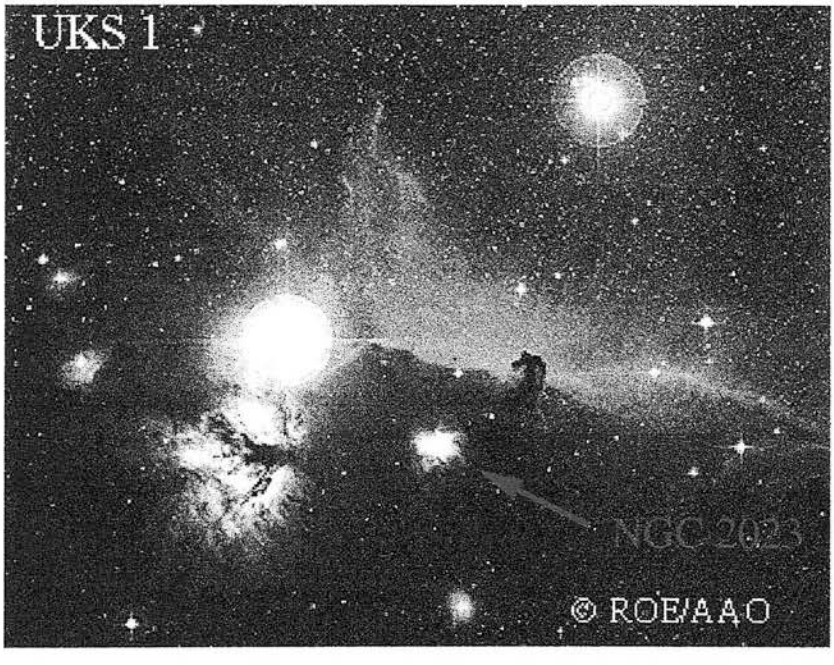

Figure 3.1: NGC 2023 beside the Horsehead Nebula in front of the dark cloud Lynds 1630. The image has been rotated through 90° anti-clockwise. The brightest star in the picture is Zeta Orionis, the left-hand star of the constellation Orion's Belt. NGC 2023 is indicated below the red HII region. Reproduced with permission from the ROE. Copyright © Royal Observatory, Edinburgh and Anglo-Australian Telescope Board.

NGC 2023 is the site where fluorescent H_2 emission was initially detected (Gatley et al. 1987; Gatley & Kaifu 1987; Hasegawa et al. 1987; Sellgren 1986) and later followed by the first optical detections of over 30 lines arising from the highest excitation levels of H_2 then observed (Burton et al. 1992a). It is also the site where the 'extended red emission' (ERE: 6000–7400 Å) was discovered (see Witt & Malin 1989 and refs. therein) and it is one of the reflection nebulae where Sellgren, Werner & Dinerstein (1983) first detected the excess 1–5 μm continuum emission attributed to non-equilibrium emission from small particles (see Section 1.3.1).

Emerson, Furniss & Jennings (1975) have shown the total far-infrared luminosity of the nebula to equate with the energy absorbed in UV from HD 37903. Far-infrared measurements by Harvey, Thronson & Gatley (1980) show the dust temperature peaks on HD 37903 and the luminosity peaks within 1′ of the star confirming that HD 37903 is the dominant heating source for the dust seen in the far-infrared. They suggest that there are no obscured stars of earlier spectral type and therefore higher luminosity than HD 37903 within NGC 2023. However, Freyberg & Schmitt (1995) find from X-ray observations that the most eastern member of the cluster S105 may be a highly obscured O9.5-type star which if true leaves the question why it does not dominate the properties of NGC 2023.

Hasegawa et al. (1987) showed that the H_2 ortho/para abundance ratio was significantly less that the thermal equilibrium value of 3, a clear indication of fluorescent excitation. Howe, Jaffe & Geballe (1990) reported near-infrared observations of H_2 lines from up to $v = 5$. They measured the 1–0 S(1) line southwest from HD 37903 peaking at 60″ with $1.5 \times 10^{-14}\,\mathrm{W\,m^{-2}\,\mu m^{-1}}$. Ratios of line fluxes were also observed to vary with distance from the exciting star. The ratio of the 1–0 S(1) to 2–1 S(1) lines is 4.2 at the peak of the southwest shell but 2.5 at position 120″ north. Burton et al. (1997) find the ratio is 2.9 ± 0.5 on the H_2 emission ridge 78″ south and 11″ west of HD 37903 and 1.5 ± 0.3 offset 105″ north and 33″ east from HD 37903. Buss et al. (1994) have observed absorption lines from the PDR region, in the line of sight to HD 37903 at ultraviolet wavelengths, and found the ratio of atomic to total hydrogen number density to be 0.56.

Witt, Schild & Kraiman (1984) carried out extensive photometry up to 450″ from HD 37903 and found the U, B, V colour maps to be consistent with reflected radiation of HD 37903 by dust, but at R and I found extended red emission in excess of that expected by simple scattering. Witt & Malin (1989) have imaged the whole of NGC 2023 with 1″ resolution in the R and B bands. Their use of unsharp masking highlights regions of ERE which trace the photodissociated hydrogen gas (see Fig. 3.3). Field et al. (1994) however, observed anti-correlations between the ERE and H_2 emission and conclude that the physical conditions responsible for H_2 emission and ERE are not necessarily identical. IR emission features at 3.3, 6.2, 7.7, and 11.3 μm commonly attributed to polycyclic aromatic hydrocarbons have also been observed in NGC 2023 (Gatley et al. 1987; Joblin et al. 1996). Burton et al. (1989) observed the 3.3 μm emission feature to be coincident with the 1–0 S(1) line suggesting the same UV photons which excite the 3.3 μm feature cause the H_2 to fluoresce.

3.2 Extinction within NGC 2023

NGC 2023 contains a cluster of sixteen stars the centre of which, taken from the mean position of the stars, is 60″ east and 67″ south of HD 37903 (Sellgren et al. 1983). DePoy et al. (1990) and Sellgren (1983) have studied the cluster and found that half of the stars are pre-main-sequence stars with infrared excesses. The extinction to them varies from $A_v \simeq 0$–10 over small spatial scales. This may be due to the cluster being embedded with the parent molecular cloud or due to clumpiness of NGC 2023 (Gatley et al. 1987). Depoy et al. (1990) carried out infrared photometry of the stars in the cluster and found that only HD 37903 is unreddened. They suggest that as the most luminous member of the cluster it may have destroyed its primeval shroud of dust with a stellar wind. Lee (1968) and Racine (1968) however found the reddening to HD 37903 to be E(B-V) = 0.36. Malin et al. (1987) point out that this reddening is much larger than to σ Orionis [E(B-V) = 0.06], confirming that the former star is partially embedded in the L1630 cloud. Massa, Savage & Fitzpatrick (1983) found anomalous extinction to HD 37903 from UV observations characterised by the ratio of total to selective extinction, $\mathcal{R} = 4.1$ (de Boer 1983).

Lee (1968) carried out optical to near-infrared photometry of the eastern region of Orion's Belt and concluded HD 37903 was embedded in nebular material with an extinction law of $\mathcal{R} = 5.5$. They found non-normal extinction laws closely associated with the bright nebulae illuminated by early spectral type stars in the Orion region. These values of $\mathcal{R}$, larger than the typical Galactic value of 3.1, are suspected to be due to strong UV radiation preventing the formation of large dust grains in star-forming regions near OB-type stars (Winkler 1997). Sellgren (1983) using J, H, K & L measurements adopted a steep extinction law $\propto \lambda^{-2.5}$ but in later work (Sellgren et al. 1990) adopted an extinction of $A_v = 1.12$ to HD 37903, from comparing the observed far-infrared intensity to the incident radiation (from a black-body source at the temperature of HD 37903) and determining what fraction of the star's radiation is absorbed and re-radiated by dust in the vicinity of the star. This is the same extinction value as that derived using a reddening, E(B-V) = 0.36 (Lee 1968; Racine 1968) and assuming $\mathcal{R} = 3.1$. Buss et al. (1994) studied the extinction properties of dust around B-type stars and used far-ultraviolet observations of HD 37903 to derive $\mathcal{R} = 4.11$ compared to the diffuse medium mean value $\mathcal{R} = 2.95$, extrapolated from mid-UV wavelengths. They define the boundary between enhancement and destruction of large dust grains to be B1.5V and B1-type stars.

The above studies can be taken to imply that there exists a relatively low extinction, of $A_v \sim 1$, to HD 37903. This may be due stellar winds, at some point in this early type star's evolution, clearing out a space in the surrounding cloud. High extinctions still exist to other members of this star cluster either due to their protostellar cocoons or the depth at which they are located into the molecular cloud. The extinction law in NGC 2023 may also differ from the average values assumed for the diffuse ISM in the Galactic plane.

3.3 Structure

Infrared observations of NGC 2023 reveal a broken bubble geometry with a shell of $H_2 \sim 75''$ (0.17 pc) from HD 37903 (see Fig. 3.2 - Gatley et al. 1987). CO observations (J=2–1 and 3–2) have been taken to imply that the gas in the shell is hot (~ 140 K), dense and optically thin (White et al. 1991). Jaffe et al. (1990) have observed the CO 7–6 and CII lines to coincide with the fluorescently excited H_2 emission observed by Gatley et al. (1987) with the CII intensity peaking 30″ southeast of HD 37903. Field et al. (1994) have imaged NGC 2023 in the 1–0 S(1) line with 1″ spatial resolution. They find the brightest spot is 27″ north, 22″ east of the exciting star, with a surface brightness slightly higher than the southern emission ridge.

There are no identified HII regions in NGC 2023, however the presence of an ionised region ($\sim 0\farcs5$), too diffuse to give rise to detectable recombination line emission from H or He, has been inferred from CII observations (Knapp, Brown & Kuiper 1975). Pankonin & Walmsley (1976, 1978) arrive at the same conclusion and find the CII emission implies gas densities of 10^5 cm^{-3}. Knapp et al. (1975) find from the CII line widths across the nebula that no expansion or turbulent motions are imparted to the gas by HD 37903 or any other nearby early type stars. However, Rouan et al. (1997) imaged a 13″ × 13″ region the close to HD 37903 (12″ east, 3″ south) in the 1–0 S(1) line using adaptive optics to achieve spatial resolutions of 0″.15. They find very small scale clumping of gas ($\sim 10^{-7}$ M$_\odot$ of H and H_2) with densities of 10^5 cm^{-3} which are an order of magnitude denser than the surrounding gas. They suggest this small scale structure may be explained by turbulence.

Near-infrared spectral observations of the H_2 emission ridge, 80″ south of HD 37903, can be explained by a two component density structure of 10^4 and 10^6 cm^{-3} and incident UV field of $G_0 = 10^3$–10^4 (Burton 1992; Burton et al. 1997). CN and HCN measurements show high density gas ($n > 10^5$ cm^{-3}) adjacent to the H_2 emission (< 0.13 pc) suggesting CN/HCN is a good tracer of enhanced UV fields (Fuente, Martín-Pintado & Gaume 1995). Field et al. (1994) find that brightness fluctuations are due to projection factors along the line of sight and explain that the 1–0 S(1) images show the surface of a molecular cloud with undulations along it. Steiman-Cameron et al. (1997) have carried out far-infrared observations of OI, CII and SiII emission lines and, with the use of models, argue that the filament and other highly structured regions of emission are due to high density clumping ($n > 10^5$ cm^{-3}) rather than limb brightening effects. Figure 3.4 shows the structure of NGC 2023 as inferred from different tracers (Steiman-Cameron et al. 1997).

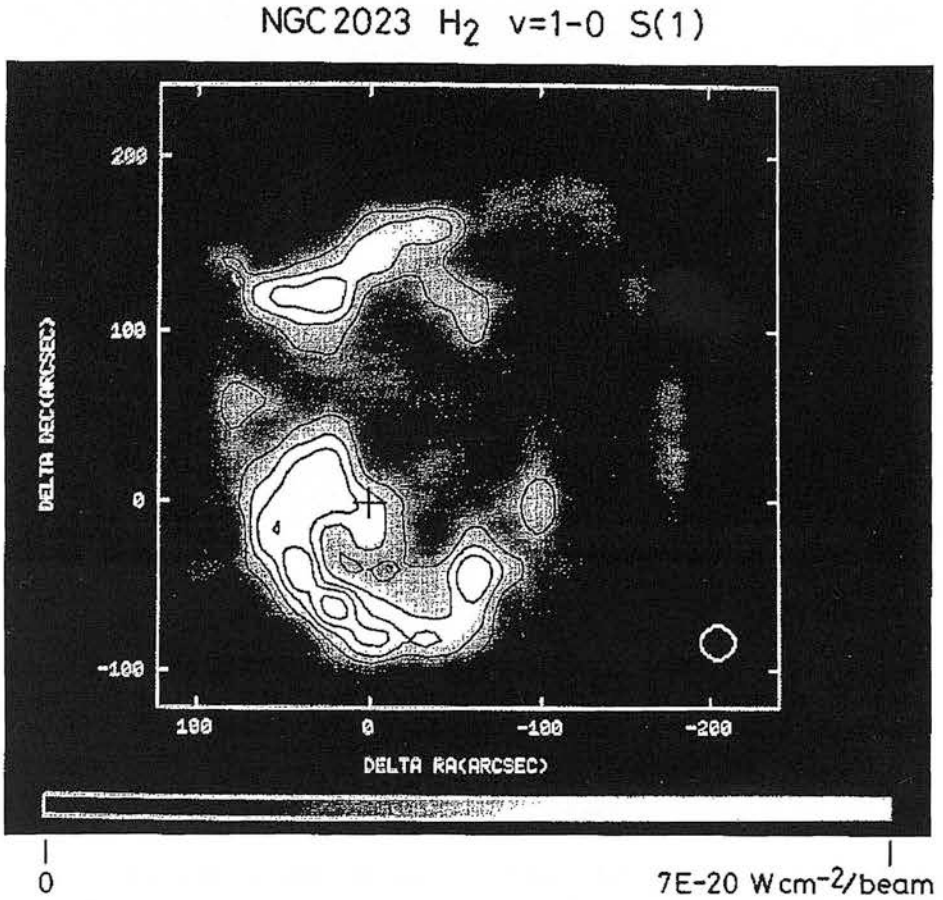

Figure 3.2: A 1–0 S(1) line map of NGC 2023 from Gatley et al. (1987). The contour interval and the level of the lowest contour correspond to an emission line strength of 9×10^{-21} W cm^{-2} in a 19″.6 beam. The position of the star HD 37903 is indicated by a cross.

3.4 S108 - A Second Source of Illumination

At the west end of the H_2 emission ridge (from which the spectra presented in this thesis were taken) 75″ south, 28″ west of HD 37903, there is a highly reddened pre-main-sequence star designated S108 by Strom et al. (1975), also known as Sellgren's Star C and HBC 500. This star has nebulosity associated with it and may be an important source of excitation for NGC 2023 and the H_2 emission ridge. A review of infrared observations is presented below.

Witt et al. (1984) conclude from visual photometry that S108 is very reddened and may have a dereddened 2.2 μm magnitude brighter than HD 37903. They suggest that the intrinsic brightness of S108 is comparable to HD 37903, consistent with a middle B star, and therefore likely to be a significant source of illumination for the reflected near-infrared light, particularly for the position south of HD 37903. This is supported by the results that S108, in comparison to HD 37903, is about 1 mag fainter at 2.2 μm (Sellgren 1983; DePoy et al. 1990) but 0.3 mag brighter at 3.8 μm (DePoy et al. 1990). Sellgren et al. (1992) suggest this is due to a combination of increasing infrared excess and decreasing reddening at longer wavelengths in S108. Malin, Ogura & Walsh (1987) agree that the near-infrared excess and Hα emission give it a high probability of being a very young star but find weak NaI and MgI absorption and tentatively suggest it is a late G or early K-type star. Its continuum shape, colours and extinction of ~ 3 mag are consistent with this spectral type. Assuming this were true, the V-magnitude of 17.69 given by Witt et al. (1984) would indicate that this star is a dwarf. Additionally, Malin et al. (1987) suggest S108 is the progenitor

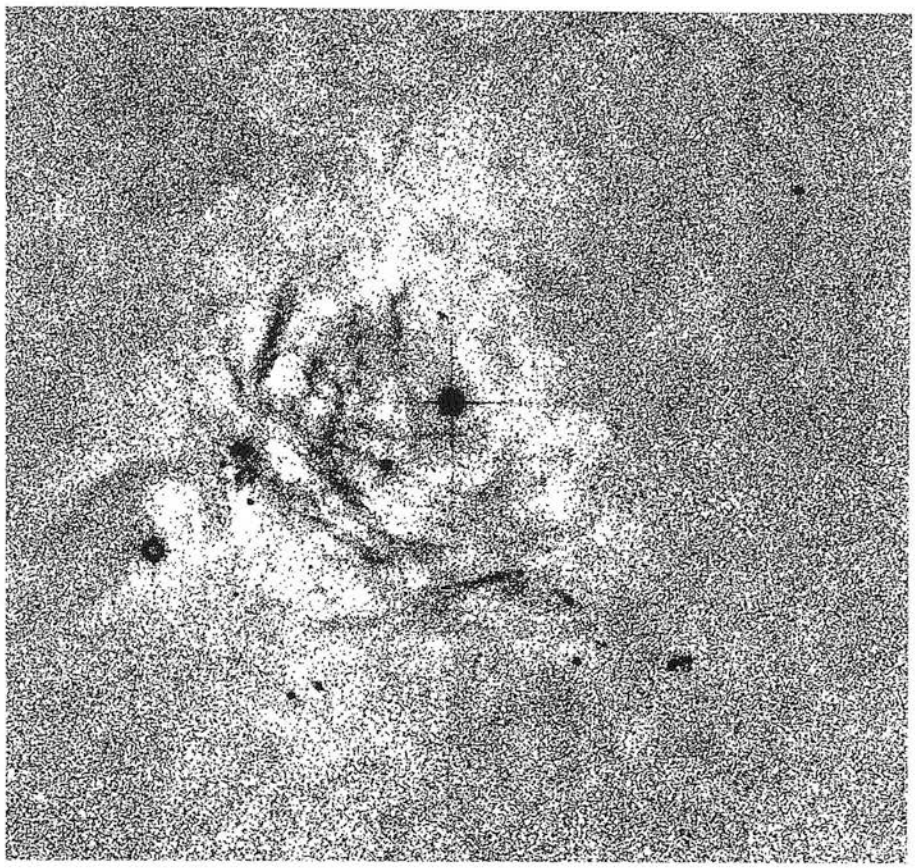

Figure 3.3: An unsharp-masked R exposure of NGC 2023 taken from Witt & Malin (1989). All image structure common to the R and B images has been photographically subtracted. The remaining structure is essentially due to the ERE.

of three nearby Herbig-Haro objects and may also be related to the outflow 50″ away observed by Bally & Lada (1983). However they point out that the 10 μm emission one would expect to detect from an emerging young star has not been detected (Harvey et al. 1980).

Sellgren (1983) found Hα emission which they concluded arose from dense circumstellar shells or stellar winds. This is because the observed stellar flux would predict optically thin free-free emission at radio wavelengths, far in excess of the 6-cm upper limits of their observations. Scarrott et al. (1989) found a small bipolar nebula associated with S108 and inferred the presence of a circumstellar disc oriented approximately east-west and perpendicular to the axis of the north-south bipolar outflow. This disc is considered to be the source of the Hα emission seen by Sellgren et al. (1983) and contributes to the obscuration of the star itself. The obscuration of the lobes suggest the star is located further into the dark cloud than HD 37903. Sellgren et al. (1992) adopt the intrinsic colours of a B5V star and find they require a K-band extinction of $\sim$ 1 mag to deredden the star. Since this extinction is likely to arise in a circumstellar disk, the extinction along the line of sight to S108 may be much higher than the extinction between S108 and much the reflection nebula. Pankonin & Walmsley (1978) find CII emission peaking 1′ south of HD 37903 and suggest S108 may contribute to the excitation. However, polarisation studies reveal that S108 illuminates the nearby nebulosity in the I and H bands but not detectably in the V and R bands (Scarrott et al. 1989; Sellgren 1992). This indicates S108 does not contribute to the UV excitation of the emission ridge 80″ south of HD 37903, the PDR which is the subject of this thesis. This conclusions appears to be confirmed by the geometry of the images presented in Chapter 4.

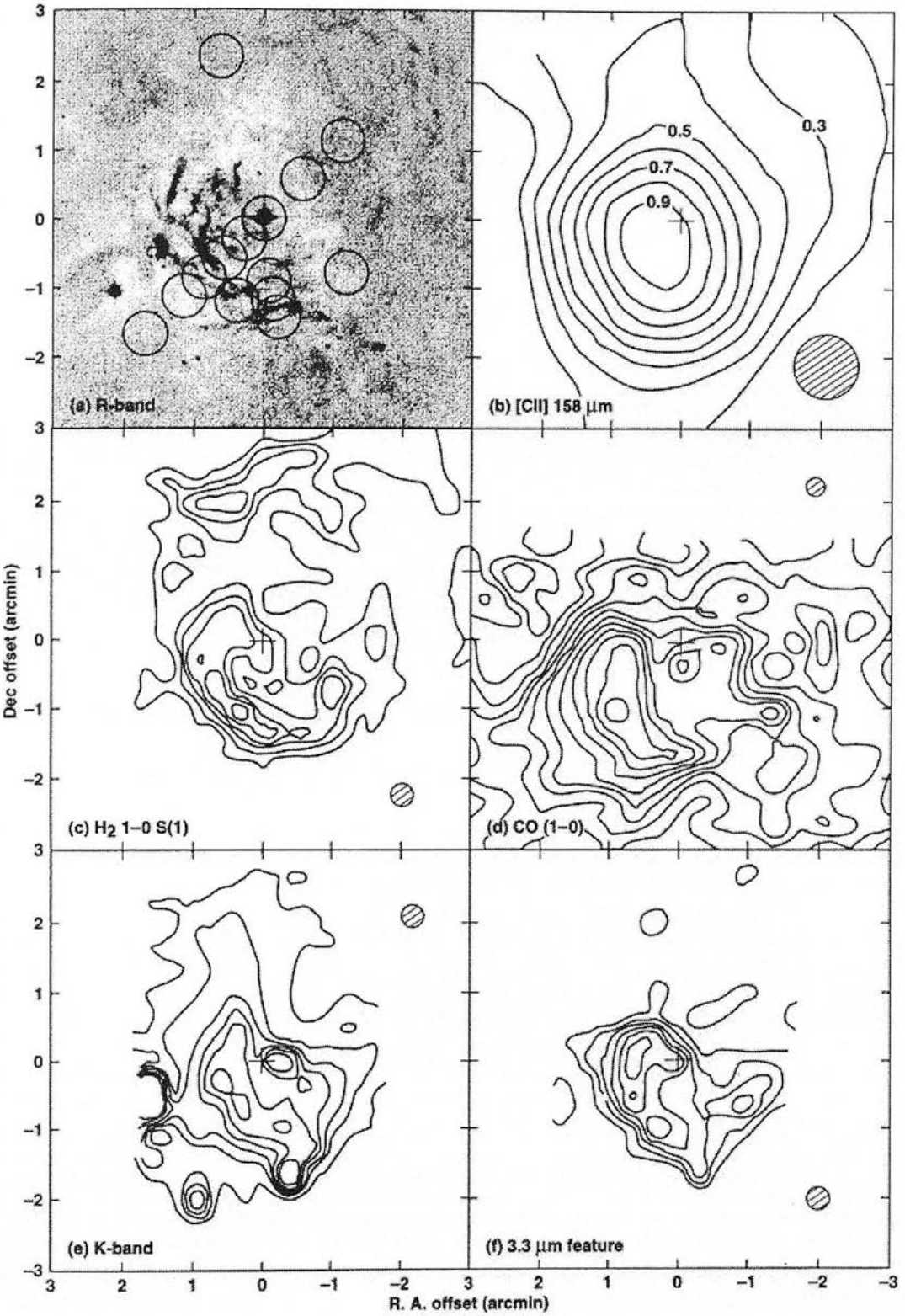

Figure 3.4: Images of NGC 2023 at both line and continuum wavelengths compiled by Steiman-Cameron et al. (1997). (a) An unsharp masked R-band image (Witt & Malin 1989); (b) CII (158 μm) map adapted from Howe et al. (1991) and maps of (c) H_2 $v = 1$–0 S(1), (d) CO $J = 1$–0, (e) K band, and (f) 3.3 μm feature adapted from Gatley et al. (1987). Beams are indicated by circles and a cross marks the position of HD 37903.

Chapter 4

The Observations

In this chapter the data from five different observing runs are collated and presented. Three of the datasets are taken from published data and the other two from observations carried out by Peter Brand[1], Michael Burton[2], Antonio Chrysostomou[3] and myself. The observations are described in Section 4.1 and the data reduction process which I have carried out on two of the datasets is described in detail in Section 4.2. The spectroscopic observations are analysed and compared with each other and with reference to infrared imaging data. The infrared images are used to calculate the beam dilutions for the different observations to allow the datasets to be combined. The quantities optical extinction and the ortho/para abundance ratio of molecular hydrogen are derived.

4.1 Data Acquisition

4.1.1 Observing at Near Infrared and Far-red Wavelengths

The 1–5 μm region of the spectrum is a rich source of atomic and molecular lines where many of the brightest H_2 transitions occur. However, it also a source of strong and interfering emission due mainly to transitions of vibrationally excited OH. These arise high up in the atmosphere between 85 km and 100 km and vary on time-scales of minutes (Ramsay, Mountain & Geballe 1992). These sky lines are typically several orders of magnitude brighter than astronomical sources. Consequently measurements must consist of exposures sufficiently short to prevent detectors becoming saturated, followed every few minutes by sky frames observed close to the source. Beyond the K-band (2.0–2.4 μm) atmospheric window the background emission is dominated by the emissivity of the telescope. The data presented here were observed at wavelengths $< 2.4\,\mu$m. The dominant contribution to atmospheric absorption comes from the H_2O molecule which is particularly noticeable beyond 1 μm. Observing at the 3.8-m UK Infrared Telescope (UKIRT) on Mauna Kea minimises this problem since the telescope is at an elevation of 14,000 feet above sea level and above 90% of the Earth's water vapour. At UKIRT, the transmission through the J, H and K atmospheric windows is close to unity, only dropping off towards the edges of the windows.

UKIRT employs infrared detectors which are fundamentally different in the way they are read out compared to optical detectors. IR detectors are read out directly whereas optical CCDs are read by charge transfer. This permits non-destructive readout (NDR - Chapman et al. 1990) in IR arrays. Multiple measurements are made of a signal as it accumulates in a pixel. By fitting a slope to these independent measurements the effective noise may be significantly reduced. The uncertainty in the measurement, for a number of readouts n, due to the readout noise $\sigma_{\rm rd}$, is given by $\sigma_{\rm ndr} = (n/12)^{-1/2}\sigma_{\rm rd}$.

At wavelengths less than 1 μm optical CCDs may be used to observe transitions arising from

[1] Institute for Astronomy, University of Edinburgh, Blackford Hill, Edinburgh, EH9 3HJ, Scotland
[2] School of Physics, University of New South Wales, Sydney, NSW 2052, Australia
[3] Joint Astronomy Centre, 660 North A'ohoku Place, University Park, Hilo, HI 96720, Hawaii

highly excited states of H_2. The disadvantages of weaker intrinsic line strengths, and increased extinction are offset by the increased sensitivity and stability of the detectors and their wide passband at high spectral resolution. This coupled with the lower sky background make flux measurements of these lines also possible in the far-red wavelength regime (0.8–1 μm).

On the nights of the 14th and 15th October 1995, UKIRT was used with the Cooled Grating Spectrometer 4 (CGS4 - Wright 1994; Mountain et al. 1990) and the Infrared Camera 3 (IRCAM3 - Puxley et al. 1994) to observe the reflection nebula, NGC 2023. The observations made use of the new 256 × 256 pixel array and voltages were recorded in non-destructive readout mode. Three and a half months later on January 30th and 31st 1996, the 3.9-m Anglo-Australian Telescope (AAT) was used with the RGO Spectrograph (Stathakis 1997) to observe the same source, the ridge of bright fluorescent H_2, 80″ south of HD 37903. In both spectroscopic observations a spectral type A0 star, HD 40335, was used as a standard for flux calibration.

4.1.2 IRCAM3 Images

The observations were taken between 4.30am and 5.30am (Hawaiian Standard Time) at an airmass of 1.1, in 1″ seeing conditions. The entire 256 × 256 pixel array was illuminated at a scale of 0″.286/pixel. A set of bias and dark frames were taken initially to provide a test of the detector chip's stability and performance and another dark frame was taken before each set of exposures was observed. The data were stored in units of data number corresponding to six readout electrons. The two narrow band filters used were:

Name	λ (Peak) (μm)	λ (Central) (μm)	λ (Half-max) (μm)	FWHM (μm)	FWHM (%)	Peak Transmission (%)
1–0 S(1)	2.122	2.119	2.109–2.129	0.020	0.9	60
Cont 2.1	2.104	2.102	2.092–2.112	0.020	0.9	60

Two mosaiced images were taken in the 1–0 S(1) line filter and one in the 2.1 μm continuum filter centred on the bright ridge, 9″ west and 78″ south of HD 37903. The exposure times were set to 50 seconds to ensure the major contribution to the noise level was due to background sky emission and not instrumental readout noise. Each mosaic consisted of 9 overlapping 'tiles' each one offset 20″ from adjacent tiles to form a square, 113″ × 113″.

HD 37903 was used as a standard and observed in the line filter once before and once after the observations of the bright ridge were taken. The resulting two mosaiced images consist of 5 'tiles', each a 30 second exposure, offset 15″ from adjacent tiles. These overlap in a pattern of positions, like the dots which form five on a die, to form a square, 103″ × 103″.

4.1.3 CGS4 Spectra

The observations were taken between 2am and 4am (Hawaiian Standard Time) at an airmass of 1.3, in 1″.5 seeing conditions. We used the 75 lines/mm grating in conjunction with the 'short' 150-mm focal length camera. This configuration allowed the whole H band to be observed at one grating position with a resolution of $\lambda/\delta\lambda = 910$, covering the wavelength range 1.44–1.78 μm. The full 90″ slit was used to illuminate the pixel array with a scale of 1″.23/pixel and a slit width corresponding to one pixel. The slit was orientated -76° east of north along the H_2 emission ridge (see Fig. 4.3).

The CGS4 detector array may be moved fractions of a pixel during the course of an observation. Stepping the detector a number of times during each observation permits a spectrum to be oversampled. For an unresolved line this convolves the profile of the slit and a pixel, which are both rectangular, to produce a triangular line profile. The line centre may then be determined with greater precision. The FWHM of the triangle is the same as the pixel width and the area under the triangle is proportional to the flux in the line. Stepping the detector across more than

one pixel has the additional benefit of covering bad pixels so information is not lost where a good pixel is stepped across the wavelength range of a bad pixel.

Since the bright sky background varies so rapidly, exposures must be short (≤ 60 s) followed by nods/chops to blank sky. This ensures the uncertainty on a measurement is dominated by photon (Poisson) noise not the amplitude fluctuations in the OH lines. During this time CGS4 can return data at up to 20 kilobytes per second. This means that a certain amount of the data reduction must be automated (see Section 4.2.2). This is carried out by the CGS4 data reduction software at the telescope (CGS4DR - Puxley et al. 1992).

CGS4DR stores data in a hierarchical structure. Observations consist of integrations which are made up of exposures. The duration of an exposure is limited to how quickly the pixel wells fill up with electrons. This is determined by how bright the sky is and the brightest object in the frame. Integrations consist of a number of exposures taken at a single detector position. These are combined to form an observation which has an error array derived from the variance of the different integrations. The different types of exposure are:

- Bias - a short blank observation, which measures the default offset due to the applied potential in each pixel.
- Dark - a blank observation with the same on-chip exposure time as other observations. This measures time-dependent sources of noise, such as the thermal activity of the chip. The dark current is about 0.2 electrons/sec.
- Flatfield - an observation of the sky, the illuminated dome or a continuum source in the calibration unit. We observed a black-body source at 1071 K.
- Arc - an observation of an arc lamp for wavelength calibration. We used the xenon lamp.
- Source - an object, standard star or sky observation. This observation records data from where the telescope is pointing.

Bias, dark and flatfield frames are observed without oversampling since they are intended to convey only information regarding the response of the detector's individual pixels. The standard star, HD 40335, was observed before and after NGC 2023 for flux calibration. HD 40335 and NGC 2023 were observed in 'quads' whereby an observation is taken of the source, followed by the sky, in this case nodding south 42″, the sky observation is repeated and then the telescope returns to observe the source once more. This procedure minimises time overheads, due to moving the telescope, and allows sky subtraction close in time to object observations. The standard was in the slit for both object and sky observations. This saved time and allowed a second order sky subtraction to take place (see Appendix A). The data were recorded as 772×85 pixel arrays.

4.1.4 RGO Spectrograph Data - 1996

On the nights of the 30$^{\text{th}}$ and 31$^{\text{st}}$ January 1996, the Anglo-Australian Telescope (AAT) was used with the RGO Spectrograph to observe the ridge of bright fluorescent H_2 in NGC 2023. The observations were taken using the 1200 lines/mm (1200R) grating, in the first order, with the 25-cm camera at the f/8 Cassegrain focus. Previous experience (Burton M. G., private communication) had shown that the Tektronix CCD, although having a high quantum efficiency, was prone to suffer high cosmic ray hit rates and excessive fringing. Thus for this reason and consistency with the 1990 RGO Spectrograph observations, the Red Thomson 1024×1024 CCD was chosen as a detector. Four grating positions were used over both nights to cover the wavelength range 7300–9600 Å with resolutions of $\lambda/\delta\lambda = 4000$–$7000$. A 250″ slit was used to illuminate the CCD with a pixel scale of 0″.61 and a slit width of 1″.5. The slit was orientated -78° east of north to match to observations of Burton et al. (1992a) (Section 4.1.5). The readout time of the CCD was half a minute. This, together with the low, stable background sky emission of the optical regime, meant we required long exposures to achieve sky background limited noise and to minimise time overheads. The source was observed for 4×1000 seconds at each grating position. The high resolution made

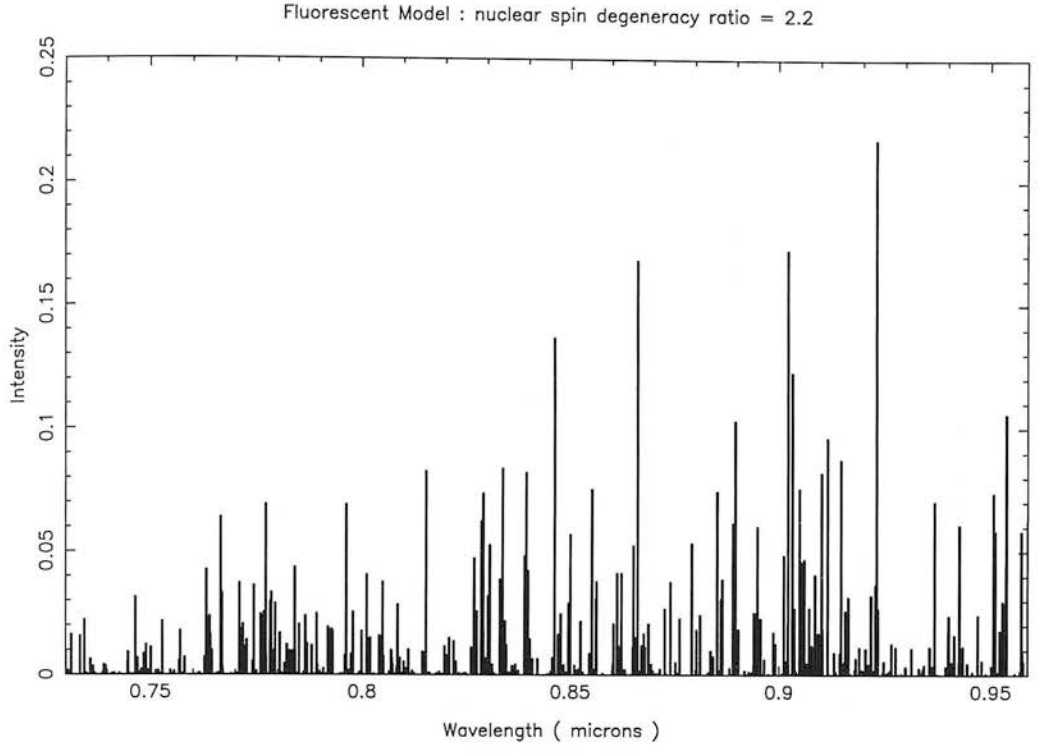

Figure 4.1: Synthetic spectrum of H_2 lines plotted with intensity as a fraction of 1–0 S(1) line strength (Brand 1996)

oversampling unnecessary and the long slit permitted the source to be observed simultaneously with the sky background (see Appendix A for details).

Bias, dark and flatfield frames were observed at the beginning of the first night. The bias frames revealed that stray light was leaking in from the dome. This increased the bias values by up to 20% so they were re-observed at the end of the second night. The light leak contributed to less than 1% of each of the flatfield frames so they were still used. The observations of NGC 2023 were carried out with the dome lights switched off and were uncontaminated. The copper-argon arc lamp was observed for 3 seconds each time the grating position was changed or the telescope was moved. Before and after each observation of NGC 2023, the standard star HD 40335 was observed. The first night was cloudless with 2″ seeing. We observed NGC 2023 at 3 grating positions giving priority to the wavelength regions with the greatest number of bright H_2 lines where the detector had a high quantum efficiency (Figs. 4.1 & 4.2). During the second night the clouds began to clear after midnight and we observed at one grating position (7320–7960 Å) with over 3″ seeing. The exposures were stored as raw 471 × 1025 pixel images with no form of reduction having been applied.

4.1.5 RGO Spectrograph Data - 1990

Burton M. G., Bulmer M., Moorhouse A., Geballe T. R., Brand P. W. J. L., 1992, MNRAS, 257, 1P
On the night of November 6th 1990, the AAT was used with the RGO Spectrograph to observe the ridge of bright, fluorescent H_2 in NGC 2023. The observations were taken using the Red Thomson 1024 × 1024 CCD and the 600 lines/mm (600R) grating, in the first order, at the f/8 Cassegrain focus. The wavelength range 7557–8837 Å was covered with a resolution of $\lambda/\delta\lambda = 2600$. A 150″ long slit (1″ wide with 0″.61 pixel scale along the slit) was orientated -78° east of north along the ridge of H_2 emission peaking 9″W, 78″S of HD 37903. The source was observed for 8 × 1000 s in photometric conditions and 36 pixels were used to calculate the intensities of the H_2 lines.

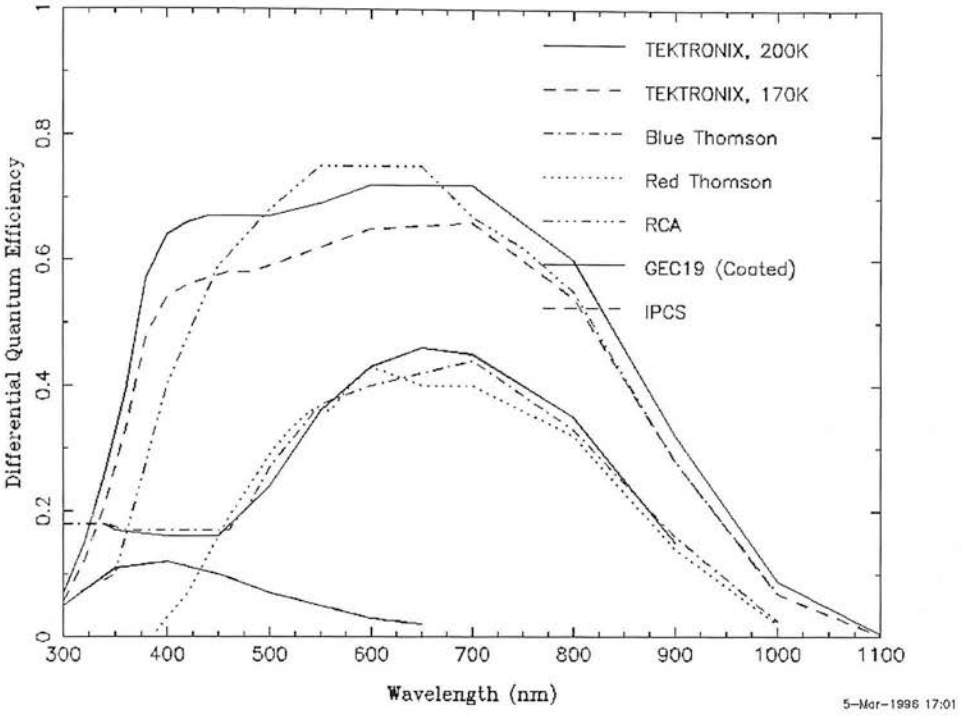

Figure 4.2: Quantum of efficiencies of different CCD detectors (AAO Observing Manual). Note the 'Red Thomson' response curve.

4.1.6 CGS2 Spectra

Burton M. G., Howe J. E., Geballe T. R., Brand P. W. J. L., 1997, PASA, in press
On the nights of November 28th–December 1st 1989, UKIRT was used with the grating spectrometer CGS2 to observe the bright bar of H_2 emission in NGC 2023 to obtain J, H and K spectra. The J and H-band measurements were made with a 633 lines/mm grating used in the first order for J and second order for H and a 300 lines/mm grating was used in the second order for K. The spectral resolutions were $\lambda/\delta\lambda$ = 300, 420, and 200 for the J, H, and K-band observations respectively. The beam used was roughly circular $5''.0 \times 4''.5$. The source was observed $11''$ west $78''$ south and sky frames were made chopping at a frequency of a few tenths of a Hertz, $120''$ from the source.

4.1.7 UKT9 Spectra

Hasegawa T., Gatley I., Garden R. P., Brand P. W. J. L., Ohishi M., Hayashi M., Kaifu N., 1987, ApJ, 318, L77
On the nights of the 28th and 29th December 1985, UKIRT was used with the photometer system UKT-9 equipped with a circular variable filter in tandem with a Fabry-Pérot (FP) filter. The spectral resolution of the FP was $100\,\mathrm{km\,s^{-1}}$. Ten H_2 lines were observed in the K band. The measurements were made toward $80''$ south of HD 37903. The aperture was $19''.6$ in diameter, and the sky chopping was made with a throw of $3'$ east–west.

4.2 Data Reduction

The H_2 lines presented here are very faint requiring careful reduction of the observational data to remove sky emission lines and instrumental artifacts and thus achieve accurate flux measurements. The reduction steps are described in detail below.

4.2.1 IRCAM3 Images

The following steps were carried out to create each mosaiced image. Hereafter an observation will refer to the set of exposures (256 × 256 pixel tiles) taken to form a mosaic when combined.

- Array tests - the bias and dark current frames were tested for array stability and performance. The readout noise was 41 e^-/sec and the dark current was 8 e^-/sec.
- Bias subtraction - the exposed frames, including the dark, were taken in non-destructive readout mode (Chapman et al. 1990) which automatically removes any d.c. offset and therefore bias subtraction is not required.
- Dark subtraction - the dark frame, taken at the beginning of each observation, was subtracted from each tile. For narrow band imaging this operation was necessary since IRCAM3 was originally designed to be used with a 58×62 pixel array with high dark current (100 e^-/sec), so is not very light tight and has a significant dark current.
- Normalise tiles to 1 second exposures.
- Create Flatfield - the median value of each tile was taken as a representative value for the tile. They were then normalised to the same median level (the median of median values). These tiles were 'stacked together' and median filtered to create a flatfield frame.
- Apply d.c. offsets between tiles - where tiles overlap the median was calculated to get the d.c. offsets between the tiles. The offsets were then subtracted (to correct for sky variation during the observation).
- Apply bad pixel mask.
- Create Mosaic - the tiles were 'quilted' together and the result was normalised to a one second exposure.

A comparison of the two 1–0 S(1) line filter images, taken 25 minutes apart, showed 11 faint star-like sources which had changed position between the observations. A comparison of the continuum and line filter images also shows 13 objects which appeared in the continuum observation but not through the line filter. This fact on its own would suggest a problem but considered together with the change in positions between observations implies these objects are in fact reflections of one or more bright stars due to inadequate baffling of stray light from the telescope beam. A possible culprit could be Zeta Orionis, the bright (V=1.79) left most star in Orion's Belt (20′ north, 13′ west of the H_2 ridge). These ghost reflections were removed from the image by interpolating values from neighbouring pixels across the affected areas. The image of the star HD 37903 may also contain point sources due to ghost reflections but without a continuum filter image to compare to the line filter image it is difficult to prove.

The average of the centroid positions of five stars were used to calculate the shift in position between the two 1–0 S(1) images (0″.3 north, 0″.1 west) ± (0″.05, 0″.05). The second image was then shifted and overlaid onto the first. A separate sky frame had not been observed at the telescope so a sky background value was taken from the lowest value (within the scatter) along a central row of the image. This adopted sky background value (14.5 counts/sec) was then subtracted from the 1–0 S(1) mosaic (Fig. 4.18). A value for the sky background of the continuum filter mosaic (9.7 counts/sec) was subtracted in the same way (Fig. 4.19).

The final two mosaiced images were then lightly smoothed with a Gaussian function, to damp out fluctuations due to noise, and the continuum image was subtracted from the 1–0 S(1) image. Since the filter widths were not precisely the same, a constant value of 1.14 was multiplied to the continuum image before subtraction. This value was determined iteratively to give the minimum stellar residuals after subtraction from the 1–0 S(1) image. The continuum subtracted image is shown in Fig. 4.20.

The absolute flux could not be accurately measured because the standard star, HD 37903, had saturated in the IRCAM3 pixel array. However, a point spread function was calculated from two stars in the field using the photometry package *Daophot* (Stetson 1987). This was scaled and applied to HD 37903 to estimate the flux which would have been received had the pixel array not saturated. The image was then rotated through 13° and the apertures shown in Fig. 4.3, were used to calculate the fluxes expected from the beams used for each instrument. Table 4.1 shows these expected fluxes for the best estimates of the positions of the apertures used to take the spectra. The absolute fluxes derived from the images agree with the spectroscopic data to within 35% (see 1–0 S(1) line at 2.12 μm in Table C.3) and the relative fluxes to within 25% (see Table 4.2). The CGS2 and UKT9 apertures were placed where the peak emission occurs from the ridge. The long slits were placed at the telescope position coordinates of their respective observations. The long slit apertures miss the peak emission from the ridge by less than 1″. Placing them on this peak increases the measured fluxes by 10–20%.

Instrument Apertures	Position offset from HD 37903	Flux ($W\,m^{-2}\,beam^{-1}$)	Beam Size (arcseconds)	Intensity ($W\,m^{-2}\,sr^{-1}$)
RGO Spectrograph 1996	9″ W 78″ S	1.96×10^{-16}	38.4 x 1.5	1.43×10^{-7}
RGO Spectrograph 1990	9″ W 78″ S	0.79×10^{-16}	22.0 x 1.0	1.59×10^{-7}
CGS4	9″ W 78″ S	1.64×10^{-16}	38.1 x 1.23	1.48×10^{-7}
CGS2	~ 80″ S	0.90×10^{-16}	5 diam	1.96×10^{-7}
UKT9	~ 80″ S	0.74×10^{-15}	19.6 diam	1.06×10^{-7}

Table 4.1: Fluxes derived from placing software apertures over IRCAM3 image.

4.2.2 CGS4 Spectra

The CGS4 data reduction software automatically carries out the following sequence of operations and stores the result as a 'reduced observation':

- Apply a bad pixel mask - pixels which are known to be 'hot' or unresponsive are flagged as bad.
- Subtract a bias frame - dark, flatfield and arc frames are short exposures taken in destructive readout mode and are bias subtracted. The source observations are all taken in non-destructive readout mode (Section 4.1.1) which automatically removes any d.c. offset and therefore bias subtraction is not required.
- Linearise the signal - for the detector array used in CGS4, no measurable non-linearity has been found to within 98% of having a full electron well (Daly 1995), so this operation was not applied.
- Divide by a flatfield - a 1D polynomial is extracted from the image and then normalised with a polynomial fit (*e.g.* 3rd order) to remove the spectrum of the black-body calibration source.
- Interleave integrations taken at different detector positions. Data from two pixels at the same wavelength (*i.e.* from adjacent good pixels) are averaged.
- Carry out an initial wavelength calibration estimate.

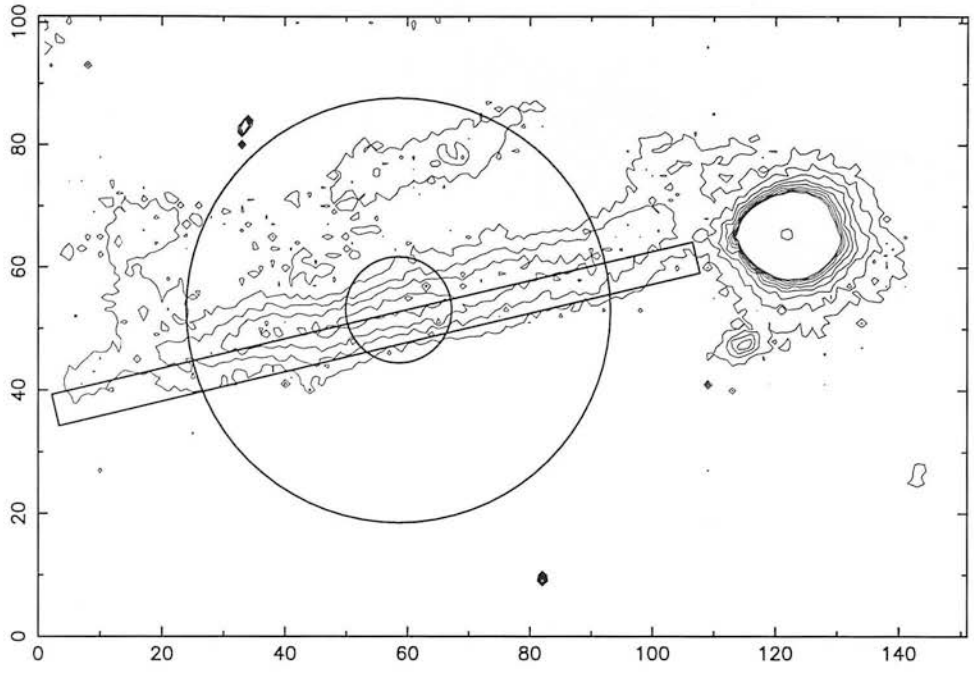

Figure 4.3: 1–0 S(1) image of NGC 2023 showing the instrumental apertures used to calculate the relative fluxes expected from the observations (Brand 1997).

The dark current was typically < 1 electron/sec which made dark frame subtraction unnecessary. The following data reduction was carried out within the *Figaro* (Shortridge 1993) and *Kappa* (Currie 1995) environments under *Unix*. The x-axis corresponds to the dispersion direction and the y-axis corresponds to the direction along the length of the slit.

- Tidy images - The bias, dark and flatfield frames were inspected for array stability and performance. Rows which were poorly illuminated or had little sensitivity at the edge of the array were removed. The resulting images were 771×73 pixels in size.
- Sky subtraction - Sky observations were subtracted from object observations, taken adjacently in time, to remove sky emission.
- Remove line curvature - There is an optical distortion in the CGS4 optics which results in emission lines appearing curved and the position of continuum sources tracing out a curve along the pixel array. This was removed in two stages.
    1. The central 11 rows of the xenon arc observation were extracted and wavelength calibrated. This spectrum was then used to find the positions of the arc lines in each row of the image, working from the central row outwards. The image was then re-binned so lines would be straight along the y-axis. This correction was then applied to all the observations.
    2. Now wavelength calibrated, the x-axes of the images were linearised. An image containing the standard, HD 40335, in two places (see Appendix A) was used to fit polynomials across the continuum emission. The image was then re-binned so lines would be straight along the x-axis. This correction was then applied to all the observations.
- Combine observations - for a given position along the slit all the rows from different observations were averaged to create a spectrum with error bars derived from the variance. A four

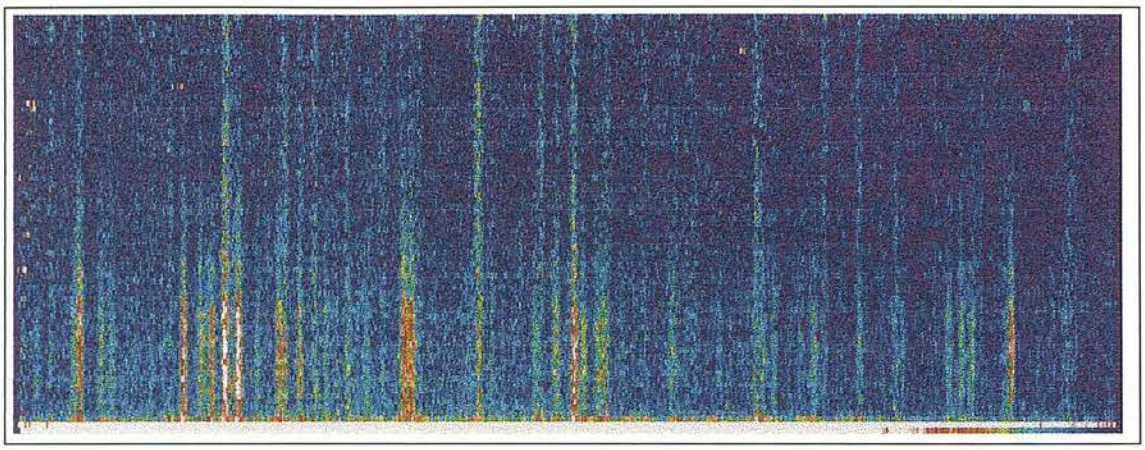

Figure 4.4: NGC 2023 in the H band (1.45–1.78 μm).

sigma cutoff was used to filter out cosmic rays. This was carried out for each row along the slit.

- Extract spectra - rows 4 to 34 were averaged to produce a spectrum which gave the maximum signal to noise and covered the same area of emission as did the aperture used in the 1996 RGO Spectrograph observations.
- Derippling - Variation in a compact object's brightness between separate integrations (*i.e.* different detector wavelength positions) can be caused by changes in seeing or slight motion of the image with respect to the slit (*e.g.* due to wind-shake). This manifests itself as a periodic pattern in the dispersion direction of the image. No periodic pattern, due the stepping of the detector, was apparent in the spectra of NGC 2023 or the standard star.
- Flux calibration - The spectra of NGC 2023 and the standard star were both normalised to exposures of one second. A *Figaro* routine 'irflux' was used to automatically flux calibrate NGC 2023. It created a black-body spectrum at 9,520 K (corresponding to the spectral type, A0, of the UKIRT standard star HD 40335) which it removed from the standard. The result was a spectrum of the atmospheric transmission. NGC 2023 was then calibrated to the H-band flux of the standard ($m_H = 6.473$) using flux values of the zero magnitude star Vega (Mountain et al. 1985). The spectrum of NGC 2023 then had the atmospheric transmission divided out from it and was corrected for the slit transmission which, for the seeing conditions and slit width, corresponded to a factor of ~ 0.6 (AAO Observing Manual).

Figure 4.4 shows an image consisting of spectra from different positions along the slit. The wavelength dispersion direction is along the horisontal axis and the slit direction (corresponding to physical direction) along the vertical axis. The continuum source S108, lies horisontally along the bottom of the image. The vertical lines spanning the whole image are residual sky lines and lines visible in only the bottom half of the image are due to H_2 emission.

4.2.3 RGO Spectrograph Data

The following data reduction was carried out within the *Figaro* (Shortridge 1993) and *Kappa* (Currie 1995) environments under *Unix*. The y-axis corresponds to the dispersion direction and the x-axis corresponds to the slit direction and one dimensional physical structure along the H_2 emission ridge.

- Tidy images - the bias, dark and flatfield frames were inspected for array stability and performance. Rows and columns which were poorly illuminated or had little sensitivity at the edge of the array were removed. Some of the light had fallen passed the slit on to the

CCD, these columns were also removed. The resulting images were 124×1021 pixels in size. The data were reflected in the y-axis to conform to increasing wavelength with y-axis values.

- Bias subtraction - the four bias frames taken at the end of the second night were median filtered and the resulting frame was subtracted from all of the data.

- Flatfielding - the continuum source was observed for 3×200 seconds for the 3 shorter wavelength grating positions and twice as long for the 9000 Å observation, due to the lower quantum efficiency of the CCD at those wavelengths (see Fig. 4.2). These exposures were then median filtered and each resulting frame was normalised to a mean count of unity. The following operations were applied to the flatfield frame for each grating position.

  - collapse flat to give slit profile - all the rows were summed together to create a profile of the slit's illumination of the detector. This was smoothed with a Gaussian filter to remove pixel to pixel variations.
  - collapse flat to give black-body profile - all the columns were summed together to create a black-body spectrum of the continuum source lamp. Flats with absorption features were smoothed using a Gaussian function, otherwise a high order polynomial was fitted.
  - create smoothed flat - the x-axis and y-axis profiles were then expanded into images and multiplied together to create a smoothed flat. This image was then normalised to mean of unity.
  - create final flatfield frame - the smoothed flat was divided into the raw flat to remove the large scale structure due to the spectral profile of the continuum source and the geometrical effect of the CCD being illuminated through the slit by a nearby source. The resulting flatfield was a measure of the pixel to pixel variations in sensitivity across the CCD.

  All the exposures were divided by the flatfield frame for that grating position.

- Cosmic ray removal - the Thomson CCD was subject to many cosmic ray hits per exposure. A 1000 second exposure would typically require removal of 40 cosmic rays by interpolating pixels on either side of the affected area. The direction of interpolation depended on the cosmic ray's proximity to a sky line or the continuum source. This process was very costly in terms of time but essential to producing high signal to noise spectra.

- Sky subtraction (1st order) - subtracting pairs of observations taken straight after each other removed sky emission and noise specific to pixel locations on the CCD. It was important to carry out this operation before removing line curvature, otherwise straightening lines would cause strong sky line emission to spill over onto neighbouring pixels rather than emission from the fainter residual sky lines.

- Remove line curvature - sky lines were used to trace the optical distortion in the x-axis across the CCD. Parabolas were fitted to the sky lines and the distortion between them was mapped by interpolating between them with parabolas in the y-axis. The data were then re-binned which successfully straightened the sky lines. This correction was calculated for each grating position and applied to the exposures taken at that grating position.

- Sky subtraction (2nd order) - the images were then bisected along the y-axis and the negative half was subtracted from the positive half and the result was normalised to one exposure (see Appendix A). This process helped to remove the residual sky lines. A further correction of removing residual sky lines was attempted. This involved subtracting low order polynomials which had been interpolated across the H_2 emission, fitted to the residual sky lines on either side. However, this introduced more noise and so was abandoned.

- Wavelength calibration - the wavelength scale was calibrated against a copper-argon arc lamp. A parabola was fitting to the wavelength positions of the identified arc lines. All the grating positions were calibrated to an r.m.s. deviation of less than 0.5 angstroms.

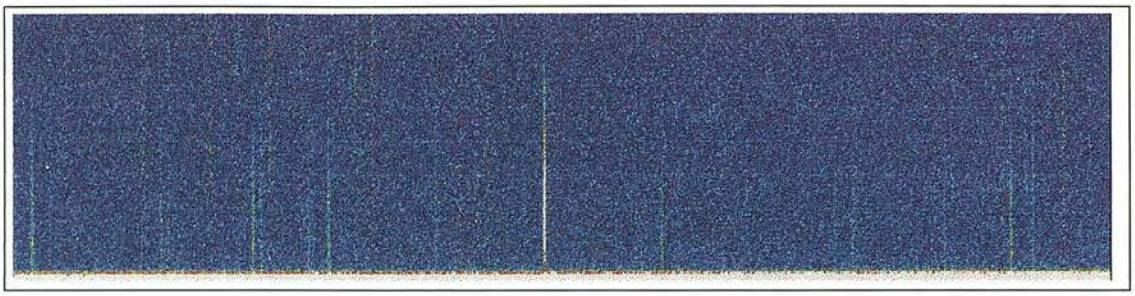

Figure 4.5: NGC 2023 in the I band (grating position 0.84–0.90 μm).

- Extract spectrum - 57″ of the slit contained detectable CI emission (8729 Å), in the grating position with the best signal to noise (8402.9–9031 Å). However, the greatest signal to noise in the H_2 lines was achieved by integrating the emission along 38″ of the slit. This was taken between 5″ and 43″ away from S108, the star at the end of the ridge.
- Reduce standard - the above steps were carried out in reducing the observations of the standard star, HD 40335, however the spectrum was extracted using the 'optimal extraction algorithm' (Horne 1986). This improves the signal to noise by non-uniform weighting of pixels determined from the spatial profile of the star. The following operations were applied to the resulting spectrum.
  - Remove HI Paschen lines - the standard star observed was spectral type A0 and had strong HI absorption features, these were removed by fitting cubic splines to the features and dividing them out (Brand 1996)
  - Remove spectral profile from standard - a black-body profile at 9,520 K was generated and scaled to a flux equivalent to that from an A0-type star with an I magnitude of 7.2.
  - Create spectrum of atmospheric transmission - the standard was divided by the black-body to give a spectrum of the atmospheric absorption in units of counts/flux. This was then corrected for the slit transmission, which for the seeing conditions and slit width, corresponded to a factor of ~ 0.6 (AAO Observing Manual).
- Flux calibrate observation - the spectra of NGC 2023 and the atmospheric transmission were both normalised to exposures of one second. The atmospheric transmission was then divided out from NGC 2023.
- Normalise the grating positions - the wavelength ranges of the different grating positions overlapped sufficiently to permit comparisons of a few of the same lines to be made. The first three grating positions (8725 Å, 8150 Å and 9280 Å) taken at the beginning of the first night agreed extremely well, there being no discernible difference between the continua of each spectrum and the fluxes in the common lines agreed to within 20%. The fourth grating position (7650 Å) was taken on the next night through intermittent patches of cloud and had to be normalised to the rest of the data with a factor of 0.5.

Figure 4.5 shows an image consisting of spectra from different positions along the slit. The wavelength dispersion direction is along the horisontal axis and the slit direction (corresponding to physical direction) along the vertical axis. The continuum source S108, lies horisontally along the bottom of the image. The vertical lines spanning the whole image are residual sky lines and lines visible in only the bottom half of the image are due to H_2 emission. The brightest line is the CI 8729 Å line.

4.2.4 H_2 Line Fluxes and Column Densities

The resulting spectra of NGC 2023 contain numerous emission lines. Due to the many hundreds of candidate H_2 transitions arising from these wavelength regions, it was important to find a

fast, reliable method of identifying the lines. The method adopted was to use the *Figaro* arc line identification program 'arc' and pass it a list of wavelengths of H_2 transitions. These were calculated from the H_2 energy levels of Dabrowski (1984), for lines which were theoretically bright enough to be detected in pure fluorescent emission (Black & van Dishoeck 1987). This provided a check on the wavelength calibration and gave an indication of the r.m.s. deviation in the wavelength of each line.

Parabolas were used to fit the wavelengths in each of the I-band grating positions with a scale of 0.62 Å/pixel. 95 lines were identified of which 65 were considered reliable, with fluxes greater than 3 times the noise level and which did not appear to suffer blending. The wavelengths of these lines deviated by no more than 0.7 Å from the calibrated wavelength. The r.m.s. deviation for the different grating positions varied between 0.2–0.4 Å.

The H-band spectrum was also wavelength calibrated by fitting a parabola to the wavelength scale. 38 lines were identified of which 28 were considered reliable at the 3 sigma detection level and which were within 3 Å from the calibrated wavelength. The overall r.m.s. deviation of the line centres were 2 Å, for a scale of 4.4 Å/pixel.

The H_2 lines were observed with spectral resolutions at which they were unresolved, their FWHM being less than 16 $\mathrm{km\,s^{-1}}$ (Burton et al. 1990a). For the H-band data, to calculate the flux in each line, the *Specdre* (Meyerdierks 1995) command 'fittri' was used. This command fits triangles to line profiles minimising χ^2 while allowing the user to specify which parameters of the line to fix or leave free to be fitted. Using this command, pairs of lines which were slightly blended were easily deconvolved. For the I-band data, to calculate the flux in each line the intensity scale was converted from flux per unit wavelength to flux per pixel and the pixels in each line were summed up. It was noticed that an I magnitude of 7.0, for the standard star HD 40335, was more accurate than the value of 7.2 used in the flux calibration. Therefore the fluxes of the I-band lines were increased by 20%.

The column densities of H_2 in the upper energy levels of the transitions, N_j, are derived from measured specific intensities, I_{ji}, through the equation,

$$N_j = \frac{4\pi I_{ji}}{A_{ji} h \nu_{ji} \Omega}. \tag{4.1}$$

Here Ω is the beam solid angle, h is the Planck constant and ν_{ji} is the frequency of the transition from the j^{th} upper level to the i^{th} lower level of the hydrogen molecule. The transition rate coefficients, A_{ji}, were taken from Abgrall & Roueff (1989) for $J < 15$ and Turner, Kirby-Docken & Dalgarno (1977) from $J \geq 15$. Where more than one line had been observed originating from the same upper level the weighted mean of the column densities was used.

4.2.5 Uncertainties on Measurements and Column Densities

The observations described above were taken with exposures sufficiently long to ensure that the dominant source of noise was due to sky emission. Other sources of noise were electronic readout noise and photon noise in the signal. The errors quoted for the line fluxes are derived from the one sigma error bars in the spectra, found close to the line, multiplied by the square root of the number of pixels used in integrating the flux in the line. The signal to noise for sky background limited observations of exposure time, t, is given by

$$s/n = \frac{I}{\sqrt{n_{\mathrm{pix}} I_{\mathrm{sky}}}} \sqrt{t} \tag{4.2}$$

where I and I_{sky} are the intensities of the source and sky background respectively and n_{pix} is the number of pixels in each line. It was assumed that systematic errors would put a lower limit on the uncertainty in the column density of an energy to 10%.

When plotting the logarithms of column densities, the apparent errors bars become distorted with each lower error bar being larger than the upper error bar, for a given point. This becomes important when comparing the data to a model and calculating χ^2 for a fit in log space. The upper

error bar corresponds to $\log(1+\sigma)$ where σ is the fractional error in the column density and the larger lower error bar corresponds to $-\log(1-\sigma)$.

4.2.6 Comparison of Data

The data presented in this thesis were collected with four different instruments on five separate observing runs. Systematic differences between the datasets are therefore expected. The infrared datasets share common lines, as do the far-red datasets, which can be used to determine these differences. Unfortunately, this method cannot be used to calibrate the far-red to infrared data. An alternative is to compare the column densities of common levels which can be inferred from both datasets. Section 4.3.3 describes an attempt to determine any systematic difference between the far-red and infrared datasets while simultaneously calculating the H_2 ortho/para abundance ratio and extinction.

4.2.6.1 Aperture Photometry of IRCAM3 Images

The absolute flux could not be accurately measured because the image of the standard star, HD 37903, had saturated in the IRCAM3 pixel array. However, the relative fluxes of the 1–0 S(1) line, expected from the different instrument apertures could be calculated. The relative intensities

Instrument Apertures	Position offset from HD 37903	*IRCAM3 image* Relative Intensity to CGS2 data	*Spectra* Relative Intensity to CGS2 data
RGO Spectrograph (1996)	9″ W 78″ S	0.73	—
RGO Spectrograph (1990)	9″ W 78″ S	0.81	—
CGS4	9″ W 78″ S	0.75	0.70
UKT9	∼ 80″ S	0.54	0.43

Table 4.2: Intensities derived from placing software apertures over IRCAM3 image and measured from spectra.

from the IRCAM3 image, in Table 4.2 are calculated from the best estimates of the positions of the apertures used to take the spectra. The CGS2 and UKT9 apertures were placed where the peak emission occurs from the ridge. The long slits were placed at the telescope position coordinates. The long slit apertures miss the peak emission from the ridge by less than 1″. Placing them on this peak increases the measured fluxes by 10–20%. The intensities derived from the UKT9 and CGS4 spectra are ∼ 50% and ∼ 70% that of the CGS2 data respectively, which is consistent with the image profiles.

4.2.6.2 Line Ratios

Figure 4.6 shows the ratios of the same lines which have been observed in both the 1990 and 1996 observing runs which used the RGO Spectrograph. The ratio of the fluxes of the same lines gives a measure of the difference in the calibration of both datasets independent of any assumed extinction law or ortho/para abundance ratio. Figures 4.7 and 4.8 show the ratios due to systemic differences between the infrared datasets. Table 4.3 summarises the differences. The first column shows the average of the line ratios, $\overline{\sum_j I_j/I'_j}$, the second shows the ratio of the sums of the lines for each dataset, $\sum_j I_j / \sum_j I'_j$. Ideally, for a normal distribution of data points, these quantities should be the same. The second column will reciprocate if the order of the datasets is reversed, however the first column will not, so these quantities offer two different comparisons of the data. These values were used to produce the relative intensities shown in Table 4.2.

Ratios were also similarly calculated for the column densities of the same energy levels from the different datasets. This provided more data points for comparison but since different transitions

Datasets	Average of line ratios	±	Ratio of sum of sets	±
RGO Spectrograph '90/'96	36.0	4.6	36.7	5.3
CGS4 H-Band/CGS2 JHK	0.67	0.17	0.73	0.21
UKT9 K-Band/CGS2 JHK	0.43	0.06	0.43	0.03

Table 4.3: Comparison of datasets to determine any systematic differences.

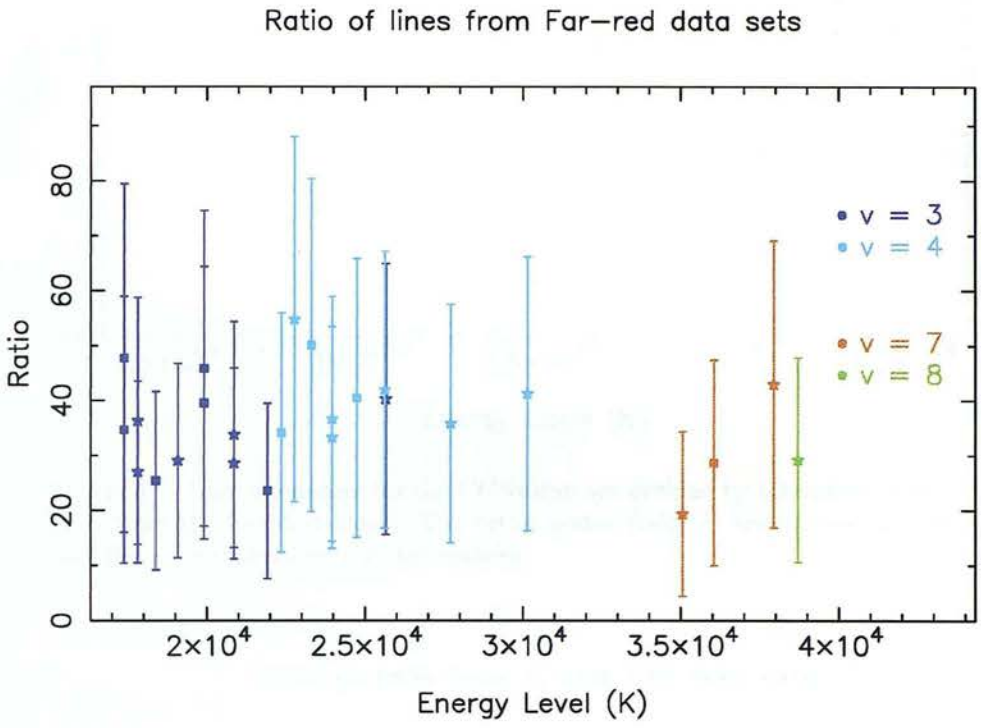

Figure 4.6: Line intensities for the RGO 1990 dataset divided by intensities of the same lines from the RGO 1996 dataset. The ortho states (odd J) are represented by stars and the para states (even J) by squares.

provided column densities for the same energy levels it was not independent of any extinction correction and was therefore not considered reliable.

4.2.6.3 Combining Datasets

In order to analyse all the data together, the datasets had to be combined taking into account the systematic differences arising from the different beams sizes and their positions on the sky. The CGS4 dataset was scaled by its beam dilution factor of 1/0.75 relative to the CGS2 dataset (Table 4.2). This value agreed well with the line ratios taken directly from both datasets (Table 4.3). The UKT9 dataset contained three lines with high signal to noise from transitions between the $v = 1$ and $v = 0$ levels. These provided a strong indication that the UKT9 dataset was a factor of 0.43 as bright as the CGS2 dataset and was scaled by 1/0.43 accordingly. Where the uncertainties in the published data of the UKT9 observations were $< 30\%$ they were scaled up by a factor of 2. This made them more representative of the rest of the infrared data and prevented the final weighted means being biased towards that dataset. The 1996 RGO Spectrograph dataset was scaled by its beam dilution factor 1/0.73. The 1990 RGO Spectrograph dataset had originally been miscalibrated and the published values were 36 times brighter than the 1996 RGO Spectrograph data. The data were therefore directly scaled to the 1996 RGO Spectrograph data ($1/0.73 \times 1/36$).

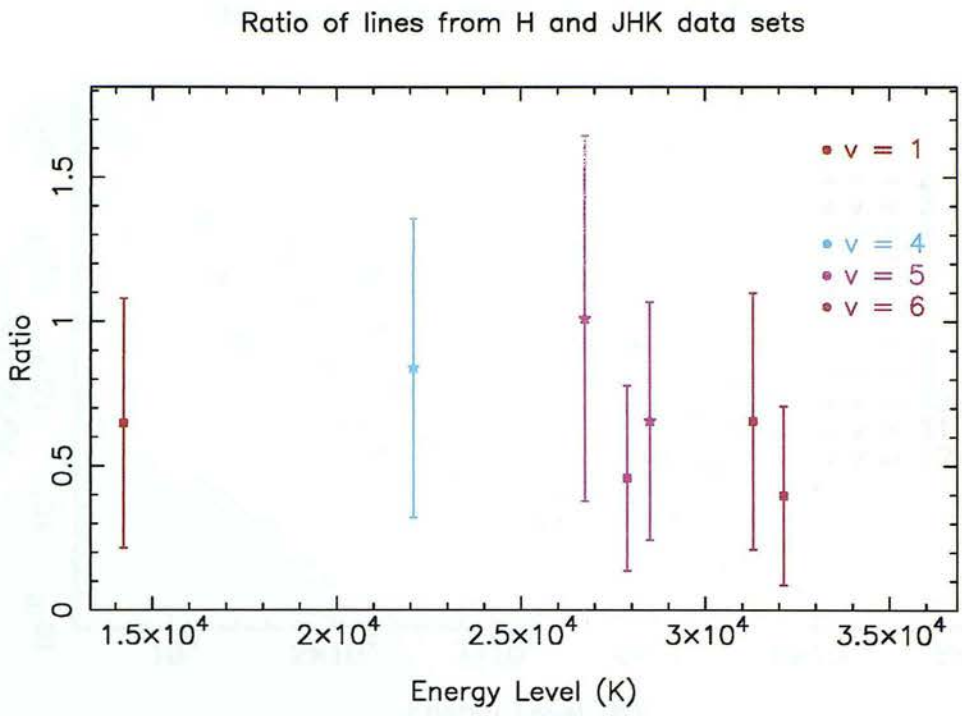

Figure 4.7: Line intensities for the CGS4 dataset divided by intensities of the same lines from the CGS2 dataset. The ortho states (odd J) are represented by stars and the para states (even J) by squares.

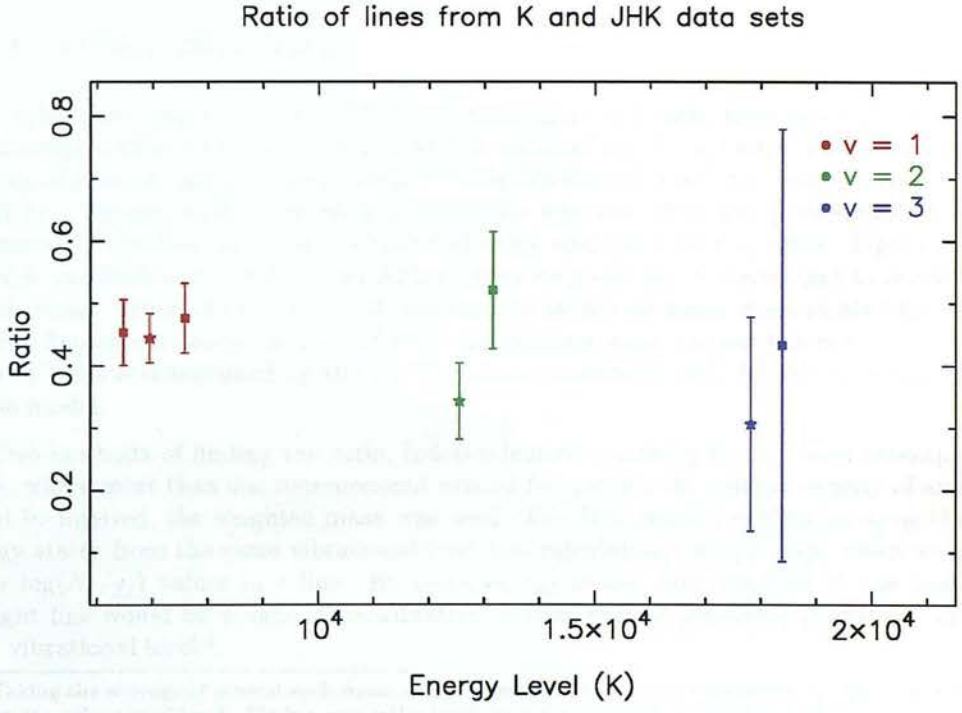

Figure 4.8: Line intensities for the UKT9 dataset divided by intensities of the same lines from the CGS2 dataset. The ortho states (odd J) are represented by stars and the para states (even J) by squares.

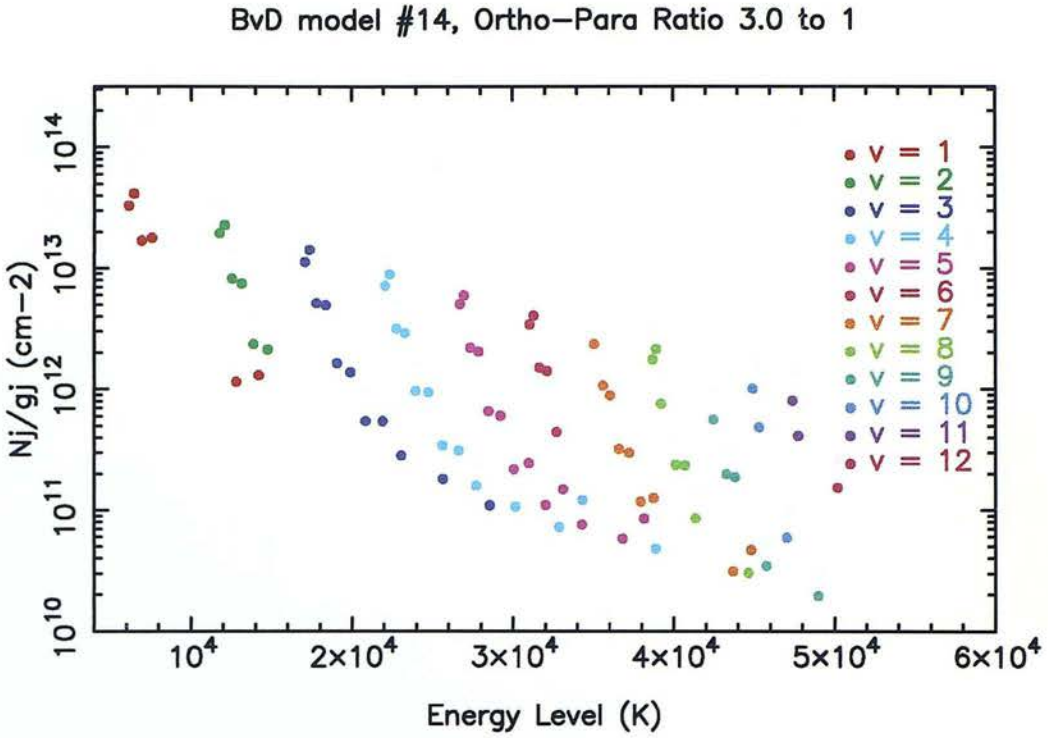

Figure 4.9: Black & van Dishoeck (1987) model #14 plotted for an ortho/para ratio of 3.0

4.3 Ortho/Para Abundance Ratio of H_2 and Extinction, A_v

4.3.1 Ortho/Para Ratio

The ortho/para abundance ratio of H_2 (see Section 2.2 - 'o/p ratio' from here on) can be determined by choosing a value which which places all the values of $\log(N_j/g_j)$ when plotted against E_j, along a series of smooth curves corresponding to each vibrational level. An incorrect choice of value will result in a 'zig-zag' pattern, where $\log(N_j/g_j)$ for adjacent ortho and para states are offset by the difference of the logarithms of the assumed value and the true o/p ratio. Figure 4.9 shows the Black & van Dishoeck (1987) model #14, plotted for levels which correspond to the data presented in this thesis, using an o/p ratio of 3. Figure 4.10 shows the same levels plotted for a ratio of 1.8. For the fluorescent model, a value of 3 is inappropriate since the gas has not thermalised and the ratio of 1.8 was determined by the H_2 formation mechanism and the photoabsorption rates used in the model.

Two methods of finding the ratio, independent of searching for A_v, were attempted. In both cases, where more than one measurement existed from which the column density of an energy state could be inferred, the weighted mean was used. The first method worked by using three adjacent energy states from the same vibrational level and calculating the o/p ratio which would place the three $\log(N_j/g_j)$ values in a line. By using energy states close together it was assumed that a straight line would be a valid approximation to that part of the curve describing $\log(N_j/g_j)$ for that vibrational level.[4]

[4] Taking the average of several such measurements should, in any case, cancel out the effect of the slope varying within the vibrational level. Fitting two ortho levels and a para level to a line will slightly overestimate the o/p ratio whereas fitting two para levels and an ortho level to a line will slightly underestimate the o/p ratio.

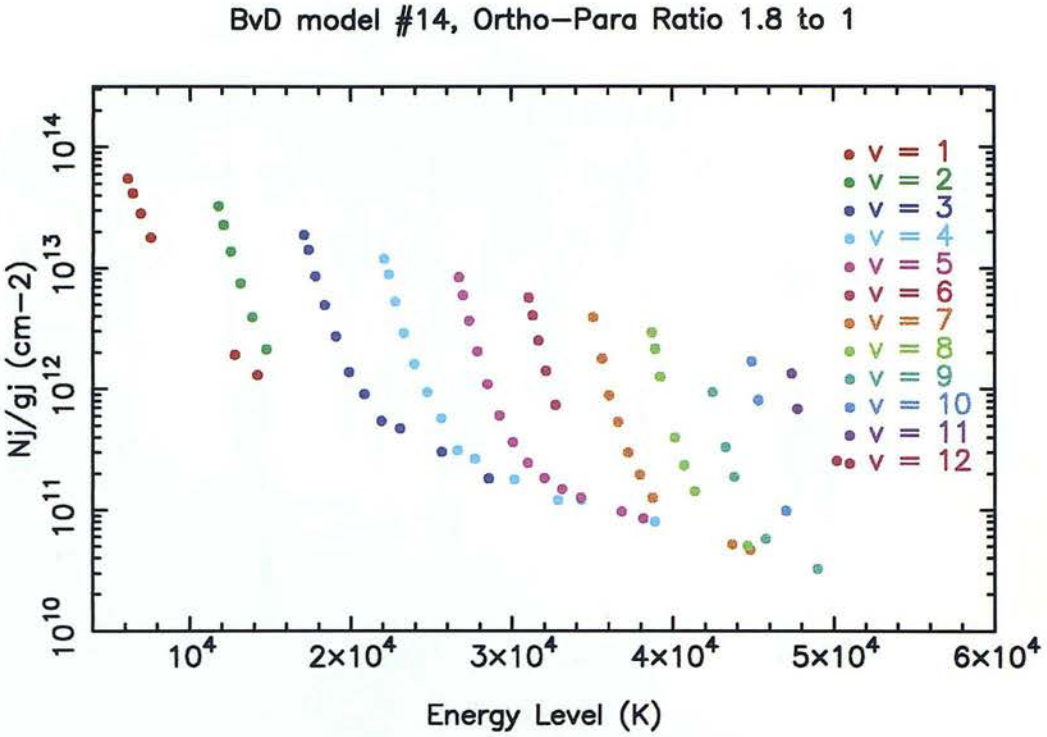

Figure 4.10: Black & van Dishoeck (1987) model #14 plotted for an ortho/para ratio of 1.8

1. The run of N_j/g_j within a v-level may be approximated with a Boltzmann distribution,

$$\frac{N_j}{g_j} = N_{H_2} \frac{e^{-E_j/T_{\rm rot}}}{\sum_j e^{-E_j/T_{\rm rot}}}, \tag{4.3}$$

where E_j are the energy levels and N_{H_2} is the column density of molecular hydrogen. From this equation, one can see that the slope on the diagram of $\log(N_j/g_j)$ plotted against E_j, is $\propto 1/T_{\rm rot}$. The populations of the H_2 energy states for $v > 1$ are primarily determined by the Einstein A_{ji} coefficients. The 'rotational temperature', $T_{\rm rot}$, has little physical significance and is really only a local measure of the slope within a v-level. It may be expressed as

$$T_{\rm rot} = (E_i - E_k) \,/\, \ln\left(\frac{g_i N_k}{g_k N_i}\right) \tag{4.4}$$

and the ortho-para ratio as

$$o/p = \frac{(2J_i+1)N_j}{(2J_j+1)N_i}\, e^{(E_j - E_i)/T_{\rm rot}}, \tag{4.5}$$

where J is the rotational quantum number of an energy level. The levels i, j and k are adjacent, within the same vibrational level, and are either ortho, para and ortho states or para, ortho and para states respectively and so $T_{\rm rot}$ is independent of the o/p ratio. The ratio is calculated from three independent measurements N_i, N_j and N_k with one sigma uncertainties σ_i, σ_j and σ_k respectively. The fractional uncertainty on the ortho/para ratio calculated from differentiating equation (4.5) is

$$\frac{\delta(o/p)}{o/p} = \sqrt{\left(\frac{\sigma_k}{N_k}\right)^2 + \left(\alpha\frac{\sigma_j}{N_j}\right)^2 + \left((1+\alpha)\frac{\sigma_i}{N_i}\right)^2} \tag{4.6}$$

where

$$\alpha = \frac{E_k - E_i}{E_i - E_j}. \tag{4.7}$$

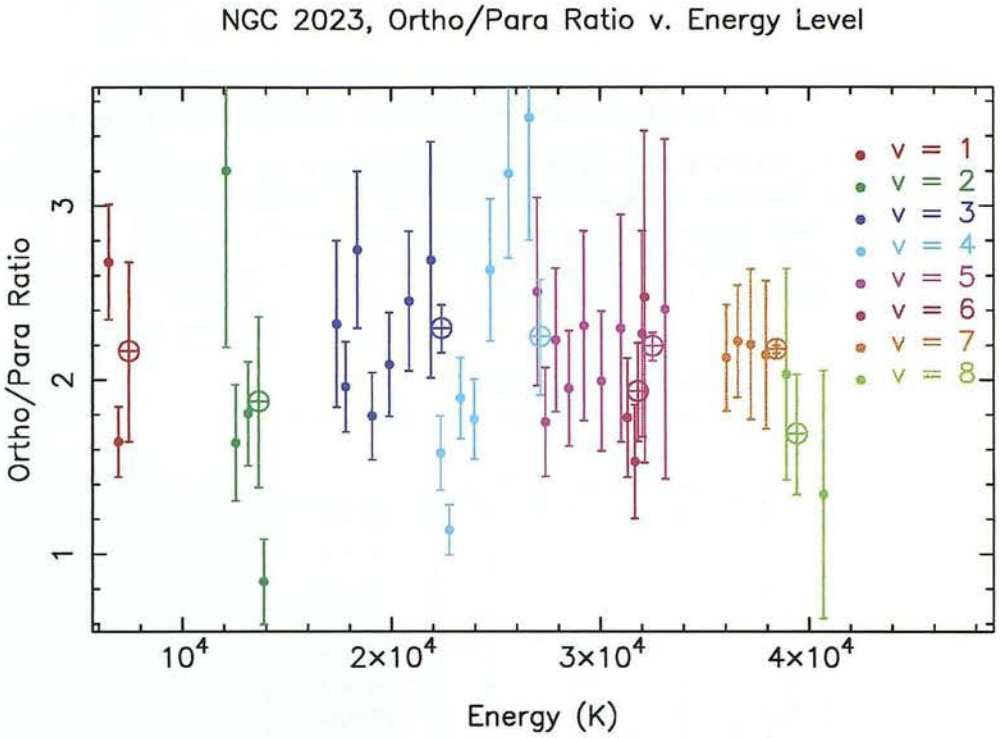

Figure 4.11: Ortho/para abundance ratios for complete dataset, calculated for groups of 3 adjacent points, across each vibrational level

Plotting the o/p ratios, calculated above, at the energy levels of the j^{th} state is useful for investigating any trends across the vibrational levels or possibly within a vibrational level. Figure 4.11 shows the o/p ratio calculated using this method at the energy level of the centre state, E_j. The crosses represent the means of the o/p ratio within that vibrational level and the error bars on the means are the standard errors calculated from the scatter of values. It should be noted that neighbouring points are highly correlated.

2. Another way of calculating the ortho/para ratio is by minimising the scatter on the column density diagram by varying the ratio. This method has the advantage of being able to use data which do not have two neighbouring points and it does not suffer biased results due to correlated data points. However, the scatter must be calculated with reference to a model which itself may not represent the true distribution. The χ^2 deviation from the model, M_j, can be calculated from

$$\sum_{j_{\rm ortho}} \frac{1}{\sigma_j^2}\left[\lg\left(\frac{N_j}{o/p}\right) - M_j\right]^2 + \sum_{j_{\rm para}} \frac{1}{\sigma_j^2}\left[\lg(N_j) - M_j\right]^2 . \tag{4.8}$$

Minimising this quantity with respect to o/p, the ortho/para ratio, depends only on the ortho states, although the model is fitted to both the ortho and para states during each iteration. The o/p ratio may be calculated using

$$\lg(o/p) = \sum_{j_{\rm ortho}} \frac{1}{\sigma_j^2}(\lg N_j - M_j) \;/\; \sum_{j_{\rm ortho}} \frac{1}{\sigma_j^2}. \tag{4.9}$$

The method is iterative :

- fit model - the routine E04HFF in the *NAG* Fortran Library (Fox & Wilkinson 1990) was used to fit the model to both the ortho and para states in the data by minimising the variance, weighted by the error bars.

- translate model - the model was then moved to lie along the para levels, using the error bars to weight the points. This step speeded up the algorithm by a factor of several.
- calculate ortho/para ratio - using equation (4.9) a new o/p ratio was calculated.
- test for convergence - while the o/p ratio was still changing the process was repeated.

Table 4.4 displays the o/p ratio inferred for each of the first eight vibrational levels assuming an A_v of 5.7 (see Section 4.3.3). Both methods produce consistent results with a mean ratio of 2.0. Figure 4.12 shows $\log(N_j/g_j)$ plotted against energy level. The open and filled in circles represent the ortho and para states respectively and the dashed lines show the models that were used. The overall o/p ratio which provided the smallest χ^2 when fitted to all the vibrational levels simultaneously was 2.0.

Vibrational level	Method 1 *3 points*		Method 2 *Minimise* χ^2	
	No. of points	o/p ratio	No. of points	o/p ratio
$v = 1$	2	2.2	6	2.3
$v = 2$	4	1.9	6	1.8
$v = 3$	7	2.3	12	2.2
$v = 4$	7	2.2	13	2.1
$v = 5$	9	2.2	13	2.2
$v = 6$	3	1.9	5	1.6
$v = 7$	4	2.2	9	2.2
$v = 8$	2	1.7	7	1.6

Table 4.4: Ortho/para ratios shown for each vibrational level. The first method fitted 3 adjacent points to a line as a function of the o/p ratio and the second worked by minimising χ^2 on plots of $\log(N_j/g_j)$ v. E_j

4.3.2 Extinction, A_v

The extinction was assumed to follow a power law,

$$A_\lambda \propto \lambda^{-\beta} \tag{4.10}$$

where λ is the wavelength of the transition and β is an empirically derived value. Mathis (1990) provides a detailed review of extinction studies and adopts the value $\beta = 1.70$, for wavelengths 0.9–10 μm, stating 'The extinction law for $\lambda > 0.9\,\mu$m seems to be independent of environment, to within the present observational errors'. Draine (1989) derived $\beta = 1.75$, for 0.7–7 μm for both in the Galaxy and in the Magellanic Clouds. Whittet (1988) has analysed the literature and derived $\beta \sim 1.7$. The earlier literature contains values scattered around those quoted above and in particular for star-forming regions the index may take on a different value (see Section 3.2), the value finally adopted was $\beta = 1.7$. Using line ratios of transitions originating from the same upper level one may determine the constant of proportionality from,

$$-2.5 \log \left(\frac{\lambda_{ij} A_{ik} I_{ij}}{\lambda_{ik} A_{ij} I_{ik}} \right) / (\lambda_{ij}^{-1.7} - \lambda_{ik}^{-1.7}). \tag{4.11}$$

Values determined this way depend greatly on the signal to noise in each of the lines and the separation of the wavelengths. Figure 4.13 is a histogram of extinction values calculated using this method which shows the mean extinction to be $A_v \sim 5.7$, where v is the Johnson filter with a central wavelength of 5500 Å. The lines from which these values were calculated are shown in Table D.1 in Appendix D.

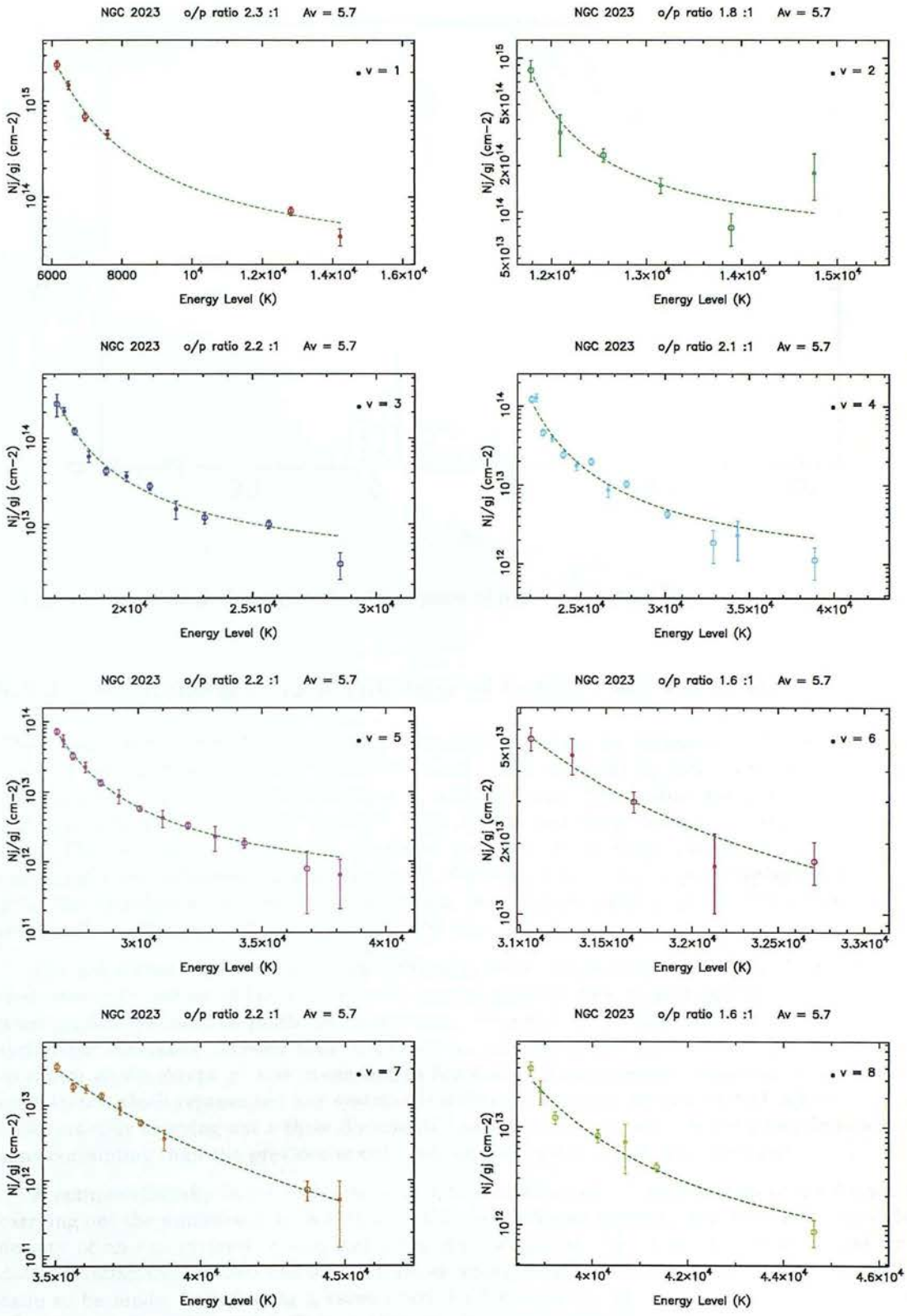

Figure 4.12: Ortho/para ratios for each vibrational level

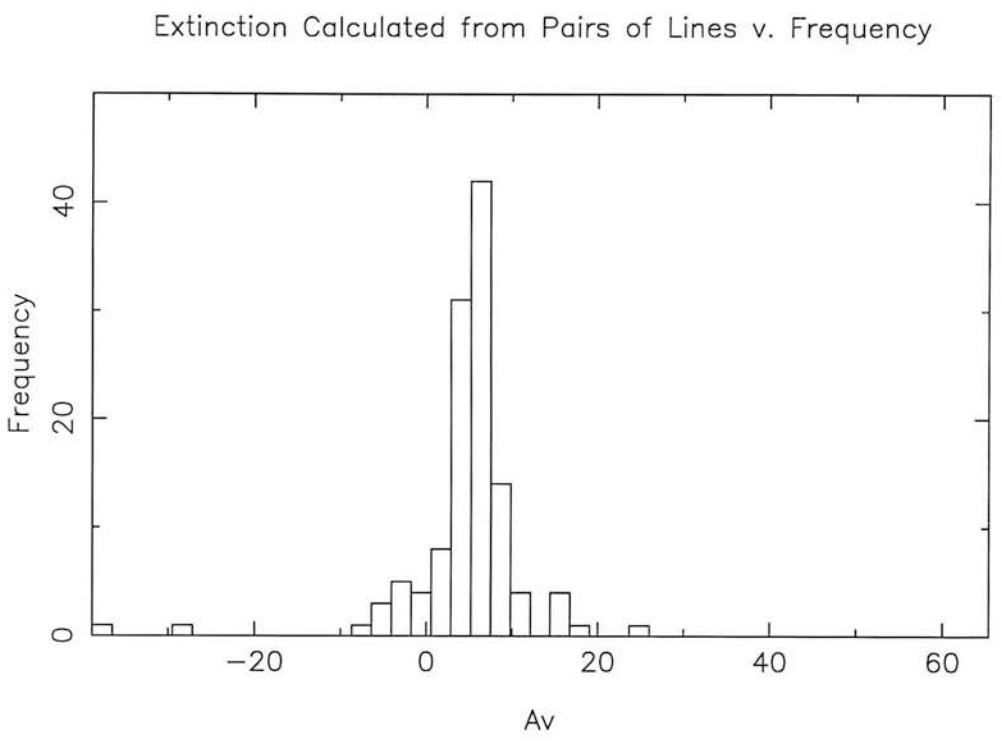

Figure 4.13: Calculating extinction from pairs of lines originating from the same upper level.

4.3.3 Minimising χ^2 as a Function of Ortho/Para Ratio and A_v

The extinction and ortho/para ratio were estimated by finding the minimum χ^2 deviation for which a model (of the form described in Section 4.3.4) could be fitted to each vibrational level of the data as a function of the two coordinates A_v and o/p ratio. The routine was passed values for A_v and o/p ratio which were kept constant while models were fitted to each vibrational level of the data. The resultant χ^2 was the accumulated deviation of the entire dataset of column densities calculated from individual lines to the model. Figure 4.14 is a contour plot displaying the reduced χ^2 at the coordinates: o/p ratio and extinction. A minimum reduced χ^2 of 2.0 (for 128 degrees of freedom)[5] was found for $A_v = 5.7$ and an o/p ratio of 2.0.

The calculated extinction depended critically on the calibration of the far-red data and since there was only one set of far-red data with reliable absolute flux measurements it was not obvious what confidence could be placed in these values. Therefore an attempt was made to ascertain any systematic difference between these data and the infrared data. The method used was the same as shown above except χ^2 was minimised as function of 3 parameters: extinction, o/p ratio and a scale factor which represented any systematic difference between the far-red and infrared datasets. Unfortunately carrying out a three dimensional parameter search was computationally much more time consuming than the previous search and required hours rather than minutes.

A computationally faster variation of this method involved initially averaging the data before carrying out the minimisation. Where more than one infrared measurement existed for the column density of an energy level, a weighted mean was calculated. The same was done for the far-red data. Treating the infrared and far-red data as separate species allowed an estimate of A_v and o/p ratio to be made, from finding a value where both species lay on the same line with a minimum χ^2 deviation from the model. This method involved calculating the deviation for 93 levels instead

[5]The likelihood of arriving at data with less than this χ^2 assuming the model were true is very small, $\ll 1\%$, which shows the error bars are possibly too small or that the model is an idealised fit but bears little physical relationship to the data.

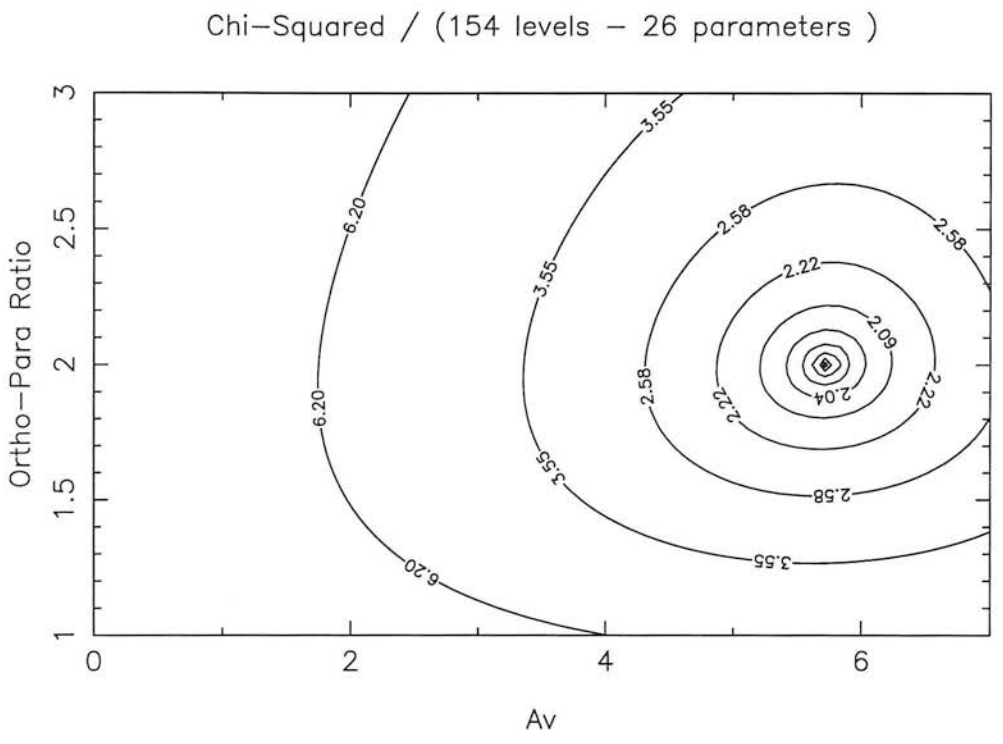

Figure 4.14: Contours of χ^2 to determine A_v and o/p.

of the full 154 and gave very similar results: $A_v = 5.8$, o/p ratio = 2.0 for a reduced χ^2 of 2.4 (for 67 degrees of freedom) and was therefore considered reliable.

This faster method was then used to calculate the minimum χ^2 as a function of ortho/para ratio, extinction and the scaling factor between the infrared and far-red datasets. Figure 4.15 shows a contour plot of χ^2 values for extinction and o/p ratio. The o/p ratio with the lowest χ^2 value is 2.07, however the extinction value is only 0.4 which occurs for a scaling factor of 5.0. Figure 4.16 shows a similar plot for extinction and the scale factor. A strong correlation is apparent between the effect of extinction and a scale factor. The wavelength ranges within the far-red and infrared datasets are too small to calculate the extinction with any precision. This method therefore failed to separate the effects of extinction from any scale factor which might exist, but confirmed the o/p ratio was $\simeq 2.0$. Mike Burton (private communication) had observed the same ridge of molecular hydrogen in the far-red at the AAT using the TEK chip and from unpublished observations of the bright CI emission line at 8729 Å derived a value for the absolute flux calibration ($8.1 \times 10^{-9}\,\mathrm{W\,m^{-2}\,sr^{-1}}$) which is consistent with our far-red data to within 20%. Therefore the far-red data calibration was considered correct and the concept of a scale factor was dropped.

The data were corrected for an extinction of $A_v = 5.7$ by multiplying the column densities inferred from equation (4.1) by factors depending on the wavelengths of the lines from which they were calculated *i.e.*

$$N_{j'} = 10^{0.4A_\lambda} N_j. \tag{4.12}$$

Here the extinction is calculated for the wavelength of the line j

$$A_\lambda = 5.7 \times \left(\frac{\lambda_j}{5500}\right)^{-1.7} \tag{4.13}$$

where λ_j is in angstroms.

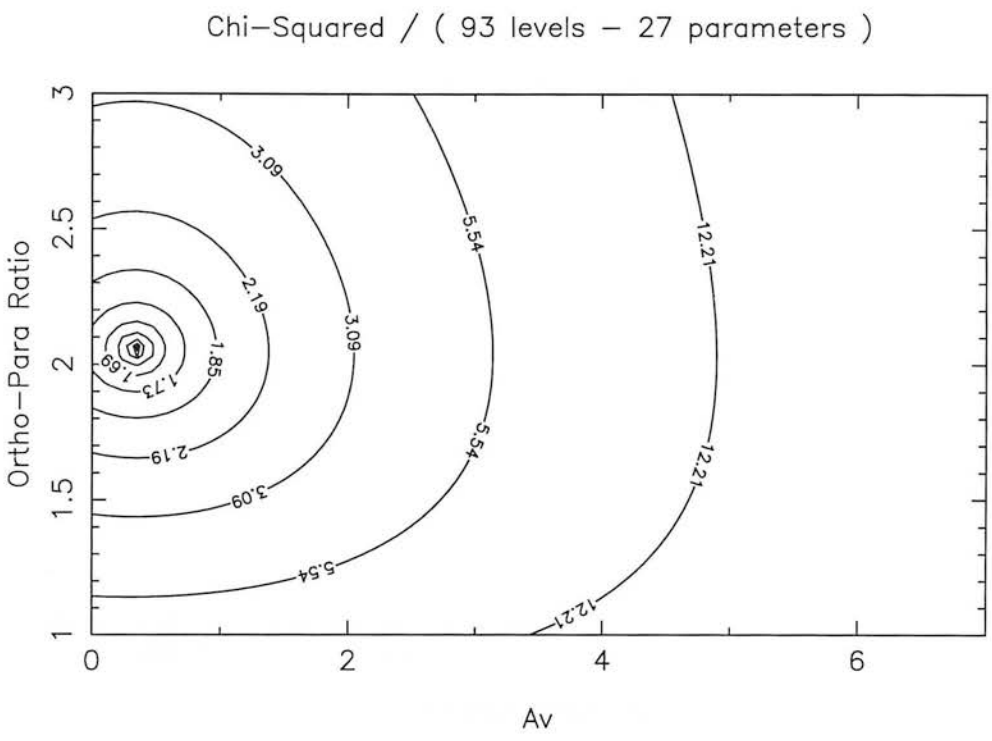

Figure 4.15: Contours of χ^2, for a 3 parameter fit, to determine A_v, o/p and any systematic difference between the far-red and infrared datasets (plotted for a scaling factor of 5.).

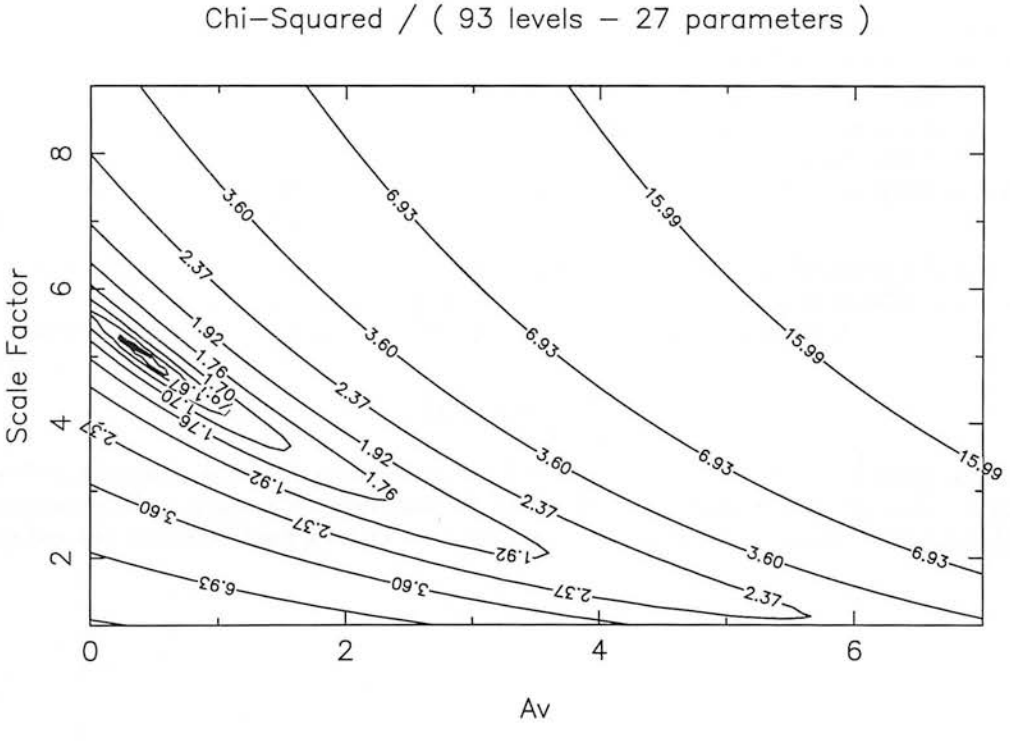

Figure 4.16: Contours of χ^2, for a 3 parameter fit, to determine A_v, o/p and any systematic difference between the far-red and infrared datasets (plotted for an o/p ratio of 2.1).

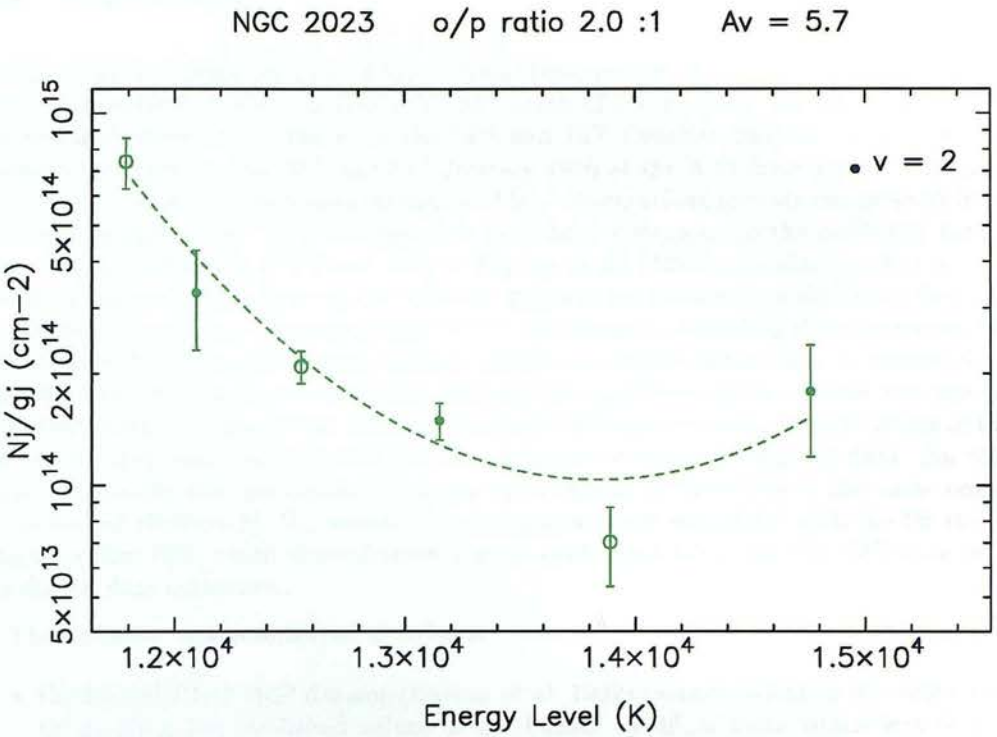

Figure 4.17: Difficulties in fitting a parabola to the data.

4.3.4 The Model for the v-level Curves

The ortho/para ratio and the extinction have been derived using several methods which involved minimising the scatter of the data points when plotting column density against excitation energy. For UV-excited gas the column densities of the rovibrational levels should approximate a series of smooth curves when plotted against the excitation energy of each level (see Fig. 4.10). To determine the scatter within each v-level a functional form of a model must be chosen which resembles the curves and has only a few free parameters so that the model is not fitted to spurious data points which occur due to noise in the data.

Initially a parabola was used as a model. This worked well for fitting to vibrational levels where there were many equally spaced data points but often there were insufficient high energy data points to constrain the shape of the fit (*e.g.* Fig. 4.17). A different functional form for the model was adopted,

$$M_j = \alpha - \frac{E_j}{\beta + \gamma E_j}. \tag{4.14}$$

This had also only three free parameters, α, β and γ, and the advantage of being monotonically decreasing with a slope, the magnitude of which, like the data, tended to zero. Appendix B describes the choice of this form and the parameter space where the required solutions exist.

4.4 Summary

In this chapter a large dataset of H_2 column densities has been compiled from far-red and infrared observations of the emission ridge 80″ south of the exciting star HD 37903 in NGC 2023. The infrared observations taken on the 14th and 15th October 1995 at UKIRT and the far-red observations taken on the 30th and 31st January 1996 at the AAT have been carefully reduced to provide over ninety line flux measurements. These observations provide the main bulk of the data presented in this thesis. The reduced data have been compared to the published far-red data of Burton et al. (1992a) and infrared data of Burton et al. (1997) and Hasegawa et al. (1987). Adjusted for beam dilution factors, the infrared datasets are consistent with each other. The far-red data permit an accurate extinction value to be calculated by extending the wavelength range of the dataset to 0.76–2.4μm. This large baseline allows an analysis of the data to provide an extinction value from minimising the scatter when plotting the logarithms of the column densities against the excitation energies of the levels. Initially the large difference between the intensities of the infrared and far-red data had been attributed to a calibration error in the far-red data. An attempt was made to quantify this discrepancy however independent observations of the same emission ridge in the far-red (Burton M. G., private communication) were consistent with the far-red RGO 1996 data to within 20% which showed there was no calibration error and the difference in brightness was due to dust extinction.

The datasets were interleaved as follows:

- the far-red RGO 1990 dataset (Burton et al. 1992a) was matched to the RGO 1996 dataset by dividing the published values of the former by 36, a value which was derived from a comparison of the intensities of identical lines.
- both far-red datasets were then normalised to the infrared CGS2 dataset (Burton et al. 1997) by dividing by a factor of 0.73. This value was determined from a comparison of the beam apertures placed over the IRCAM3 continuum subtracted 1–0 S(1) line image and measuring the relative fluxes expected from each aperture.
- the infrared CGS4 data were divided by a beam dilution factor of 0.75 (relative to the CGS2 dataset) which was also determined from the continuum subtracted 1–0 S(1) line image.
- the infrared UKT9 dataset (Hasegawa et al. 1987) was divided by 0.43 to bring the bright, high signal-to-noise $v = 1$–0 transitions in line with the CGS2 data.
- all five spectroscopic datasets were combined to produce column densities for 81 different excited states of H_2.

An ortho/para abundance ratio of 2.0±0.2 was derived from the complete dataset by minimising χ^2 (*i.e.* the scatter on $\log(N_j/g_j)$ v. E_j diagrams) and by calculating the ratio for groups of 3 adjacent levels within a vibrational level. The derived value was found to be insensitive to the assumed extinction value and is consistent with measurements of other PDRs where the ratio varies within the range 1.7–2.4 (Hoban et al. 1991; Chrysostomou et al. 1993; Ramsay et al. 1993; Ramsay Howat et al. 1997).

An optical extinction of $A_v = 5.7 \pm 1.0$ was found by minimising the scatter as function of ortho/para ratio and extinction simultaneously. The ortho/para ratio derived in this way was 2.0. The extinction value is significantly higher than previous estimates which were derived from infrared data with shorter wavelength baselines *i.e.* $A_v = 2$–3 (Burton 1993; Draine & Bertoldi 1996)[6]. The calculated extinction depends on the assumed extinction law (see Section 4.3.2). As discussed in Section 3.2 the extinction law found in star-forming regions may be steeper than that assumed for the average interstellar medium. Applying a steep extinction law $\propto \lambda^{-2.5}$ results in a measured extinction of $A_v = 6.8$ (o/p ratio= 2.0) with a reduced χ^2 value of 2.4. Therefore a steeper extinction law does not decrease the measured extinction or reduce the amount of scatter (*i.e.* for extinction law $\propto \lambda^{-1.7}$, $\chi^2 = 2.0$).

[6]Burton (1993) derived an extinction of $A_v = 3$ by taking flux ratios of lines with common upper energy levels. Draine & Bertoldi (1996) calculate $A_v = 2$ from the same dataset which is described in Section 4.1.6 and comprises part of the dataset used in this analysis.

4.5 Results

4.5.1 IRCAM3 Images

Figures 4.18 and 4.19 display the IRCAM3 images taken in the 1–0 S(1) line filter and 2.1 μm continuum filter. The H_2 emission ridge, from which the spectroscopic measurements were taken, shows up brightly in the line filter and to some degree in the continuum filter. This is being irradiated by HD 37903, the star at the centre of NGC 2023, responsible for producing the exciting UV radiation which is causing the fluorescence. The star at the end of the ridge, S108, is an emission type star and may contribute to the fluorescence a few arcseconds around it but does not appear to contribute significantly to the emission ridge (see Section 3.4). Figure 4.20 shows the continuum subtracted 1–0 S(1) line filter image from which the software aperture measurements were taken (Table 4.2) which profile the expected fluxes from the spectroscopic observations. Figure 4.21 shows HD 37903. This image was constructed from a set of observations with shorter exposure times and has a lower signal to noise than the image of the H_2 emission ridge. Some of the point-like sources may be ghost reflections (see Section 4.2.1). Figure 4.22 is a mosaic in the 1–0 S(1) filter of the emission ridge and HD 37903. The structure of the H_2 emission may be due to sheets of H_2 which have wrinkled exposing limb brightened edges or formed higher density clumps.

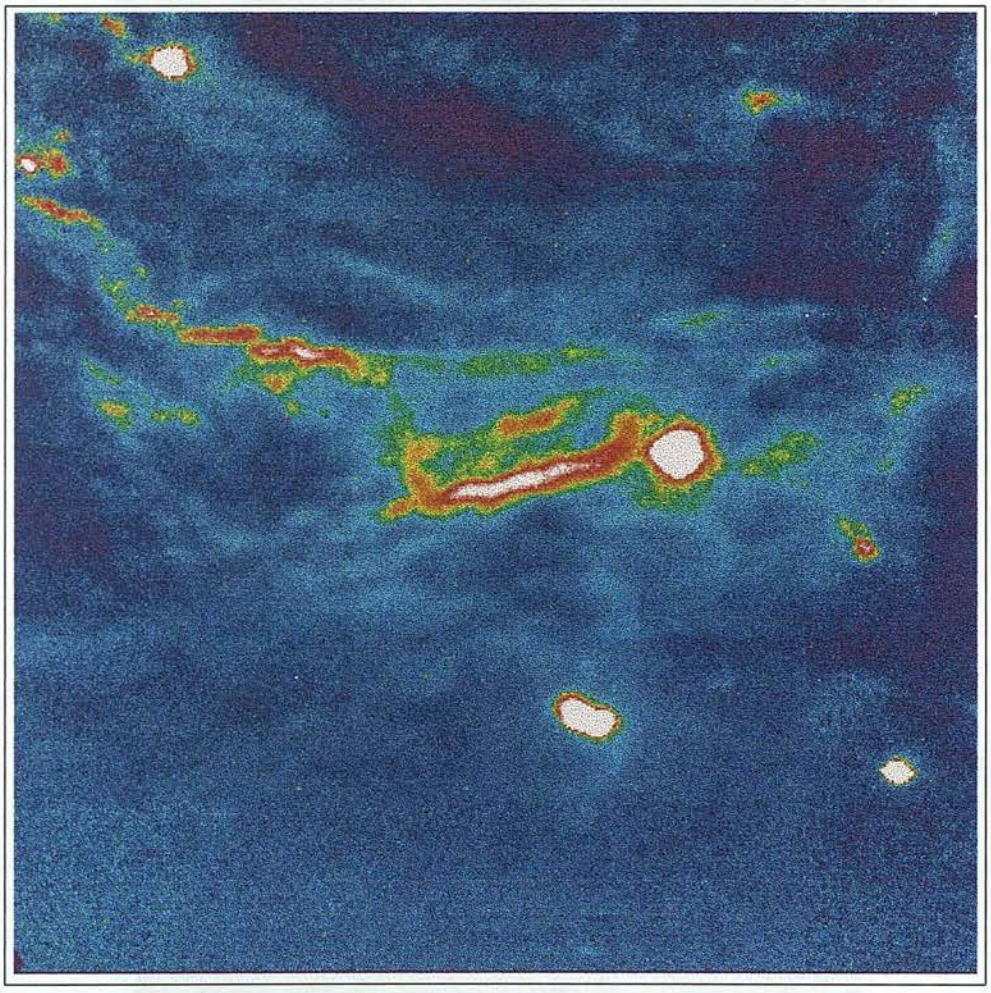

Figure 4.18: 1–0 S(1) filter image of NGC 2023 taken 8″ west, 78″ south of HD 37903. The colour scale is from -0.3 to 2.3 counts/sec and the image size is 113″ × 113″.

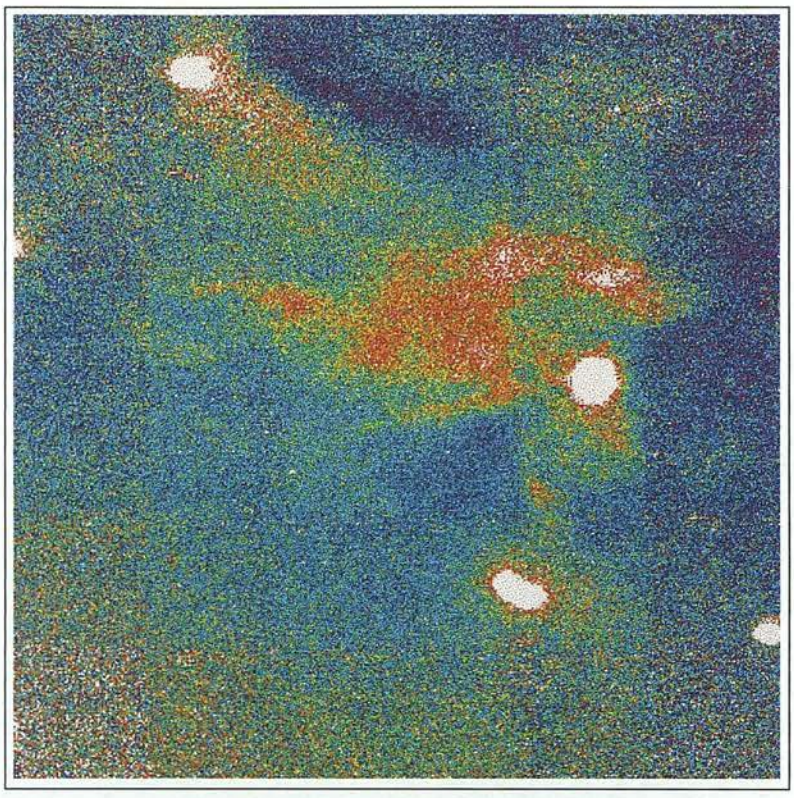

Figure 4.19: 2.1 μm continuum filter image. The colour scale is from -0.3 to 0.5 counts/sec and the image size is 113″ × 113″.

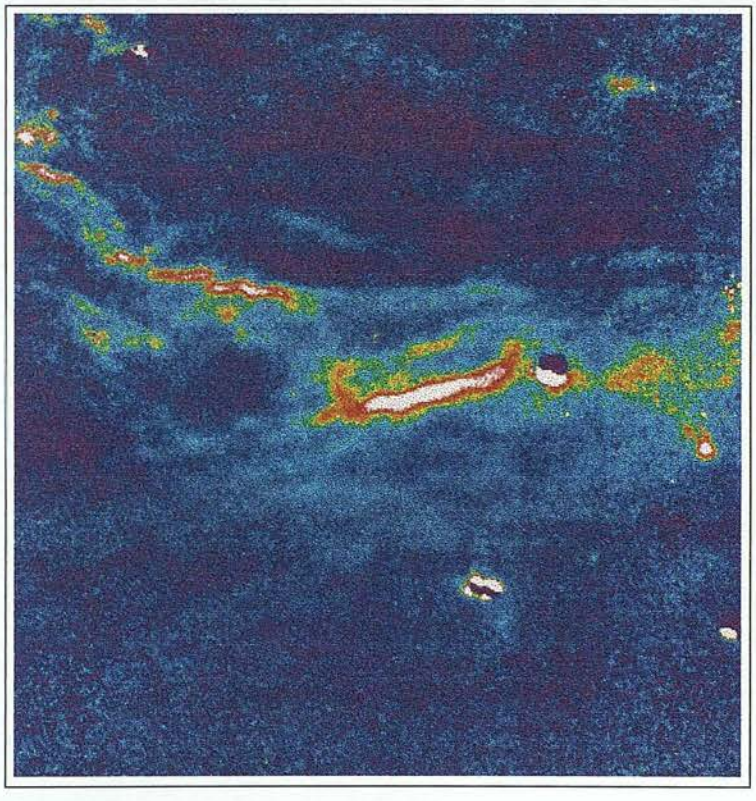

Figure 4.20: Continuum subtracted 1–0 S(1) filter image. The colour scale is from 0.0 to 1.8 counts/sec and the image size is 105″ × 110″.

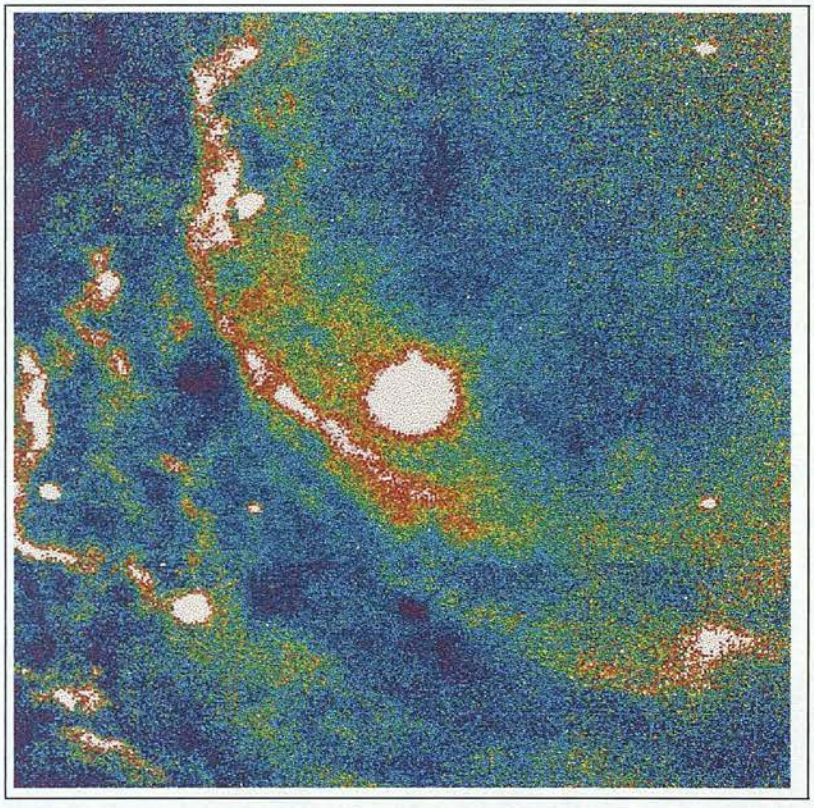

Figure 4.21: 1–0 S(1) filter image of HD 37903. The colour scale is from 0.0 to 1.8 counts/sec and the image size is $103'' \times 103''$.

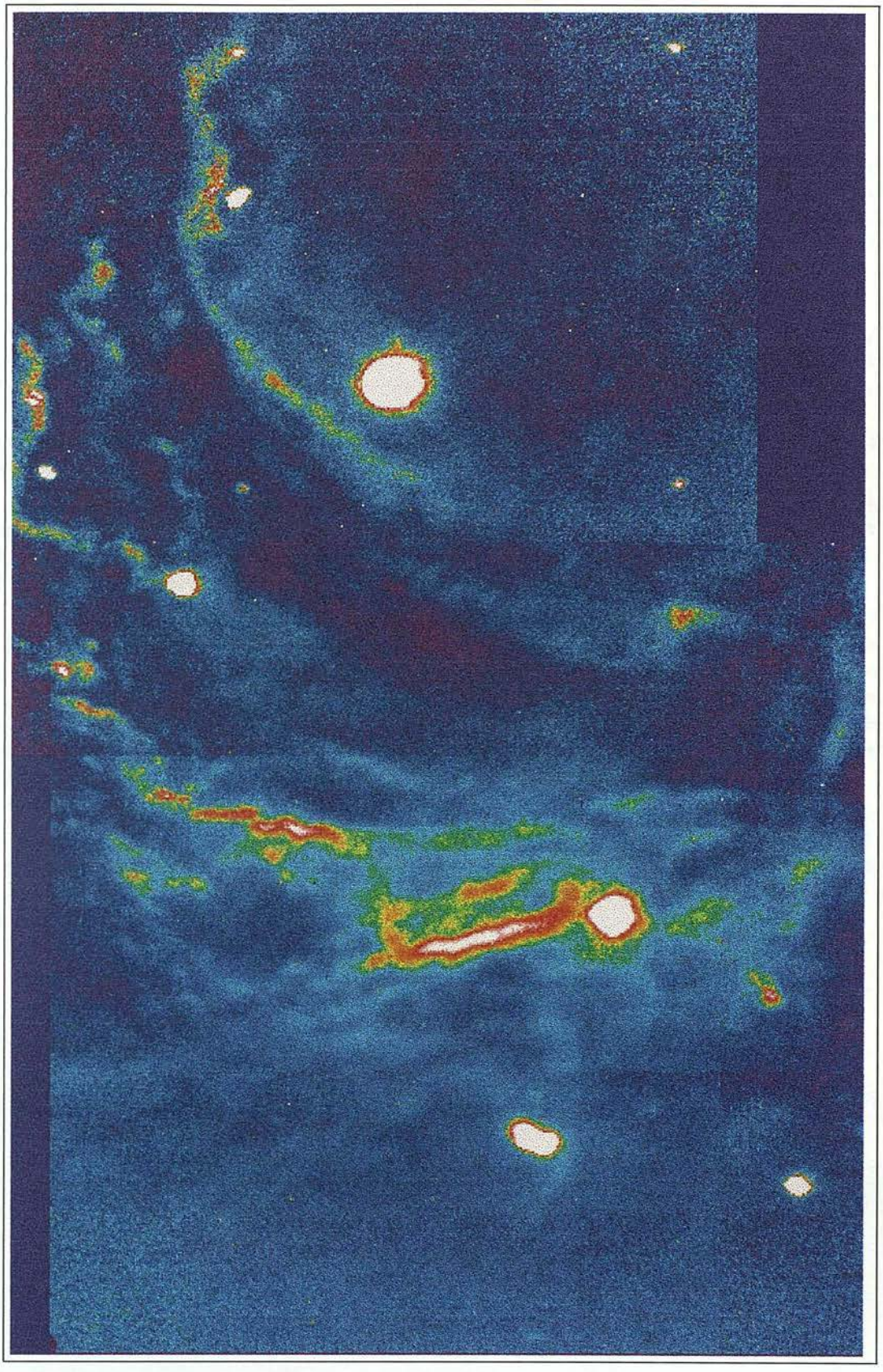

Figure 4.22: 1–0 S(1) filter image of NGC 2023, emission ridge and HD 37903. The colour scale is from -0.3 to 2.3 counts/sec and the image size is 118″ × 186″.

4.5.2 Spectra

Figures 4.23–4.26 show I-band spectra taken at four overlapping grating positions, with the RGO Spectrograph during the January 1996 observing run. In each diagram the black line is the observed spectrum and the red line is the background sky emission. The green lines show a synthetic spectrum of the expected emission inferred from the observations. The column densities presented in Table 4.7 were calculated from the weighted means of column densities derived from individual emission lines (see equation 4.1). A synthetic spectrum was created using these column densities to calculate the strength of each line which would be expected to arise from this upper level in the case of pure fluorescence. For levels where there were no data but where column density values had been calculated using the model described in Section 4.3.4, these interpolated values were used instead. These lines are presented in Tables C.4 and C.5 in Appendix C.

The strongest line is a CI transition at 8729 Å. There is also a strong line at 8449 Å due to an unresolved OI triplet. The highest signal to noise occurs in the central two grating positions (7830–9033 Å). The last grating position has lower signal to noise, especially beyond 9300 Å, due to the lower quantum efficiency of the Red Thomson CCD at high wavelengths (see Fig. 4.2). The first grating position was taken on a different night from the other three grating positions, in poor weather conditions. Fluxes were measured for a total of 65 lines.

Figure 4.27 shows a spectrum of the same region taken in the H band, three and a half months earlier with CGS4. Higher spectral resolution observations would have assisted in separating blended lines, however some partially blended lines were successfully deconvolved and the fluxes of 28 lines were measured.

The synthetic spectra (green lines) shows up many potential line identifications which had initially been discounted on grounds of poor signal to noise or blending. The following lists (Table 4.5 and 4.6) contain potential lines of interest derived this way from the I-band and H-band spectra. They have either a significant signal to noise or arise from an upper level which is of high excitation or has no data. These lines are worth further consideration but since (apart from the lines identified in bold font[7]) they were derived after the bulk of the analysis they have not been included in the main dataset and the calculation of A_v and the ortho/para ratio.

Due to the large number of H_2 emission lines which have been detected, it has not been practical to label each one on the spectra. However, Tables C.1–C.3 show lists of the measured far-red and infrared lines in ascending wavelength order which may be used with the spectra to identify lines. Tables C.4 and C.5 contain lists of the H_2 lines derived for the synthetic spectra which may also aid line identification.

[7]The lines shown in bold font were identified and measured before creating the synthetic spectra and are likely to suffer from blending. Theses are included in the main dataset since the blending only became apparent from a study of the synthetic spectra derived after the analysis of the dataset and calculation of A_v and the o/p ratio.

Line	λ (Å)	Comments
7–3 S(3)	7665	1st grating position
7–3 S(7)	7668	—
12–6 S(3)	7759	the large predicted intensity of this line derives from only one measurement, that of the bright 12–6 Q(5) line
10–5 Q(1)	7919	2nd grating position
7–3 Q(2)	8041	—
4–1 S(7)	8286	blended with 4–1 S(8) (8287 Å) line which is predicted to be three times fainter for a pure fluorescent cascade. The column density of the $v = 4$, $J = 9$ level has been determined solely from the measurement of this line and thus the uncertainty is increased by 30%.
8–4 S(3)	8290	blended with 8–4 S(6) (8291 Å) line which is predicted to be 40% as bright suggests the column density for the $v = 8, J = 5$ level has been overestimated. The UKT9 measurement of the 8–6 S(3) (1.7018 μm) line indicates a column density 40% greater than that measured from the 8–4 S(3) line which suggests the uncertainty due blending is within the errors of the measurements.
3–0 Q(4)	8613	3rd grating position
4–1 S(14)	8673	—
5–2 S(10)	8941	—
11–6 Q(3)	8944	—
3–0 Q(9)	9065	4th grating position
8–4 Q(7)	9145	—

Table 4.5: Lines of interest derived from synthetic I-band spectrum.

Line	λ (μm)	Comments
6–4 S(3)	1.4456	—
3–1 Q(11)	1.4479	—
6–4 S(2)	1.4712	near a small sky line
9–6 O(5)	1.4755	low signal to noise
5–3 Q(3)	1.5056	fits well into column density plot but may be blended with 7–5 S(7) (1.5058 μm) and is on top of a bright sky line so is not trustworthy.
3–1 O(5)	1.5220	line deconvolved from neighbouring sky line but may suffer contamination from nearby H_2 lines.
7–5 S(3)	1.5615	bright line, may be blended with dim H_2 and sky lines on either side.
6–4 Q(2)	1.6074	fits well into column density plot but sits on a small sky line and maybe partially blended with 5–3 Q(9) (1.6084 μm) about 3× fainter.
11–8 O(3)	1.7609	is strongly blended with 7–5 Q(4) (1.7604 μm)

Table 4.6: Lines of interest derived from synthetic H-band spectrum.

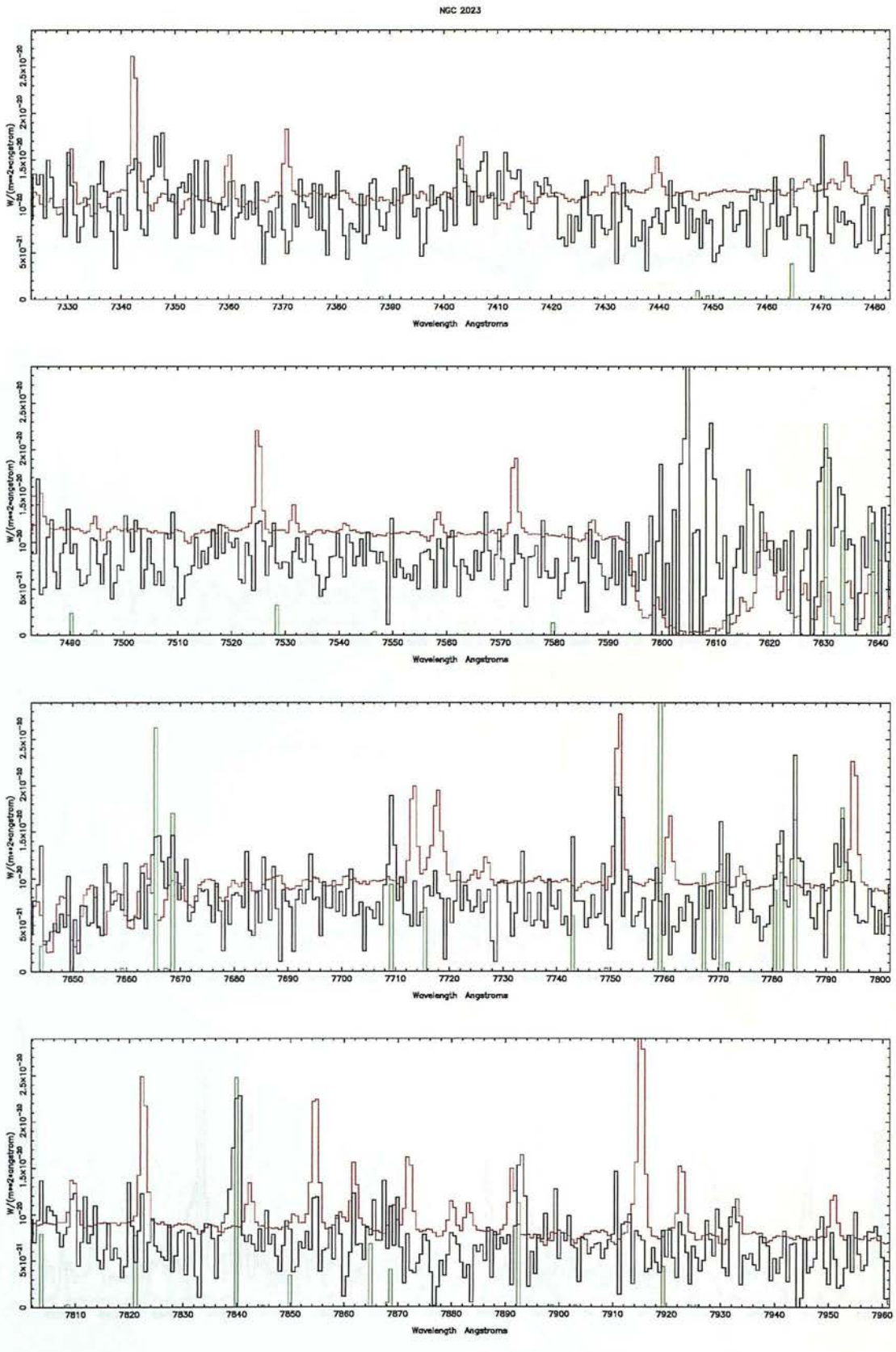

Figure 4.23: Spectrum of NGC 2023, taken at the 1st grating position 7323–7961 Å in the 1996 RGO Spectrograph observing run. The intensity is in units of flux per angstrom per $0''.61 \times 1''.5$ pixel. The black line shows the observed spectrum and the red line shows the background sky emission. The green lines show a synthetic spectrum derived from the observations for comparison.

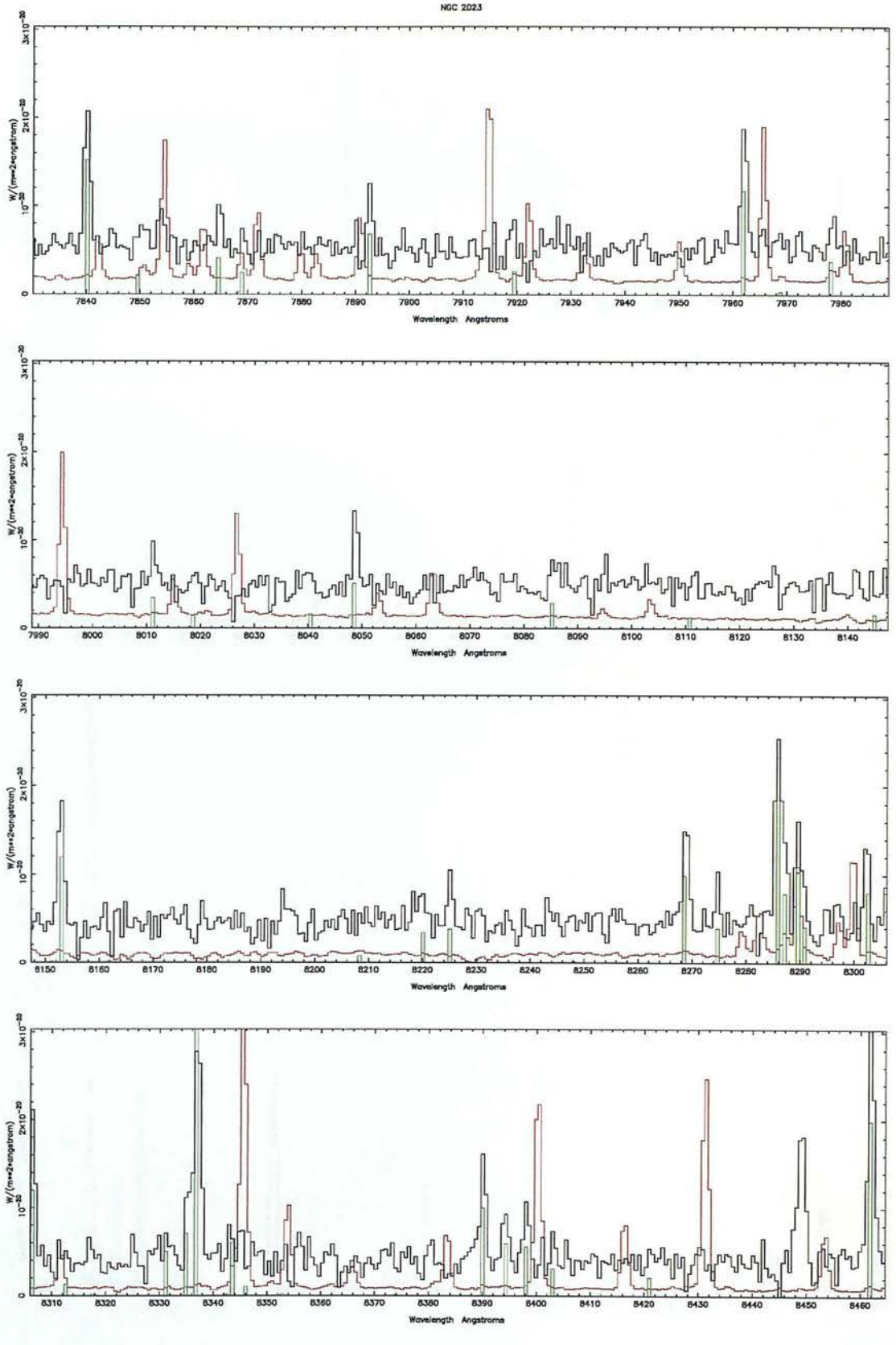

Figure 4.24: Spectrum of NGC 2023, taken at the 2nd grating position 7830–8464 Å in the 1996 RGO Spectrograph observing run. The intensity is in units of flux per angstrom per $0''.61 \times 1''.5$ pixel. The black line shows the observed spectrum and the red line shows the background sky emission. The green lines show a synthetic spectrum derived from the observations for comparison.

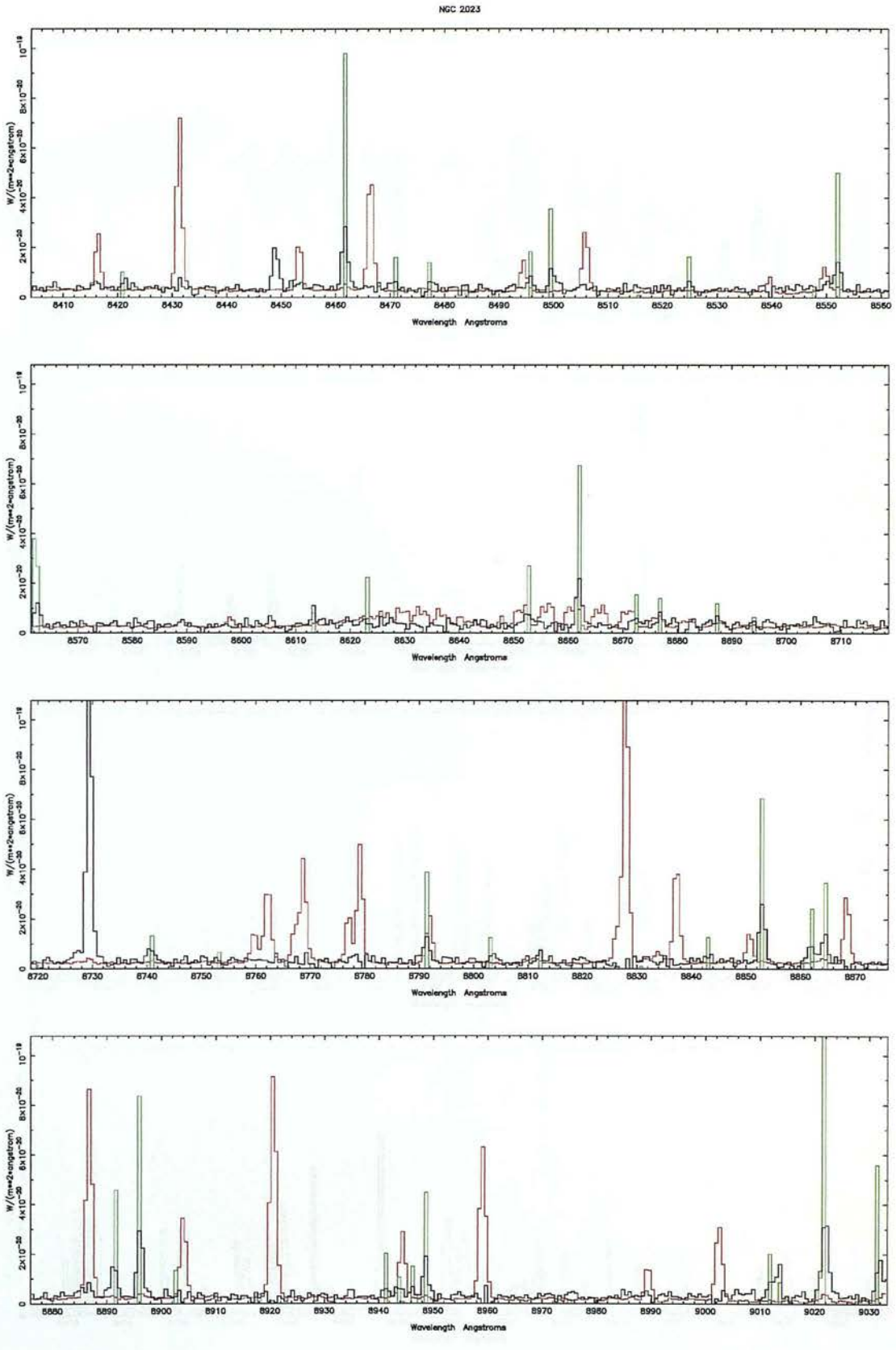

Figure 4.25: Spectrum of NGC 2023, taken at the 3rd grating position 8404–9033 Å in the 1996 RGO Spectrograph observing run. The intensity is in units of flux per angstrom per $0''.61 \times 1''.5$ pixel. The black line shows the observed spectrum and the red line shows the background sky emission. The green lines show a synthetic spectrum derived from the observations for comparison.

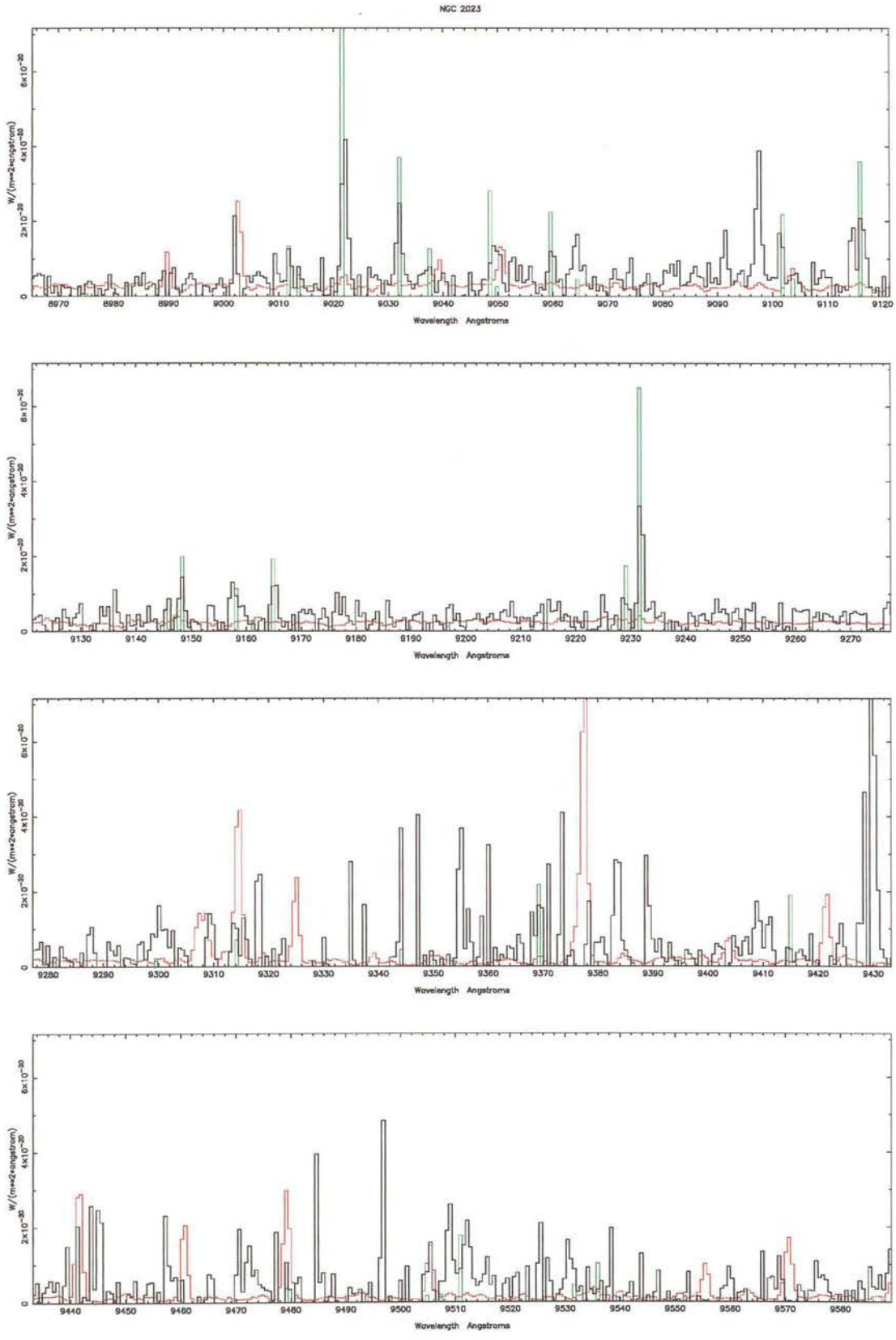

Figure 4.26: Spectrum of NGC 2023, taken at the 4th grating position 8965–9589 Å in the 1996 RGO Spectrograph observing run. The intensity is in units of flux per angstrom per $0''.61 \times 1''.5$ pixel. The black line shows the observed spectrum and the red line shows the background sky emission. The green lines show a synthetic spectrum derived from the observations.

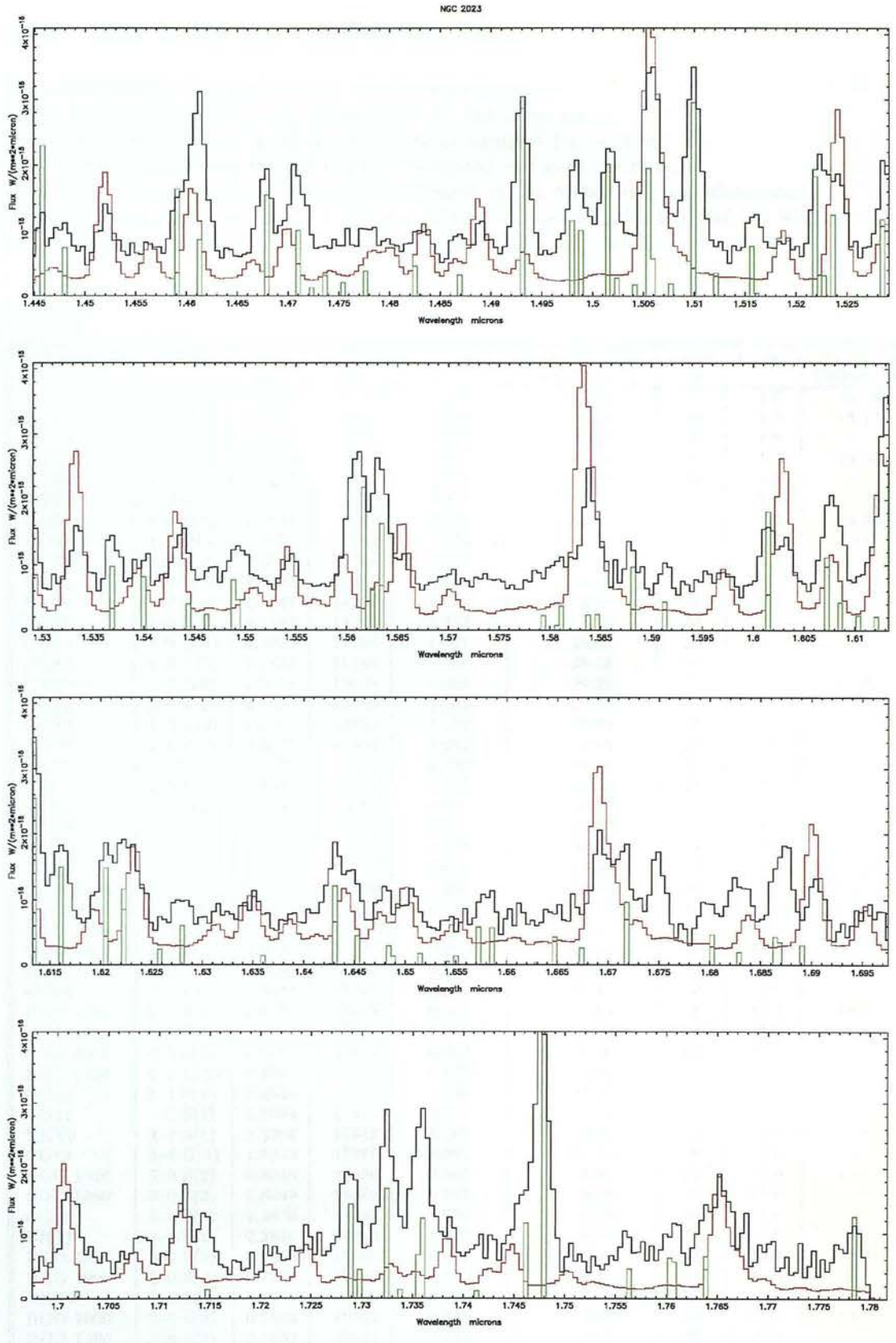

Figure 4.27: H band spectrum of NGC 2023, observed with CGS4. The intensity is in units of flux per micron per $1''.23 \times 1''.23$ pixel. The black line shows the observed spectrum and the red line shows the background sky emission. The green lines show a synthetic spectrum derived from the observations.

4.5.3 Line fluxes and Column Densities

The 1990 RGO Spectrograph results have been normalised to the 1996 RGO Spectrograph intensity values to compensate for a miscalibration in the published results. Table 4.7 presents the intensities of the lines measured in all the observations adjusted for the beam dilution (Section 4.2.6.3). The column densities are derived from the weighted means of the fluxes divided by their statistical weights due to rotational degeneracy, adjusted for an ortho/para abundance ratio of 2.0 and corrected for an extinction of $A_v = 5.7$. Appendix C contains Tables C.1 and C.3 which show the raw fluxes measured for the beam of the each observation, ordered in wavelength.

Observation	Line	λ (μm)	Energy (K)	$A_{ji} \times 10^{-7}$ (s^{-1})	Intensity$\times 10^{-9}$ (W m^{-2} sr^{-1})	Error (%)	$F(A_v)$	$\lg(N_j/g_j)$ ($\lg(cm^{-2})$)
CGS2	1–0 Q(1)	2.4066	6149	4.301	304.20	7	1.5	15.44
CGS2	1–0 S(0)	2.2233	6471	2.534	80.84	8	1.6	15.17
UKT9	1–0 S(0)	2.2233	6471	2.534	85.26	16	1.6	—
CGS2	1–0 S(1)	2.1218	6951	3.481	174.44	8	1.7	14.90
CGS2	1–0 Q(3)	2.4237	6951	2.790	121.25	9	1.5	—
UKT9	1–0 S(1)	2.1218	6951	3.481	180.36	8	1.7	—
CGS2	1–0 S(2)	2.0338	7584	3.994	68.07	11	1.8	14.66
CGS2	1–0 Q(4)	2.4375	7584	2.659	46.80	22	1.5	—
UKT9	1–0 S(2)	2.0338	7584	3.994	75.42	10	1.8	—
CGS4	1–0 S(7)	1.7480	12817	2.994	40.34	6	2.1	13.91
CGS2	1–0 S(8)	1.7147	14220	2.352	8.93	29	2.1	13.59
CGS4	1–0 S(8)	1.7147	14220	2.352	7.73	29	2.1	—
CGS2	2–0 Q(1)	1.2383	11789	1.941	25.53	26	3.7	14.87
CGS2	2–0 O(3)	1.3354	11789	1.606	29.78	19	3.2	—
UKT9	2–1 S(0)	2.3556	12095	3.694	26.23	30	1.6	14.52
CGS2	2–0 S(1)	1.1622	12550	1.902	25.53	25	4.4	14.32
CGS2	2–0 Q(3)	1.2473	12550	1.288	20.85	26	3.7	—
CGS2	2–1 S(1)	2.2477	12550	4.992	61.69	10	1.6	—
UKT9	2–1 S(1)	2.2477	12550	4.992	49.19	30	1.6	—
CGS2	2–0 S(2)	1.1382	13150	2.383	25.53	27	4.6	14.17
CGS2	2–1 S(2)	2.1542	13150	5.614	29.78	15	1.7	—
UKT9	2–1 S(2)	2.1542	13150	5.614	36.07	20	1.7	—
UKT9	2–1 S(3)	2.0735	13890	5.788	39.35	24	1.7	13.85
CGS2	2–0 S(4)	1.0998	14763	3.076	20.42	33	5.0	14.25
RGO 1996	3–0 Q(1)	0.8500	17098	0.259	0.64	29	12.2	14.43
RGO 1996	3–0 S(0)	0.8275	17387	0.215	0.23	42	13.8	14.31
RGO 1996	3–0 Q(2)	0.8525	17387	0.186	0.21	48	12.1	—
RGO 1990	3–0 S(0)	0.8275	17387	0.215	0.22	36	13.8	—
RGO 1990	3–0 Q(2)	0.8525	17387	0.186	0.28	29	12.1	—
CGS4	3–1 O(4)	1.4677	17387	2.859	14.47	12	2.7	—
RGO 1996	3–0 S(1)	0.8153	17818	0.363	0.88	8	14.7	14.11
RGO 1996	3–0 Q(3)	0.8563	17818	0.175	0.52	4	11.9	—
RGO 1990	3–0 S(1)	0.8153	17818	0.363	0.66	12	14.7	—
RGO 1990	3–0 Q(3)	0.8563	17818	0.175	0.53	15	11.9	—
CGS2	3–1 S(1)	1.2330	17818	4.685	31.91	22	3.8	—
CGS2	3–2 S(1)	2.3864	17818	5.167	27.65	25	1.5	—
UKT9	3–2 S(1)	2.3864	17818	5.167	19.68	50	1.5	—
CGS4	3–1 O(5)	1.5220	17818	1.982	15.12	15	2.5	—
RGO 1996	3–0 S(2)	0.8049	18386	0.507	0.51	22	15.6	13.79
RGO 1990	3–0 S(2)	0.8049	18386	0.507	0.36	22	15.6	—
CGS2	3–2 S(2)	2.2870	18386	5.670	9.79	39	1.6	—
UKT9	3–2 S(2)	2.2870	18386	5.670	9.84	70	1.6	—
RGO 1996	3–0 S(3)	0.7962	19086	0.650	0.93	17	16.4	13.65
RGO 1990	3–0 S(3)	0.7962	19086	0.650	0.75	11	16.4	—
UKT9	3–2 S(3)	2.2014	19086	5.667	19.68	34	1.6	—
RGO 1996	3–0 S(4)	0.7892	19911	0.786	0.41	27	17.1	13.56
RGO 1996	3–0 S(4)	0.7892	19911	0.786	0.35	31	17.1	—
RGO 1990	3–0 S(4)	0.7892	19911	0.786	0.45	18	17.1	—
CGS2	3–1 S(4)	1.1672	19911	7.199	18.29	29	4.3	—

Table 4.7: Line intensities adjusted for beam dilution and column densities corrected for extinction factor, $F(A_v)$.

Observation	Line	λ (μm)	Energy (K)	$A_{ji} \times 10^{-7}$ (s^{-1})	Intensity$\times 10^{-9}$ (W m^{-2} sr^{-1})	Error (%)	$F(A_v)$	$\lg(N_j/g_j)$ ($\lg(cm^{-2})$)
RGO 1996	3–0 S(5)	0.7840	20856	0.910	0.85	13	17.7	13.47
RGO 1996	3–0 S(5)	0.7840	20856	0.910	1.00	5	17.7	—
RGO 1990	3–0 S(5)	0.7840	20856	0.910	0.80	10	17.7	—
RGO 1996	3–0 S(6)	0.7804	21911	1.014	0.39	34	18.1	13.18
RGO 1990	3–0 S(6)	0.7804	21911	1.014	0.25	32	18.1	—
RGO 1996	3–0 S(7)	0.7784	23069	1.093	0.54	18	18.3	13.11
CGS2	3–1 S(7)	1.1304	23069	7.492	19.15	28	4.7	—
RGO 1996	3–0 S(9)	0.7793	25659	1.161	0.58	27	18.2	13.03
RGO 1990	3–0 S(9)	0.7793	25659	1.161	0.65	12	18.2	—
RGO 1996	3–0 S(11)	0.7865	28555	1.105	0.26	34	17.4	12.57
RGO 1996	4–1 Q(1)	0.9032	22079	0.932	0.98	19	9.6	14.10
RGO 1996	4–1 Q(1)	0.9032	22079	0.932	1.29	21	9.6	—
CGS2	4–2 O(3)	1.5099	22079	7.724	23.40	15	2.6	—
CGS4	4–2 O(3)	1.5099	22079	7.724	26.16	9	2.6	—
RGO 1996	4–1 S(0)	0.8792	22352	0.740	0.77	22	10.6	14.10
RGO 1996	4–1 Q(2)	0.9060	22352	0.668	0.58	51	9.5	—
RGO 1990	4–1 S(0)	0.8792	22352	0.740	0.73	22	10.6	—
CGS4	4–2 O(4)	1.5635	22352	5.199	16.50	18	2.4	—
RGO 1996	4–1 S(1)	0.8662	22759	1.221	1.15	8	11.3	13.68
RGO 1996	4–1 Q(3)	0.9102	22759	0.626	0.70	27	9.3	—
RGO 1990	4–1 S(1)	0.8662	22759	1.221	1.74	9	11.3	—
CGS4	4–2 O(5)	1.6223	22759	3.694	12.15	19	2.3	—
RGO 1996	4–1 S(2)	0.8552	23295	1.669	0.67	27	11.9	13.60
RGO 1990	4–1 S(2)	0.8552	23295	1.669	0.93	9	11.9	—
CGS2	4–2 S(2)	1.2846	23295	9.197	23.40	23	3.5	—
RGO 1996	4–1 S(3)	0.8462	23955	2.097	1.82	8	12.5	13.40
RGO 1996	4–1 S(3)	0.8462	23955	2.097	1.65	10	12.5	—
RGO 1990	4–1 S(3)	0.8462	23955	2.097	1.68	9	12.5	—
CGS2	4–3 S(3)	2.3445	23955	4.597	9.15	58	1.6	—
CGS4	4–2 O(7)	1.7563	23955	1.892	3.34	67	2.1	—
RGO 1996	4–1 S(4)	0.8390	24733	2.491	0.78	21	12.9	13.25
RGO 1990	4–1 S(4)	0.8390	24733	2.491	0.88	18	12.9	—
RGO 1996	4–1 S(5)	0.8337	25623	2.833	2.14	12	13.3	13.31
RGO 1990	4–1 S(5)	0.8337	25623	2.833	2.49	3	13.3	—
CGS2	4–2 S(5)	1.2263	25623	11.363	23.40	24	3.8	—
RGO 1996	4–1 S(6)	0.8302	26616	3.102	0.64	19	13.6	12.93
RGO 1996	4–1 S(7)	0.8286	27706	3.286	1.85	7	13.7	13.02
RGO 1990	4–1 S(7)	0.8286	27706	3.286	1.84	9	13.7	—
RGO 1996	4–1 S(9)	0.8306	30139	3.368	0.85	24	13.5	12.64
RGO 1990	4–1 S(9)	0.8306	30139	3.368	0.97	8	13.5	—
RGO 1996	4–1 S(11)	0.8398	32854	3.087	0.46	45	12.9	12.28
RGO 1996	4–1 S(12)	0.8471	34295	2.839	0.28	52	12.4	12.36
RGO 1996	4–1 S(15)	0.8803	38859	1.870	0.26	43	10.6	12.06
CGS2	5–3 Q(1)	1.4929	26735	11.716	18.93	18	2.6	13.90
CGS4	5–3 Q(1)	1.4929	26735	11.716	25.49	9	2.6	—
CGS4	5–3 O(3)	1.6135	26735	11.216	21.16	11	2.3	—
CGS4	5–3 O(4)	1.6718	26992	7.702	8.92	20	2.2	13.73
RGO 1996	5–2 S(1)	0.9232	27374	2.536	1.67	28	8.8	13.55
CGS4	5–3 Q(3)	1.5056	27374	7.713	18.31	12	2.6	—
RGO 1996	5–2 S(2)	0.9116	27878	3.397	1.26	34	9.2	13.35
CGS2	5–3 Q(4)	1.5158	27878	7.435	9.36	36	2.6	—
CGS4	5–3 Q(4)	1.5158	27878	7.435	5.71	22	2.6	—
RGO 1996	5–2 S(3)	0.9022	28498	4.189	2.41	8	9.6	13.17
RGO 1996	5–2 S(3)	0.9022	28498	4.189	2.34	10	9.6	—
CGS2	5–3 Q(5)	1.5286	28498	7.241	12.34	19	2.5	—
CGS4	5–3 Q(5)	1.5286	28498	7.241	10.78	17	2.5	—
RGO 1996	5–2 S(4)	0.8949	29228	4.892	0.88	26	9.9	12.94
CGS2	5–3 Q(6)	1.5443	29228	7.069	8.51	35	2.5	—
RGO 1996	5–2 S(5)	0.8896	30063	5.471	1.80	8	10.2	12.80
RGO 1996	5–2 S(6)	0.8865	30994	5.899	0.74	27	10.3	12.63
RGO 1996	5–2 S(7)	0.8853	32014	6.154	1.45	11	10.4	12.56
RGO 1996	5–2 S(8)	0.8862	33115	6.227	0.51	39	10.3	12.36
RGO 1996	5–2 S(9)	0.8891	34288	6.121	0.99	17	10.2	12.30
RGO 1996	5–2 S(11)	0.9012	36818	5.426	0.45	78	9.7	11.93

Table 4.7: Line intensities adjusted for beam dilution and column densities corrected for extinction factor, $F(A_v)$.

Observation	Line	λ (μm)	Energy (K)	$A_{ji} \times 10^{-7}$ (s^{-1})	Intensity$\times 10^{-9}$ (W m^{-2} sr^{-1})	Error (%)	$F(A_v)$	$\lg(N_j/g_j)$ ($\lg(cm^{-2})$)
RGO 1996	5–2 S(12)	0.9104	38158	4.881	0.17	67	9.3	11.80
CGS2	6–4 Q(1)	1.6015	31063	14.065	6.81	44	2.3	13.65
CGS4	6–4 O(3)	1.7326	31063	14.094	21.44	10	2.1	—
CGS2	6–4 S(0)	1.5369	31303	8.308	9.36	32	2.5	13.67
CGS2	6–4 Q(2)	1.6074	31303	9.976	6.81	63	2.3	—
CGS4	6–4 S(0)	1.5369	31303	8.308	8.17	22	2.5	—
CGS4	6–4 S(1)	1.5016	31661	11.502	16.54	8	2.6	13.39
CGS4	6–4 Q(3)	1.6162	31661	9.211	11.98	15	2.3	—
CGS2	6–4 Q(4)	1.6281	32132	8.841	8.51	50	2.3	13.20
CGS4	6–4 Q(4)	1.6281	32132	8.841	4.50	50	2.3	—
CGS4	6–4 Q(5)	1.6431	32711	8.565	10.96	21	2.3	13.14
RGO 1996	7–3 Q(1)	0.8011	35057	0.881	0.30	27	16.0	13.55
RGO 1990	7–3 Q(1)	0.8011	35057	0.881	0.16	49	16.0	—
CGS4	7–5 Q(1)	1.7288	35057	15.089	14.07	16	2.1	—
RGO 1990	7–3 S(1)	0.7771	35613	1.395	0.54	15	18.5	13.28
CGS4	7–5 S(1)	1.6205	35613	11.705	9.96	23	2.3	—
RGO 1996	7–3 S(2)	0.7709	36050	2.002	0.39	14	19.2	13.22
RGO 1990	7–3 S(2)	0.7709	36050	2.002	0.31	26	19.2	—
CGS4	7–5 S(2)	1.5883	36050	13.252	5.86	31	2.4	—
RGO 1996	7–3 Q(5)	0.8220	36588	0.592	0.29	41	14.2	13.16
RGO 1990	7–3 S(3)	0.7665	36588	2.616	1.01	8	19.8	—
CGS4	7–5 Q(5)	1.7784	36588	9.031	7.57	24	2.0	—
RGO 1990	7–3 S(4)	0.7639	37220	3.213	0.40	20	20.2	12.97
CGS2	7–5 S(4)	1.5400	37220	13.628	6.38	47	2.5	—
RGO 1996	7–3 S(5)	0.7631	37941	3.763	0.68	16	20.3	12.81
RGO 1996	7–3 Q(7)	0.8421	37941	0.614	0.08	89	12.7	—
RGO 1990	7–3 S(5)	0.7631	37941	3.763	0.81	10	20.3	—
RGO 1990	7–3 S(6)	0.7640	38743	4.231	0.27	30	20.1	12.56
RGO 1996	7–3 S(11)	0.7978	43693	4.686	0.25	29	16.3	11.91
RGO 1996	7–3 S(12)	0.8111	44812	4.349	0.09	77	15.1	11.74
RGO 1996	8–4 Q(1)	0.8652	38707	1.705	0.60	25	11.4	13.50
RGO 1990	8–4 Q(1)	0.8652	38707	1.705	0.48	22	11.4	—
RGO 1996	8–4 S(0)	0.8477	38913	1.433	0.25	28	12.4	13.36
RGO 1996	8–4 S(1)	0.8394	39219	2.431	0.43	19	12.9	13.00
RGO 1996	8–4 Q(3)	0.8741	39219	1.162	0.41	27	10.9	—
CGS4	8–6 S(1)	1.7639	39219	10.618	7.67	29	2.1	—
RGO 1996	8–4 S(3)	0.8290	40115	4.324	0.79	19	13.7	12.81
CGS2	8–6 S(3)	1.7018	40115	11.710	9.57	27	2.2	—
CGS4	8–6 S(4)	1.6801	40695	11.023	4.30	52	2.2	12.85
RGO 1990	8–4 S(5)	0.8269	41355	5.938	0.77	10	13.8	12.49
RGO 1996	8–4 S(9)	0.8496	44641	6.892	0.33	31	12.3	11.84
RGO 1996	9–5 S(1)	0.9148	42462	3.685	0.72	56	9.1	12.87
RGO 1996	9–5 S(3)	0.9049	43274	6.127	0.98	49	9.5	12.60
RGO 1996	9–5 S(4)	0.9037	43798	7.124	0.43	41	9.6	12.41
RGO 1996	9–5 S(7)	0.9165	45761	8.540	0.70	33	9.1	12.05
RGO 1996	9–4 S(11)	0.7633	48987	3.782	0.37	40	20.2	12.24
CGS2	10–7 O(3)	1.5489	44902	10.632	6.38	47	2.5	13.38
RGO 1996	10–5 Q(3)	0.8019	45317	0.683	0.10	76	15.9	12.93
RGO 1996	10–5 Q(7)	0.8484	47021	0.729	0.09	69	12.3	12.42
CGS4	11–8 O(3)	1.7609	47390	11.150	5.58	40	2.1	13.28
CGS4	11–8 S(1)	1.5915	47748	8.039	3.73	48	2.4	12.90
RGO 1996	12–6 Q(5)	0.8225	50203	0.497	0.29	32	14.1	13.29

Table 4.7: Line intensities adjusted for beam dilution and column densities corrected for extinction factor, $F(A_v)$.

4.5.4 Column Density Diagrams

The following figures display column densities for the complete dataset and the individual observations from which it is comprised. The column densities are the weighted means of the upper levels of transitions whose values are presented in Table 4.7. The column densities of the ortho states have been divided by the ortho/para ratio 2.0 and all the lines have been corrected for an optical extinction of 5.7 magnitudes, derived in Section 4.3.

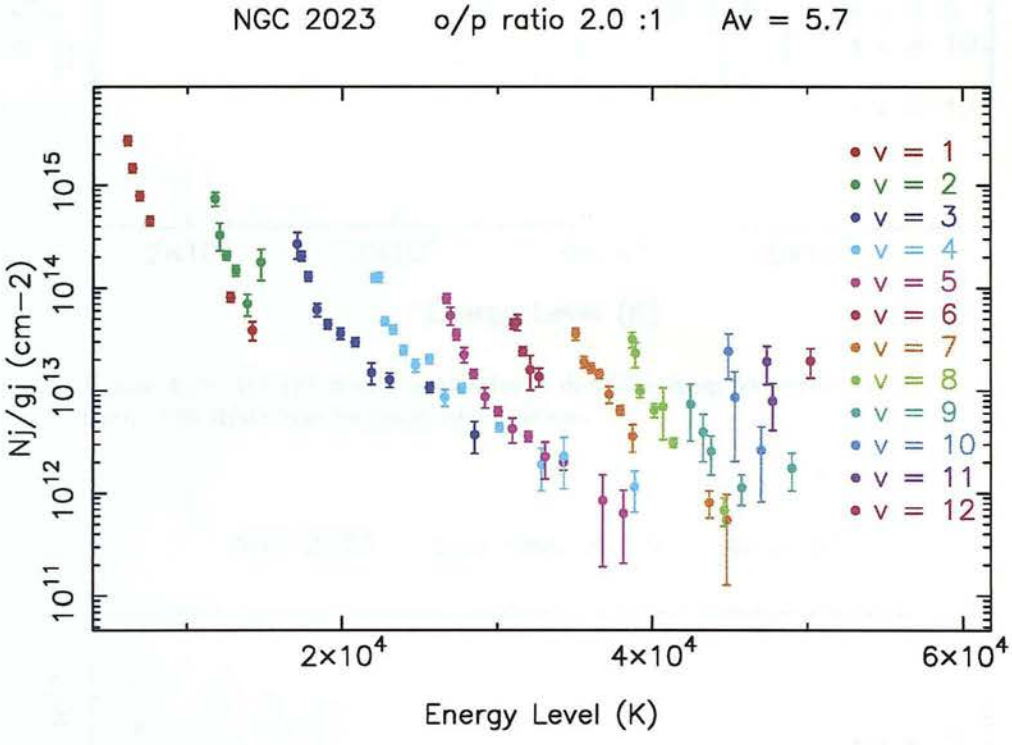

Figure 4.28: Weighted means of column densities from 81 upper levels derived from complete dataset (Table 4.7).

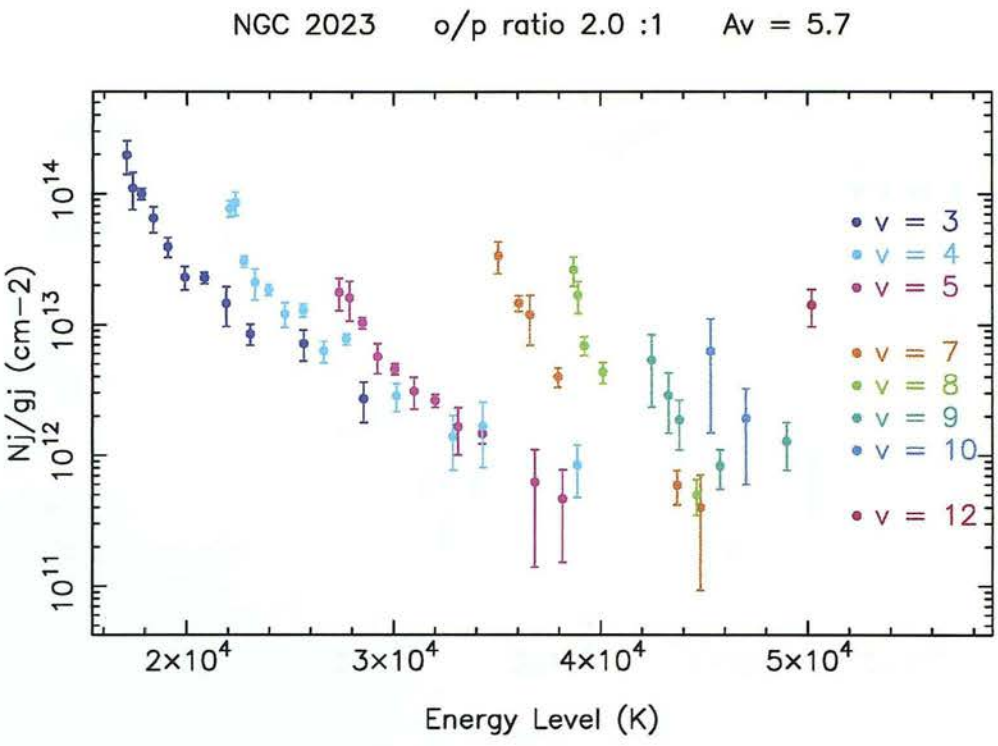

Figure 4.29: Weighted means of column densities from 54 upper levels derived from 1996 RGO Spectrograph observations.

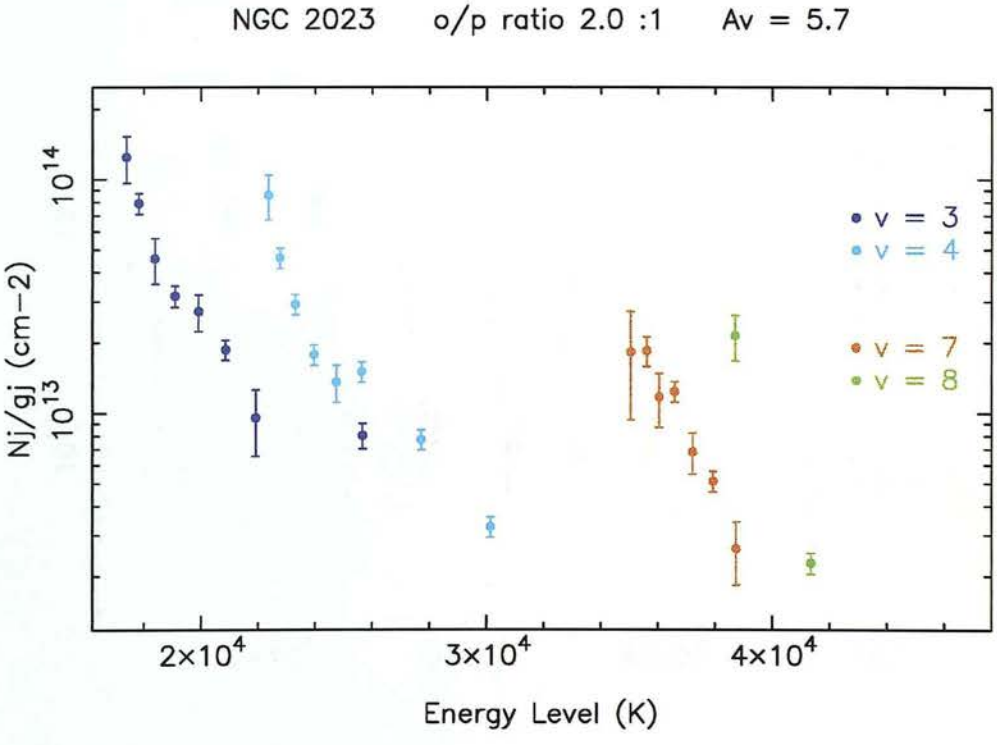

Figure 4.30: Weighted means of column densities from 25 upper levels derived from 1990 RGO Spectrograph observations.

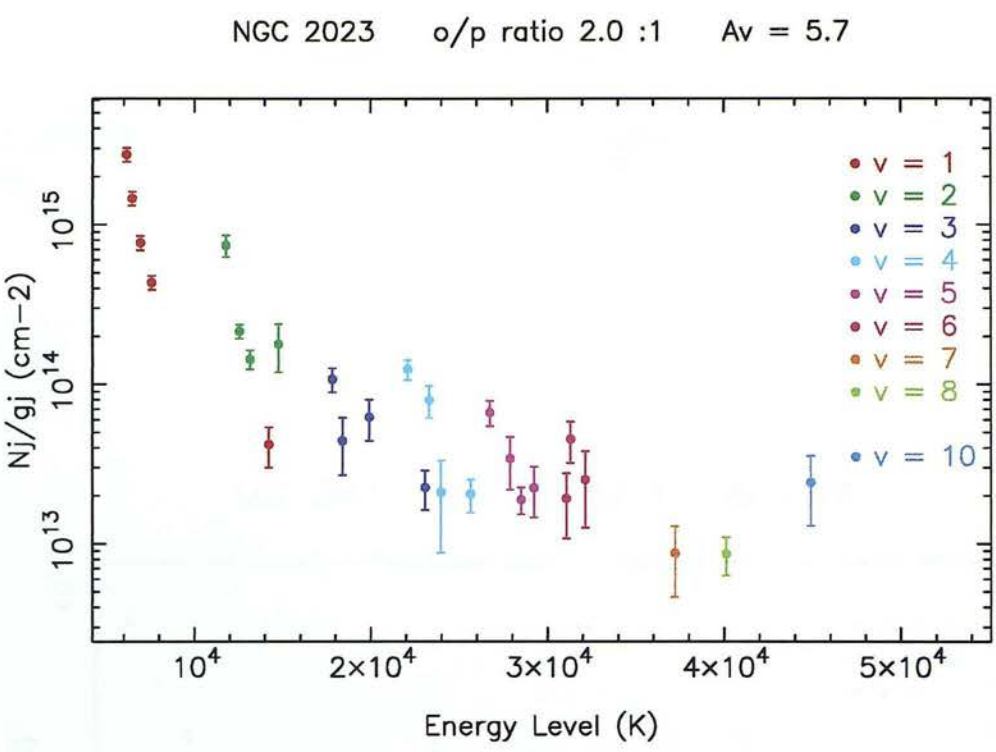

Figure 4.31: Weighted means of column densities from 27 upper levels derived from 1989 CGS2 observations.

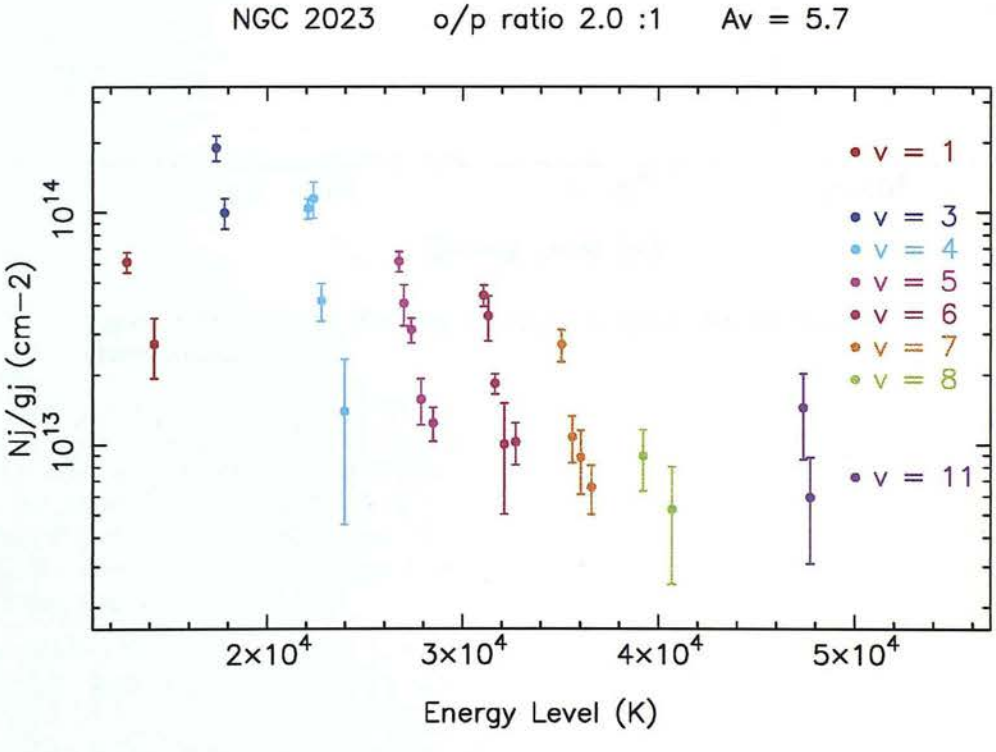

Figure 4.32: Weighted means of column densities from 26 upper levels derived from 1995 CGS4 observations.

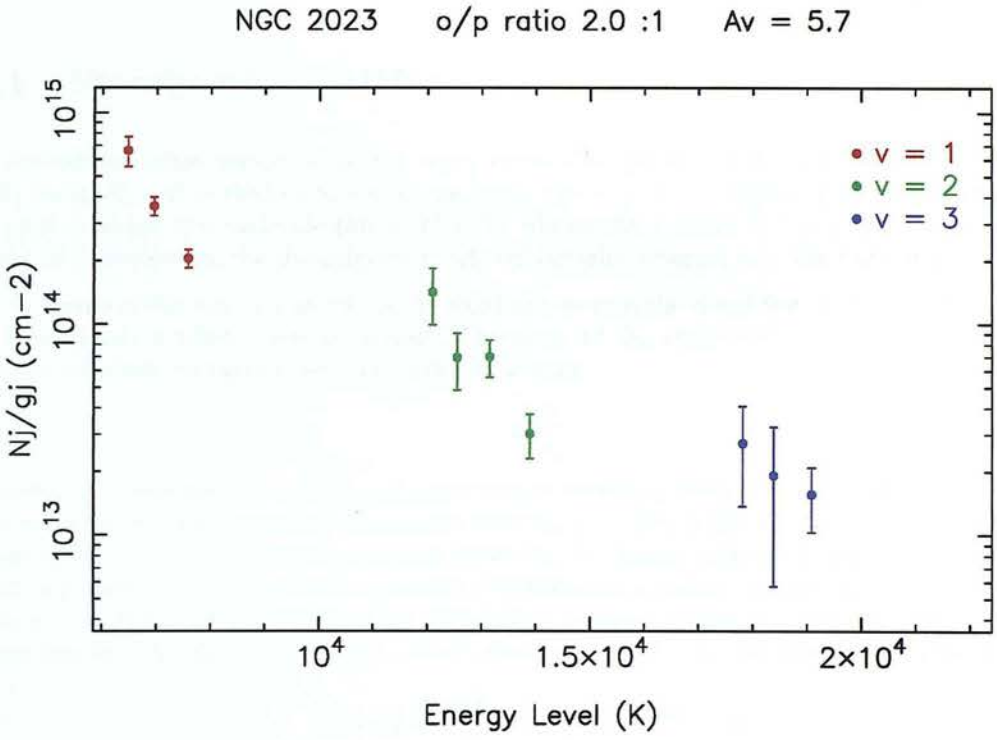

Figure 4.33: Column densities of 10 upper levels derived from 1985 UKT9 observations.

Chapter 5

Photodissociation Regions: Theory and Interpretation of Data

5.1 Steady-State PDRs

A photodissociation region is created when ultraviolet photons sufficiently energetic to electronically excite H_2 out of the low rovibrational levels ($h\nu > 11.2\,\mathrm{eV}$) without directly photodissociating or photoionising the molecule ($h\nu < 14.7\,\mathrm{eV}$) illuminate a cloud of molecular hydrogen. At the onset of illumination, the dissociation front will initially advance into the molecular cloud.

In terms of the velocity at which the front moves into the cloud the limiting case can be taken to be a situation where there is no dust. Therefore all the ultraviolet radiation is absorbed by H_2 and no reformation takes place. The velocity is then

$$\eta . \frac{F_\nu}{n_2} \tag{5.1}$$

where η accounts for the fraction of dissociations resulting from UV absorptions ($\eta \simeq 0.16$ - see Section 2.5), F_ν is the number of photons arriving per second per unit area which are capable of electronically exciting H_2 and n_2 is the molecular hydrogen number density. In Galactic PDRs dust is present which absorbs the photons and provides a surface for the H_2 to reform on. In the case of a stationary front where photodissociation balances formation of H_2 at a distance into the cloud specified by the optical depths due to dust, τ_d, and H_2, τ_2, the equilibrium can be expressed as

$$Rnn_H = \eta \int n_2 \sigma_2(\nu) F_\nu e^{-(\tau_d + \tau_2)}\, d\nu \tag{5.2}$$

where Rnn_H is the formation rate (see Section 2.4) and the right hand side of the equation is the dissociation rate integrated over the frequency of the radiation (see Section 2.5). The electronic transitions occur through absorptions in the Lyman and Werner bands. These transitions have discrete frequencies and thus the interaction cross section $\sigma_2(\nu)$ is strongly frequency dependent. This has the result that in regions of high density where dissociated H_2 reforms rapidly, it competes more effectively at absorbing UV photons than dust grains. As a consequence the H_2 absorbs a larger fraction of UV photons which are at the frequencies of the Lyman and Werner systems. This effectively causes a shadow to be cast at these frequencies and the H_2 molecules further into the cloud are shielded from these 'photodissociating' photons. This process is known as 'line self-shielding'.

5.1.1 Self-Shielding

Self-shielding can be expressed as a factor in the balance equation. At the very front (optical depth zero) of the PDR, equation (5.2) becomes

$$Rnn_H = \eta\, n_2 \int \sigma_2(\nu) F_\nu\, d\nu \tag{5.3}$$

which can be written

$$= n_2 G_0 D$$

where D is the unattenuated interstellar dissociation rate $5.43 \times 10^{-11}\,\mathrm{s}^{-1}$ (Sternberg 1988) and G_0 is the incident UV field in units of the average interstellar radiation field, $1.6 \times 10^{-6}\,\mathrm{W\,m}^{-2}$ (Habing 1968). At finite optical depth, the balance equation becomes (neglecting the small variation in σ_d with ν)[1]

$$R n n_H = \eta n_2 e^{-\tau_d} \int \sigma_2(\nu) F_\nu e^{-\tau_2}\, d\nu \tag{5.4}$$

$$= n_2 G_0 D e^{-\tau_d} \beta(N_2) \tag{5.5}$$

where $\beta(N_2)$ is the self-shielding factor

$$\beta(N_2) = \frac{\int \sigma_2(\nu) F_\nu e^{-\tau_2}\, d\nu}{\int \sigma_2(\nu) F_\nu\, d\nu} \tag{5.6}$$

which is unity at the surface of the cloud and drops to zero as $N_2 \to \infty$. To assess how the density of molecular hydrogen varies with depth into the cloud an expression for $\beta(N_2)$ must be found. The interaction cross section depends on the sum of the UV absorption line profiles, $\psi(\nu - \nu_j)$, *i.e.*

$$\sigma_2(\nu) = \sum_j \sigma_j(\nu) = \sum_j b_j \psi(\nu - \nu_j) \tag{5.7}$$

where the strength of each line, b_j, is proportional to the oscillator strength for that transition. Allison & Dalgarno (1970) have calculated values for the oscillator strengths of the Lyman and Werner systems. The optical depth due to molecular hydrogen, $\tau_2 = N_2\sigma_2$. One may assume the UV flux to be a constant, F_j, for each absorption line. The numerator of equation (5.6) thus becomes,

$$\sum_j b_j F_j \int \psi_j e^{-\sum_i b_i \psi_i N_2}\, d\nu. \tag{5.8}$$

The expression refers to the absorption of radiation in the j^{th} line of a molecule. The radiation has been attenuated by previous interactions with H_2. If one assumes there is negligible line overlap then for a given frequency, within the integral, only one line will be significant in the exponential term, *i.e.* $i = j$. The line profiles are described well by a Lorentzian function. Since the optical depth is enormously greater than unity in the Doppler cores and furthermore, the frequency shifts are much greater than the intrinsic width, $(\delta\nu_j^2 = (\nu - \nu_j)^2 \gg a^2)$, therefore

$$\psi_j = \frac{a/\pi}{a^2 + (\nu - \nu_j)^2} \simeq \frac{a}{\pi \delta \nu_j^2}. \tag{5.9}$$

Combining equations (5.8) and (5.9) and substituting $u = -1/\delta\nu$ the integral becomes

$$\sum_j b_j F_j \int \frac{a}{\pi} e^{-b_j N_2 (a/\pi) u^2} du = \sum_j F_j \sqrt{\frac{b_j a}{N_2}}. \tag{5.10}$$

The denominator of equation (5.6) integrates directly[2] to $\sum_j b_j F_j$ and so the self-shielding function becomes

$$\beta(N_2) = \sqrt{\frac{a}{N_2}} \cdot \frac{\sum_j \sqrt{b_j} F_j}{\sum_j b_j F_j}. \tag{5.11}$$

The above approximation indicates the importance of self-shielding and how the factor β varies asymptotically as $N_2^{-1/2}$ for large cloud depth. The approximation does not apply directly at the surface of the cloud $(N_2 = 0)$ where $\beta = 1$.

[1] Within the wavelength range where the bulk of the UV pumping occurs, $\lambda = 91.2 \to 110.8$nm (Draine & Bertoldi 1996), for an extinction law $\tau_d \propto \lambda^{-1.7}$ (see Section 4.3.2) the optical depth drops by a factor 0.7. Using the Draine (1978) formula for the interstellar UV radiation field it can be seen that F_ν increases by a factor of 8.5 across this wavelength range. Draine & Bertoldi (1996) find the PDR emission spectrum is essentially independent of the colour temperature, T_c, of the radiation for $T_c \geq 10^4$ K (A0 spectrum).

[2] The line profiles are normalised ($\int \psi_j\, d\nu = 1$) so $\int \sigma_j\, d\nu = \int b_j \psi(\nu - \nu_j)\, d\nu = b_j$.

Replacing the integral of the balance equation (5.2) with the right hand side of equation (5.10) and using the substitution $dN_H/dN_2 = n_H/n_2$, the equilibrium between formation and destruction of H_2 is then given by

$$Rn\, dN_H = \eta e^{-\tau_d} \sum_j F_j \sqrt{\frac{b_j a}{N_2}}\, dN_2 \tag{5.12}$$

Substituting in the known values and rearranging equation (5.12) one finds

$$dN_2 = 8.0 \times 10^{-14} S(T) T^{0.5} \frac{n}{G_0 e^{-\tau_d}} \sqrt{N_2}\, dN_H \tag{5.13}$$

where $S(T)$ is the probability of an H atom sticking to the dust grain, during a collision (Hollenbach & McKee 1979), at a temperature T for an incident UV field G_0. Integrating equation (5.13) reveals that $N_2 \propto (n/G_0)^2 {N_H}^2$ at low optical depth. The rapidity at which H_2 reforms with depth into the cloud depends strongly on n/G_0, the ratio of formation to destruction of H_2, and it is self-shielding which amplifies this effect. The onset of self-shielding occurs at an H_2 column density of $\sim 10^{14}\,\mathrm{cm}^{-2}$ (Draine & Bertoldi 1996) which is much less than the column densities at which gas becomes optically thick due to dust, $1/\sigma_d \sim 10^{21}\,\mathrm{cm}^{-2}$. Turbulence within the PDR will also affect the column density of excited H_2. An increase in the Doppler width of a few $\mathrm{km\,s}^{-1}$ will cause self-shielding to occur deeper into the cloud and can increase the H_2^* column density by up to a third (Black & van Dishoeck 1987). A more detailed analysis of self-shielding is carried out by Draine & Bertoldi (1996) who include the effect of line overlap and show that the treatment above is most valid over the column density range $10^{17} \leq N_2 \leq 10^{20}\,\mathrm{cm}^{-2}$.

5.1.2 Structure

The ultraviolet radiation at the surface of a PDR will photoionise elements with ionisation potential less than the Lyman limit (13.6 eV) leaving the gas mostly H, He, O, C^+ and N. Photodissociation regions consist primarily of a mixture of H and H_2 with densities ranging from $n = 10^2$–$10^7\,\mathrm{cm}^{-3}$. Tielens & Hollenbach (1985) (hereafter TH) produced the first theoretical model covering the full chemical heat balance of dense ($n = 10^3$–$10^6\,\mathrm{cm}^{-3}$) gas illuminated by ultraviolet radiation ($G_0 = 10^3$–10^6). They considered a steady-state PDR adjacent to an HII region and approximated the excited H_2 states with a pseudo-level at $v = 6$. A plan of the PDR is shown in Fig. 5.1. The gas heating and cooling mechanisms which determine the temperature structure of the cloud are plotted as a function of extinction into the cloud in Fig. 5.2.

The main contribution to heating in the infrared bright surface layers of gas at moderate densities ($n < 10^4\,\mathrm{cm}^{-3}$) is from the photoelectric emission from dust grains. At higher densities the contribution from collisional de-excitation of H_2 (vibrational heating) dominates (Sternberg & Dalgarno 1989 - hereafter SD). Photodissociation plays a minor part in heating the gas (SD) except at very low densities (Hollenbach, Takahashi & Tielens 1991). The contribution to heating from H_2 formation depends greatly on the formation process. TH assume that the critical temperature above which H_2 will not occur on dust grains is 75 K. Since the grain temperatures found in PDRs are generally less than this (see Fig. 5.3a) they assume once an atom is adsorbed on the surface the formation process is 100% efficient. SD assume a third of the binding energy is distributed statistically across all the rovibrational energy levels. The formation process is then the third most important contribution to heating and dominates photodissociation. The rate at which collisional de-excitation of H_2 heats the gas is far greater (at temperatures found in PDRs) than the rate at which collisionally excited H_2 cools via radiative decays. The cooling in these regions is dominated by fine structure lines of OI (63 μm) and CII (158 μm), continuum dust emission and at temperatures of a few thousand degrees the rovibrational transitions of H_2 while at temperatures less than 50 K the low rotational lines of CO are the dominant coolant (Burton, Hollenbach & Tielens 1990 - hereafter BHT).

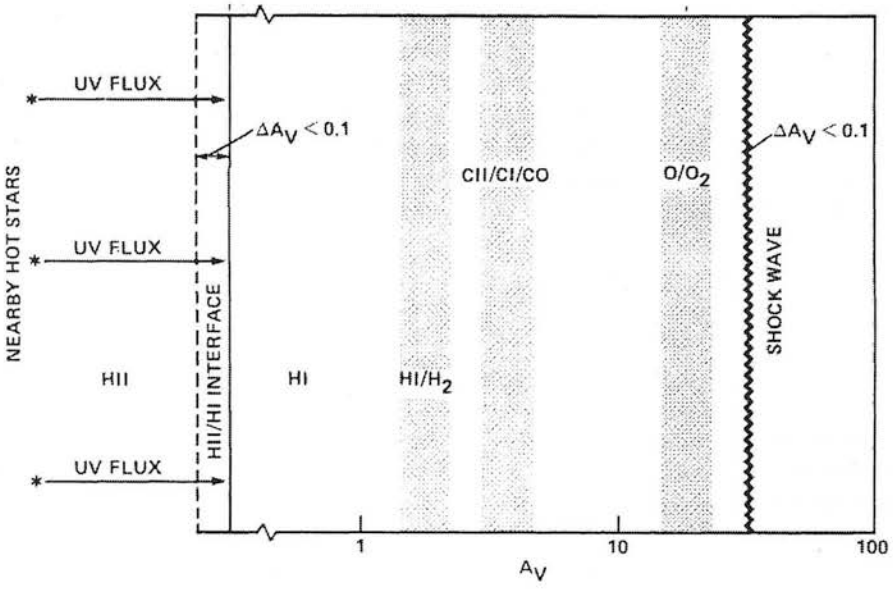

Figure 5.1: Schematic of a molecular exposed to ultraviolet radiation from Tielens & Hollenbach (1985)

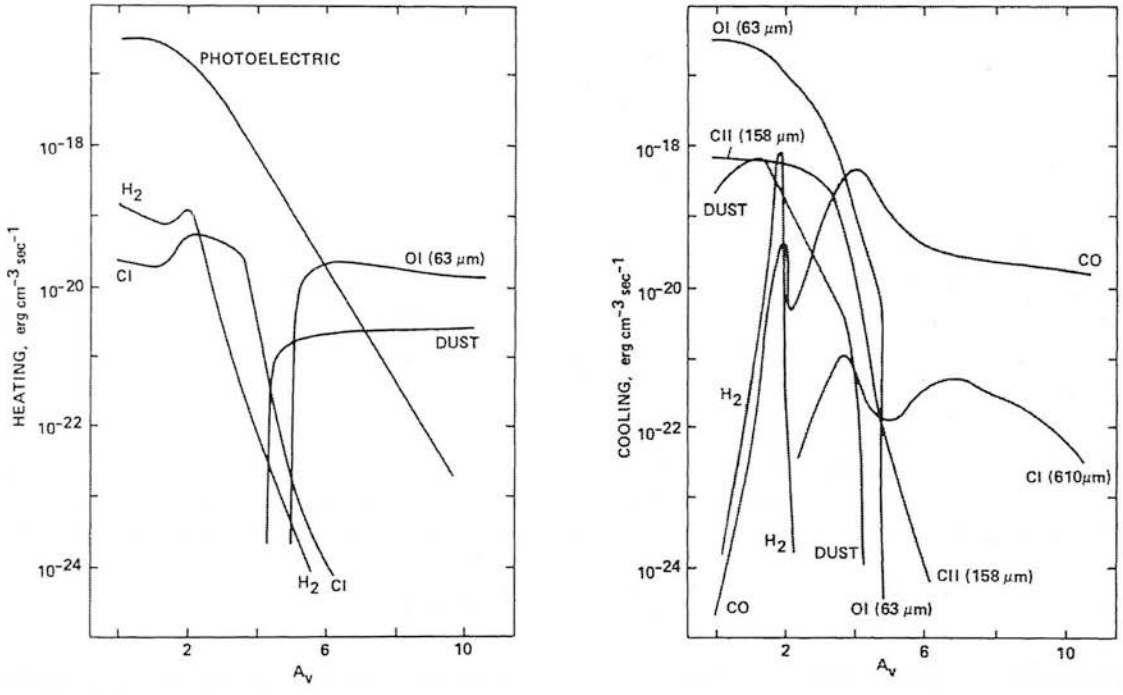

Figure 5.2: The different heating and cooling terms in the energy balance plotted as a function of extinction A_v into the cloud taken from the model of Tielens & Hollenbach (1985). The gas density is $n = 10^5\,\mathrm{cm}^{-3}$ with an incident UV radiation field of $G_0 = 10^5$. The CI and OI heating terms, not mentioned in the text, are due to ionisation of neutral carbon and collisional de-excitation of the neutral oxygen $^3P_1$ fine structure level. The heating due to collisional de-excitation of H_2 is underestimated by an order of magnitude using the simple two level model and adopted collision rates (Sternberg & Dalgarno 1989).

At the edge of the PDR, hydrogen is mainly in atomic form but becomes progressively more molecular further into the cloud due to dust extinction and self-shielding. The transition from atomic to molecular hydrogen depends on the ratio of the hydrogen number density to UV radiation (n/G_0). Self-shielding will become significant, bringing the transition zone to $A_v \leq 1$, when the ratio n/G_0 is large, *i.e.* $\gg 40\,\mathrm{cm}^{-3}$ (BHT; Jura 1975). Here the photoelectric heating reaches its maximum rate and vibrational heating becomes important allowing temperatures much greater than 100 K to be attained. In the standard model of TH for gas of density $n \sim 10^5\,\mathrm{cm}^{-3}$ illuminated by radiation fields of strength $G_0 \sim 10^5$ the transition zone occurs at $A_v \sim 2$, with the abundance of vibrationally excited H_2 increasing until $A_v = 2$, for both high and low density PDRs (see Fig. 5.3a). The column density of excited H_2 in all levels with $v \geq 1$ is $4.5 \times 10^{16}\,\mathrm{cm}^{-2}$. In low density PDRs ($n \leq 10^4\,\mathrm{cm}^{-3}$) the gas temperature is several times smaller than in high density PDRs (*i.e.* ~ 100 K) however the depth dependence is very similar and in both cases the grain photoelectric heating heats the gas to higher temperatures than the grains for $A_v \leq 4$ (Hollenbach et al. 1991; see also Fig. 5.3b). Beyond $A_v > 4$, molecular hydrogen plays little part in the heating of cooling of the cloud. The chemistry and thermal balance in these regions is still determined by the ultraviolet photons which penetrate this far. Further into the cloud ionised carbon gives way to neutral carbons atoms and further still, beyond $A_v \simeq 5$, carbon monoxide forms. Oxygen however remains atomic except in the densest of cores (see Fig. 5.1). In the furthest regions H_2O may be found where there are potential wells[3].

5.1.3 Dependence of H_2 Emission on Radiation Field

Equation 5.5 can be expressed as

$$Rnn_H = n_2 G_0 D\beta(N_2) e^{-\sigma_d(N_H+2N_2)} \tag{5.14}$$

where the exponential term is continuum attenuation due to dust scattering and absorption. The effective ultraviolet continuum cross section, σ_d, depends on the gas to dust ratio and the grain ultraviolet scattering properties. Substituting for $dN_H/dN_2 = n_H/n_2$ into equation (5.14) and integrating it follows that

$$N_H = \frac{1}{\sigma_d} \ln\left(\frac{G_0 D}{Rn}\xi(N_2) + 1\right) \mathrm{cm}^{-2} \tag{5.15}$$

where the dimensionless integral $\xi(N_2) = \int_0^{N_2} \sigma_d \beta(N_2') \exp(-2\sigma_d N_2')\, dN_2'$. This integral converges to a constant $\xi = 5 \times 10^{-5}$ as $N_2 \to \infty$ and the total atomic hydrogen column density,

$$N_H^{\mathrm{tot}} = \frac{1}{\sigma_d} \ln\left(\frac{G_0 D}{Rn}\xi + 1\right) \mathrm{cm}^{-2}. \tag{5.16}$$

Since photons of the same energy dissociate and excite H_2, the column density of excited molecular hydrogen, N_2^* is proportional to N_H^{tot}. For every photon which dissociates H_2, there are $(1-\eta)/\eta$ photons which instigate radiative or collisional de-excitation ($\eta \simeq 0.16$ - see Section 2.5). With formation and destruction in equilibrium the total column density of excited H_2 is therefore

$$N_2^* = \frac{1-\eta}{\eta} \cdot \frac{Rn}{A + \gamma(n_H + n_2)} N_H^{\mathrm{tot}} \tag{5.17}$$

where A is the average radiative transition rate ($\sim 2 \times 10^{-7}\,\mathrm{s}^{-1}$ - BHT) and γ is the average collisional de-excitation rate coefficient of H_2^* by H or H_2. Substituting typical values into equation (5.16) the logarithm term becomes

$$\ln\left(91 \times (n/G_0)^{-1} + 1\right). \tag{5.18}$$

It is apparent that for small values of n/G_0 (*i.e.* $< 40\,\mathrm{cm}^{-3}$) the column densities N_H^{tot} and N_2^* are insensitive to changes in the UV field whereas for large values of the ratio H_2 emission is strongly dependent on G_0.

[3] Joke.

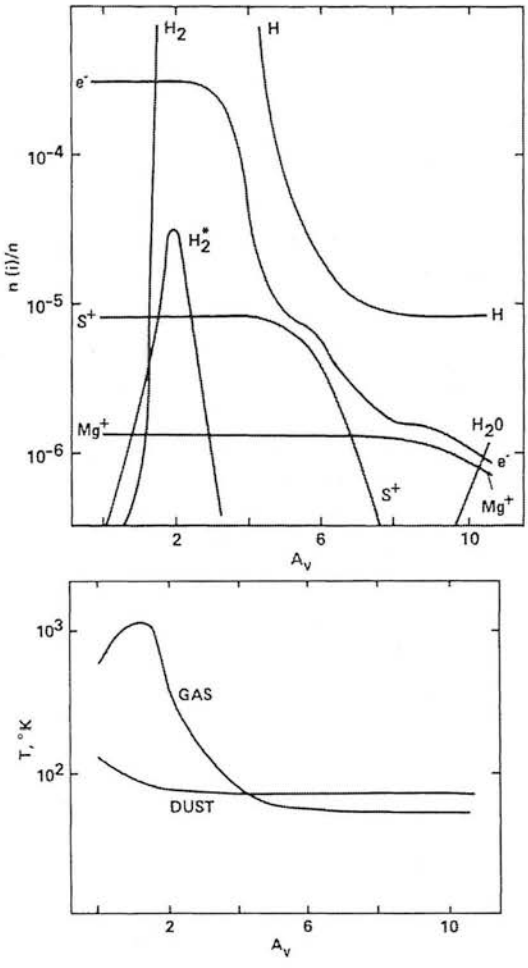

Figure 5.3: a) Molecular abundances and b) gas and dust temperatures as a function of extinction from Tielens & Hollenbach (1985).

5.1.4 Dependence of H_2 Emission on Density

Since absorption of a UV photon by an H_2 molecule is $(1-\eta)/\eta$ times more likely to result in a stable, excited molecule than dissociation the equilibrium between formation and destruction may be expressed by

$$\eta^{-1}(1-\eta).Rnn_H = n_2^* A(1+n/n_{cr}) \tag{5.19}$$

where n_2^* is the density of excited H_2 and the critical density[4] $n_{cr} = A/\gamma$. Integrating over a column of gas where dust attenuates the UV field (*i.e.* $n/G_0 \ll 40\,\mathrm{cm}^{-3}$), the column density of atomic hydrogen can be taken to be $N_H \sim 10^{21.5}\,\mathrm{cm}^{-2}$ and only logarithmically dependent on density and the UV field (see equation 5.16). The column density of excited H_2 is then

$$N_2^* \propto \frac{n}{1+n/n_{cr}}. \tag{5.20}$$

Therefore to a first approximation, ignoring the temperature dependence of R and n_{cr}, for $n \ll n_{cr}$ ($n_{cr} \sim 10^5\,\mathrm{cm}^{-3}$) the observed column density of excited H_2 emission proportionally traces the total gas density. For $n \gg n_{cr}$ the H_2 emission saturates and is proportional to n_{cr}. In the extreme self-shielding case ($n/G_0 \gg 40\,\mathrm{cm}^{-3}$) where H_2 attenuates the UV flux within one optical depth, the column density is a constant $N_2 \sim 10^{21}\,\mathrm{cm}^{-2}$. Equating H_2 formation and destruction (equation 5.5) we obtain the limit $N_H \propto G_0/n$ and then the H_2 excitation is proportional to the UV radiation field for $n \ll n_{cr}$ and proportional to $G_0 n_{cr}/n$ for $n \gg n_{cr}$.

Another contribution to the column density of excited molecular hydrogen comes from thermal excitation. As the gas density increases so does the temperature and collisional excitation becomes more important. Where the gas density is less than the critical density $N_2^* \propto nN_2\gamma_{ex}$. For densities greater than the critical density $N_2^* \propto N_2$ and the levels are populated with a thermal Boltzmann energy distribution. Since the first excited rotational state is 170 K above ground, gas temperatures higher than 100 K are required to significantly populate these levels and temperatures greater than 1000 K to populate the vibrationally excited levels, which have excitation temperatures over 6000 K. Figure 5.4 shows model predictions by BHT of how the populations of the rovibrational states are redistributed as the gas becomes thermalised with increasing density ($n = 10^3$–$10^7\,\mathrm{cm}^{-3}$) for a UV flux of $G_0 = 10^4$. The lowest pure rotational states are nearly always in local thermal equilibrium at the local gas temperature. As the density increases the lowest vibrational levels thermalise and move towards the curve defined by the low-J levels of the $v = 0$ level while the $v \geq 2$ levels remain dominated by radiative excitation. This density and UV field dependence permits the relative intensities of H_2 lines to be used as diagnostics. Figure 5.5 shows predictions from BHT of how the 1–0 S(1)/2–1 S(1) and 0–0 S(13)/1–0 O(7) line ratios vary with UV field and density.

5.2 Comparisons of Models with Observations

5.2.1 Steady-State Models

Black & van Dishoeck (1987) (hereafter BvD) produced the first detailed models of PDRs which included UV absorption and IR emission from all the 211 rovibrational levels of H_2 with $J \leq 15$. This permitted modelling for UV radiation fields of strength $G_0 \geq 10^4$ where an excited molecule is as likely to undergo IR radiative de-excitation as UV excitation (Shull 1978). Vibrationally inelastic collisions for the $v > 0$ levels and UV emission from H_2 as a source of excitation were not included. Therefore these models apply primarily to purely fluorescent emission from regions with densities $n \leq 10^4\,\mathrm{cm}^{-3}$ and temperatures $T < 2000\,\mathrm{K}$.

The models describe steady-state PDRs, computed as functions of depth into the cloud at given temperatures and densities which remain constant throughout the PDR. The H_2 populations are determined primarily by the formation rate and destruction rate following radiative absorption in

[4] The critical density refers to the particle number density (*i.e.* $n_T = n_H + n_2$) at which collisional de-excitation is equal to radiative de-excitation of rovibrational states of H_2. The approximation here is used that $n \simeq n_T$ which is nearly exact for the surface of the cloud ($n = n_H$) but less accurate further into the PDR. The uncertainties in the collision rates are sufficiently large to make this approximation valid.

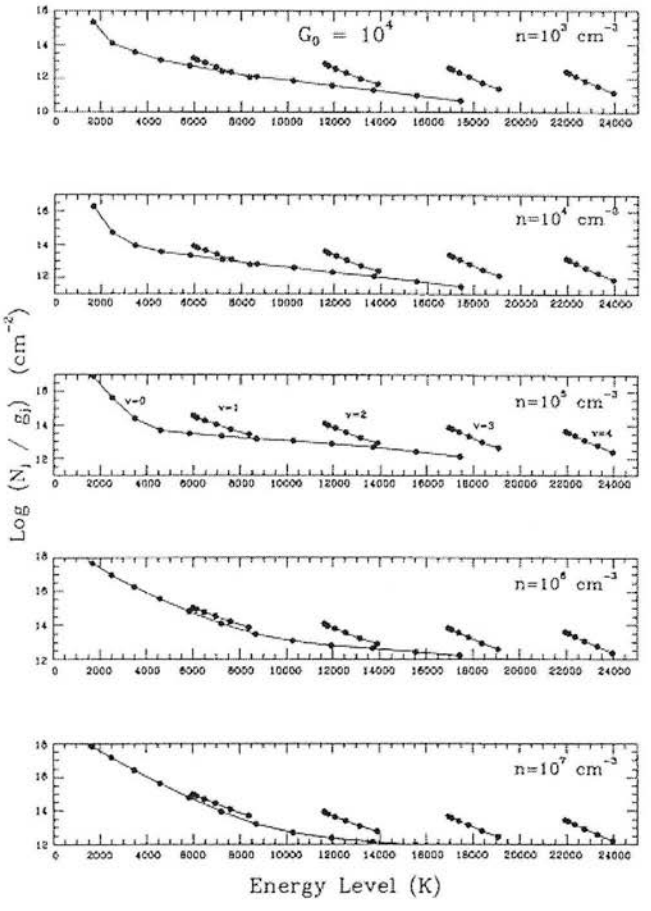

Figure 5.4: Model of gas thermalising at high densities (BHT). The H_2 column density, N_j, divided by the level degeneracy, g_j (assuming an ortho to para ratio of 3:1) is plotted against energy level.

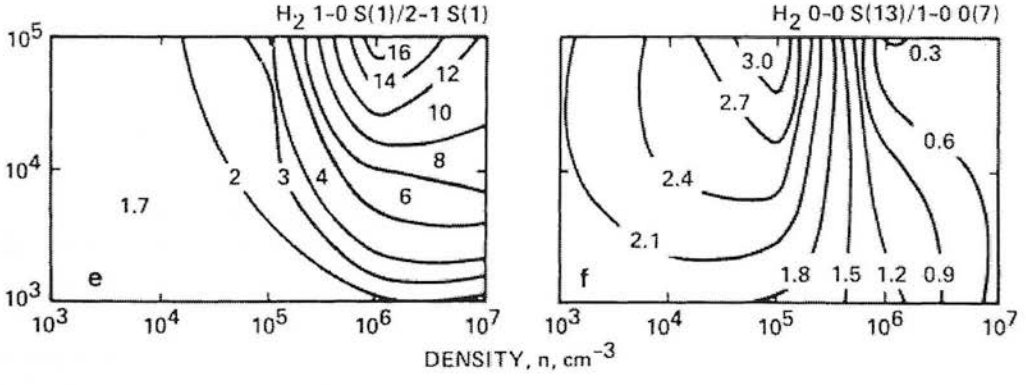

Figure 5.5: Contour plots of line intensity ratios for the 1–0 S(1)/2–1 S(1) K-band and 0–0 S(13)/1–0 O(7) L-band lines (BHT). The y-axis is the UV radiation field, G_0, in units of the average Galactic interstellar radiation field.

the Lyman and Werner band systems. To explicitly calculate the population of each rovibrational level the following equation must be solved in which all the processes populating the rovibrational level vJ of the ground electronic state are balanced by the transitions and destruction processes which depopulate level vJ.

$$\overbrace{nn_H R_{vJ}^{\varphi}}^{formation} + \sum_{v'=0}^{14}\sum_{J'=0}^{15} n_{v'J'}\left[\overbrace{A_{v'J',vJ} + k_{v'J',vJ}^{fl}}^{IR+UV\ emission} + \overbrace{\sum_i n(i)\gamma_i(J',J)\delta_{v',0}}^{collisional\ population}\right](1-\delta_{v'J',vJ})$$

$$= n_{vJ}\left[\overbrace{A_{vJ}^{X} + (k_{vJ}^{ex} - k_{vJ,vJ}^{fl})}^{IR\ emission+UV\ absorption} + \sum_i\sum_{J'\neq J}\overbrace{n(i)\gamma_i(J,J')\delta_{v,0}}^{collisional\ depopulation} + \overbrace{k_{vJ}^{d} + k_{vJ}^{pi} + 1.051\zeta_0}^{destruction\ of\ H_2}\right] \quad (5.21)$$

The formation term refers to H_2 formation on dust grains according to three processes which were used to determine the sensitivity of the H_2 populations to their initial distribution among the energy levels, $E(vJ)$, upon formation:

- $\varphi = 1$ one-third of the 4.5 eV binding energy of H_2 (52,000 K) is deposited statistically as internal excitation of the newly formed molecule, *i.e.* $R_{vJ} \propto g_j e^{-E(vJ)/51940}$,
- $\varphi = 2$ molecules are formed in the $v = 14$ level with $R_{vJ} \propto 1/4$ for $J = 0$ and $R_{vJ} \propto 3/4$ for $J = 1$,
- $\varphi = 3$ molecules are formed in the $v = 6$ level at the temperature of the grain, *i.e.* $R_{vJ} \propto g_j e^{-E(6,J)/T_d}$.

The infrared quadrupole transition probabilities from levels $v'J' \rightarrow vJ$ are given by $A_{v'J',vJ}$ and out of level vJ to any rovibrational level by A_{vJ}^{X}. The rates of UV absorption for the following processes are given by: k_{vJ}^{ex} which leads to fluorescent excitation; $k_{v'J',vJ}^{fl}$ for the transition $v'J' \rightarrow vJ$; k_{vJ}^{pi} for photoionisation (for $v \geq 4$) and k_{vJ}^{d} for photodissociation[5] (for $v \geq 3$). The ionisation frequency of H_2 is given by $1.051\zeta_0$ where $\zeta_0 = 5 \times 10^{-17}\,s^{-1}$ is the ionisation frequency of atomic hydrogen by cosmic rays. The Kronecker delta function, $\delta_{v,0}$, specifies that collisional terms are included only for rotational transitions within $v = 0$, where $n(i)$ is the number density of collision partners (i = H, H_2 and H^+) and $\gamma_i(J, J')$ is the collisional rate coefficient for transitions $J \rightarrow J'$. The collision rates were based on the results of Green & Truhlar (1979).

5.2.1.1 Comparison with BvD Model #14

Model #14 from BvD was calculated for a low density PDR ($n = 3000\,cm^{-3}$) at a temperature of 100 K, illuminated by an ultraviolet flux of $G_0 = 2200$. The $\psi = 2$ formation process was used which assumed all formation took place in the first 2 rotational levels of the $v = 14$ level. The resulting column density of excited molecular hydrogen was $N_2^* = 4.7 \times 10^{15}\,cm^{-2}$ with the number density of vibrationally excited H_2 reaching a maximum of $n_2^* = 9.6 \times 10^{-3}\,cm^{-3}$. This model has been compared to the observational data presented in Chapter 4. Figure 5.6 shows the complete dataset (all five observations) divided by the model. The individual ratios for each energy level are shown in Table F.1.

The entire dataset is an order of magnitude brighter than that predicted by the model. The $v = 1$ level shows an excess population in the low-J states which is characteristic of a thermal distribution where the gas is close to its critical density and collisions are redistributing the vibrationally excited molecules into the $v = 0$ and $v = 1$ energy states. Within the $v > 1$ levels there is a trend towards excessively populated levels as J increases. Individual levels which stand out against the overall pattern are described below.

[5] BvD found that where UV fluxes are high enough to maintain significant populations of H_2 in levels with $v \geq 3$ ($G_0 \sim 10^4$) then photoionisation occurred for H_2 with $v \geq 4$ and direct photodissociation for H_2 with $v \geq 3$ although neither process contributed to more that 11% to the overall destruction rate of H_2 at any depth.

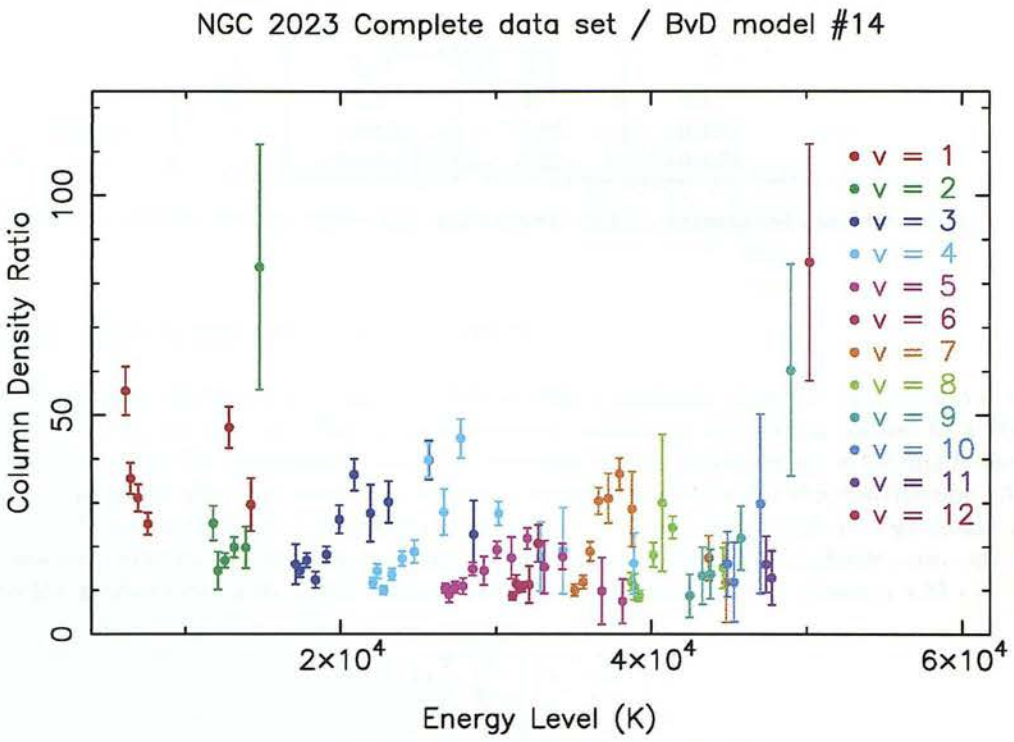

Figure 5.6: The complete dataset derived from the far-red and infrared observations of NGC 2023 divided by BvD model #14.

v	J	Line	$\lambda(\mu m)$	Observations	Comments
1	9	1–0 S(7)	1.7480	CGS4	possible contamination from FeII ($A^4D_{1/2}$–$A^4F_{3/2}$) at 1.7454 μm and FeII ($A^4P_{3/2}$–$A^4D_{7/2}$) at 1.7488 μm
1	10	1–0 S(8)	1.7148	CGS4, CGS2	line deconvolved from sky line - OK
2	6	2–0 S(4)	1.0998	CGS2	no obvious contaminants - OK
3	13	3–0 S(11)	0.7865	RGO 1996	not visible in 1st grating position only in 2nd, low signal to noise
4	7	4–1 S(5)	0.8337	RGO 1996/90	possible blend with 8–4 S(7) at 8335 Å which is predicted to be 4× fainter
		4–2 S(5)	1.2263	CGS2	no obvious blends, consistent with 4–1 S(5) lines - OK
4	9	4–1 S(7)	0.8286	RGO 1996/90	possible contribution from HI (13–3) 8286 Å
9	13	9–4 S(11)	0.7633	RGO 1996	in a noisy part of the spectrum in an O_2 absorption band

For comparison the levels arising from the far-red and infrared observations are plotted in Fig. F.1. Evidence of excess populations, over the model, are evident in both the infrared and far-red datasets. The far-red data also suggest a 'turnover' at high-J along the v-levels, where the gradient drops to zero and the excess populations begin to decrease as J increases.

Gas at densities higher than the critical density will experience significant collisional processes. The column density inferred for an excited level from equation (4.1) will therefore represent the gas which is fluorescing. The component which is collisionally de-excited from that level will not be seen. Energy levels with high critical densities will therefore produce relatively more fluorescent emission. Collision rate calculations presented in Martin et al. (1996) indicate that for vibrational levels v = 2–8, critical densities peak at $J = 5$ dropping off steeply either side of this J-level. These results are for H_2-H collisions in gas at 2000 K. This is not the temperature found within PDRs but it may prove an important insight into the profile of the v-levels shown in Fig. 5.6.

J-level	N_j^{th}/g_j ($10^{15}\,\mathrm{cm}^{-2}$)	σ_j ($10^{14}\,\mathrm{cm}^{-2}$)	BvD#14 ($10^{14}\,\mathrm{cm}^{-2}$)	Energy (K)
1	2.51	3.1	0.550	6149
2	1.06	1.5	0.416	6471
3	0.599	0.88	0.283	6951
4	0.274	0.45	0.179	7584

Table 5.1: Values used to derive the temperature of the thermalised gas from the $v = 1$ level.

5.2.1.2 Thermalisation of the $v = 1$ level

The population distribution in the $v = 1$ level differs markedly from the other v-levels and after dividing by the model resembles an exponentially decreasing population similar to a Boltzmann distribution. On the assumption that this emission can be explained by a thermally excited gas component an attempt has been made to find a temperature which fits this distribution. A straight line was fitted to the $v = 1$ populations of the first 4 rotational levels[6] in $\log_e$ space, after the fluorescent contribution was divided out. In $\log_e$ space a thermal distribution appears as a line with the gradient equal to $-1/T$ where T is the gas temperature (see equation 4.3) *i.e.*

$$\ln\left(\frac{N_j^{th}}{g_j}\right) = \frac{-E_j}{T} + c \tag{5.22}$$

where N_j^{th} is the column density of the thermal component contributing to the excess in Fig. 5.6 and c is the y-axis intercept. An expression for T was found from a minimum χ^2 fit of a line to the data in $\log_e$ space:

$$T = \frac{\sum_i (E_i/\sigma_i)^2}{\sum_j (E_j/\sigma_j^2)(-\ln N_j + c)}. \tag{5.23}$$

Here N_j is the thermally excited component of the column density divided by the degeneracy (*i.e.* N_j^{th}/g_j). An expression for c was found in the same manner :

$$c = \frac{\sum_j (1/\sigma_j^2)(\ln N_j + E_j/T)}{\sum_i (E_i/\sigma_i)^2}. \tag{5.24}$$

Substituting equation (5.24) into (5.23) and rearranging for T provided an expression for calculating the temperature of the gas component which would be able to excite the H_2 population into a Boltzmann distribution capable of reproducing the $v = 1$ level in Fig. 5.6,

$$T = \frac{\sum_i \sigma_i^{-2} \sum_j (E_j/\sigma_j)^2 - \left(\sum_k E_k/\sigma_k^2\right)^2}{\sum_l (E_l/\sigma_l^2) \sum_m \sigma_m^{-2} \ln N_m - \sum_n \sigma_n^{-2} \sum_o \sigma_o^{-2} E_o \ln N_o}. \tag{5.25}$$

Table 5.1 shows the parameters of the first 4 rotational levels used in the fit. The column density contribution from the thermalised gas was estimated by subtracting 10 (which was considered to be a representative value of the baseline in Fig. 5.6) from the values used in Fig. 5.6 (Table F.1). These values were multiplied by the respective fluorescent model column density[7] for that level (*i.e.* turned from ratios back into column densities). Fitting to all four levels, the resulting temperature is 740 K. If the $J = 1$ level is not included then the temperature rises to 820 K. The $J = 3$ and $J = 4$ levels on their own provide a temperature of 810 K. This analysis does not account for the effect of vibrationally excited levels being collisionally depopulated into the $v = 1$ level. I therefore tentatively estimate a temperature of $T \simeq 800 \pm 100$ K for the thermalised gas contributing to the emission from the $v = 1$ level.

[6] The $J = 9, 10$ levels stand out from the rest of the $v = 1$ level, possibly due to the same process which enhances the population of the high-J levels in the $v > 1$ levels. Therefore these levels were not included in the fit.

[7] The fluorescent model column densities were adjusted for an ortho/para ratio of 1.8 and the observational data for a ratio of 2.0.

5.2.2 Discussion

The relative line intensities of the BvD models are very insensitive to density and radiation field strength for $n \leq 10^4\,\mathrm{cm}^{-3}$ and $G_0 < 10^5$. They are also insensitive to the grain surface H_2 formation rate coefficient, R, and the effective grain UV continuum absorption cross section, σ_d, while the absolute line intensities depend critically upon them. The excess populations found in the $v = 1$ level indicate that the gas is sufficiently dense ($n \geq 10^5\,\mathrm{cm}^{-3}$) to produce a 'collisional fluorescent' or 'thermal fluorescent' spectrum (see Section 2.3.3). Model #14 has been calculated for a gas temperature of 100 K which may not be representative of the PDR temperature since an increase in temperature results in an increase in brightness, due to an increase in formation rate[8]. Additionally higher temperatures will cause the lowest levels $v = 0, J$ to be collisionally redistributed over more levels thus causing the UV absorption lines out of these levels to become optically thick deeper into the cloud, thereby increasing the total H_2 excitation (*e.g.* an increase in the temperature from $T = 30$–$300\,\mathrm{K}$ can increase the total emission by a factor of 4 - BvD). This may contribute to observed excess brightness of the southern emission ridge in NGC 2023. The excessively populated $J \geq 6$ levels have been noted by Burton (1993) who suggested that this may be a signature of H_2 formation.

The radiation from a B1.5V star such as HD 37903 at the distance of the H_2 emission ridge is expected to have a UV-field strength of $G_0 \simeq 5000$ (BvD find $G_0 \simeq 2800$ whereas Draine & Bertoldi (1996) adopt $G_0 \simeq 5000$). BvD use the upper density limit of their models $n = 10^4\,\mathrm{cm}^{-3}$ to reproduce the low resolution spectra of Hasegawa et al. (1987) (Section 4.1.7). The thermalisation of the $v = 1$ level shown in Fig. 5.6 however indicates emission arises from gas at densities greater than the critical density ($n \geq 10^5\,\mathrm{cm}^{-3}$). BvD find the UV field to be consistent with $G_0 \simeq 670$ with temperature $T \sim 100\,\mathrm{K}$ with formation occurring in the $v = 6$ level (formation model $\psi = 3$). The UV field of $G_0 = 670$ is also in disagreement with the results shown in the following sections which indicate a stronger radiation field and a higher temperature.

More recently Draine & Bertoldi (1996) (hereafter DB) have carried out a detailed analysis of structure of steady-state PDRs and the resulting H_2 emission. They use the most recent radiative and collisional rate coefficients and include a careful analysis of the effects of the UV absorption lines which overlap in wavelength range. The consequence of line overlap is to reduce σ_2 and the effectiveness of self-shielding so that dust absorbs relatively more UV photons thus reducing H_2 excitation. They find the effect to be important at high column densities with pumping rates being suppressed by a factor of 2 for $\mathrm{N(H_2)} \simeq 3 \times 10^{20}\,\mathrm{cm}^{-2}$. The models use more recent dissociation probabilities for the Werner bands which have larger overall values which lead to an estimate that 16% of UV absorptions by H_2 result in dissociation. These new parameters and the line overlap analysis indicate the BvD models overestimate the PDR surface brightness by a factor of ~ 3 which increases the difference between the surface brightness of NGC 2023 and the steady-state models. DB include inelastic collisions with H, He, H_2, H^+ and e^- and are therefore applicable to high density PDRs. The H_2 formation temperature on the surface of the dust grain is assumed to be $5 \times 10^4\,\mathrm{K}$ which results in o/p ratio of 2.78 for the newly formed molecule which is ejected in a mean excited state of $v \simeq 5$, $J \simeq 9$.

DB attempt to reproduce the far-red and infrared observations of NGC 2023 by Burton et al. (1992a) (Section 4.1.5) and Burton et al. (1997) (Section 4.1.6) with a steady-state PDR model. They assumed an extinction law of $\mathcal{R} = 5.5$ and optical extinction $A_v = 1.5$. Having adjusted the absolute fluxes of the far-red data to match the infrared observations they find they are able to approximately reproduce the data with a PDR model of density $n = 10^5\,\mathrm{cm}^{-3}$ illuminated by a UV field of strength $G_0 = 5000$ at temperature $T \simeq 900\,\mathrm{K}$. The resulting ortho/para ratio is 2.5. Their model requires appreciable limb brightening (~ 5) to account the high surface brightness of the observations. DB put an upper limit on any limb brightening which increases the H_2 emission along the line of sight for gas of density $n = 10^5\,\mathrm{cm}^{-3}$, of a factor of 15. This would occur if the emission arose from a section of a shell with radius of curvature which was the distance to the star. Figure 4.22 shows a series of what could be filaments or undulations in a shell of circumstellar

[8] The formation rate depends on the velocity of the H atoms (see equation 2.1) and hence the square root of the gas temperature. However, if the dust temperature exceeds $\simeq 100\,\mathrm{K}$ then the H atoms are likely to evaporate from the grain surface before forming H_2 thus significantly reducing the formation rate (see Section 2.4).

material. If the emission originates from a ripple in the shell this would greatly reduce the radius of curvature and very likely the resulting limb brightening. DB have difficulty reproducing the observed line fluxes with their steady-state limb brightened models. Possible explanations are that the gas may consist of a range of densities or the dissociation front in NGC 2023 may be propagating into the molecular cloud.

The flux ratio of the 1–0 S(1) and 2–1 S(1) lines has been commonly used in the past to distinguish between UV excitation (values of $\sim$ 2–3 - BvD) and shocked excitation (values of ≥ 10 - Shull & Hollenbach 1978). The ratio is fairly constant for gas densities of $n < 10^5\,\mathrm{cm}^{-3}$ (BHT, SD) but at high densities ($n \geq 10^5\,\mathrm{cm}^{-3}$) it becomes sensitive to both n and G_0 and can display high values similar to shock excitation. This is because collisions preferentially depopulate the $v = 2, J = 1$ level (Martin et al. 1996) and end up populating the $v = 1, J = 1$ level thus increasing the ratio. The value obtained for 1–0 S(1)/2–1 S(1) ratio from the data is 3.4. Fig. 5.5 can be taken to imply that this emission is originating from gas at densities of $n \geq 10^5\,\mathrm{cm}^{-3}$ (BHT). An incident UV field strength of $G_0 = 10^4$ is used by Burton (1992) to reproduce the 1.0–2.4 μm observations described in Section 4.1.6 which forms the major part of the infrared data used in this thesis. Adopting a density of $n = 10^5\,\mathrm{cm}^{-3}$ and incident UV field of $G_0 = 10^4$ the ratio $n/G_0 = 10\,\mathrm{cm}^{-3}$ indicates that self-shielding is not a dominant effect (BHT; Jura 1975). Applying the diagnostics from DB to a PDR with $n/G_0 = 10\,\mathrm{cm}^{-3}$ the 1–0 S(1)/2–1 S(1) line ratio of 3.4 for $G_0 = 10^4$ implies a temperature of $\sim$ 1000–1200 K. The 2–1 S(1)/6–4 Q(1) ratio is sensitive to collisional de-excitation but is unlikely to be affected by collisional excitation except for very high densities. The value of the line ratio is 5.6 which is consistent with a PDR of density $n \geq 10^5\,\mathrm{cm}^{-3}$. Burton (1992) finds the data are fitted well by a steady-state PDR with a clumpy density structure with surface filling factors for the gas of 0.3 parts $10^4\,\mathrm{cm}^{-3}$ and 0.7 parts $10^6\,\mathrm{cm}^{-3}$ in the $5'' \times 5''$ beam which was centred on the brightest part of the emission ridge.

5.2.3 Time-Dependent PDRs

The assumption of the PDR being in a steady state, with formation balancing destruction of H_2, may not be correct. The time-scales required for H/H_2 dissociation fronts to reach equilibrium are often long ($t_{eq} = 10^9/n\,\mathrm{yr}$ - Hill & Hollenbach 1978) compared to the turn-on times ($\sim 10^5$ yr for OB-type stars) or lifetimes ($\leq 10^7$ yr OB-type stars) of the UV radiation sources. Also dynamics within clumpy star-forming regions may cause fresh material to become suddenly exposed to UV fields. Goldshmidt & Sternberg (1995) have calculated the time-dependent infrared fluorescent emission-line response of H_2 (for $n = 10^2$–$10^4\,\mathrm{cm}^{-3}$) exposed to UV radiation ($G_0 = 10^0$–10^6) in interstellar clouds. They consider a simplified model where there is one level from which absorption occurs, an electronically excited level and a level which corresponds to the excited rovibrational levels from which the line emission originates.

Figure 5.7 illustrates for low density gas how the total H_2 emission intensity increases linearly with the radiation field for all values of the incident field at early times. It also illustrates how the emission can be orders of magnitude more intense at early times compared to when equilibrium has been established. This is caused by the initial presence of greater column densities of excited H_2 within a UV optical depth of unity compared to the equilibrium case, so that H_2 initially competes more effectively with dust at absorbing UV photons. Hollenbach & Natta (1995) model time-dependent PDRs for higher densities $n = 10^3$–$10^6\,\mathrm{cm}^{-3}$ and UV fluxes $G_0 = 10^3$–10^6 and find that the total H_2 emission is independent of time when self-shielding dominates the UV attenuation ($n/G_0 > 100\,\mathrm{cm}^{-3}$). In the case where dust opacity dominates attenuation ($n/G_0 < 100\,\mathrm{cm}^{-3}$), at early times before the dissociation front has reached an optical depth of unity ($t < t_\sigma$ where $t_\sigma = 7.9 \times 10^6\,G_0^{-1}$ yr) the total infrared emission is constant ($I_0 = 4 \times 10^{-9}\,G_0\,\mathrm{W\,m^{-2}\,sr^{-1}}$) but afterwards decreases to its equilibrium value ($\simeq I_0(t_\sigma/t)$ for $t_\sigma < t < t_{eq}$). Most of the H_2 emission originates from a column density of $N \sim 10^{21}\,\mathrm{cm}^{-2}$ which corresponds to $A_v = 1$ (see Fig. 5.8). The propagation speed of the dissociation front slows with time as molecules reform.

Hollenbach & Natta (1995) make predictions relating n, G_0 and the age of the PDR to the intensity of the 1–0 S(1) line (its fluorescent and thermalised contributions) and the 1–0 S(1)/2–1 S(1) line ratio. Correcting for an extinction of $A_v = 5.7$, the intensities of the 1–0 S(1) and 2–1 S(1)

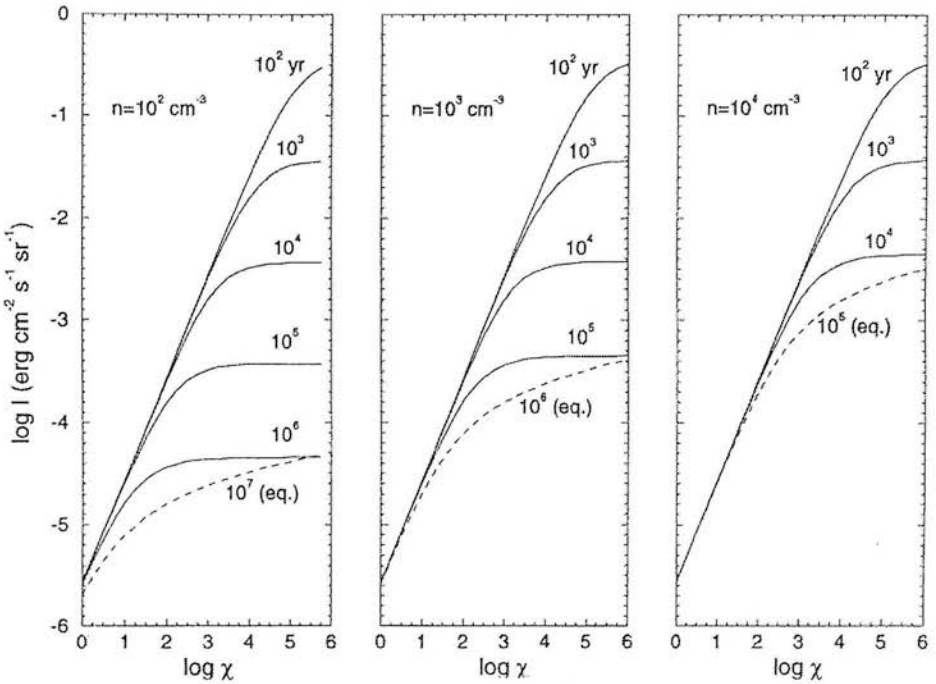

Figure 5.7: Total intensity of H_2 emission as a function of UV intensity (N.B. $\chi \equiv G_0$) at different densities and times since the onset of irradiation, from Goldshmidt & Sternberg (1995). The dashed curves show the intensities after the clouds have reached equilibrium.

lines are 3.0×10^{-7} and $8.8 \times 10^{-8}\,\mathrm{W\,m^{-2}\,sr^{-1}}$ respectively. The 1–0 S(1) line intensity translates to a value of -3.5 on the y-axis of Fig. 5.9. The 2–1 S(1)/1–0 S(1) line ratio is independent of limb brightening and has the value 0.29 which translates to a value of -0.5 on the y-axis of Fig. 5.10. A third diagnostic is the intensity of a purely fluorescent emission line. Any line may be chosen which has a sufficiently high excitation energy such that the energy level from which it originates is not collisionally populated by hot gas. Fig. 5.11 shows the fluorescent contribution of the 1–0 S(1) line to which the intensity of any fluorescent line may be scaled. The 5–2 S(5) line was chosen as a diagnostic. This line arises from a high excitation level (30,063 K) and should therefore be free from the effects of thermal excitation. It has a high signal to noise ($\simeq 13$), is uncontaminated by sky emission lines and fits in well with the other $v = 5$ levels (see Fig. E.9). Correcting for an extinction of $A_v = 5.7$, it has an intensity of $1.8 \times 10^{-8}\,\mathrm{W\,m^{-2}\,sr^{-1}}$. If this line intensity is due to pure fluorescence then it should be 10.3 times fainter than 1–0 S(1) line which corresponds to a y-axis value of -3.7 on Fig. 5.11.

These diagrams may be used to determine whether the large surface brightness of the PDR is due to a projection effect, time dependence or a combination, while constraining n and G_0. It has been shown that the gas is dense enough to suffer collisional redistribution of the energy level populations *i.e.* $n \geq 10^5\,\mathrm{cm^{-3}}$. Figure 5.5 indicates that for $G_0 >$ a few 10^3 a 1–0 S(1)/2–1 S(1) flux line ratio of 3.4 indicates that most of the gas we see has a density $n < 10^6\,\mathrm{cm^{-3}}$. The following analysis uses Figs. 5.9–5.11 and assumes a density $n \sim 10^5$ (consistent with DB and BHT) to constrain the models of the PDR. DB require a projection factor of 5 to explain the brightness of their best fit (steady-state) model for NGC 2023 ($G_0 = 5000$, $n = 10^5\,\mathrm{cm^{-3}}$). Figure 5.10 shows that in a steady-state model G_0 must lie within the limits $10^3 < G_0 < 10^4$ (independent of any projection factor). Figure 5.11 shows that in the steady-state case (or $t > 10,000\,\mathrm{yr}$) a projection factor no larger than 3 can explain the observed brightness (for G_0 close to 10^3 or a factor no larger than 2, if G_0 is closer to 10^4). Time dependence may therefore provide a contribution to the excess surface brightness. Figure 5.9 shows that with any projection factor the 1–0 S(1) brightness could be explained by a young PDR, but to constrain the age an accurate estimate of G_0 is required with Fig. 5.10 replotted at the appropriate value of G_0. The lines used in these predictions are very bright with uncertainties of no more than 10% in their fluxes. These uncertainties may shift their y-axis values by 0.05 in the Figs. 5.9 and 5.11 or by 0.07 for the line ratio in Fig.5.10. These shifts however are small and do not affect the conclusions of this section.

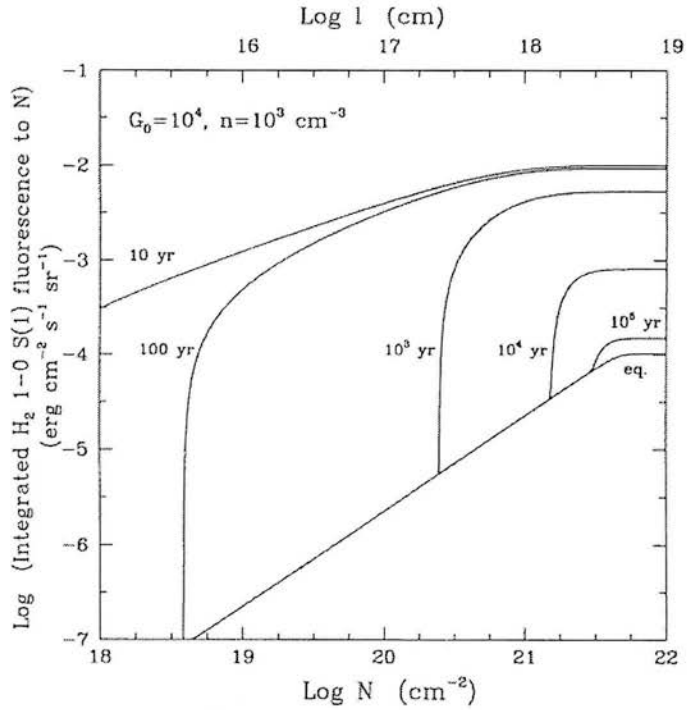

Figure 5.8: Cumulative fluorescent 1–0 S(1) intensity shown as a function of the gas column density N shown at various times for a case where $G_0 = 10^4$, $n = 10^3\,\mathrm{cm}^{-3}$ taken from Hollenbach & Natta (1995).

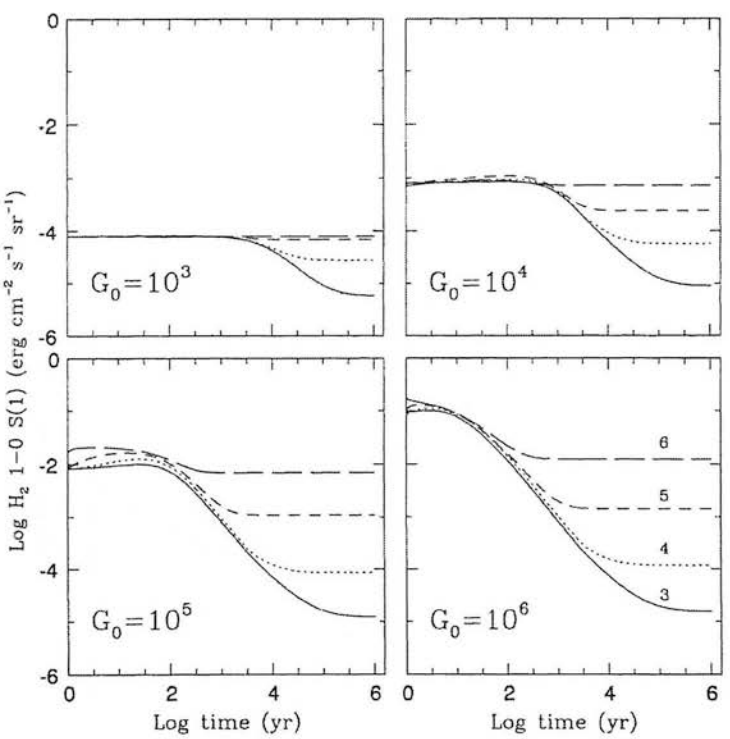

Figure 5.9: Total intensity of 1–0 S(1) line as a function of time taken from Hollenbach & Natta (1995). The solid lines are for $n = 10^3\,\mathrm{cm}^{-3}$, the dotted lines for $n = 10^4\,\mathrm{cm}^{-3}$, the short-dashed lines for $n = 10^5\,\mathrm{cm}^{-3}$, and the long-dashed lines for $n = 10^6\,\mathrm{cm}^{-3}$.

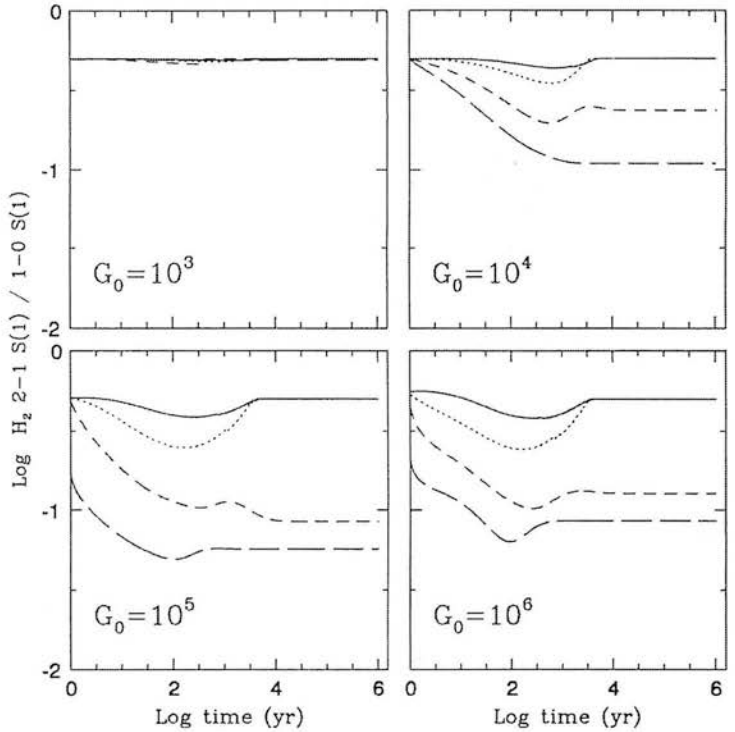

Figure 5.10: Ratio of the 2–1 S(1) to the 1–0 S(1) line intensities as a function of time taken from Hollenbach & Natta (1995). Lines denote values of n as in Fig. 5.9. A ratio of 0.5 indicates pure fluorescence, lower ratios indicate contributions from thermal sources.

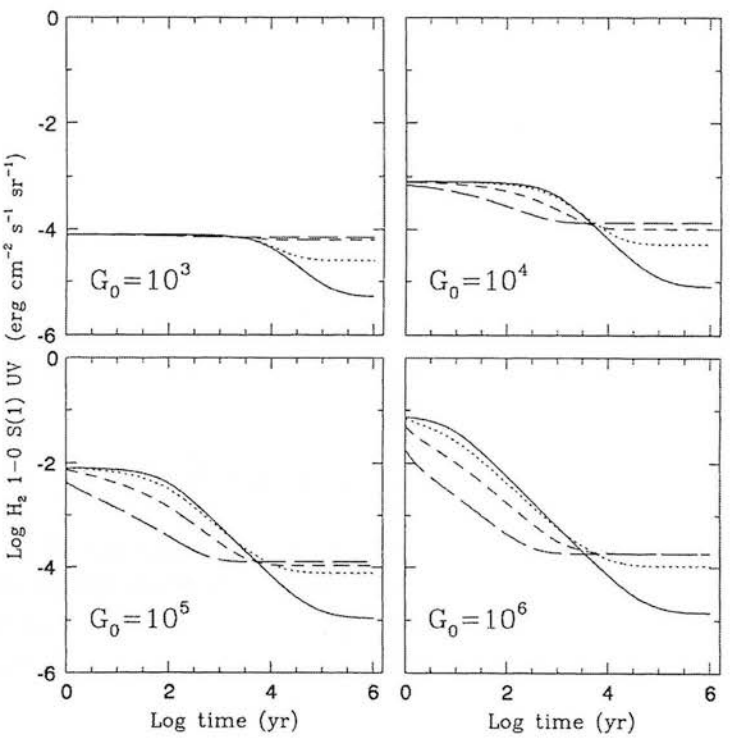

Figure 5.11: Fluorescent component of the 1–0 S(1) line, for comparison with pure fluorescent lines from high excitation levels - taken from Hollenbach & Natta (1995). Lines denote values of n as in Fig. 5.9.

5.2.4 Summary

The observed H_2 line emission from the PDR observed in NGC 2023 is very likely to be brightened by a projection effect. However, it is unlikely to increase the surfaces brightness by a factor of more than a few and it is very possible that the excess brightness is also contributed to by large column densities of excited H_2 in a dissociation front which has not yet settled to equilibrium. The most recent steady-state models (DB) can explain the line fluxes fairly well using a projection factor of 5. Time-dependent models (HN) can account for the large surface brightness and the thermalised line ratios without introducing limb brightening, however an accurate estimate of the radiation field is required to constrain the age of the PDR. A comparison of the entire dataset with the fluorescent model #14 of BvD confirms that not only only are the column densities of excited H_2 too great to be explained by face-on, steady-state PDR models but that collisional processes are important and therefore the density must be greater than $n = 10^4\,\mathrm{cm}^{-3}$. The observed excess in the $v = 1$ level can be explained by thermalised gas at $\sim 800\,\mathrm{K}$ contributing to the emission. UV fluxes of $G_0 = 3\text{–}5 \times 10^3$ have been inferred from the spectral type of the exciting source and the geometry of the region (BvD; DB). The time-dependent models of HN also require an incident UV field of $10^3 < G_0 < 10^4$. Adopting a density of $n = 10^5\,\mathrm{cm}^{-3}$ and incident UV field of $G_0 = 5 \times 10^3$ the ratio $n/G_0 = 20\,\mathrm{cm}^{-3}$ is small enough to ensure that self-shielding is not a dominant effect and dust grains primarily attenuate the UV flux. Therefore the surface brightness along the southern emission ridge is fairly insensitive to changes in the UV field and variations reflect changes in the geometry and the density of the PDR, saturating in brightness at the critical density $n_{cr} \sim 10^5\,\mathrm{cm}^{-3}$.

5.3 Extinction

Figure 4.16 shows that in the absence of any dust extinction correction the ratio of the intensity of the infrared to far-red datasets is about 5.6. The following analysis shows that this attenuation of the far-red flux is very probably due to intervening material this side of the PDR and not due to internal reddening within the PDR itself.

When radiation of intensity I_0 at a frequency ν, passes through material with an optical depth τ_ν it is attenuated so that the emerging radiation has an intensity,

$$I = I_0 e^{-\tau_\nu}. \tag{5.26}$$

If one considers the far-red dataset to be centred around a wavelength of $0.8\,\mu$m (I band) and the infrared dataset at an average wavelength of $2.0\,\mu$m (K band) then, assuming an extinction law $A_\lambda \propto \lambda^{-1.7}$ (see Section 4.3.2), the attenuation experienced by the far-red data corresponds to an optical depth, τ_I, which is 4.7 times that of the infrared data, τ_K. Assuming the intensity ratio of 5.6 is due to foreground dust extinction one can calculate the extinction from the ratio of the datasets using equation (5.26) to give,

$$\frac{I_K}{I_I} = e^{-(\tau_K - \tau_I)} = e^{3.7\tau_K} = 5.6 \tag{5.27}$$

and therefore $\tau_K = 0.46$, equivalent to $A_v = 4.5$ which is close to the adopted value of 5.7 derived from minimising the scatter on the column density diagrams in Chapter 4.

Alternatively if one assumes that the extinction occurs internally within the region from which the emission arises then intensity of the emerging radiation is given by,

$$I = I_0 \left(\frac{1 - e^{-\tau_\nu}}{\tau_\nu} \right) \tag{5.28}$$

where I_0 is the source function integrated over the cloud, and thus is the intensity which would be

observed were there no attenuation[9]. In this case,

$$\frac{I_K}{I_I} = \frac{(1-e^{-\tau_K})}{(1-e^{-\tau_I})}\frac{\tau_I}{\tau_K} = \frac{(1-e^{-\tau_K})}{(1-e^{-4.7\tau_K})} \times 4.7. = 5.6 \tag{5.29}$$

There is no real solution for τ_K in equation (5.29) or more generally in any situation where the ratio of intensities is greater than the ratio of optical depths for data collected at long and shorter wavelengths respectively. The interpretation follows that there is a cloud in front of the PDR which is responsible for the majority of the obscuration.

5.4 Ortho/Para Abundance Ratio

The value of the ortho/para ratio (see Section 2.2) is initially set on molecule formation and depends on the formation process, the local temperature on the surface of the dust grain and the duration the molecule resides before it evaporates (Tielens & Allamandola 1987). Its value can only be altered by a limited number of conversion processes, such as spin exchange reactions on the surface of dust grains or collisions with H and H^+ (Dalgarno et al. 1973; Flower & Watt 1984)[10]. All other radiative processes and collisional reactions that the molecule undergoes are quadrupole, thus only changing the rotational level by an even number. Therefore in environments which are not in thermal equilibrium the ratio may be used to provide an insight into the formation mechanism and the processes which convert the ratio. In gas which has reached thermal equilibrium the ratio reflects the temperature of the gas (see Fig. 5.12) or if gas-grain interactions dominate then the o/p ratio will be determined by the grain temperature. The lowest rovibrational state ($v = 0, J = 0$) is a para state and the next excited state ($v = 0, J = 1$) occurs at 170 K above ground and is an ortho state. Therefore for gas in thermal equilibrium a low temperature is reflected by a low o/p ratio and a high ratio reflects a high temperature (*i.e.* $\geq$ 250 K). The spin degeneracy of the H_2 states is given by $2I + 1$ (see Section 2.1) where I is 1 for the ortho states and 0 for the para states so for hot gas the ratio tends towards 3. Since H_2 formation is an exothermic process which releases 4.5 eV of binding energy (see Section 2.4), if the molecule leaves the grain surface immediately after formation one would also expect the subsequent H_2 to display a high ortho/para ratio. It is generally thought that molecular hydrogen leaves the grain surface quickly after formation with an o/p ratio of 3 (Draine & Bertoldi 1996, adopt a value of 2.78) and that the gas temperature determines the thermalised ratio (Tielens & Allamandola 1987). Since the temperatures in PDRs are high one might expect to find an ortho/para ratio of 3. However observations of PDRs provide consistently low values ranging from 1.7–2.4 (Hoban et al. 1991; Chrysostomou et al. 1993; Ramsay et al. 1993; Ramsay Howat et al. 1997). In this case it is reasonable to expect a low ortho/para ratio in the $v = 1$ level to indicate ortho $\rightarrow$ para conversion since this level is most likely to thermalise first and the ratio will reflect the local temperature. In comparison, the o/p ratio in the $v > 1$ levels is more likely to represent the H_2 formation temperature or the temperature of the gas before it was exposed to UV radiation.

Interpretation of the observed ortho/para ratio, is complicated by the fact that the ratio is derived from the small fraction of the H_2 which is excited within the PDR. This H_2 may be subject to self-shielding which can affect the o/p ratio of excited H_2. To understand how self-shielding affects the observed ratio it is useful to consider the limiting case of a cloud of molecular hydrogen which contains no dust. Neglecting line overlap, the ortho and para modifications of hydrogen will absorb UV radiation at different frequencies until all the absorption lines have saturated. For an incident UV field where the flux distribution is constant across frequency, the same number of photons will be absorbed by the ortho states as by the para states and therefore in this photon limited case the observed o/p ratio will be unity. Where dust dominates the opacity, the UV field can be approximated by a flat frequency distribution throughout the cloud

[9]The emission arising from material experiencing internal extinction is $I = \int_0^\tau S_\nu e^{-\tau'}\, d\tau'$ where S_ν is the source function. Assuming S_ν is independent of τ the integral becomes $I = S_\nu(1-e^{-\tau})$ where the source function integrated over the cloud is $I_0 = S_\nu\tau$.

[10]The H^+ is produced by cosmic ray ionisation and by photodissociation and photoionisation out of the $v \geq 3$ levels (BvD).

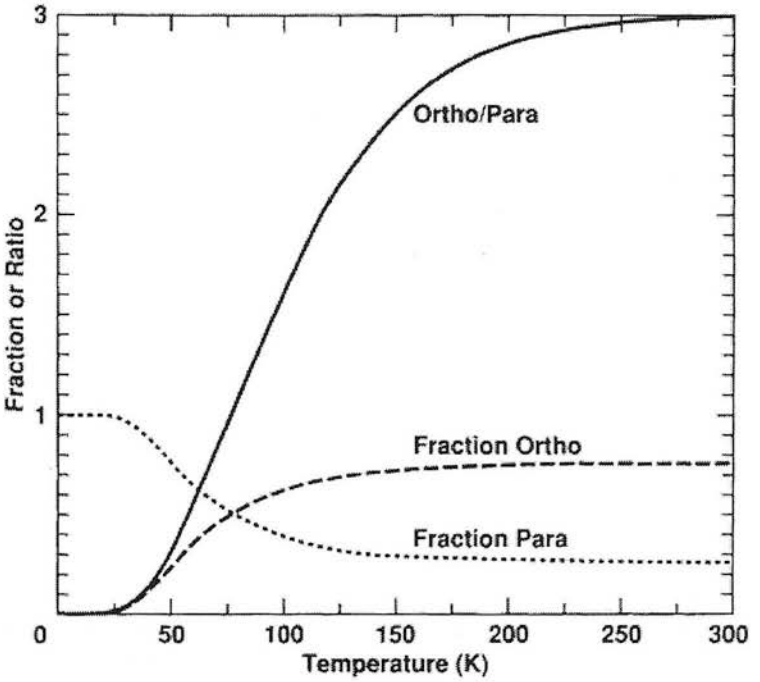

Figure 5.12: The ortho/para ratio as a function of temperature for gas in thermal equilibrium - taken from Burton et al. (1992b).

and thus the observed o/p ratio will reflect the actual abundance ratio throughout the cloud. A competing process may however, increase the observed o/p ratio. DB find from their models that for $G_0 = 10^5, n = 10^6\,\mathrm{cm}^{-3}$ and $T = 200\,\mathrm{K}$ the ratio is 4.3. A possible explanation might be that the observed large value may be due to the greater ability of ortho-H_2 to self-shield in which case the dissociation front for ortho-H_2 will occur closer to the surface. Dust will disproportionately dominate UV attenuation for the para-H_2 and thus there will be less vibrationally excited para-H_2.[11] Figure 4.12 shows the o/p ratio derived from 3 adjacent J-levels within each vibrational level and for some vJ levels (*e.g.* $v = 4$) it appears there is an o/p ratio greater than 3. However, the uncertainties on these values are large, bringing the lower limits to these values all within an o/p ratio of less than 3. In any case, it is not obvious what mechanism would raise the o/p ratio at high J and depress its value at low J, for the $v = 4$ level.

As discussed above, based on the 1–0 S(1) line intensity and 1–0 S(1)/2–1 S(1) flux ratios, the steady-state and time-dependent PDR models indicate the density of the emission ridge is $n \sim 10^5\,\mathrm{cm}^{-3}$ and the incident radiation field is of strength $G_0 \simeq 5000$. These diagnostics are independent of the ortho/para ratio. The ratio which determines the effectiveness of self-shielding, in this case, has a low value ($n/G_0 \sim 20\,\mathrm{cm}^{-3}$). Since self-shielding is not the dominant source of UV attenuation (*i.e.* for self-shielding: $n/G_0 \gg 40\,\mathrm{cm}^{-3}$ - BHT, $n/G_0 > 100\,\mathrm{cm}^{-3}$ - HN; Jura 1975) the ortho and para dissociation fronts are most likely coincident and the observed ortho/para ratio reflects the true ortho/para ratio within the PDR.

Burton (1993) derives an ortho/para ratio of 2.1 ± 0.2 from the infrared data included in the results of this thesis (see Section 4.1.6). The ortho/para ratio derived from the overall dataset presented in this thesis is 2.0 ± 0.2 and does not appear to vary systematically with energy level. As can be seen from Fig. 4.12 the vibrational levels with the most data indicate a ratio of 2.2 which is included within the uncertainties. The o/p ratio of the $v = 1$ level is likely to thermalise before the higher v-levels so one would expect to see a high o/p ratio in this level if the there was signification collisional excitation. The measured value is $\simeq 2.3 \pm 0.1$ (see Table 4.4). Although

[11] If the PDR width is small (*i.e.* $A_v \leq 2$) the para-H_2 may not self-shield and this will be observed as a high ortho/para ratio.

this value is high it does not rise significantly above that of the other v-levels and on its own does not prove conclusive evidence for collisional excitation.

The observed ortho/para ratio is also sensitive to the photoabsorption rates of the two species, which depend on the UV-absorption cross sections and IR-transition rates (see Hasegawa 1989, for a discussion). However it is not obvious how this affects the observed value. The models of Sternberg & Dalgarno (1989) and Black & van Dishoeck (1987) are able to reproduce low o/p ratios ($\sim$ 1.8) independent of any formation mechanism. In contrast to this the more recent models of Draine & Bertoldi (1996) can produce o/p ratios greater than 3. Other factors which may affect the ortho/para ratio include the dynamics and clumpiness of the PDR and whether fresh material from within the clumps gets exposed to the UV field. Chrysostomou et al. (1993) considered clumps which were stripped of their warm surface layers by the advancing dissociation front and which revealed colder H_2 which could explain the observed low ortho/para ratios. Since the PDR emission seems to originate from hot gas $\sim$ 1000 K one might expect the o/p ratio to reflect a high temperature value of close to 3 if it had enough time to thermalise. However the $v = 1$ level is clearly affected by collisional processes and if collisional excitation dominates its population distribution then the thermalised component of the gas can be described by a temperature of $\sim$ 800 K (Section 5.2.1.1). The o/p ratio for the $v = 1$ level does not reflect this high temperature which leaves the implication that the emission is originating from a dissociation front which is advancing into the molecular cloud and that fresh material with a low ortho/para ratio typical of the low temperature gas is being observed. However the effects of collisional de-excitation into the $v = 1$ level need to be fully understood before this can be proven.

To destroy the equilibrium between the formation and destruction of H_2 the time-scale for the formation must be longer than the time it takes for material to leave the PDR or equivalently for the dissociation front to pass through. The time-scale for reformation can be estimated from

$$\tau = \frac{1}{Rn} = \frac{1}{3 \times 10^{-17} n} \text{ s}. \tag{5.30}$$

The crossing distance $A_v = 1$ for gas of density $n = 10^5\,\text{cm}^{-3}$ is $\sim 10^{16}$ cm. Therefore the PDR front must propagate into the cloud at a speed of $> 1\,\text{km s}^{-1}$ to destroy the chemical equilibrium. Chrysostomou et al. (1993) find that to preserve the o/p ratios typical of cooler gas, at these densities and UV field strengths the dissociation front must advance into the cloud at speeds of greater than $0.1\,\text{km s}^{-1}$. This suggests that if the large surface brightness of NGC 2023 can be explained by time-dependent emission the PDR front would have sufficient speed to unearth cold gas which would display a low o/p ratio.

In summary, a variety of factors can effect the observed ortho/para ratio and detailed models are required to disentangle the dominant contributions from the less important effects. A low o/p ratio is characteristic of UV irradiated gas but whether the ratio is due to cold H_2 recently exposed to UV photons as the dissociation front passes into the cloud or whether it is due to a difference in the absorption rates of the ortho and para hydrogen species is uncertain. However the explanation of an advancing PDR front appears to be consistent with a low ortho/para ratio.

Chapter 6

Conclusions

This thesis is devoted to the study of photodissociation regions in the context of the star-forming environment. Since the first direct detection of molecular hydrogen in the 1970s (*e.g.* Carruthers 1970; Rogerson et al. 1973) many theoretical investigations have been made into the behaviour of H_2 in the interstellar medium (*e.g.* Field et al. 1966; Stecher & Williams 1967; Black & Dalgarno 1976; Tielens & Hollenbach 1985; Black & van Dishoeck 1987; Sternberg & Dalgarno 1989; Burton, Hollenbach & Tielens 1990; Hollenbach & Natta 1995; Draine & Bertoldi 1996). Advances in detector technology have closely followed in the wake of these studies to provide a means to test these predictions. However observations of molecular hydrogen require excellent observing conditions followed by careful and time consuming data reduction to pick out the faint emission lines which span the energy levels required to address the topics of investigation. As a result most PDR models remain largely untested by observational evidence. The work in this thesis has been based around observations of the reflection nebula NGC 2023 where the first detections of the emission spectrum of fluorescent H_2 were made (Gatley et al. 1987; Hasegawa et al. 1987). This bright and nearby object is well studied and an obvious candidate to test the predictions of PDR theory.

New observations have been made of the H_2 emission spectrum of the reflection nebula NGC 2023. Infrared and far-red spectra are presented; these were taken from the photodissociation region 80″ south of the illuminating star HD 37903. The observations were carefully reduced to reveal the very faint quadrupole emission lines arising from the rovibrational states of molecular hydrogen. Accurate flux measurements have been made of over ninety emission lines. These data have been compared to published infrared and far-red observations of the same bright ridge of molecular gas. These five sets of observations were then carefully combined to form the most extensive dataset of H_2 column densities yet compiled for any photodissociation region. 81 column densities are presented and analysed for vibrational levels spanning the range $v = 1$–12 and energy levels 6,000–50,000 K. In theory, when the column densities of UV-excited gas are divided by their statistical weights and plotted against excitation energy the vibrational levels should each be represented by a separate smooth curve. In practice, observational and physical effects cause these data points to be scattered around smooth curves predicted by models. Choosing parameters to minimise the scatter can divulge physical information. To approximate the observed data to the theoretical curves an ortho/para ratio must be chosen. Since the gas is not in thermal equilibrium at a high temperature, this value will not be equal to the ratio of statistical weights due to the spin degeneracy of the ortho and para species, which is 3. In addition to choosing this value an observational parameter must be determined which also affects the scatter of data points on the diagram. Since the column densities are derived from numerous emission lines from a wide wavelength range, an accurate value must be calculated for the reddening correction.

An extinction of $A_v = 5.7 \pm 1.0$ and ortho/para abundance ratio of 2.0 ± 0.2 have been inferred from minimising the χ^2 deviation of the data from smoothed model fits to the vibrational levels. The ortho/para ratio does not exhibit any systematic trend across the vibrational levels. The extinction is found to be surprisingly large; previous estimates were in the range $A_v = 2$–3 (Burton 1993; Draine & Bertoldi 1996). The opacity is interpreted to be due to dust extinction from

foreground material as opposed to internal reddening within the PDR. The exciting star HD 37903 is on the near side of the dark cloud L1630 (see Chapter 3). Much of the cluster to which it belongs suffers considerable extinction which may be due to the intrinsic clumpiness of NGC 2023 or the cluster being partially embedded in the background molecular cloud. HD 37903 itself is only obscured by an $A_v \sim 1$; therefore it seems likely that the intervening material is local to the PDR and possibly part of the 80″ radius shell of material observed by Gatley et al. (1987). The implications of the ortho/para ratio are discussed at length in Chapter 5 and although there are a variety of factors which affect the ratio it is suggested the low value is due to the dissociation front exciting cold, fresh material as it advances into the molecular cloud.

H_2 line intensities are found to be an order of magnitude larger than can be explained by 'face-on' steady-state PDR models (*e.g.* Black & van Dishoeck 1987). Limb brightening is likely to contribute to this brightness, however steady-state models have difficulty explaining the line fluxes arising from the vibrationally excited levels (*e.g.* Draine & Bertoldi 1996). Non-equilibrium photodissociation fronts early on in the PDRs life have large column densities of excited molecular hydrogen. Therefore time-dependent PDR models can account for the large surface brightness and the thermalised line ratios without introducing limb brightening (Hollenbach & Natta 1995). The observations are consistent with both steady-state and time-dependent models of density $n \sim 10^5\,\mathrm{cm}^{-3}$ illuminated by an ultraviolet radiation field $\simeq 5 \times 10^3$ times the Habing (1968) background interstellar field. This implies that self-shielding is not a dominant effect and that dust grains primarily attenuate the UV flux. Therefore the surface brightness along the emission ridge is relatively insensitive to changes in the UV field and any variations reflect changes in the geometry and the density of the PDR. A comparison of the entire dataset with a pure fluorescent PDR model (Black & van Dishoeck model #14) shows many discrepancies. An intriguing trend within the vibrational levels is apparent where column densities increase with rotational level. There is also an indication of this trend levelling out and decreasing for very high rotational levels. This may be due to the relative variations of the critical densities within the vibrational levels. The $v = 1$ level exhibits populations with increasingly large excesses for the lowest energy states. This is consistent with thermal excitation and by assigning a Boltzmann energy distribution the presence of a gas component at $\sim 800\,\mathrm{K}$ can be inferred. However, gas at this high temperature in local thermodynamic equilibrium is expected to have an ortho/para ratio of 3. The $v = 1$ level is likely to thermalise first by being populated by collisional de-excitations out of high vJ states and by thermal excitation. At high temperatures this would preferentially raise the ortho/para ratio for this level to its equilibrium value through spin exchange reactions with atomic hydrogen and protons. The measured ratio for the $v = 1$ level is 2.3 which, although high, is not significantly greater than the other v-levels (see Table 4.4). An explanation of a travelling PDR front exciting cold molecular gas as it passes through the cloud is consistent with this low ratio.

One of the most surprising findings of this thesis is that the extinction towards the H_2 emission ridge is so large compared to previous estimates. This result has important consequences on interpreting the geometry of the region. Since the measured extinction $A_v = 5.7$ differs greatly from previously estimated values it is prudent to review the evidence for the measurement and explore what results would change were the extinction much lower.

Evidence for $A_v = 5.7$: The measured extinction depends on the accuracy of the infrared and far-red line flux measurements. The infrared flux measurements from the three datasets agree well with each other (the CGS4 and UKT9 datasets have an overall calibration to within 20% of the CGS2 dataset with reference to the IRCAM3 1–0 S(1) and 2.1 μm images). Therefore the accuracy of the far-red calibration is critical, since it provides the broad wavelength baseline from which the most precise extinction estimates can be made. The flux measurements of the far-red dataset were taken at 4 grating positions. Three of these grating positions were observed on the same night and the resulting line fluxes agree very well, there being no discernible difference between the continua of each spectrum and the fluxes of the lines in the overlap regions match to within 20%. The fourth grating position was taken on the next night through intermittent patches of cloud and required a normalisation factor of 0.5 to match the rest of the data. The same data reduction procedures were carried out for each grating position. The data reduction procedure has been checked and independently verified by a measurement of the same ridge of gas observed using the TEK chip at the AAT. The CI 8729 Å line is the brightest line detected during the far-red observations and the

measured flux is found to be consistent with that derived from unpublished data to within 20% (Mike Burton, private communication).

Evidence for $A_v \leq 3$: Burton (1993) derives an extinction to the H_2 emission ridge of $A_v = 3$ using lines with common upper state energy levels determined from the CGS2 dataset taken in the J, H and K bands. Draine & Bertoldi (1996) assume an extinction of $A_v = 2$ from the same data. The pairs of lines available for this calculation are listed below with the extinction calculated for each case (see Section 4.3.2 for details).

Line 1	$\lambda(\mu m)$	Line 2	$\lambda(\mu m)$	$\delta\lambda(\mu m)$	A_v	δA_v
1 – 0 S(1)	2.1218	1 – 0 Q(3)	2.4237	0.30	-0.5	15
1 – 0 S(2)	2.0338	1 – 0 Q(4)	2.4375	0.40	8.1	21
2 – 0 Q(1)	1.2383	2 – 0 O(3)	1.3354	0.10	15	27
2 – 0 S(1)	1.1622	2 – 0 Q(3)	1.2473	0.09	8.8	28
2 – 0 S(1)	1.1622	2 – 1 S(1)	2.2477	1.09	3.3	3.6
2 – 0 Q(3)	1.2473	2 – 1 S(1)	2.2477	1.00	2.2	4.3
2 – 0 S(2)	1.1382	2 – 1 S(2)	2.1542	1.02	-0.4	4.0
3 – 1 S(1)	1.2330	3 – 2 S(1)	2.3864	1.15	2.7	4.9
6 – 4 S(0)	1.5369	6 – 4 Q(2)	1.6074	0.07	-39	137

The last column shows the 1-σ errors associated with each extinction value (see Appendix D). As can be seen from the list only four pairs of lines are separated by enough wavelength coverage ($\delta\lambda > 1\,\mu$m) to allow reasonable extinction estimates to be made. Even so, the uncertainties are large. While the weighted mean is $A_v = 2.1 \pm 0.7$, an inspection of the values for A_v in the list indicates that an uncertainty of ± 2 is more appropriate which does not rule out a high extinction.

Consequences of a low A_v : If the extinction has been over estimated then a calibration error exists in the far-red dataset and this data would be required to be scaled up to make it consistent with the infrared line fluxes. Since applying a reddening correction has a very similar effect to simply scaling up the dataset the overall shape of the column density plot would be largely unaffected. However, the overall brightness of the PDR would be decreased. Using Fig. 4.16 one can see that adopting an extinction of $A_v = 2.1$ the least scatter on a column density plot occurs for a scale factor of $\simeq 3.2$. Therefore before applying the reddening correction the far-red data is assumed to be 3.2 times brighter and the infrared data remains the same. After correcting for the low extinction value the 1–0 S(1) line is 70% as bright compared to its value after correcting for $A_v = 5.7$. The overall dataset is roughly two thirds as bright compared to the dataset when assuming the high extinction. The minimum χ^2 ortho/para ratio then becomes 2.1. The diagnostics which are used to discuss the thermalisation and time-dependence of the PDR are the 5–2 S(5) line flux and the 1–0 S(1)/2–1 S(1) line ratio. Correcting for $A_v = 2.1$ the 5–2 S(5) line is 75% dimmer (compared to the high extinction value) and the 1–0 S(1)/2–1 S(1) line ratio changes by less than a few percent. Therefore the conclusions of Chapter 5 concerning the gas density, incident radiation field and reasons behind the large surface brightness of the PDR remain unaffected. The temperature of the hot, thermalised gas component was estimated from the shape of the $v = 1$ distribution by fitting a straight line to the distribution of points in $\log_e$ space, once the pure fluorescent component had been removed. Applying a low extinction value reduces the overall observed H_2^* column density but the estimated temperature is not affected since it depends on the gradient of the line (see Section 5.2.1.2), not the overall column density. Thus the estimated temperature, density, radiation field and ortho/para ratio are insensitive to the assumed extinction. The discussion regarding the high surface brightness of the PDR is also unchanged by adopting the low extinction value of Draine & Bertoldi (1996) or Burton (1993). Therefore the main conclusions of this thesis appear robust even in view of possible uncertainties in the assumed extinction to NGC 2023.

This work has exploited recent advances in detector technology. Further observational work will determine whether the trends mentioned above are due to collisional effects, from comparisons with observations of low density PDRs. Mid-infrared observations of the low-excitation $v = 0$ energy levels, which are most easily thermalised, will offer a better understanding of the temperature structure within the PDR and help discern how much of the large surface brightness is due to limb brightening or time-dependent emission which predicts high temperature spikes early on

in the PDRs life (Hollenbach & Natta 1995). Modelling the southern emission ridge in NGC 2023 and including the collision rates coefficients of Martin & Mandy (1995) is the immediate corollary to this work and should answer the question of whether the discrepancies between the pure fluorescent model and the observed trends in the data are due to collisional processes or effects as yet unaccounted for. The sensitivity of the population distribution in the $v = 1$ level to collisional de-excitation can then be compared to that of a thermal Boltzmann distribution. If the rotational levels of the $v = 1$ level are best described by a high temperature, regardless of collisional de-excitation then this will constrain explanations of the ortho/para ratio within that level and help determine whether the low observed ratio (2.3) is due to time-dependent PDR emission. This modelling shall coincide with comparisons of the data to the static PDR models of Draine & Bertoldi (1996) which contain the most up-to-date transition rate parameters and accurate radiative transfer for molecular hydrogen. The same UV photons which excite molecular hydrogen also excite atomic carbon. Bright CI lines at 8729 Å and 9852 Å provide powerful diagnostics of PDR emission. Data from NGC 2023 are already under investigation to study the correlation of the 8729 Å CI line with H_2 emission. The subject of coupled photodissociation and ionisation fronts has recently been investigated by Bertoldi & Draine (1996). PDRs within Orion, M17 and NGC 7027, of which we have several hours of CGS4 data, may be best described by these models however predictions which can be tested by observations are currently very limited. The work included in this thesis has used present detector technology pushed to the extreme limits of sensitivity. Within the next decade a new generation of instruments such as CGS6 on UKIRT and the Gemini Near-Infrared Spectrograph will permit detections of an order of magnitude greater sensitivity. This will allow new related areas to be investigated such as detecting the H_2^+ molecule for the first time. This ion occurs at the surface of PDRs and may be detectable in coupled photodissociation/ionisation fronts (Bertoldi & Draine 1996). Molecular clouds which are irradiated by X-ray sources have lately been the subject of theoretical investigation (Maloney, Hollenbach & Tielens 1996; Tiné et al. 1997). These regions (XDRs) share similarities with PDRs with H_2 line emission and 158 μm CII and 63 μm OI cooling lines however, they may be distinguished by their large 1–0 S(1)/2–1 S(1) lines ratios ($\simeq$ 15 - Tiné et al. 1997). Observational studies of XDRs would be useful for studying the environments of molecular clouds containing embedded X-ray sources such as massive stars, young stellar objects with X-ray chromospheres, X-ray binaries or accreting compact objects. Other sources which would benefit from observational investigations and development of H_2 diagnostics include supernova remnants, fast shocks and active galactic nuclei.

References

Abgrall H., Roueff E., 1989, A&AS, 79, 313

Abgrall H., Le Bourlot J., Pineau des Forêts G., Roueff E., Flower D. R., Heck L., 1992, A&A, 253, 525

Allison A. C., Dalgarno A., 1970, Atomic Data, 1, 289

Bally J., Lada C. J., 1983, ApJ, 265, 824

Bennett C. L. et al., 1994, ApJ, 434, 587

Barlow M. J., Silk J., 1976, ApJ, 207, 131

Bertoldi F., Draine B. T., 1996, ApJ, 458, 222

Bertoldi F., McKee C. F., 1992, ApJ, 395, 140

Black J. H., Dalgarno A., 1973, ApJ, 184, L101

Black J. H., Dalgarno A., 1976, ApJ, 203, 132

Black J. H., van Dishoeck E. F., 1987, ApJ, 322, 412

Blais N. C., Truhlar D. G., 1982, ApJ, 258, L79

Blitz L., Thaddeus P., 1980, ApJ, 241, 676

Brand P. W. J. L., 1996, Private Communication

Brand P. W. J. L., 1997, Private Communication

Brand P. W. J. L., Moorhouse A., Burton M. G., Geballe T. R., Bird M., Wade R., 1988, ApJ, 344, L103

Burton M. G., 1992, Aust. J. Phys., 45, 463

Burton M. G., 1993, Publ. Astron. Soc. Aust., 10, 322

Burton M. G., Moorhouse A., Brand P. W. J. L., Roche P. F., Geballe T. R., 1989, in Tielens A. G. G. M., Allamandola L. J., eds, Proc. IAU Symp. 135 NASA CP-3036, Interstellar Dust, NASA, Washington D. C., p. 87

Burton M. G., Geballe T. R., Brand P. W. J. L., Moorhouse A., 1990a, ApJ, 352, 625

Burton M. G., Hollenbach D. J., Tielens A. G. G. M., 1990b, ApJ, 365, 620

Burton M. G., Bulmer M., Moorhouse A., Geballe T. R., Brand P. W. J. L., 1992a, MNRAS, 257, 1P

Burton M. G., Hollenbach D. J., Tielens A. G. G. M., 1992b, ApJ, 399, 563

Burton M. G., Howe J. E., Geballe T. R., Brand P. W. J. L., 1997, Publ. Astron. Soc. Aust., in press

Burton W. B., 1976, ARA&A, 14, 275

Buss R. H., Jr., Allen M., McCandliss S., Kruk J., Liu J.-C., Brown T., 1994, ApJ, 430, 630

Carruthers G., 1970, ApJ, 161, L81

Chapman A. R., Beard S. M., Mountain C. M., Pettie D. G., Pickup D. A., Wade R., 1990, in Crawford D. L., ed, Proc. SPIE - Int. Soc. Opt. Eng. 1235, Instrumentation in Astronomy VII, Bellingham, WA, p. 34

Chrysostomou A., Brand P. W. J. L., Burton M. G., Moorhouse A., 1993, MNRAS, 265, 329

Currie M. J., 1995, Kappa User's Guide, Starlink User Note 95.9

de Boer K. S., 1983, A&A, 125, 258

Dabrowski I., 1984, Can. J. Phys., 62, 1639

Dabrowski I., Herzberg G., 1974, Can. J. Phys., 52, 1110

Dalgarno A., Black J. H., Weisheit J. C., 1973, Astrophys. Lett., 14, 77

Dalgarno A., Stephens T. L., 1970, ApJ, 160, L107

Daly P. N., 1995, Portable-CGS4DR CGS4 Data Reduction User's Guide, Starlink User Note 27.4, p. 11

DePoy D. L., Lada E. A., Gatley I., Probst R., 1990, ApJ, 356, L55
Dove J. E., Mandy M. E., 1986, ApJ, 311, L93
Draine B. T., 1978, ApJS, 36, 595
Draine B. T., 1989, in Kaldeich, ed, Proc. 22nd Eslab Symp. ESA SP-290, Infrared Spectroscopy in Astronomy, ESA Pub. Div., Noordwijk, p. 93
Draine B. T., Anderson N., 1985, ApJ, 292, 494
Draine B. T., Bertoldi F., 1996, ApJ, 468, 269
Duley W. W., 1996, MNRAS, 279, 591
Duley W. W., Williams D. A., 1984, Interstellar Chemistry, Academic Press, London
Duley W. W., Williams D. A., 1986, MNRAS, 223, 177
Duley W. W., Williams D. A., 1993, MNRAS, 260, 37
Eddington A. S., 1937, Observatory, 60, 99
Elmegreen B. G., 1990, in Blitz L., ed, Astron. Soc. Pac. Conf. Ser. 12, The evolution of the ISM, ASP, San Francisco, p. 247
Emerson J. P., Furniss I., Jennings R. E., 1975, MNRAS, 172, 411
Field D., Gerin M., Leach S., Lemaire J. L., Pineau des Forêts G., Rouan D., Simons D., 1994, A&A, 286, 909
Field G. B., Somerville W. B., Dressler K., 1966, ARA&A, 4, 207
Flower D. R., Watt G. D., 1984, MNRAS, 209, 25
Fox L., Wilkinson J. H., 1990, The NAG Fortran Library Manual, Mark 14, NAG Ltd, Oxford
Freyberg M. J., Schmitt J. H. M. M., 1995, A&A, 296, L21
Fuente A., Martín-Pintado J., Gaume R., 1995, ApJ, 442, L33
Gatley I. Hasegawa T., Suzuki H., Garden R. P., Brand P. W. J. L., Lightfoot J., Glencross W., Okuda H., Nagata T., 1987, ApJ, 318, L73
Gatley I., Kaifu N., 1987, in Vardya M. S., Tarafdar S. P., eds, Proc. IAU Symp. 120, Astrochemistry, Dordrecht, Reidel, p. 153
Gautier T. N. III, Fink U., Treffers R. R., Larson H. P., 1976, ApJ, 207, L129
Genzel R., Harris A. I., Stutzki J., 1989, in Kaldeich, ed, Proc. 22nd Eslab Symp. ESA SP-290, Infrared Spectroscopy in Astronomy, ESA Pub. Div., Noordwijk, p. 115
Goldshmidt O., Sternberg A., 1995, ApJ, 439, 256
Goudis C., 1982, in Blamont J. E. et al., eds, The Orion Complex: A Case Study of Interstellar Matter, Reidel, Dordrecht
Gough S., Schermann C., Pichou F., Landau M., Čadež I., Hall R. I., 1996, A&A, 305, 687
Gould R. J., Harwit M., 1963, ApJ, 137, 694
Green S., Truhlar D. G., 1979, ApJ, 231, L101
Habing H. J., 1968, Bull. Astron. Inst. Netherlands, 19, 421
Harris A. I., Stutzki J., Genzel R., Lugten J. B., Stacey G., Jaffe D. T., 1987, ApJ, 322, L49
Harvey P. M., Thronson H. A., Gatley I., 1980, ApJ, 235, 894
Hasegawa T., 1989, in Tenorio-Tagle et al., eds, Proc. IAU Colloq. 120, Structure and Dynamics of Interstellar Matter, p. 24
Hasegawa T., Gatley I., Garden R. P., Brand P. W. J. L., Ohishi M., Hayashi M., Kaifu N., 1987, ApJ, 318, L77
Heitler, London, 1927, Z. Physik, 44, 455
Herzberg G., 1950, Spectra of Diatomic Molecules, Van Nostrand Company Inc., New York
Hill J. K., Hollenbach D. J., 1978, ApJ, 225, 390
Hippelein H., Münch G., 1978, A&A, 68, L7
Hoban S., Reuter D. C., Mumma M. J., Storrs A. D., 1991, ApJ, 370, 228
Hollenbach D. J., McKee C. F., 1979, ApJS, 41, 555
Hollenbach D. J., McKee C. F., 1980, ApJ, 241, L47
Hollenbach D. J., Natta A., 1995, ApJ, 455, 133
Hollenbach D. J., Salpeter E. E., 1971, ApJ, 163, 155
Hollenbach D. J., Takahashi T., Tielens A. G. G. M., 1991, ApJ, 377, 192
Hora J. L., Latter W. B., 1996, ApJ, 461, 288
Horne K., 1986, PASP, 98, 609
Howe J. E., Jaffe D. T., Geballe T. R., 1990, Bull. Am. Astron. Soc., 22, 1328
Howe J. E., Jaffe D. T., Genzel R., Stacey G. J., 1991, ApJ, 373, 158
Hunter D. A., Watson W. D., 1978, ApJ, 226, 477

Israel F. P., Hawarden T. G., Wade R., Geballe T. R., van Dishoeck E. F., 1989, MNRAS, 236, 89
Jaffe D. T., Genzel R., Harris A. I., Howe J. E., Stacey G. J., Stutzki J., 1990, ApJ, 353, 193
Joblin C., Tielens A. G. G. M., Allamandola L. J., Geballe T. R., 1996, ApJ, 458, 610
Jura M., 1974, ApJ, 191, 375
Jura M., 1975, ApJ, 197, 575
Knapp G. R., Brown R. L., Kuiper T. B. H., 1975, ApJ, 196, 167
Lada E. A., Bally J., Stark A., 1991, ApJ, 368, 432
Lada E. A., 1992, ApJ, 393, L25
Le Bourlot J., Pineau des Forêts G., Roueff E., Dalgarno A., Gredel R., 1995, ApJ, 449, 178
Lee T. A., 1968, ApJ, 152, 913
Leger A., Puget J. L., 1984, A&A, 137, L5
Leonas V. B., Pjarnpuu A. A., 1981, Sov. Astron. Lett., 7, 33
Lepp S., Shull J. M., 1983, ApJ, 270, 578
Loren R. B., 1976, ApJ, 209, 466
Luhman M. L., Jaffe D. T., Keller L. D., Pak S., 1994, ApJ, 436, L185
Luhman M. L., Jaffe D. T., 1996, ApJ, 463, 191
Malin D. F., Ogura K., Walsh J. R., 1987, MNRAS, 227, 361
Maloney P. R., Hollenbach D. J., Tielens A. G. G. M., 1996, ApJ, 466, 561
Martin P. G., Mandy M. E., 1995, ApJ, 455, L89
Martin P. G., Schwarz D. H., Mandy M. E., 1996, ApJ, 461, 265
Massa D., Savage B. D., Fitzpatrick E. L., 1983, ApJ, 266, 662
Mathis J. S., 1990, ARA&A, 28, 37
McKee C. F., 1989, ApJ, 345, 782
Meyerdierks H., 1995, Specdre User's Guide, Starlink User Note 140.4
Mountain C. M., Leggett S. K., Selby M. J., Blackwell D. E., Petford A. D., 1985, A&A, 151, 399
Mountain C. M., Robertson D. J., Lee T. J., Wade R., 1990, in Crawford D. L., ed, SPIE Proc. Ser. 1235, Instrumentation in Astronomy VII, Bellingham, WA, p. 25
Mouri H., Taniguchi Y., 1995, ApJ, 449, 134
Pankonin V., Barsuhn J., Thomasson P., 1977, A&A, 54, 335
Pankonin V., Walmsley C. M., 1976, A&A, 48, 341
Pankonin V., Walmsley C. M., 1978, A&A, 67, 129
Parmar P., Lacy J., Achtermann M., 1991, ApJ, 372, L25
Perault M., Falgarone E., Puget J., 1985, A&A, 152, 371
Puxley P. J., Beard S. M., Ramsay S. K., 1992, in Grosbol P., ed, Proc. "Fourth Data Analysis Workshop" ESO/ST-ECF, München, p. 117
Puxley P. J., Hawarden T. G., Mountain C. M., 1988, MNRAS, 234, 29
Puxley P. J., Sylvester J., Pickup D. A., Paterson M. J., Laird D. C., Atad-Ettedgui E. I., 1994, in Crawford D. L., Craine E. R., eds, Proc. SPIE - Int. Soc. Opt. Eng. 2198, Instrumentation in Astronomy VIII, Bellingham, WA, p. 350
Racine R., 1968, AJ, 73, 233
Ramsay S. K., Chrysostomou A., Geballe T. R., Brand P. W. J. L., Mountain M., 1993, MNRAS, 263, 695
Ramsay S. K., Mountain C. M., Geballe T. R., 1992, MNRAS, 259, 751
Ramsay Howat S. K., Chrysostomou A., Mountain C. M., Brand P. W. J. L., 1997, MNRAS, in press
Rieke G. H., Lebofsky M. J., 1985, ApJ, 288, 618
Rogerson J. B., Spitzer L., Drake J. F., Dressler K., Jenkins E. B., Morton D. C., York D. G., 1973, ApJ, 181, L97
Rouan D., Field D., Lemaire J.-L., Lai O., Pineau des Forêts G., Falgarone E., Deltorn J.-M., 1997, MNRAS, 284, 395
Russell R., Melnick G., Gull G., Harwit M., 1980, ApJ, 240, L99
Russell R., Melnick G., Smyers S., Kurtz N., Gosnell T., Harwit M., Werner M., 1981, ApJ, 250, L35
Savage B. D.,, Bohlin R. C., Drake J. F., Budich W., 1977, ApJ, 216, 291
Scarrott S. M., Rolph C. D., Mannion M. D., 1989, MNRAS 237, 1027
Sellgren K., 1983, AJ, 88, 983
Sellgren K., 1984, ApJ, 277, 623

Sellgren K., 1986, ApJ, 305, 399
Sellgren K., Allamandola L. H., Bregman J. D., Werner M. W., Wooden D. H., 1985, ApJ, 299, 416
Sellgren K., Luan L., Werner M. W., 1990, ApJ, 359, 384
Sellgren K., Werner M. W., Dinerstein H. L., 1983, ApJ, 271, L13
Sellgren K., Werner M. W., Dinerstein H. L., 1992, ApJ, 400, 238
Sharpless S., 1952, ApJ, 116, 251
Shibai H. et al., 1991, ApJ, 374, 522
Shortridge K., 1993, in Hanisch R. J., Brissenden R. J. V., Barnes J., eds, Astron. Soc. Pac. Conf. Ser. 52, Astronomical Data Analysis Software and Systems II, ASP, San Francisco, p. 219
Shull J. M., 1978, ApJ, 219, 877
Shull J. M., Beckwith S., 1982, ARA&A, 20, 163
Shull J. M., Hollenbach D. J., 1978, ApJ, 220, 525
Solomon P. M., Rivolo A. R., Barrett J. W., Yahil A., 1987, ApJ, 319, 730
Solomon P. M., Sanders D. B., Scoville N. Z., 1979, in Burton W. B., ed, Proc. IAU Symp. 84, The Large Scale Characteristics of the Galaxy, Kluwer, Dordrecht, p. 35
Stathakis R., 1997, RGO Spectrograph Operations Manual, AAO, PO Box 296, Epping, Sydney, Australia; available in draft form from Ray Stathakis (ras@aaoepp.aao.gov.au)
Stecher T. P., Williams D. A., 1967, ApJ, 388, 197
Steiman-Cameron T., Haas M. R., Tielens A. G. G. M., Burton M. G., 1997, ApJ, 478, 261
Sternberg A., 1988, ApJ, 332, 400
Sternberg A., Dalgarno A., 1989, ApJ, 338, 197
Stetson P. B., 1987, PASP, 99, 191
Strom K. M., Strom S. E., Carrasco L., Vrba F. J., 1975, ApJ, 196, 489
Stutzki J., Stacey G. J., Genzel R., Harris A. I., Jaffe D. T., Lugten J. B., 1988, ApJ, 332, 379
Takayanagi K., Sakimoto K., Onda K., 1987, ApJ, 318, L81
Tielens A. G. G. M., Allamandola L. J., 1987, in Hollenbach D. J., Thronson H. A., eds, Proc. of the Symp. on Interstellar Processes, Reidel, Dordrecht, p. 397
Tielens A. G. G. M., Hollenbach D., 1985, ApJ, 291, 722
Timmermann R., Bertoldi F., Wright C. M., Drapatz S., Draine B. T., Haser L., Sternberg A., 1996, A&A, 315, 281
Tiné S., Lepp S., Gredel R., Dalgarno A., 1997, ApJ, 481, 282
Treffers R. R., Fink U., Larson H. P., Gautier T. N., 1976, ApJ, 209, 793
Turner J., Kirby-Docken K., Dalgarno A., 1977, ApJS, 35, 281
van Dishoeck E. F., Black J. H., 1988, ApJ, 334, 771
Ward-Thompson D., Buckley H. D., Greaves J. S., Holland W. S., André P., 1996, MNRAS, 281, L53
Webster A., 1993, MNRAS, 263, 385
White G. J., Padman R., 1991, Nature, 354, 511
White G. J., Sanderson C., Richardson K. J., Monteiro T. S., Hayashi S. S., 1990, A&A, 227, 200
Whittet D. C. B., 1988, in Bailey M. E., Williams D. A., eds, in Dust in the Universe, Cambridge Univ. Press, Cambridge, p. 25
Whitworth A., 1979, MNRAS, 186, 59
Williams J. P., Blitz L., Stark A. A., 1995, ApJ, 451, 252
Winget D. E., Hansen C. J., Liebert J., van Horn H. M., Fontaine G., Nather R. E., Kepler S. O., Lamb D. Q., 1987, ApJ, 315, L77
Winkler H., 1997, MNRAS, 287, 481
Witt A., Schild R. E., Kraiman J. B., 1984, ApJ, 281, 708
Witt A. N., Malin D. F., 1989, ApJ, 347, L25
Wood M. A., 1992, ApJ, 386, 539
Wright G. S., 1994, in Beckers J. M. et al., eds, Exp. Astron. 3, Spectroscopy with CGS4 on UKIRT, Kluwer Acad. Publ., Dordrecht, p. 17
Zuckerman B., Palmer P., 1974, ARA&A, 12, 279
Zuckerman B., Gatley I., 1988, ApJ, 324, 501

Appendix A

'Sliding' the Telescope

The usual method for performing spectroscopy on an extended source is to point the telescope at the source and then at empty sky for the required exposure time. This method aims to ensure the sky frame is as free of extraneous emission as possible and contains only background emission from the sky close to the source. An alternative method exists when the source is compact with respect to the angular size of the slit. The source is observed through one half of the slit and then the telescope 'slides' along the direction the slit projects on the sky until the source is within the other half of the slit. Pairs of observations are made at each of these positions. The sky subtraction is carried out in two steps :

1. One of the pairs is subtracted from the other, removing sky emission to the first order and any residual dark current or errors arising from differences in the flat response. The resulting frame then consists of a positive image of the source in one half of the array and a negative image in the other. These are both superimposed over the difference in the sky emission between the two exposures.
2. The negative image is then positioned across the positive image and subtracted from it. The result is normalised to the duration of one exposure (*i.e.* divided by two). This results in an image of the source on top of a sky background which is half the difference of the residual skies from the previous frame (Fig A.1).

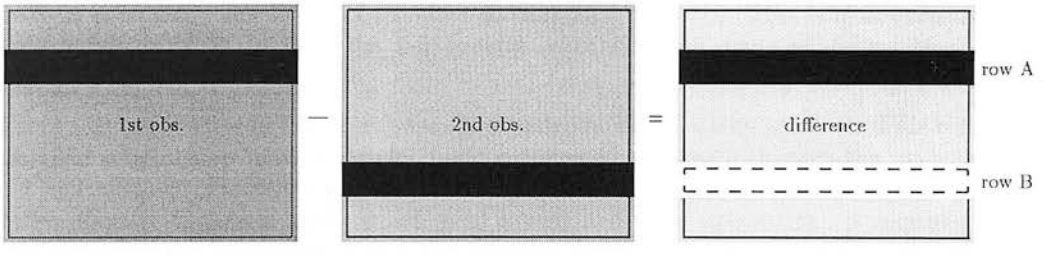

Figure A.1: Sky subtraction by 'sliding along the slit'.

Assuming the data have been successfully flatfielded and dark subtracted the background level under the source will be dominated by the residual sky emission, given by

$$\frac{1}{2}(\delta sky_{\,A} - \delta sky_{\,B})$$

where δsky is the change in sky emission between the exposures at a given row. For short exposures, in stable conditions, the second step serves to remove variations over time since, $\delta sky_{\,A} \simeq \delta sky_{\,B}$. This method of observing doubles the integration time compared to nodding the telescope off source to the sky, thus increasing the signal to noise by a factor of $\sqrt{2}$. It also reduces the noise, due to sky emission, to that contribution originating from the difference in the rate of sky variation across the slit.

Appendix B

Choice of Functional Form for Model

Each vibrational level of a fluorescent cascade approximates, by eye, fairly well to a Boltzmann distribution, *e.g.*

$$\log N_j/g_j = k - \frac{0.43E_j}{T_{ex}}$$

where k is a constant, E_j is the energy level and T_{ex} is the excitation temperature of the gas in that state. Following on from this, an initial attempt was made to fit a model to the data with equation,

$$y = \alpha - \frac{0.43x}{\beta + \gamma x}. \tag{B.1}$$

where α, β and γ are the free parameters to be fitted to each vibrational level. This model included the assumption that the populated states could be characterised by an excitation temperature which varied linearly with energy level. This had the advantage that the magnitude of the slope decreased monotonically and tended to zero as the energy level increased, which was apparent in the data.

Unfortunately, for a positive excitation temperature, this form only has an asymptote for negative x. This can be understood since the Boltzmann distribution it is derived from has a finite population for its ground energy state at $x = 0$ and thus cannot have an asymptote for positive x. However, for a fluorescent cascade, this is not appropriate as the population for each vibrational level approaches an asymptote for low rotational quantum numbers, J. The way around this problem is to move the origin of the data so that $E(J = 0) = 0$. This transformation permits the model a better fit to the data but still greatly constrains the shape of the model so that the fit is less than ideal.

A more successful approach is to release the constraint of T_{ex} being positive. This removes any semi-physical relationship that the model might carry and completely changes the parameter space for α, β and γ where the solutions lie. The model was fitted to the data using a *NAG* routine (E04HFF - Fox & Wilkinson 1990) which used a weighted least squares fit. It required accurate initial estimates of the parameters α, β and γ which were critical to it finding a global solution and preventing the search routine finding a local solution in the wrong part of parameter space or getting stuck in a flat part of parameter space. Differentiating equation (B.1) and solving for γ and β simultaneously provided computable forms of the parameters with no negative square roots,

$$\gamma = -0.43\left(\sqrt{\frac{\nabla_1}{\nabla_2}} - 1\right)\left(\frac{x_2 - x_1\sqrt{\nabla_1/\nabla_2}}{\nabla_1(x_2 - x_1)^2}\right) \tag{B.2}$$

$$\beta = \frac{0.43}{(x_2 - x_1)^2}\left(\frac{x_2}{\sqrt{|\nabla_1|}} - \frac{x_1}{\sqrt{|\nabla_2|}}\right)^2 \tag{B.3}$$

where ∇_1 and ∇_2 are the gradients at the beginning and end of the vibrational level being considered. α was calculated by rearranging equation (B.1) for α and averaging the result of two equations, one for the beginning and one for the end of the vibrational level.

Appendix C

Raw Line Flux Measurements and Predicted Values

Line	λ (Å)	RGO Spectrograph Data 1996 Flux W m^{-2} beam^{-1}	1996 Error %	1990 Flux W m^{-2} beam^{-1}	1990 Error %
7–3 S(5)	7631	0.67E-18	16	0.80E-18	10
9–4 S(11)	7633	0.36E-18	40	—	—
7–4 S(4)	7639	—	—	0.40E-18	20
7–3 S(6)	7640	—	—	0.26E-18	30
7–3 S(3)	7665	—	—	0.10E-17	8
7–3 S(2)	7709	0.38E-18	14	0.30E-18	26
7–3 S(1)	7771	—	—	0.54E-18	15
3–0 S(7)	7784	0.53E-18	18	—	—
3–0 S(9)	7793	0.58E-18	27	0.65E-18	12
3–0 S(6)	7804	0.38E-18	34	0.25E-18	32
3–0 S(5)	7840	0.84E-18	13	0.79E-18	10
3–0 S(4)	7892	0.40E-18	27	0.44E-18	18
3–0 S(5)	7840	0.99E-18	5	—	—
3–0 S(11)	7865	0.25E-18	34	—	—
3–0 S(4)	7892	0.35E-18	31	—	—
3–0 S(3)	7962	0.92E-18	17	0.74E-18	11
7–3 S(11)	7978	0.25E-18	29	—	—
7–3 Q(1)	8011	0.30E-18	27	0.16E-18	49
10–5 Q(3)	8019	0.10E-18	76	—	—
3–0 S(2)	8049	0.51E-18	22	0.36E-18	22
7–3 S(12)	8111	0.89E-19	77	—	—
3–0 S(1)	8153	0.87E-18	8	0.65E-18	12
7–3 Q(5)	8220	0.29E-18	41	—	—
12–6 Q(5)	8225	0.29E-18	32	—	—
8–4 S(5)	8269	—	—	0.76E-18	10
3–0 S(0)	8275	0.23E-18	42	0.22E-18	36
4–1 S(7)	8286	0.18E-17	7	0.18E-17	9
8–4 S(3)	8290	0.78E-18	19	—	—
4–1 S(6)	8302	0.63E-18	19	—	—
4–1 S(9)	8306	0.84E-18	24	0.96E-18	8
4–1 S(5)	8337	0.21E-17	12	0.25E-17	3
4–1 S(4)	8390	0.77E-18	21	0.87E-18	18
8–4 S(1)	8394	0.42E-18	19	—	—
4–1 S(11)	8398	0.46E-18	45	—	—
4–1 S(3)	8462	0.18E-17	8	0.17E-17	9

Table C.1: Raw flux values (corrected for slit transmission) from the first two grating positions of the far-red 1996 data and the far-red 1990 data (see Section 4.2.6.3 for details).

Line	λ (Å)	RGO Spectrograph Data 1996 Flux W m^{-2} beam^{-1}	1996 Error %	1990 Flux W m^{-2} beam^{-1}	1990 Error %
7–3 Q(7)	8421	0.77E-19	89	—	—
4–1 S(3)	8462	0.16E-17	10	—	—
4–1 S(12)	8471	0.28E-18	52	—	—
8–4 S(0)	8477	0.25E-18	28	—	—
10–5 Q(7)	8484	0.86E-19	69	—	—
8–4 S(9)	8496	0.33E-18	31	—	—
3–0 Q(1)	8500	0.63E-18	29	—	—
3–0 Q(2)	8525	0.21E-18	48	0.28E-18	29
4–1 S(2)	8552	0.66E-18	27	0.92E-18	9
3–0 Q(3)	8563	0.52E-18	4	0.52E-18	15
8–4 Q(1)	8652	0.59E-18	25	0.48E-18	22
4–1 S(1)	8662	0.11E-17	8	0.17E-17	9
8–4 Q(3)	8741	0.41E-18	27	—	—
4–1 S(0)	8792	0.76E-18	22	0.72E-18	22
4–1 S(15)	8803	0.25E-18	43	—	—
5–2 S(7)	8853	0.14E-17	11	—	—
5–2 S(8)	8862	0.51E-18	39	—	—
5–2 S(6)	8865	0.73E-18	27	—	—
5–2 S(9)	8891	0.98E-18	17	—	—
5–2 S(5)	8896	0.18E-17	8	—	—
5–2 S(4)	8949	0.87E-18	26	—	—
5–2 S(3)	9022	0.24E-17	8	—	—
4–1 Q(1)	9032	0.96E-18	19	—	—
5–2 S(11)	9012	0.45E-18	78	—	—
5–2 S(3)	9022	0.23E-17	10	—	—
4–1 Q(1)	9032	0.13E-17	21	—	—
9–5 S(4)	9037	0.43E-18	41	—	—
9–5 S(3)	9049	0.97E-18	49	—	—
4–1 Q(2)	9060	0.58E-18	51	—	—
4–1 Q(3)	9102	0.69E-18	27	—	—
5–2 S(12)	9104	0.17E-18	67	—	—
5–2 S(2)	9116	0.13E-17	34	—	—
9–5 S(1)	9148	0.71E-18	56	—	—
9–5 S(7)	9165	0.69E-18	33	—	—
5–2 S(1)	9232	0.17E-17	28	—	—

Table C.2: Raw flux values (corrected for slit transmission) from the last two grating positions of the far-red 1996 data and the far-red 1990 data (see Section 4.2.6.3 for details).

Line	λ (Å)	Infrared Data CGS2 Flux W m^{-2} beam^{-1}	CGS2 Error %	CGS4 Flux W m^{-2} beam^{-1}	CGS4 Error %	UKT9 Flux W m^{-2} beam^{-1}	UKT9 Error %
2–0 S(4)	10998	0.96E-17	33	—	—	—	—
3–1 S(7)	11304	0.90E-17	28	—	—	—	—
2–0 S(2)	11382	0.12E-16	27	—	—	—	—
2–0 S(1)	11622	0.12E-16	25	—	—	—	—
3–1 S(4)	11672	0.86E-17	29	—	—	—	—
4–2 S(5)	12263	0.11E-16	24	—	—	—	—
3–1 S(1)	12330	0.15E-16	22	—	—	—	—
2–0 Q(1)	12383	0.12E-16	26	—	—	—	—
2–0 Q(3)	12473	0.98E-17	26	—	—	—	—
4–2 S(2)	12846	0.11E-16	23	—	—	—	—
2–0 O(3)	13354	0.14E-16	19	—	—	—	—
3–1 O(4)	14677	—	—	0.12E-16	12	—	—
5–3 Q(1)	14929	0.89E-17	18	0.21E-16	9	—	—
6–4 S(1)	15016	—	—	0.14E-16	8	—	—
5–3 Q(3)	15056	—	—	0.15E-16	12	—	—
4–2 O(3)	15099	0.11E-16	15	0.22E-16	9	—	—
5–3 Q(4)	15158	0.44E-17	36	0.47E-17	22	—	—
3–1 O(5)	15220	—	—	0.12E-16	15	—	—
5–3 Q(5)	15286	0.58E-17	19	0.89E-17	17	—	—
6–4 S(0)	15369	0.44E-17	32	0.68E-17	22	—	—
7–5 S(4)	15400	0.30E-17	47	—	—	—	—
5–3 Q(6)	15443	0.40E-17	35	—	—	—	—
10–7 O(3)	15489	0.30E-17	47	—	—	—	—
4–2 O(4)	15635	—	—	0.14E-16	18	—	—
7–5 S(2)	15883	—	—	0.48E-17	31	—	—
11–8 S(1)	15915	—	—	0.31E-17	48	—	—
6–4 Q(1)	16015	0.32E-17	44	—	—	—	—
6–4 Q(2)	16074	0.32E-17	63	—	—	—	—
5–3 O(3)	16135	—	—	0.17E-16	11	—	—
6–4 Q(3)	16162	—	—	0.99E-17	15	—	—
7–5 S(1)	16205	—	—	0.82E-17	23	—	—
4–2 O(5)	16223	—	—	0.10E-16	19	—	—
6–4 Q(4)	16281	0.40E-17	50	0.37E-17	50	—	—
6–4 Q(5)	16431	—	—	0.91E-17	21	—	—
5–3 O(4)	16718	—	—	0.74E-17	20	—	—
8–6 S(4)	16801	—	—	0.36E-17	52	—	—
8–6 S(3)	17018	0.45E-17	27	—	—	—	—
1–0 S(8)	17147	0.42E-17	29	0.64E-17	29	—	—
7–5 Q(1)	17288	—	—	0.12E-16	16	—	—
6–4 O(3)	17326	—	—	0.18E-16	10	—	—
1–0 S(7)	17480	—	—	0.33E-16	6	—	—
4–2 O(7)	17563	—	—	0.28E-17	67	—	—
11–8 O(3)	17609	—	—	0.46E-17	40	—	—
8–6 S(1)	17639	—	—	0.63E-17	29	—	—
7–5 Q(5)	17784	—	—	0.63E-17	24	—	—
1–0 S(2)	20338	0.32E-16	11	—	—	0.23E-15	10
2–1 S(3)	20735	—	—	—	—	0.12E-15	24
1–0 S(1)	21218	0.82E-16	8	—	—	0.55E-15	8
2–1 S(2)	21542	0.14E-16	15	—	—	0.11E-15	20
3–2 S(3)	22014	—	—	—	—	0.60E-16	34
1–0 S(0)	22233	0.38E-16	8	—	—	0.26E-15	16
2–1 S(1)	22477	0.29E-16	10	—	—	0.15E-15	30
3–2 S(2)	22870	0.46E-17	39	—	—	0.30E-16	70
4–3 S(3)	23445	0.43E-17	58	—	—	—	—
2–1 S(0)	23556	—	—	—	—	0.80E-16	30
3–2 S(1)	23864	0.13E-16	25	—	—	0.60E-16	50
1–0 Q(1)	24066	0.14E-15	7	—	—	—	—
1–0 Q(3)	24237	0.57E-16	9	—	—	—	—
1–0 Q(4)	24375	0.22E-16	22	—	—	—	—

Table C.3: Raw flux values (corrected for slit transmission) taken from the infrared datasets (see Section 4.2.6.3 for details).

λ (μm)	Int	Line
0.7447	0.00	9–4 Q(5)
0.7495	0.00	5–1 Q(9)
0.7631	0.05	7–3 S(5)
0.7640	0.02	7–3 S(6)
0.7668	0.04	7–3 S(7)
0.7743	0.01	10–5 S(1)
0.7771	0.03	7–3 S(1)
0.7782	0.02	7–3 S(9)
0.7804	0.02	3–0 S(6)
0.7850	0.01	7–3 S(0)
0.7892	0.03	3–0 S(4)
0.7968	0.00	9–4 Q(9)
0.8019	0.01	10–5 Q(3)
0.8085	0.01	7–3 Q(3)
0.8153	0.04	3–0 S(1)
0.8225	0.01	12–6 Q(5)
0.8275	0.01	3–0 S(0)
0.8290	0.04	8–4 S(3)
0.8306	0.04	4–1 S(9)
0.8335	0.03	8–4 S(7)
0.8346	0.00	7–3 O(3)
0.8398	0.02	4–1 S(11)
0.8462	0.07	4–1 S(3)
0.8484	0.00	10–5 Q(7)
0.8525	0.01	3–0 Q(2)
0.8562	0.03	4–1 S(13)
0.8623	0.02	11–6 S(1)
0.8673	0.01	4–1 S(14)
0.8694	0.00	7–3 Q(9)
0.8792	0.03	4–1 S(0)
0.8812	0.01	8–4 Q(4)
0.8860	0.00	7–3 Q(10)
0.8891	0.03	5–2 S(9)
0.8918	0.00	9–4 Q(13)
0.8946	0.01	3–0 O(3)
0.9012	0.02	5–2 S(11)
0.9022	0.08	5–2 S(3)
0.9049	0.03	9–5 S(3)
0.9065	0.01	3–0 Q(9)
0.9116	0.04	5–2 S(2)
0.9148	0.02	9–5 S(1)
0.9165	0.02	9–5 S(7)
0.9229	0.02	4–1 Q(5)
0.9300	0.00	8–4 Q(8)
0.9369	0.02	5–2 S(0)
0.9479	0.00	8–4 Q(9)
0.9511	0.02	4–1 O(3)

λ (μm)	Int	Line
0.7465	0.01	6–2 Q(1)
0.7528	0.01	6–2 Q(3)
0.7633	0.03	9–4 S(11)
0.7644	0.01	6–2 Q(5)
0.7709	0.02	7–3 S(2)
0.7759	0.07	12–6 S(3)
0.7772	0.00	6–2 O(3)
0.7784	0.04	3–0 S(7)
0.7821	0.02	3–0 S(10)
0.7865	0.02	3–0 S(11)
0.7919	0.01	10–5 Q(1)
0.7978	0.01	7–3 S(11)
0.8041	0.01	7–3 Q(2)
0.8111	0.00	7–3 S(12)
0.8208	0.00	10–5 O(3)
0.8269	0.03	8–4 S(4)
0.8286	0.09	4–1 S(7)
0.8291	0.02	8–4 S(6)
0.8312	0.00	7–3 Q(6)
0.8337	0.11	4–1 S(5)
0.8390	0.04	4–1 S(4)
0.8403	0.01	8–4 S(8)
0.8471	0.01	4–1 S(12)
0.8496	0.01	8–4 S(9)
0.8548	0.00	7–3 Q(8)
0.8563	0.02	3–0 Q(3)
0.8652	0.02	8–4 Q(1)
0.8677	0.01	3–0 Q(5)
0.8741	0.01	8–4 Q(3)
0.8803	0.01	4–1 S(15)
0.8843	0.01	3–0 Q(7)
0.8862	0.02	5–2 S(8)
0.8896	0.06	5–2 S(5)
0.8941	0.02	5–2 S(10)
0.8947	0.00	3–0 Q(8)
0.9014	0.01	8–4 Q(6)
0.9032	0.04	4–1 Q(1)
0.9050	0.00	7–3 Q(11)
0.9102	0.03	4–1 Q(3)
0.9145	0.01	8–4 Q(7)
0.9158	0.01	4–1 Q(4)
0.9197	0.00	3–0 Q(10)
0.9232	0.07	5–2 S(1)
0.9314	0.01	4–1 Q(6)
0.9395	0.00	3–0 O(5)
0.9505	0.00	7–3 Q(13)
0.9532	0.01	4–1 Q(8)

λ (μm)	Int	Line
0.7490	0.01	6–2 Q(2)
0.7580	0.00	6–2 Q(4)
0.7639	0.03	7–3 S(4)
0.7665	0.06	7–3 S(3)
0.7715	0.02	7–3 S(8)
0.7767	0.02	10–5 S(5)
0.7781	0.02	3–0 S(8)
0.7793	0.04	3–0 S(9)
0.7840	0.06	3–0 S(5)
0.7869	0.01	7–3 S(10)
0.7962	0.04	3–0 S(3)
0.8011	0.01	7–3 Q(1)
0.8049	0.02	3–0 S(2)
0.8145	0.01	7–3 Q(4)
0.8220	0.01	7–3 Q(5)
0.8269	0.04	8–4 S(5)
0.8287	0.03	4–1 S(8)
0.8302	0.03	4–1 S(6)
0.8331	0.02	8–4 S(2)
0.8343	0.02	4–1 S(10)
0.8394	0.02	8–4 S(1)
0.8421	0.01	7–3 Q(7)
0.8477	0.01	8–4 S(0)
0.8500	0.03	3–0 Q(1)
0.8552	0.04	4–1 S(2)
0.8613	0.01	3–0 Q(4)
0.8662	0.05	4–1 S(1)
0.8688	0.01	8–4 Q(2)
0.8753	0.01	3–0 Q(6)
0.8812	0.01	11–6 Q(1)
0.8853	0.05	5–2 S(7)
0.8865	0.03	5–2 S(6)
0.8903	0.01	8–4 Q(5)
0.8944	0.01	11–6 Q(3)
0.8949	0.03	5–2 S(4)
0.9021	0.01	8–4 O(3)
0.9037	0.01	9–5 S(4)
0.9060	0.03	4–1 Q(2)
0.9104	0.01	5–2 S(12)
0.9147	0.00	11–6 O(3)
0.9161	0.00	3–0 O(4)
0.9212	0.00	8–4 O(4)
0.9263	0.00	7–3 Q(12)
0.9344	0.01	3–0 Q(11)
0.9415	0.02	4–1 Q(7)
0.9507	0.00	3–0 Q(12)
0.9536	0.01	9–5 Q(3)

Table C.4: Line intensities used to create synthetic I-band spectra in Figs. 4.23–4.26. Intensities are quoted relative to the strength of the 1–0 S(1) line.

λ (μm)	Int	Line
1.4432	0.05	4–2 Q(6)
1.4592	0.12	4–2 Q(7)
1.4712	0.07	6–4 S(2)
1.4755	0.01	9–6 O(5)
1.4831	0.00	8–5 O(8)
1.4980	0.08	5–3 Q(2)
1.5024	0.02	3–1 Q(13)
1.5058	0.04	7–5 S(7)
1.5122	0.03	7–5 S(6)
1.5220	0.13	3–1 O(5)
1.5286	0.08	5–3 Q(5)
1.5400	0.06	7–5 S(4)
1.5464	0.02	2–0 O(7)
1.5615	0.16	7–5 S(3)
1.5792	0.02	4–2 Q(12)
1.5840	0.02	5–3 Q(8)
1.5915	0.03	11–8 S(1)
1.6084	0.03	5–3 Q(9)
1.6135	0.18	5–3 O(3)
1.6223	0.08	4–2 O(5)
1.6361	0.01	5–3 Q(10)
1.6453	0.03	3–1 O(7)
1.6515	0.01	8–6 S(7)
1.6571	0.04	11–8 Q(1)
1.6646	0.03	8–6 S(5)
1.6802	0.03	8–6 S(4)
1.6870	0.02	11–8 Q(3)
1.7021	0.01	5–3 Q(12)
1.7288	0.10	7–5 Q(1)
1.7338	0.01	4–2 Q(16)
1.7412	0.01	5–3 Q(13)
1.7563	0.03	4–2 O(7)
1.7639	0.05	8–6 S(1)

λ (μm)	Int	Line
1.4456	0.16	6–4 S(3)
1.4614	0.06	10–7 Q(1)
1.4723	0.01	9–6 Q(9)
1.4778	0.03	4–2 Q(8)
1.4870	0.02	2–0 O(6)
1.4989	0.07	4–2 Q(9)
1.5042	0.01	7–5 S(8)
1.5076	0.01	7–5 S(9)
1.5158	0.05	5–3 Q(4)
1.5228	0.02	4–2 Q(10)
1.5299	0.00	7–5 S(11)
1.5404	0.00	8–5 O(9)
1.5489	0.05	10–7 O(3)
1.5626	0.05	5–3 Q(7)
1.5807	0.01	9–6 O(7)
1.5845	0.02	10–7 Q(7)
1.6015	0.13	6–4 Q(1)
1.6104	0.02	2–0 O(8)
1.6162	0.11	6–4 Q(3)
1.6260	0.02	12–8 O(7)
1.6428	0.00	9–6 O(8)
1.6483	0.02	10–7 O(5)
1.6540	0.00	8–6 S(8)
1.6585	0.04	7–5 S(0)
1.6673	0.02	5–3 Q(11)
1.6830	0.01	9–6 Q(13)
1.6892	0.02	4–2 Q(15)
1.7147	0.06	1–0 S(8)
1.7297	0.03	8–6 S(2)
1.7357	0.05	7–5 Q(2)
1.7463	0.08	7–5 Q(3)
1.7604	0.04	7–5 Q(4)
1.7784	0.09	7–5 Q(5)

λ (μm)	Int	Line
1.4479	0.05	3–1 Q(11)
1.4677	0.11	3–1 O(4)
1.4738	0.02	3–1 Q(12)
1.4827	0.03	10–7 Q(3)
1.4929	0.20	5–3 Q(1)
1.5016	0.14	6–4 S(1)
1.5056	0.14	5–3 Q(3)
1.5099	0.21	4–2 O(3)
1.5160	0.00	7–5 S(10)
1.5236	0.09	7–5 S(5)
1.5369	0.07	6–4 S(0)
1.5443	0.03	5–3 Q(6)
1.5495	0.03	4–2 Q(11)
1.5635	0.12	4–2 O(4)
1.5812	0.03	3–1 O(6)
1.5883	0.07	7–5 S(2)
1.6074	0.08	6–4 Q(2)
1.6123	0.01	4–2 Q(13)
1.6205	0.11	7–5 S(1)
1.6281	0.04	6–4 Q(4)
1.6431	0.09	6–4 Q(5)
1.6489	0.01	4–2 Q(14)
1.6550	0.01	8–6 S(6)
1.6630	0.00	8–6 S(9)
1.6718	0.07	5–3 O(4)
1.6865	0.03	4–2 O(6)
1.7018	0.05	8–6 S(3)
1.7149	0.01	3–1 O(8)
1.7326	0.12	6–4 O(3)
1.7359	0.09	5–3 O(5)
1.7480	0.29	1–0 S(7)
1.7609	0.04	11–8 O(3)
—	—	—

Table C.5: Line intensities used to create synthetic H-band spectrum in Fig. 4.27. Intensities are quoted relative to the strength of the 1–0 S(1) line.

Appendix D

Extinction Values Calculated from Pairs of Lines

The extinctions shown in Table D.1 were calculated from line ratios of transitions which originated from the same energy level. This removed the need to know the column density of that excited state leaving the ratio dependent only on the transition rate coefficients, the wavelengths and the observed intensities of the lines. The extinction, A_λ, calculated from the observed intensities of a pair of lines, I_1 and I_2 which share the same upper levels is given by

$$A_\lambda = 2.5\,\lambda^{-1.7} \log\left(\frac{I_2 A_1 \lambda_2}{I_1 A_2 \lambda_1}\right)\left(\lambda_1^{-1.7} - \lambda_2^{-1.7}\right)^{-1} \tag{D.1}$$

where A_1 and A_2 are the transition rate coefficients and λ_1 and λ_2 are the respective wavelengths of the two lines. The uncertainty on each extinction value was calculated using the equation,

$$\frac{\delta A_\lambda}{A_\lambda} = \left[\log\left(\frac{I_2 A_1 \lambda_2}{I_1 A_2 \lambda_1}\right)\right]^{-1} \sqrt{\left(\frac{\delta I_1}{I_1}\right)^2 + \left(\frac{\delta I_2}{I_2}\right)^2} \tag{D.2}$$

The measured extinction depends greatly on the length of the baseline over which the wavelengths of the lines range. This derivation of the extinction assumes that the emission spectrum is purely fluorescent and that collisional de-excitation is not significant. If collisions contributed significantly to the de-excitation of the energy levels, then values of extinction which depended on lines with substantially different Einstein A_j coefficients would not reflect the true extinction. As can be seen from Fig. 4.13, the mean extinction calculated from this method is in the range $A_v = 5$–7 with a few extreme values scattered over a large range. The primary reason for these extreme values is their low signal to noise and the short wavelength baseline. The most extreme values, for example, taken from Table D.1 are:

Line 1	$\lambda(\mu m)$	Line 2	$\lambda(\mu m)$	A_1/A_2	A_v	δA_v
6–4 Q(1)	1.6015	6–4 O(3)	1.7326	0.998	65.3	55.3
6–4 Q(2)	1.6074	6–4 S(0)	1.5369	1.201	-27.2	129.5
6–4 S(0)	1.5369	6–4 Q(2)	1.6074	0.833	-38.7	137.0.

which when compared to equation (D.2) show the limited importance of the relative transition rates compared to errors due to low signal to noise. Additionally transitions from the $v = 6$ level have relatively large transition rate coefficients (see Fig. 2.2) which makes them less susceptible to collisional effects. The entire dataset covers the wavelength range 0.73–2.4μm and contains many transitions from sufficiently different wavelengths regions to provide accurate extinction values. Therefore any effect collisional de-excitation will have on the calculated extinction has been assumed to be minor.

Line 1	Line 2	A_v	±
1–0 S(1)	1–0 Q(3)	-0.5	14.7
1–0 S(2)	1–0 Q(4)	8.1	21.1
2–0 Q(1)	2–0 O(3)	15.0	26.6
2–0 S(1)	2–1 S(1)	3.3	3.5
2–0 Q(3)	2–1 S(1)	2.2	4.3
2–0 S(2)	2–1 S(2)	-0.4	4.0
3–0 S(0)	3–0 Q(2)	3.7	64.7
3–0 S(0)	3–1 O(4)	7.4	3.5
3–0 Q(2)	3–1 O(4)	7.7	4.3
3–0 S(0)	3–1 O(4)	7.6	3.1
3–0 S(1)	3–0 Q(3)	6.9	5.2
3–0 S(1)	3–1 S(1)	6.1	2.3
3–0 S(1)	3–2 S(1)	3.9	2.9
3–0 Q(3)	3–0 S(1)	14.5	7.7
3–0 Q(3)	3–2 S(1)	4.5	1.6
3–0 Q(3)	3–1 O(5)	5.6	1.3
3–0 S(1)	3–1 S(1)	7.3	2.4
3–0 S(1)	3–2 S(1)	4.6	3.0
3–0 Q(3)	3–1 S(1)	5.9	3.1
3–0 Q(3)	3–2 S(1)	3.5	3.4
3–1 S(1)	3–2 S(1)	2.7	4.9
3–1 S(1)	3–1 O(5)	4.6	8.7
3–2 S(1)	3–1 O(5)	-2.8	13.8
3–0 S(2)	3–2 S(2)	4.0	4.2
3–0 S(2)	3–2 S(2)	4.8	4.2
3–0 S(3)	3–2 S(3)	5.2	2.0
3–0 S(4)	3–1 S(4)	8.8	4.1
3–0 S(7)	3–1 S(7)	8.4	3.2
4–1 Q(1)	4–2 O(3)	7.3	2.1
4–1 Q(1)	4–2 O(3)	6.1	2.2
4–1 S(0)	4–2 O(4)	6.5	2.5
4–1 Q(2)	4–2 O(4)	7.7	5.2
4–1 S(1)	4–1 Q(3)	6.4	19.1
4–1 Q(3)	4–1 S(1)	-5.8	19.3
4–1 S(1)	4–2 O(5)	5.2	1.7
4–1 S(2)	4–2 S(2)	8.9	2.6
4–1 S(3)	4–2 O(7)	4.6	5.0
4–1 S(3)	4–2 O(7)	4.9	5.0
4–1 S(3)	4–2 O(7)	4.8	5.0
4–1 S(5)	4–2 S(5)	6.4	2.8
5–3 Q(1)	5–3 O(3)	11.2	23.0
5–2 S(1)	5–3 Q(3)	8.2	3.3
5–2 S(2)	5–3 Q(4)	5.5	4.1
5–2 S(3)	5–3 Q(5)	6.3	1.8
5–2 S(3)	5–3 Q(5)	6.4	1.9
6–4 Q(1)	6–4 O(3)	65.3	55.3
6–4 Q(2)	6–4 S(0)	-27.2	129.5
7–3 Q(1)	7–5 Q(1)	5.0	2.1
7–3 S(1)	7–5 S(1)	4.1	1.7
7–3 S(2)	7–5 S(2)	4.8	2.5
7–3 Q(5)	7–5 Q(5)	3.9	3.2
7–3 S(4)	7–5 S(4)	5.5	3.2
7–3 Q(7)	7–3 S(5)	-5.2	25.2
8–4 S(1)	8–6 S(1)	6.7	2.5
8–4 S(3)	8–6 S(3)	6.8	2.3

Line 1	Line 2	A_v	±
1–0 Q(3)	1–0 S(1)	-2.3	14.7
1–0 Q(4)	1–0 S(2)	4.2	20.9
2–0 S(1)	2–0 Q(3)	8.8	28.1
2–0 S(1)	2–1 S(1)	2.0	5.2
2–0 Q(3)	2–1 S(1)	0.6	6.3
2–0 S(2)	2–1 S(2)	0.7	4.3
3–0 S(0)	3–0 Q(2)	16.2	51.5
3–0 Q(2)	3–0 S(0)	5.4	60.9
3–0 S(0)	3–0 Q(2)	17.8	46.6
3–0 Q(2)	3–1 O(4)	6.7	2.7
3–0 S(1)	3–0 Q(3)	7.1	10.4
3–0 S(1)	3–2 S(1)	4.7	1.5
3–0 S(1)	3–1 O(5)	5.7	1.3
3–0 Q(3)	3–1 S(1)	5.9	2.6
3–0 Q(3)	3–2 S(1)	3.5	3.2
3–0 S(1)	3–0 Q(3)	14.8	11.8
3–0 S(1)	3–2 S(1)	5.4	1.6
3–0 S(1)	3–1 O(5)	6.7	1.4
3–0 Q(3)	3–2 S(1)	4.5	1.9
3–0 Q(3)	3–1 O(5)	5.5	1.8
3–1 S(1)	3–2 S(1)	0.5	8.0
3–2 S(1)	3–1 O(5)	1.1	7.8
3–0 S(2)	3–2 S(2)	3.9	2.6
3–0 S(2)	3–2 S(2)	4.8	2.6
3–0 S(3)	3–2 S(3)	4.7	2.2
3–0 S(4)	3–1 S(4)	8.2	3.8
3–0 S(4)	3–1 S(4)	7.8	3.2
4–1 Q(1)	4–2 O(3)	6.8	2.4
4–1 Q(1)	4–2 O(3)	5.6	2.5
4–1 S(0)	4–1 Q(2)	-7.3	62.3
4–1 Q(2)	4–1 S(0)	-4.7	62.1
4–1 S(0)	4–2 O(4)	6.7	2.5
4–1 S(1)	4–2 O(5)	6.7	1.7
4–1 Q(3)	4–2 O(5)	6.8	3.1
4–1 S(2)	4–2 S(2)	10.4	3.7
4–1 S(3)	4–3 S(3)	5.1	3.7
4–1 S(3)	4–3 S(3)	5.3	3.7
4–1 S(3)	4–3 S(3)	5.3	3.7
4–3 S(3)	4–2 O(7)	8.2	41.3
4–1 S(5)	4–2 S(5)	5.7	2.5
5–3 Q(1)	5–3 O(3)	-3.1	15.2
5–2 S(2)	5–3 Q(4)	7.6	5.0
5–2 S(3)	5–3 Q(5)	6.9	2.0
5–2 S(3)	5–3 Q(5)	7.0	2.1
5–2 S(4)	5–3 Q(6)	10.0	4.1
6–4 S(0)	6–4 Q(2)	-38.7	137.0
6–4 S(1)	6–4 Q(3)	-1.3	19.8
7–3 Q(1)	7–5 Q(1)	6.7	3.3
7–3 S(2)	7–5 S(2)	4.2	2.1
7–3 Q(5)	7–3 S(3)	5.1	16.5
7–3 S(3)	7–5 Q(5)	4.0	1.4
7–3 S(5)	7–3 Q(7)	-3.1	25.5
8–4 S(1)	8–4 Q(3)	25.0	25.5
8–4 Q(3)	8–6 S(1)	4.8	3.1
—	—	—	—

Table D.1: Extinction calculated from pairs of lines originating from the same upper level.

Appendix E

Distribution of Data Points

Figures E.1, E.2 and E.3 display column densities for the energy states derived from all the observations of transitions before weighted means were taken. They give an indication of the scatter within the larger datasets. Figure E.4 shows a histogram of the deviation of column densities from the model for the entire 165 lines of the dataset. The distribution describes a somewhat flattened bell curve with a full width half maxima of about one sigma. Figures E.5 to E.12 compare the data from the different observations and display the individual contribution of each data point to the overall χ^2. This provides a fast way of judging how reliable any data point is and testing the validity of any suspected trends.

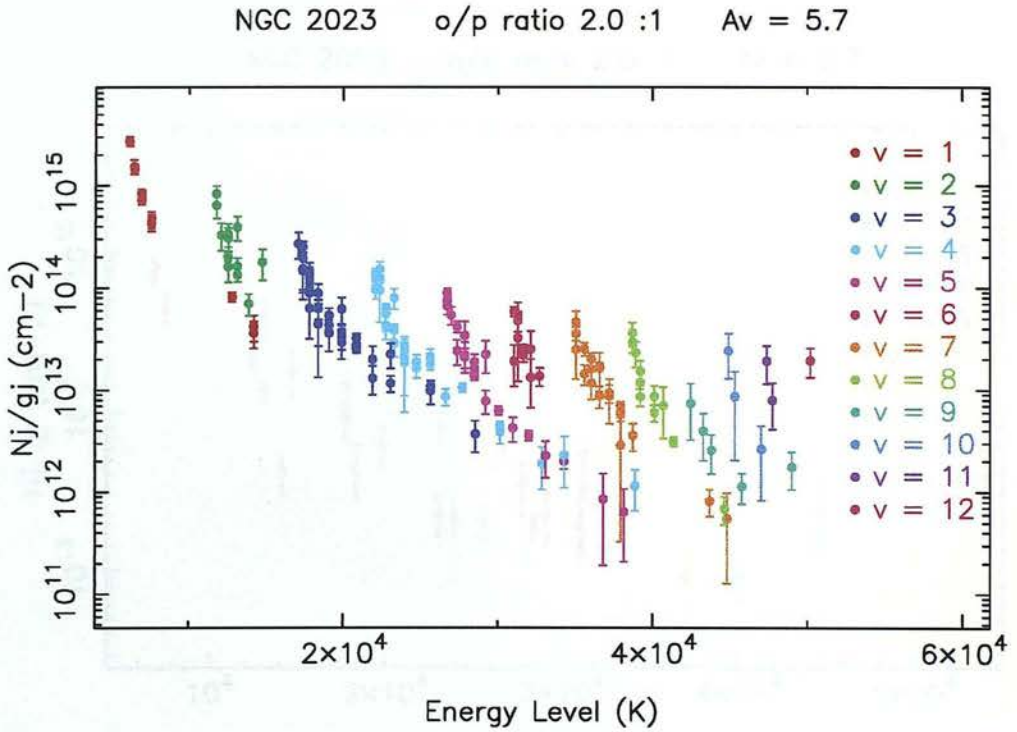

Figure E.1: Column densities of all levels derived from complete dataset (165 points).

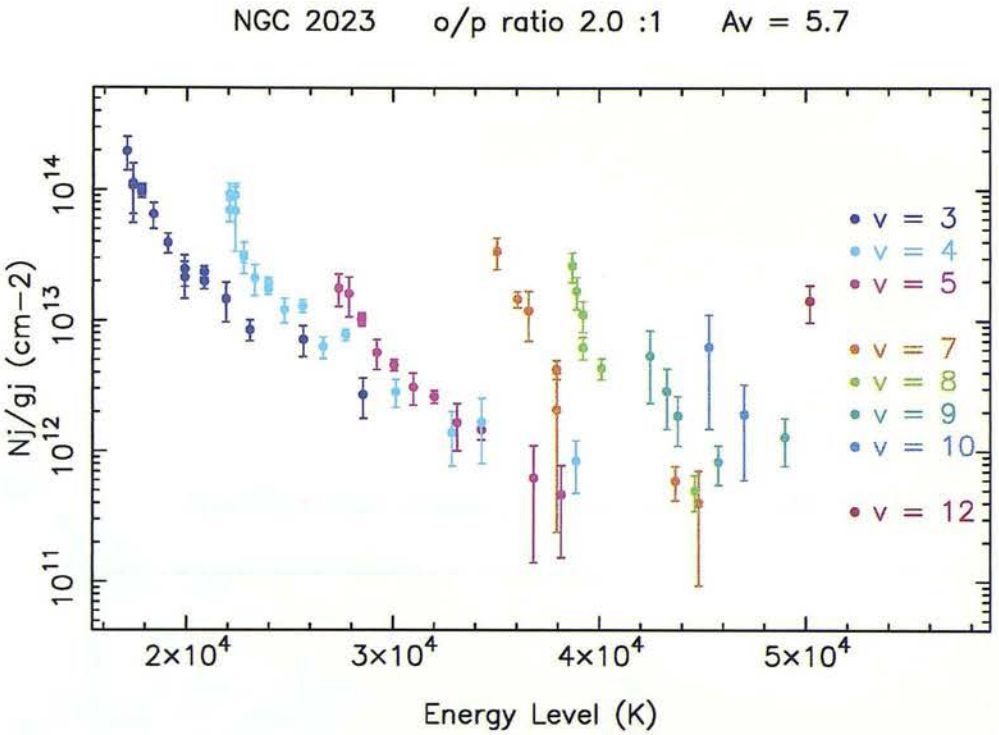

Figure E.2: Column densities of all levels derived from 1996 RGO Spectrograph observations (65 points).

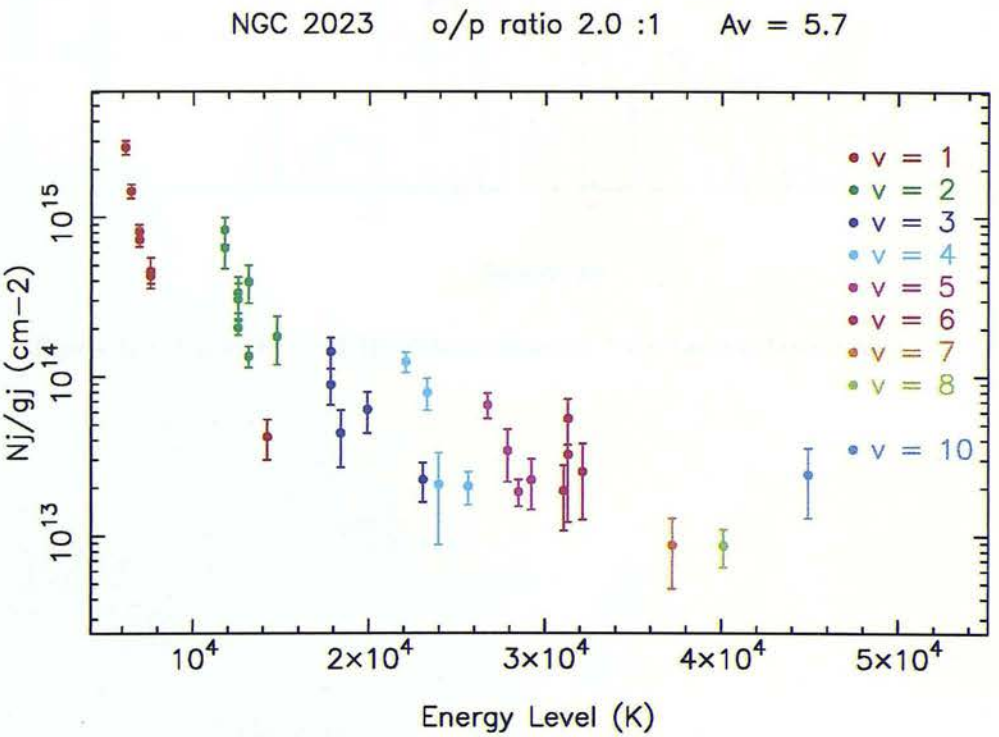

Figure E.3: Column densities of all levels derived from 1989 CGS2 observations (35 points).

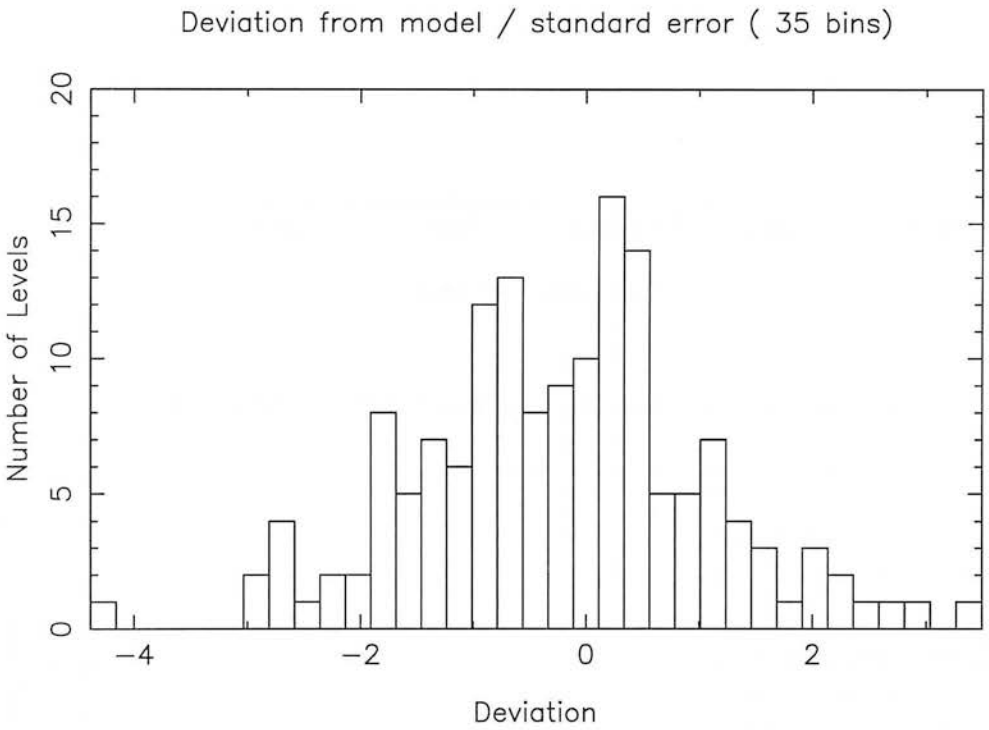

Figure E.4: Distribution of 165 column densities for complete dataset about the model.

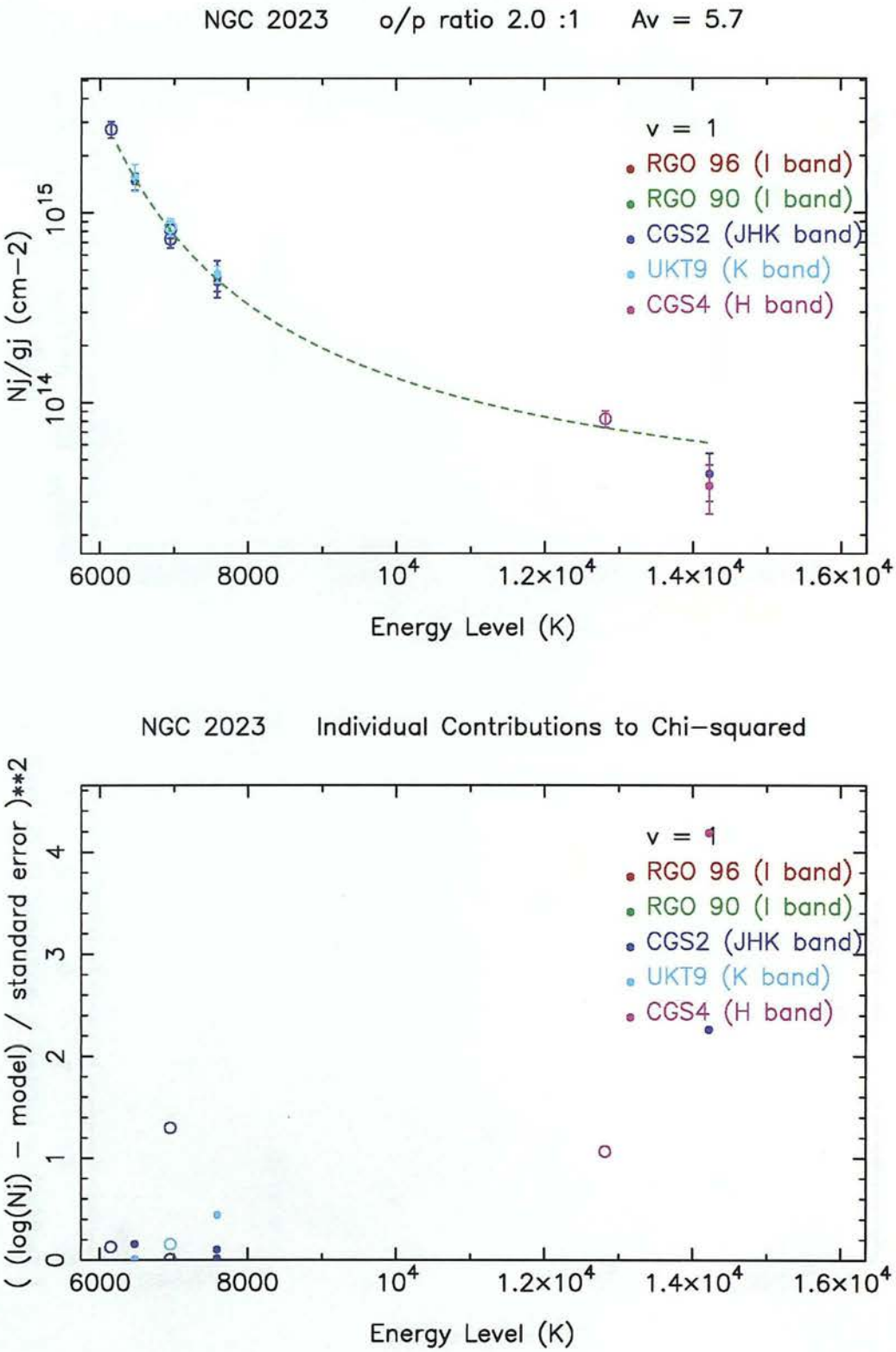

Figure E.5: Comparison of data points and contribution to χ^2 from the different observations for the 1st vibrational level.

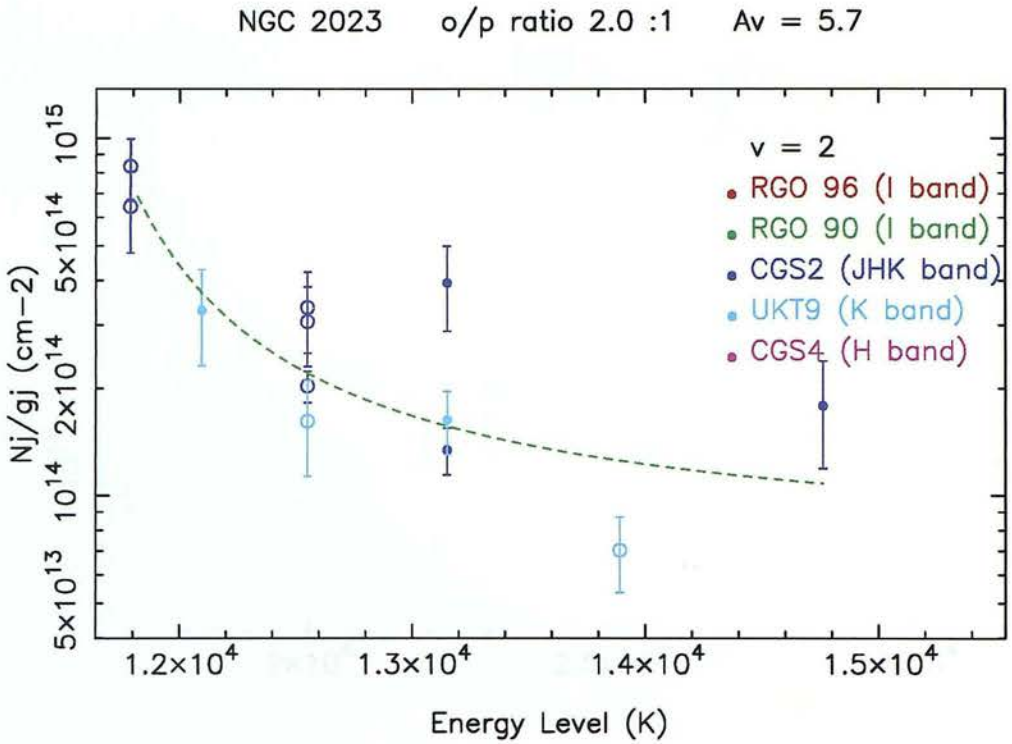

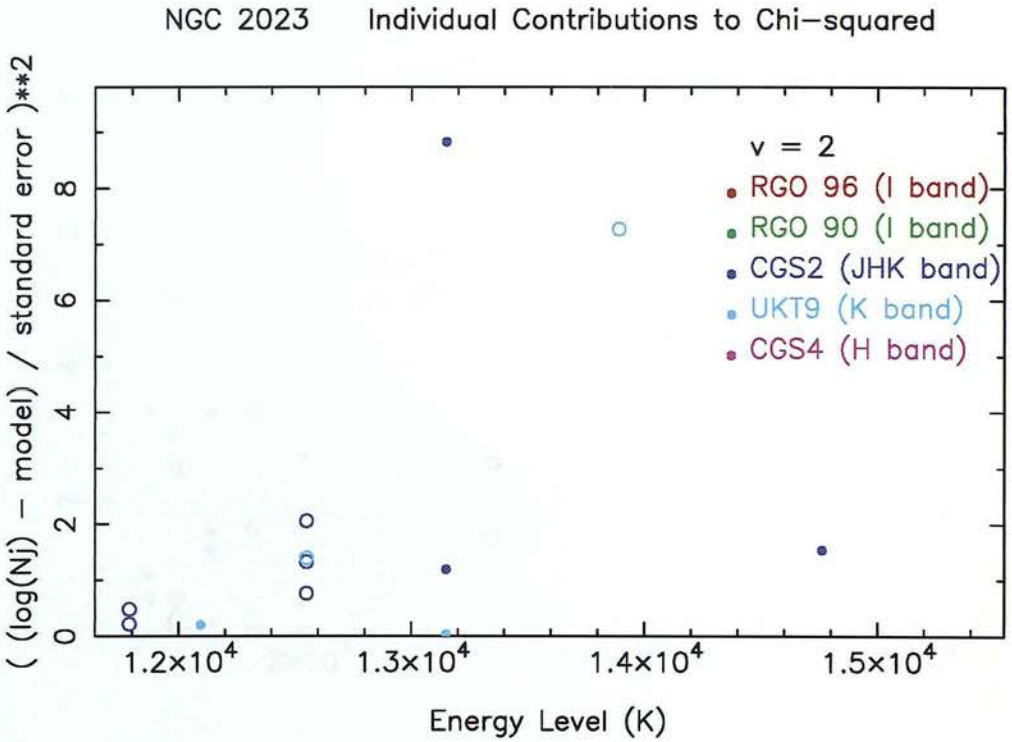

Figure E.6: Comparison of data points and contribution to χ^2 from the different observations for the 2nd vibrational level.

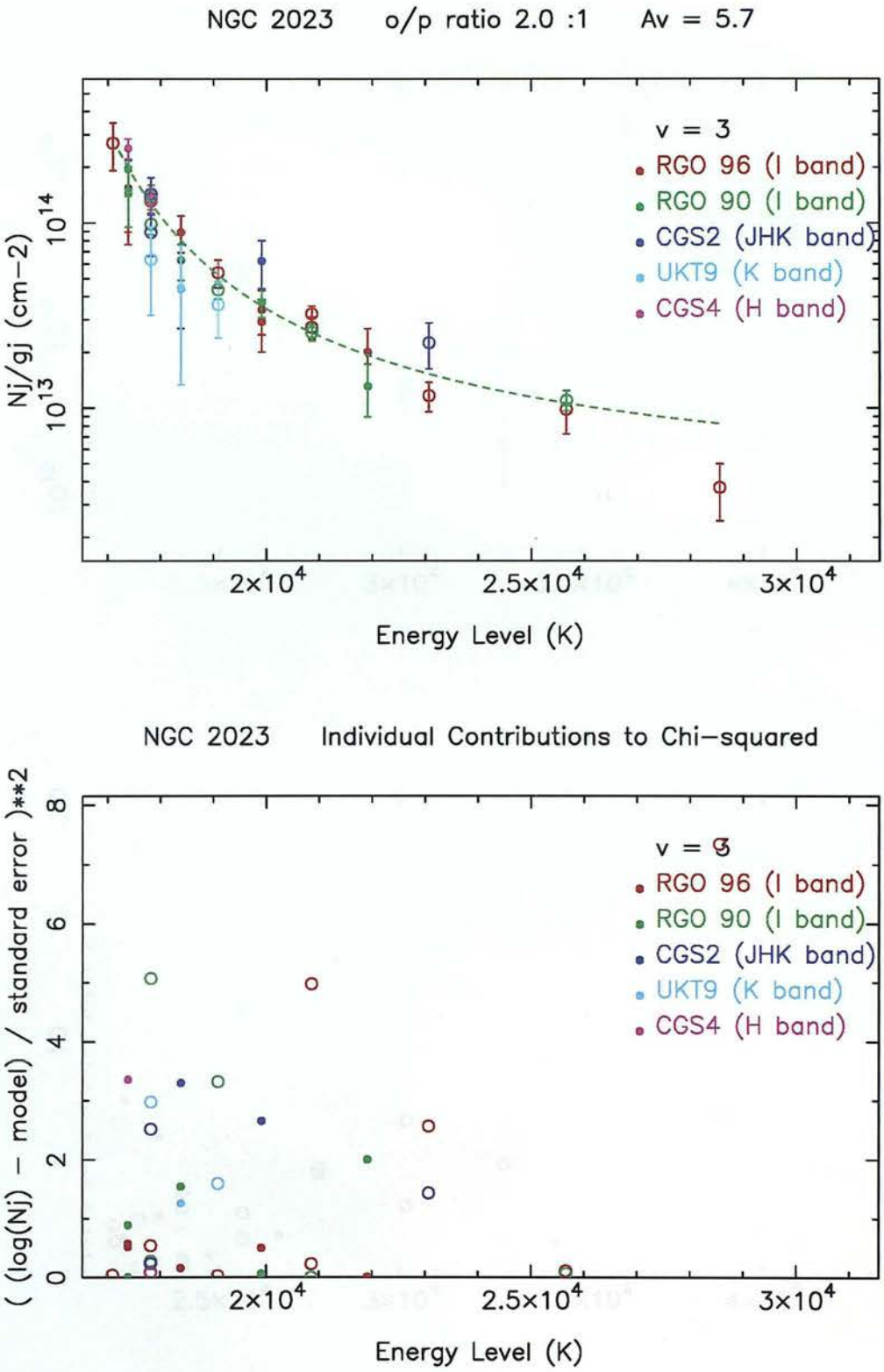

Figure E.7: Comparison of data points and contribution to χ^2 from the different observations for the 3rd vibrational level.

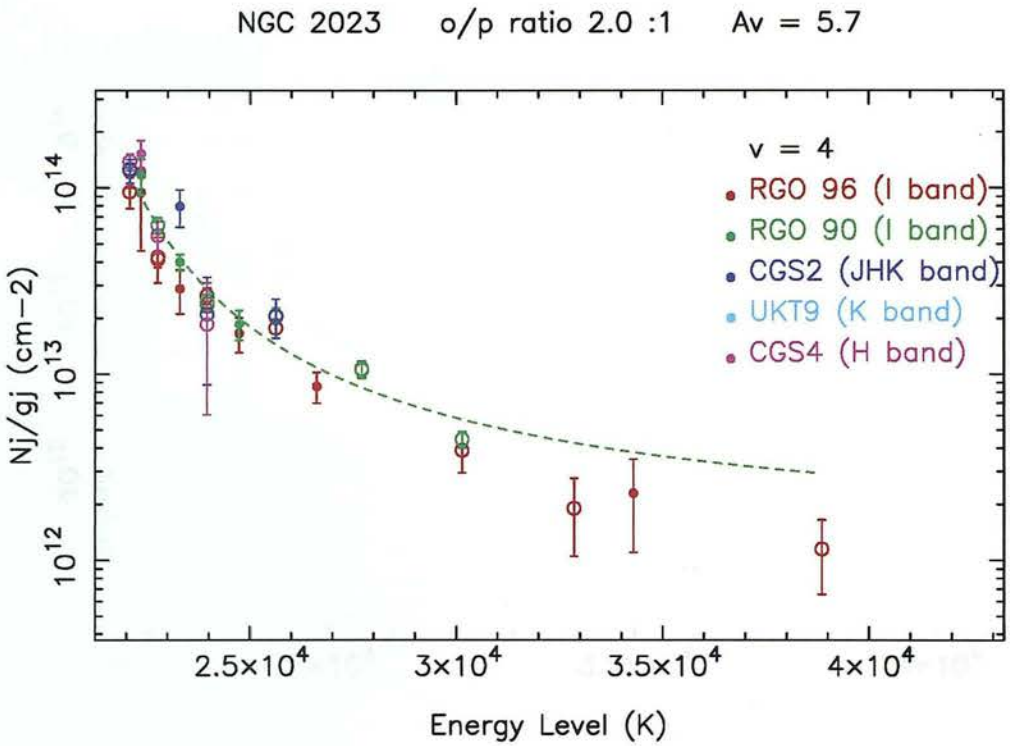

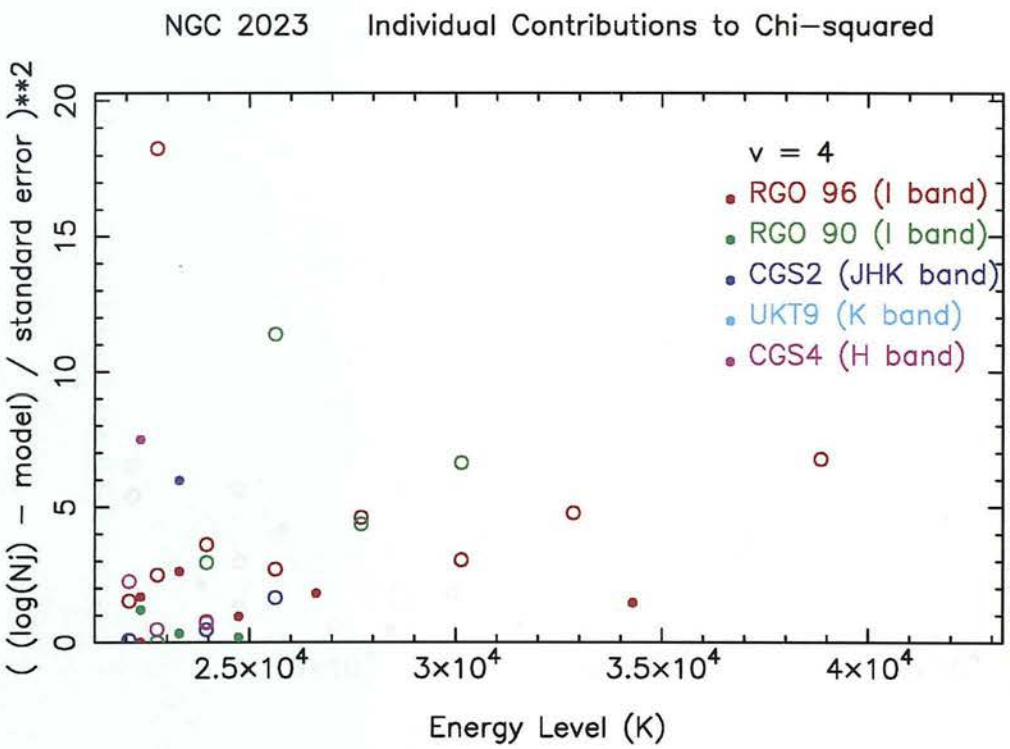

Figure E.8: Comparison of data points and contribution to χ^2 from the different observations for the 4th vibrational level.

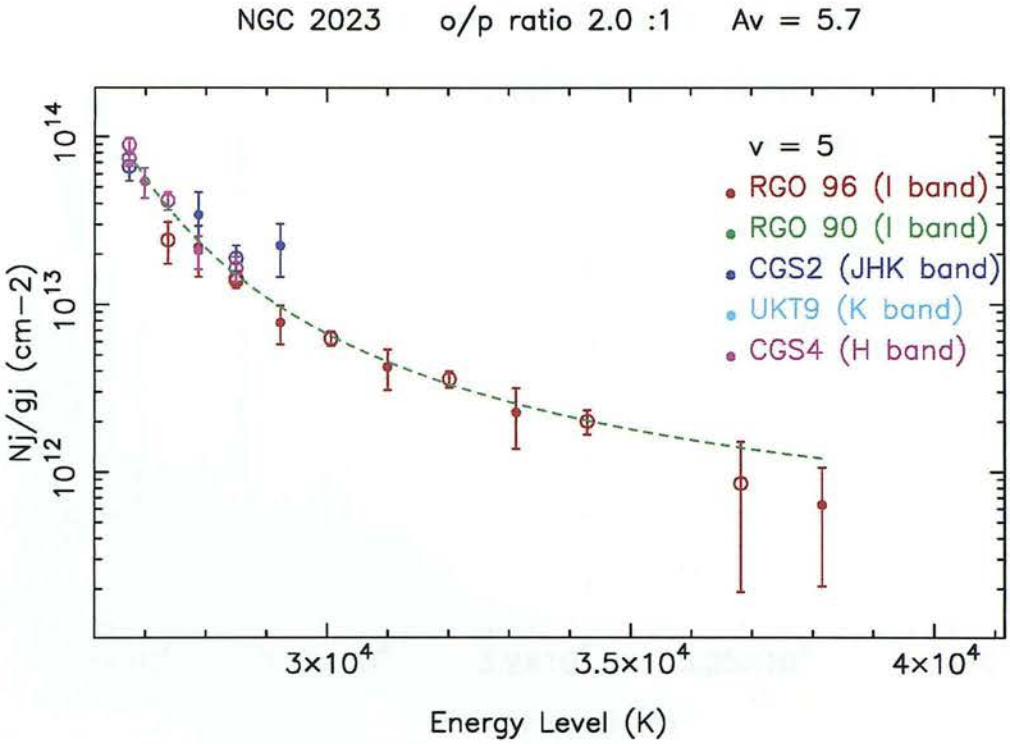

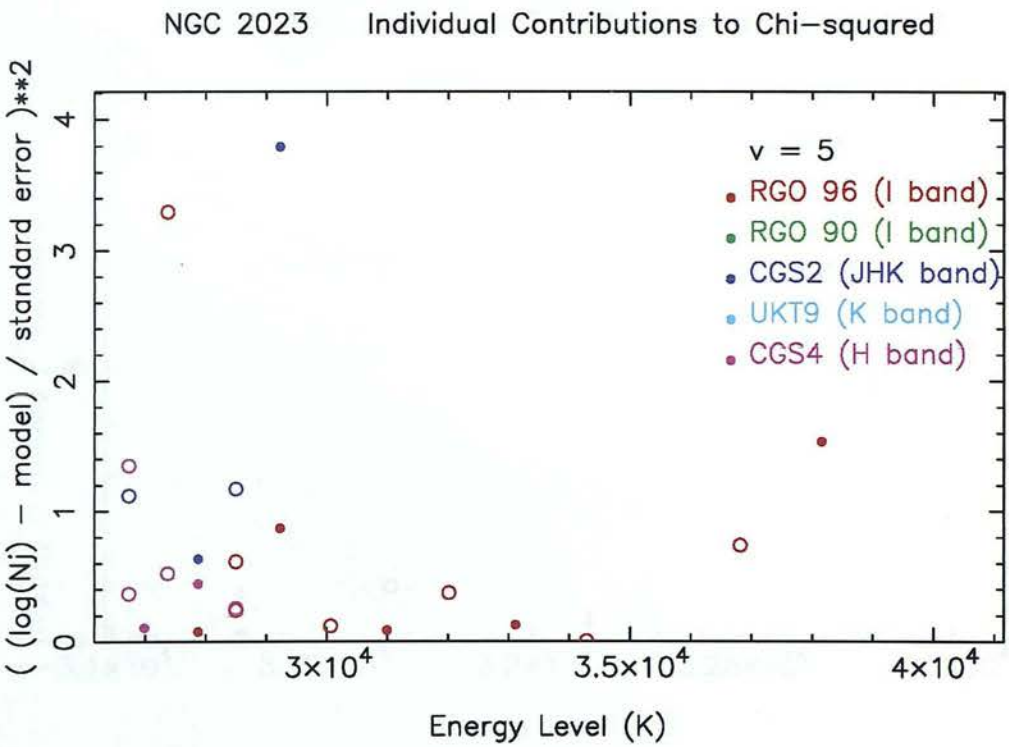

Figure E.9: Comparison of data points and contribution to χ^2 from the different observations for the 5th vibrational level.

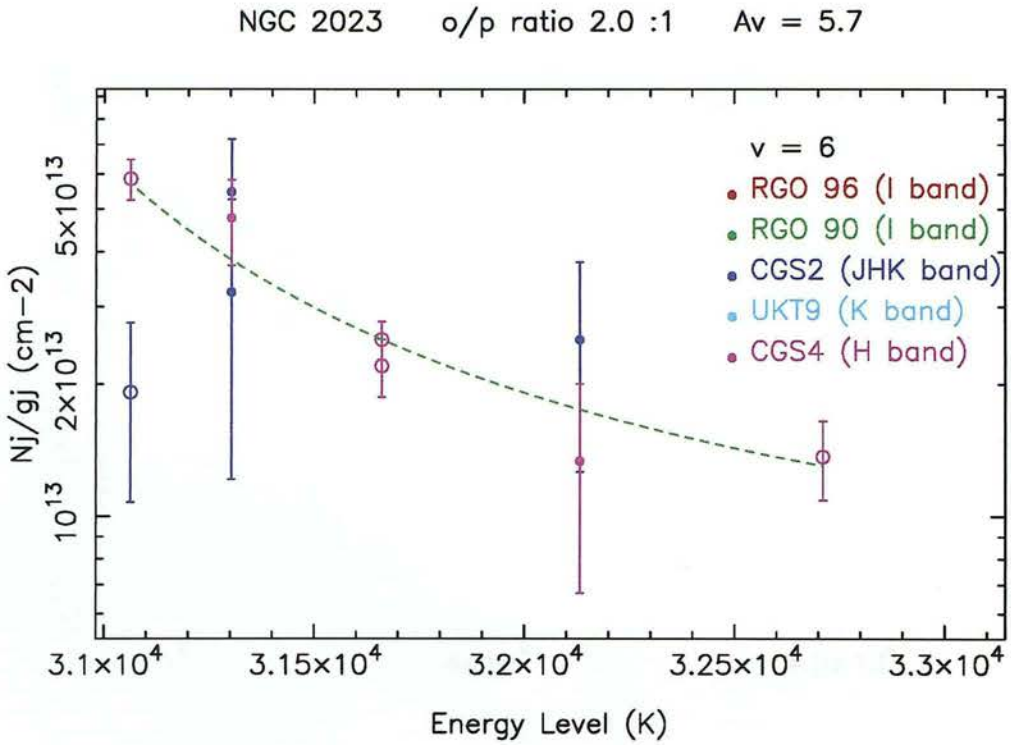

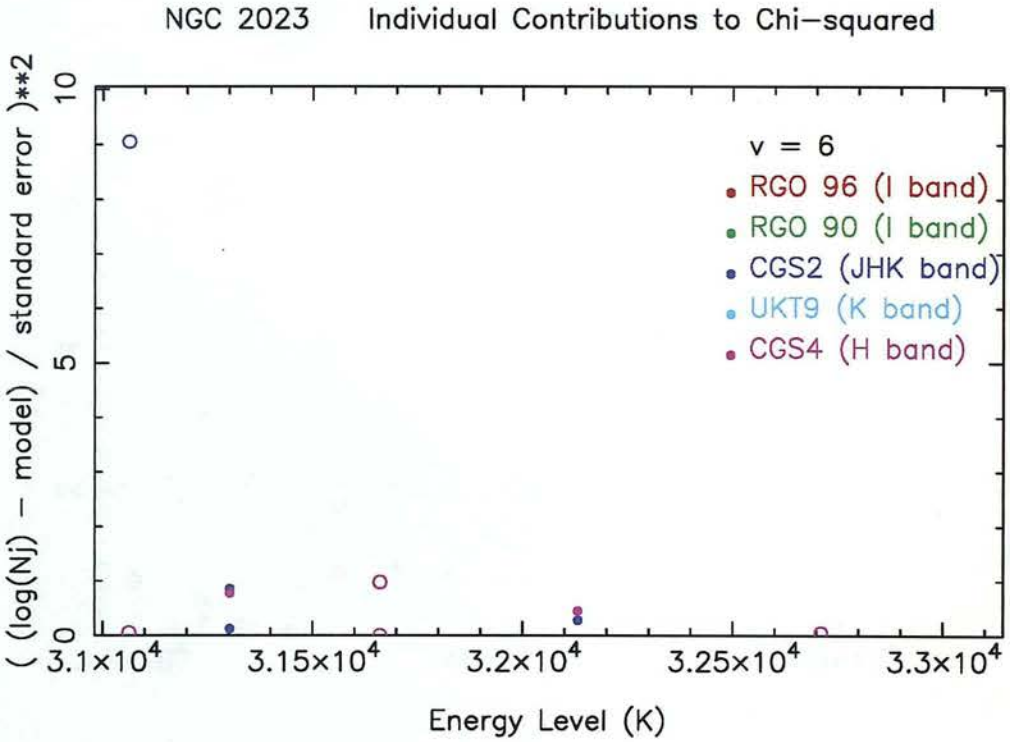

Figure E.10: Comparison of data points and contribution to χ^2 from the different observations for the 6th vibrational level.

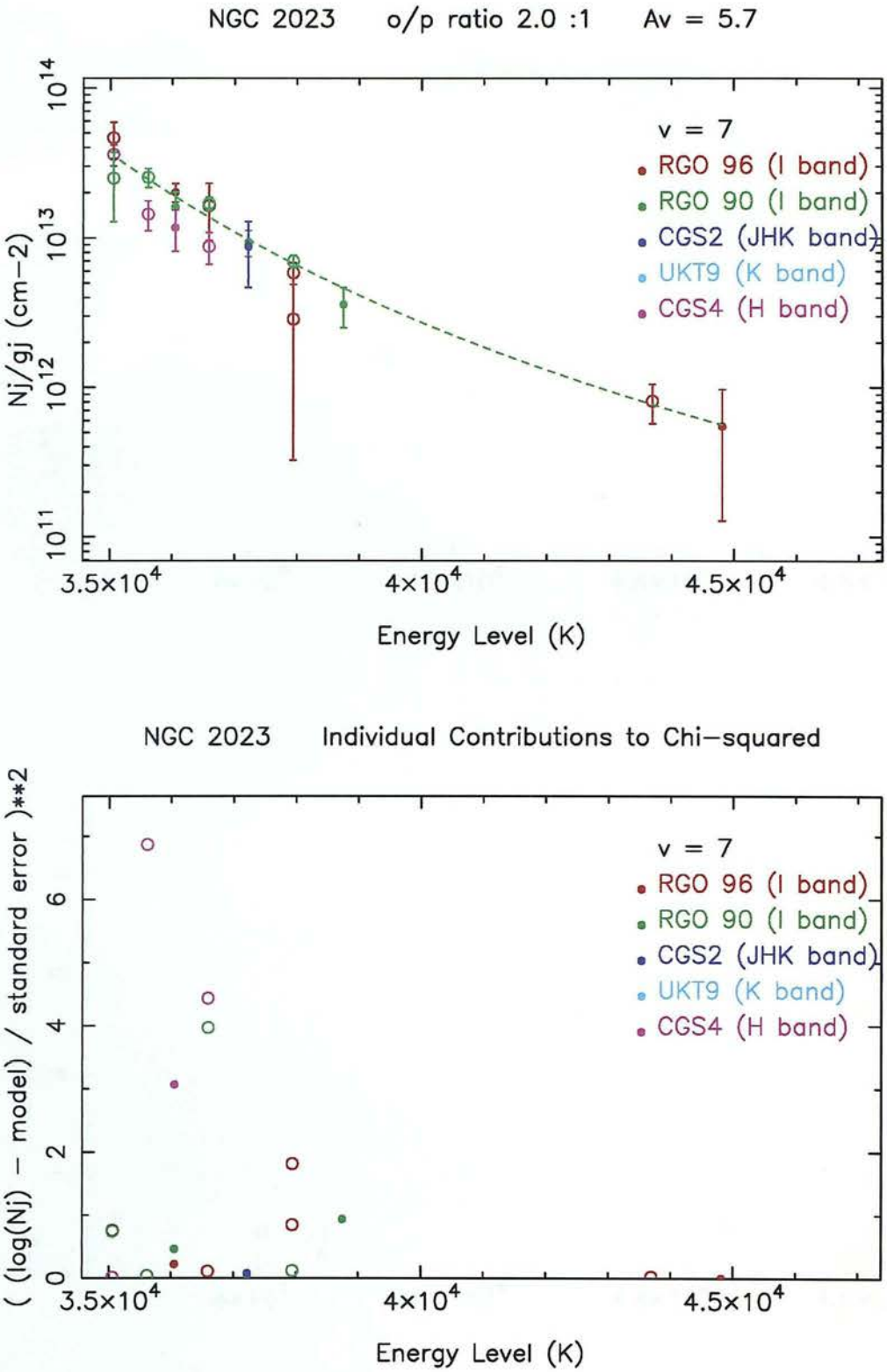

Figure E.11: Comparison of data points and contribution to χ^2 from the different observations for the 7th vibrational level.

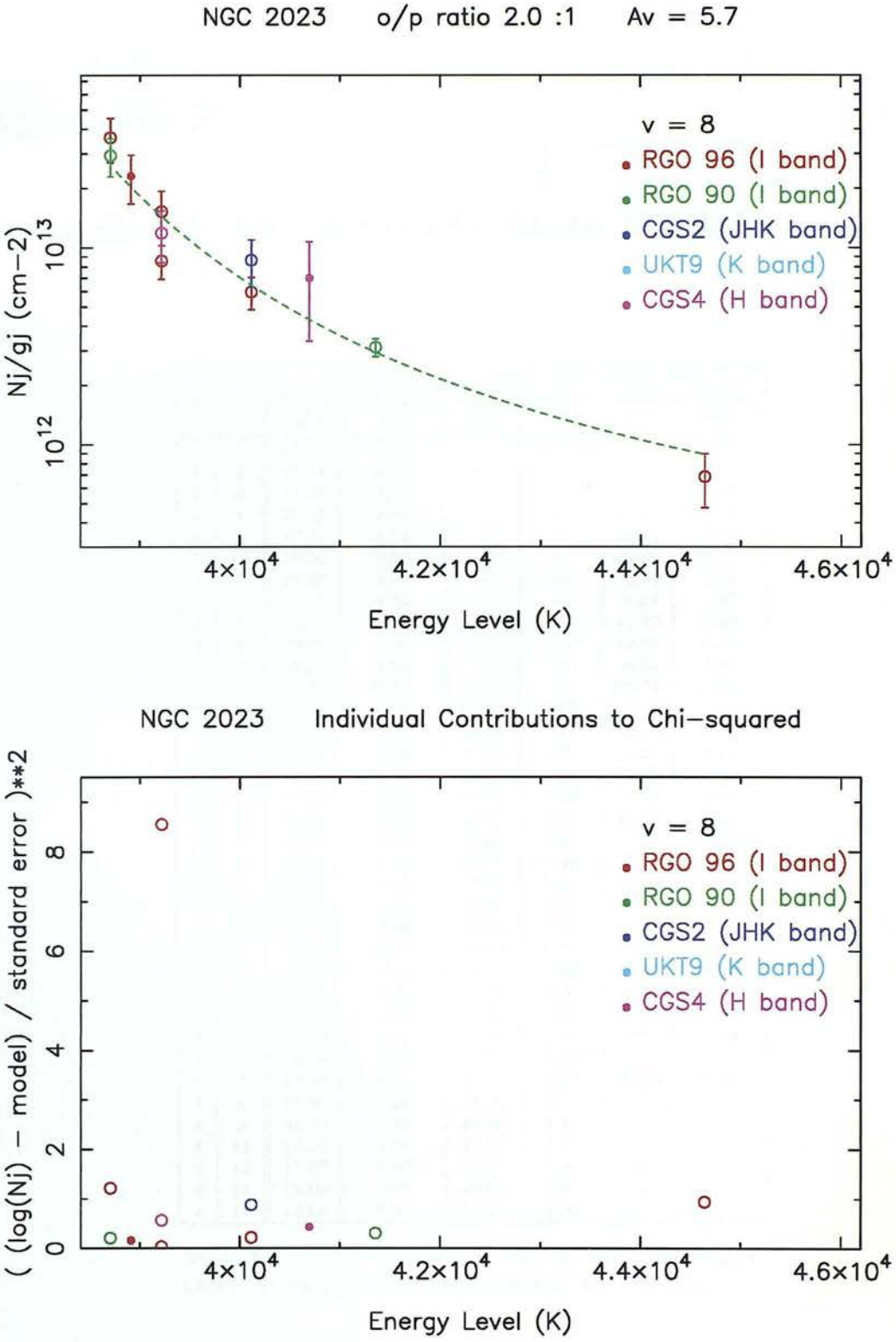

Figure E.12: Comparison of data points and contribution to χ^2 from the different observations for the 8th vibrational level.

Appendix F

Data Divided by a Steady-State Model

v	J	Ratio of Observed data to BvD Model #14					
		Complete dataset		Far-red dataset		Infrared dataset	
		ratio	error	ratio	error	ratio	error
1	1	55.55	5.56	—	—	55.55	5.56
1	2	35.53	3.55	—	—	24.12	2.41
1	3	31.16	3.12	—	—	18.82	1.88
1	4	25.25	2.53	—	—	13.93	1.39
1	9	47.22	4.72	—	—	35.42	3.54
1	10	29.60	6.05	—	—	24.20	5.05
2	1	25.33	3.95	—	—	25.33	3.95
2	2	14.49	4.35	—	—	6.23	1.87
2	3	16.84	1.68	—	—	12.20	1.22
2	4	19.85	2.26	—	—	12.61	1.52
2	5	19.81	4.75	—	—	8.52	2.04
2	6	83.74	27.91	—	—	83.74	27.91
3	1	15.95	4.59	15.95	4.59	—	—
3	2	14.49	1.53	11.48	2.11	13.35	1.66
3	3	16.85	1.69	17.12	1.71	9.21	1.14
3	4	12.41	1.83	14.39	2.30	5.74	2.13
3	5	18.16	1.82	18.55	1.86	6.33	2.15
3	6	26.20	3.26	24.95	3.37	45.10	13.11
3	7	36.40	3.64	36.40	3.64	—	—
3	8	27.57	6.49	27.57	6.49	—	—
3	9	30.16	4.75	27.50	5.02	53.08	14.75
3	11	39.68	4.40	39.68	4.40	—	—
3	13	22.71	7.76	22.71	7.76	—	—
4	1	11.66	1.17	9.81	1.38	10.05	1.00
4	2	14.33	1.64	13.16	1.95	12.89	2.28
4	3	9.98	1.00	9.85	0.99	8.78	1.63
4	4	13.56	1.36	13.15	1.32	27.39	6.22
4	5	17.20	1.72	17.28	1.73	11.39	5.12
4	6	18.78	2.60	18.78	2.60	—	—
4	7	39.69	3.97	39.68	3.97	39.86	9.42
4	8	27.80	5.21	27.80	5.21	—	—
4	9	44.60	4.46	44.60	4.46	—	—
4	11	27.53	2.75	27.53	2.75	—	—
4	13	17.67	7.90	17.67	7.90	—	—
4	14	19.00	9.87	19.00	9.87	—	—
4	17	16.06	6.94	16.06	6.94	—	—

Table F.1: Ratio of observed data to BvD model #14. Observed data has been normalised to the CGS2 data.

v	J	Ratio of Observed data to BvD Model #14					
		Complete dataset		Far-red dataset		Infrared dataset	
		ratio	error	ratio	error	ratio	error
5	1	10.43	1.04	—	—	8.17	0.82
5	2	9.06	1.83	—	—	6.79	1.37
5	3	10.69	1.23	7.34	2.04	9.46	1.16
5	4	10.95	1.84	10.78	3.61	8.32	1.65
5	5	14.84	1.48	14.37	1.44	14.18	1.81
5	6	14.46	3.26	12.94	3.36	37.15	13.00
5	7	19.27	1.93	19.27	1.93	—	—
5	8	17.38	4.77	17.38	4.77	—	—
5	9	21.81	2.42	21.81	2.42	—	—
5	10	15.30	6.02	15.30	6.02	—	—
5	11	17.69	2.96	17.69	2.96	—	—
5	13	9.83	7.63	9.83	7.63	—	—
5	14	7.49	5.05	7.49	5.05	—	—
6	1	8.71	0.96	—	—	7.43	0.79
6	2	11.51	2.02	—	—	9.42	1.67
6	3	10.79	1.08	—	—	8.09	0.81
6	4	11.29	4.17	—	—	8.55	3.29
6	5	20.70	4.25	—	—	15.52	3.19
7	1	10.09	1.36	9.96	2.48	7.61	1.22
7	3	11.92	1.52	15.77	2.31	6.72	1.52
7	4	18.86	2.21	21.24	2.64	9.91	3.05
7	5	30.40	3.04	35.18	3.52	13.66	3.25
7	6	31.01	5.67	31.36	6.23	29.32	13.68
7	7	36.56	3.66	36.56	3.66	—	—
7	8	28.55	8.57	28.55	8.57	—	—
7	13	17.40	5.11	17.40	5.11	—	—
7	14	11.82	9.07	11.82	9.07	—	—
8	1	11.97	2.00	11.97	2.00	—	—
8	2	10.77	2.97	10.77	2.97	—	—
8	3	8.74	1.24	8.40	1.36	7.85	2.30
8	5	18.15	2.80	16.74	3.11	24.24	6.46
8	6	29.94	15.65	—	—	22.45	11.74
8	7	24.39	2.52	24.39	2.52	—	—
8	11	15.12	4.64	15.12	4.64	—	—
9	3	8.74	4.93	8.74	4.93	—	—
9	5	13.33	6.51	13.33	6.51	—	—
9	6	13.67	5.64	13.67	5.64	—	—
9	9	21.91	7.29	21.91	7.29	—	—
9	13	60.27	24.09	60.27	24.09	—	—
10	1	15.95	7.44	—	—	15.95	7.44
10	3	11.87	9.08	11.87	9.08	—	—
10	7	29.77	20.49	29.77	20.49	—	—
11	1	15.94	6.42	—	—	11.96	4.82
11	3	12.84	6.20	—	—	9.63	4.65
12	5	84.85	26.93	84.85	26.93	—	—

Table F.1: Ratio of observed data to BvD model #14. Observed data has been normalised to the CGS2 data.

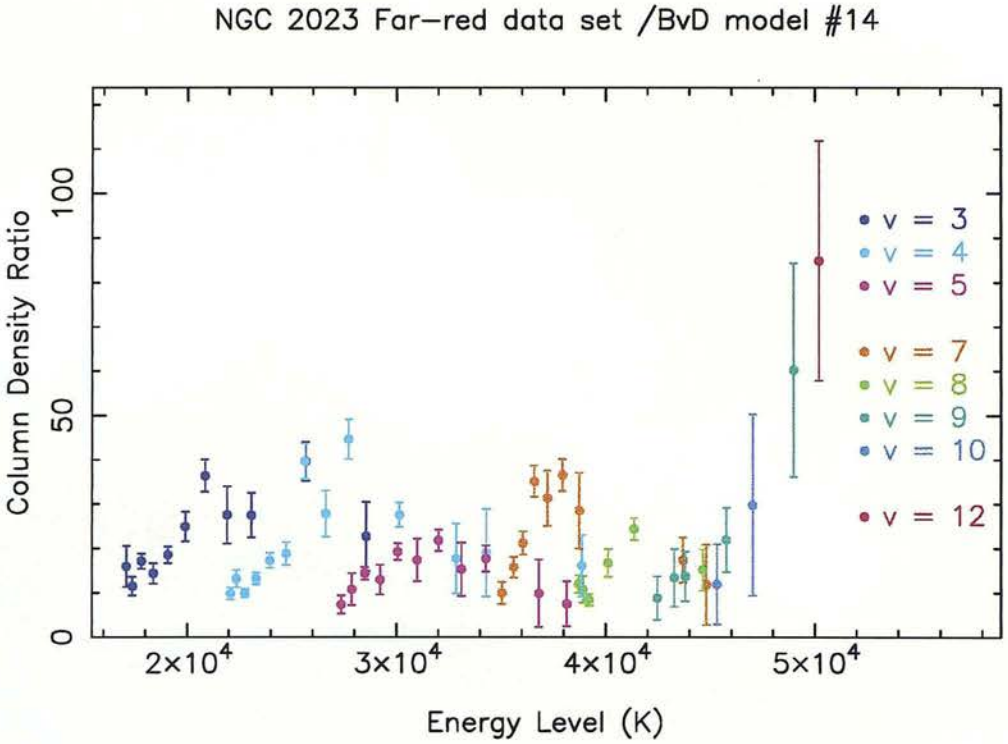

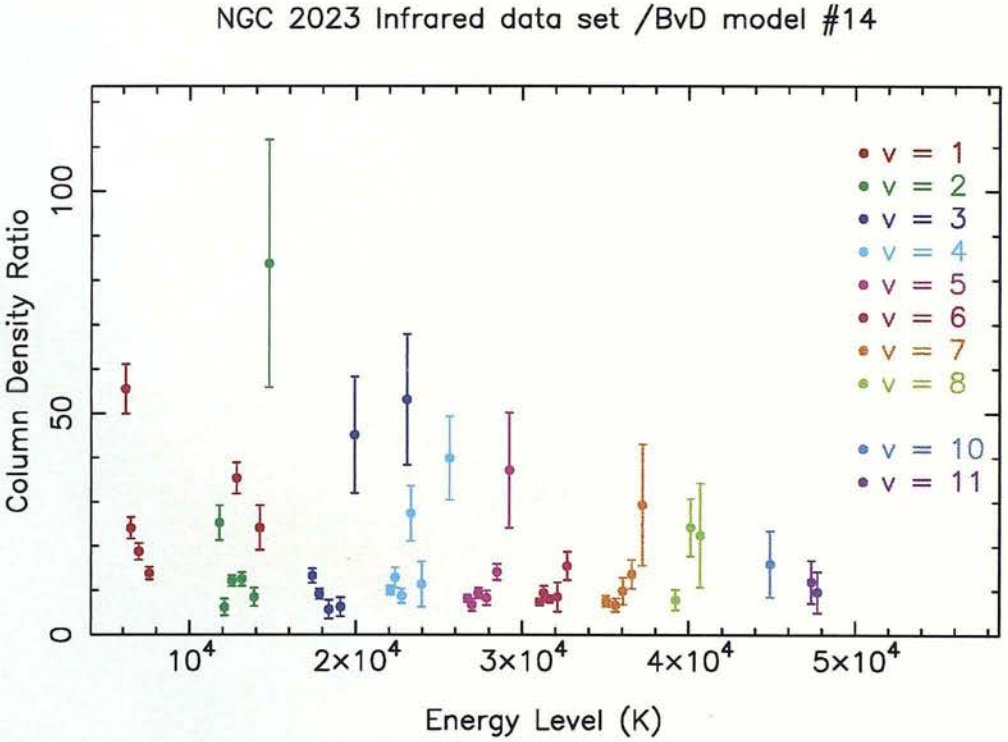

Figure F.1: The far-red and infrared datasets plotted separately, each divided by BvD model #14.